

**Studies on the heterogeneous catalytic process for production
of liquid fuels and fine chemicals from hemicellulose derived
furfural and furfuryl alcohol**

By
THUPPATI Upender Rao

A Dissertation Submitted to
Nagoya University
In Partial Fulfilment of the Requirements for
The Degree of Doctor of Philosophy

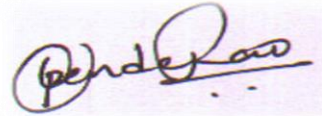


Department of Chemical Systems Engineering

Approved by the Faculty Council: July, 2022

Declaration

I declare that this written submission represents my ideas in my own words, and where others' ideas or words have been included, I have adequately cited and referenced the original sources. I also declare that I have adhered to all principles of academic honesty and integrity and have not misrepresented or fabricated or falsified any idea/data/fact/source in my submission. I understand that any violation of the above will be a cause for disciplinary action by the Institute and can also evoke penal action from the sources that have thus not been properly cited, or from whom proper permission has not been taken when needed.



(Signature)

THUPPATI Upender Rao

(– Student Name –)

481933050

(Student ID.)

Dedication

To my beloved family

Acknowledgments

I would like to thank everyone who supported me in completing this thesis work. First and foremost, I would like to express my sincere gratitude to my supervisor, **Prof. NORINAGA Koyo** sensei, for guiding me during the past three years. I have been fortunate to have him as my thesis advisor. The support, knowledge, and the encouragement given to me during the research work are indelible and also thankful to him for his insightful suggestions and generous patience. I would like to express my sincere regards to **Associate Prof. Machida Hiroshi** sensei for his constant support throughout the course, encouraging me, and being a panel member to evaluate my thesis. I am also conveying my sincere thanks to the panel members Prof. Takami Seiichi sensei, Department of Chemical Systems Engineering, Nagoya University, Prof. Matsuo Yutaka sensei, Department of Chemical Systems Engineering, Nagoya University, and Prof. Hayashi Junichiro Sensei, Department of Advanced Device Materials, Kyushu University for their invaluable suggestions and serving as my thesis evaluation committee members. I also would like to extend my thanks to Prof. Huo Zhibao, Shanghai Jiao Tong University, a collaboration member of the Nori lab.

I would like to express my sincere gratitude to Assistant professors Dr. Choi Cheylong, Dr. Tran Khuyen, and Dr. Suchada in Nori lab for providing laboratory and departmental facilities to complete this thesis work. I also thank Dr. Fukumoto, Dr. Yanase, Dr. Wei Zhang and Dr. Hirayama for their support. I am also very thankful to all the faculty members for their support and guidance during the course work. I would like to thank Nori lab supporting staff Tobe san, Minami san, Kozaki san, Aiko san, and Yamaguchi san for their assistance in administration related and daily life proceedings. I also extend my sincere acknowledgements to the Nagoya University former President Prof. Seiichi Matsuo and the current President Prof. Naoshi Sugiyama for providing the opportunity to pursue my doctoral course in Nagoya University.

I stand firm to appreciate the support and opportunity provided by JICA to receive IITH- FRIENDSHIP scholarship. I would like to express my sincere gratitude for JICA members especially Chikako Hiura san, Takenaga Chihiro san, and Tomioka Ryoko san for supporting and guiding me throughout the course. I take this opportunity to express

my sincere regards to Dr. Swapnil Ghodke, my IITH senior and first JICA student at Nagoya University who guided, mentored, and helped me during the past three years. I also extend my sincere thanks to other JICA seniors Dr. Mahendra and Dr. Pravin, and family members Prof. Veenadhari, Dr. Srinivas, Ms. Revathi, Ms. Ashwini, Dr. Frank, Dr. Satya, and Ms. Leiko for their support and guidance in Japan.

I will be forever grateful to my family (Father, Mother, younger brother, younger sister, brother-in-law, nephew, and other family members), who supported me throughout my education and showed immense love and affection. I also convey my sincere regards to my best friends G Vamsi Vikram and K Nikhilesh, and all of my friends who motivated me in hard times and being with me always.

I am very thankful and glad to have Zhang Lijuan, and Lin Yixiong as fellow doctoral students and for their support. I also extend my sincere thanks to other PhD members of Nori lab Angakan san, Park san, Wasnik san, Dai san, and especially Li Qiuaos san for his assistance in Aspen Plus simulations. I also take this opportunity to express my sincere thanks to Fukuoka kun, Furuta kun, Kuroyanagi kun, Nakaoka chan, Ninomi chan, Mizoguchi chan, Hashiride kun, Kobayashi kun, Takumi kun, Ogawa kun, Harada kun and Shimada kun for their friendship and support during my course.

Table of Contents

Declaration	ii
Approval Sheet.....	Error! Bookmark not defined.
Dedication.....	iii
Acknowledgments.....	iv
Table of Contents.....	vi
List of Figures	x
List of Tables.....	xiii
List of Publications	xv
List of Conferences	xv
Abstract	xvi
Chapter 1: Introduction, literature review, and objectives	1
1.1 Introduction and background	1
1.2 Hemicellulose derived furfural as a platform chemical for fuel additives, biofuels and fine chemicals	5
1.2. Research focus	7
1.2.1 Butyl levulinate from FAL.....	7
1.2.1.1 Literature review on butanolysis of FAL	7
1.2.1.2 Summary and gap analysis on butanolysis of FAL	11
1.2.1.4 Objectives of butanolysis of FAL.....	13
1.2.2 Hydrogenation of furfural to THFA.....	14
1.2.2.1 Literature review and gap analysis on furfural to THFA	15
1.3. Thesis outline	18
1.4 References.....	20
Chapter 2: A comprehensive study on butanolysis of furfuryl alcohol to butyl levulinate using tungstated zirconia and sulfonated carbon catalysts.....	26
2.1 Introduction.....	26
2.2 Materials and methods	28
2.2.1 Materials.....	28
2.2.2 Catalyst synthesis	29
2.2.2.1 Preparation of Tungstated Zirconia (WO ₃ -ZrO ₂).....	29

2.2.2.2 Preparation of sulfonated carbon	29
2.2.3 Catalyst characterization	30
2.2.4 Butanolysis of FAL.....	31
2.2.5 Catalyst reuse	32
2.3 Results and discussion on the characterization of WO ₃ -ZrO ₂ catalyst.....	32
2.3.1 Textural properties	32
2.3.2 NH ₃ -TPD analysis	34
2.3.3 Pyridine-FTIR analysis	36
2.4 Results and discussion on the characterization of sulfonated carbon catalysts	38
2.4.1 Textural properties	38
2.4.2 FTIR analysis	41
2.4.4 Pyridine FTIR analysis.....	42
2.4.5 TGA analysis carbon catalysts	44
2.5 Butanolysis of FAL reaction study	45
2.6 Butanolysis of FAL with WO ₃ -ZrO ₂	46
2.7 Reaction with sulfonated carbon catalysts.....	49
2.7.1 Effect of reaction temperature	49
2.7.2 Effect of reaction time.....	50
2.7.3 Effect of initial FAL concentration	52
2.7.4 Optimization of catalyst loading	53
2.7.5 Comparison with various acid catalysts	54
2.7.6 Hot filtration test	56
2.7.7 Spent analysis.....	58
2.8 Reaction with carbon black catalyst	59
2.9 Conclusions.....	60
2.10 References.....	61
Chapter 3: Selective hydrogenation of furfural to tetrahydrofurfuryl alcohol in 2-	
butanol over an equimolar Ni-Cu-Al catalyst prepared by the co-precipitation	
method	69
3.1 Introduction.....	70
3.2 Methodology	72
3.2.1 Chemicals	72
3.2.2 Catalysts preparation	72
3.2.3 Catalyst characterization	73
3.2.4 Catalytic hydrogenation of furfural.....	74

3.3 Results and discussions on catalysts characterization	75
3.3.1 Textural properties	75
3.3.2 XRD characterization.....	78
3.3.3 Structure and morphology characterization (SEM, TEM, and STEM-EDS). 81	
3.3.4 H ₂ -Temperature programmed reduction study (H ₂ -TPR).....	89
3.3.5 CO and N ₂ O chemisorption.....	92
3.3.6 NH ₃ -TPD study	96
3.3.7 XPS analysis.....	97
3.4 Results and discussion on hydrogenation of furfural.....	102
3.4.1 Catalytic performances.....	102
3.4.2 Optimization of reaction parameters	106
3.4.3 Turnover frequency (TOF) study	109
3.4.4 Influence of the solvent	111
3.2.2 Catalyst loading and reusability analysis	112
3.5 Spent analysis	113
3.5.1 TGA analysis.....	113
3.5.2 Textural properties	114
3.5.3 SEM, STEM-EDS, and XPS analysis	115
3.6 Conclusions.....	119
3.7 References.....	120
Chapter 4: The catalytic performance of Ni-Cu-Al catalysts on hydrogenation of	
furfural through thermo catalytic and electrocatalytic routes.....	128
4.1. Introduction.....	128
4.1.1 Furfural conversion pathway.....	129
4.1.2 Parameter selection for the design of ECH of furfural experiment.....	131
4.2 Methodology	134
4.2.1 Materials and Chemicals	134
4.2.2 Electrocatalyst preparation.....	134
4.2.3 Experimental	134
4.3 Results and Discussion	137
4.3.1 Cyclic voltammetry study	137
4.3.2 Electrocatalytic hydrogenation.....	138
4.3.3 Performance of Ni ₁ Cu ₁ -Al ₁ R in TCH and ECH processes	140
4.4 Conclusions.....	141
4.5 References.....	142

Chapter 5: Economic potential of tetrahydrofurfuryl alcohol (THFA) from the hydrogenation of furfural in 2-butanol	145
5.1 Introduction.....	145
5.2 Methodology	146
5.2.1 Process simulation.....	146
5.2.2 Details of process simulation	147
5.2.3 Economic analysis.....	148
5.3 Results and discussions.....	149
5.3.1 Stream results	149
5.3.2 Cost flow analysis	150
5.4 Conclusions.....	152
5.5 References.....	153
Chapter 6: Summary and future prospects	154
6.1 butanolysis of FAL to BL	154
6.1.1 Summary	154
6.1.2 Future prospects of butanolysis of FAL to BL.....	155
6.2 Hydrogenation furfural	156
6.2.1 Summary of hydrogenation of furfural	156
6.2.2 Future prospects of furfural utilization.....	158
APPENDIX	159
A.1 Methodology	159
A.2 Catalyst preparation	159
A.3 Liquid product analysis.....	162
A.3.1 Butanolysis of FAL	163
A.3.2 Furfural hydrogenation.....	164

List of Figures

Fig.1.1: World Total primary energy supply 2019 (Source: IEA).....	2
Fig.1.2: Lignocellulosic biomass fractionation and derived platform chemicals.	3
Fig.1.3: Furfural as a platform chemical for a wide range of products.....	6
Fig.2.1: BET analysis of tungstated zirconia catalysts a) N ₂ physisorption isotherms (b) BJH Pore size distribution	34
Fig.2.2: NH ₃ -TPD spectra of a) Tungstated zirconia catalysts b) Metal promoted catalysts	35
Fig.2.3: Pyridine-FTIR spectra of a) Tungstated zirconia catalysts b) Metal promoted catalysts	37
Fig.2.4: BET analysis of carbon catalysts a) N ₂ physisorption isotherms of sulfonated carbon catalysts b) Micropore distribution.....	39
Fig.2.5: FTIR analysis of the sulfonated carbon catalysts	41
Fig.2.6: Pyridine-FTIR analysis of the sulfonated carbon catalysts	43
Fig.2.7: TGA analysis of sulfonated carbon catalysts.....	44
Fig.2.8: GC-MS spectra of butanolysis of FAL reaction	46
Fig.2.9: Effect reaction temperature with WO ₃ -ZrO ₂ catalyst.....	47
Fig.2.10: Effect of reaction temperature, S- Selectivity, Y- Yield	50
Fig.2.11: Effect of reaction time	51
Fig.2.12: Effect of initial FAL concentration.....	52
Fig.2.13: Catalyst loading	53
Fig.2.14: Reaction with dilute H ₂ SO ₄	55
Fig.2.15: Butanolysis reaction results of a) hot filtration test, b) Hot filtration test in the interval of 15 to 30 minutes.....	57
Fig.2.16: Spent analysis of sulfonated carbon catalyst	58
Fig.2.17: Effect of carbon black catalyst loading	59

Fig.3.1: N ₂ adsorption-desorption isotherms: a) calcined catalysts and b) reduced catalysts	77
Fig.3.2: BJH pore size distribution: a) calcined catalysts and b) reduced catalysts	77
Fig.3. 3: XRD patterns of a) calcined catalysts and b) reduced catalysts	80
Fig.3.4: SEM images of (a) Ni-Al R, (b) Cu-Al R, (c) Ni ₁ Cu ₁ -Al ₁ R, (d) Ni ₂ Cu ₂ -Al ₁ R	82
Fig.3.5: TEM images and the corresponding particle size distribution of (a) Ni-Al R, (b) Cu-Al R, (c) Ni ₁ Cu ₁ -Al ₁ R, (d) Ni ₂ Cu ₂ -Al ₁ R	83
Fig.3.6: TEM images of Al ₂ O ₃ support prepared by the co-precipitation method	83
Fig.3.7: STEM-EDS mapping of the corresponding elements of the catalyst Ni-Al R .	84
Fig.3. 8: STEM-EDS mapping of the corresponding elements of the catalyst Cu-Al R	85
Fig.3.9: STEM-EDS mapping of the corresponding elements of the catalyst Ni ₁ Cu ₁ -Al ₁ R	86
Fig.3.10: STEM-EDS mapping of the corresponding elements of the catalyst Ni ₂ Cu ₂ -Al ₁ R	87
Fig.3.11: H ₂ -TPR profiles of a) calcined catalysts and b) reduced catalysts	90
Fig.3.12: H ₂ -TPR profile of CuO sample	91
Fig.3.13: NH ₃ -TPD profiles of a) calcined catalysts and b) reduced catalysts	96
Fig.3. 14: XPS spectra of a) Ni ₂ p of calcined catalysts, b) Cu ₂ p of calcined catalysts, c) Ni ₂ p of reduced catalysts, d) Cu ₂ p of reduced catalysts.....	99
Fig.3.15: Catalytic performances of the reduced catalysts	104
Fig.3.16: Furfural conversion pathway for monometallic and bimetallic catalysts in 2-butanol	105
Fig.3.17: Plausible reaction mechanism of hydrogenation of furfural over Ni ₁ Cu ₁ -Al ₁ R catalyst	106
Fig.3.18: Influence of reaction parameters on hydrogenation of furfural.....	108
Fig.3.19: Study of a) Catalyst loading, b) reusability analysis	112
Fig.3.20: TGA analysis of the fresh and spent catalyst.....	114
Fig.3.21: Textural properties a) N ₂ adsorption isotherms, b) BJH pore size distribution	115
Fig.3.22: SEM images of the fresh and spent catalysts.....	116

Fig.3.23: STEM-EDS mapping of the corresponding elements of the catalyst Ni1Cu1-A11 R Spent	117
Fig.3.24: XPS analysis, a) Ni2p spectra and b) Cu2p spectra.....	118
Fig.4.1: Conversion of furfural into fine chemicals.....	130
Fig.4.2: Schematic (left) and photograph (right) of high-pressure batch reactor.....	136
Fig.4. 3 Schematic (left) and photograph (right) of electrochemical reactor	136
Fig.4.4: Cyclic voltammograms of the working electrodes (a) Ni foam, (b) Cu foam, (c) Cu foil, (d) Ni1Cu1-A11 R on Cu foam.....	138
Fig.4.5 ECH of furfural	139
Fig.4.6: Catalytic activity of Ni-Cu-Al 111 R through TCH and ECH routes.....	140
Fig.5.1: a) Schematic and b) Aspen plus flowsheet of furfural hydrogenation to THFA	147
Fig.A2: Schematic (left) and photograph (right) of high-pressure batch reactor.....	159
Fig.A3: Preparation of mesoporous WO ₃ -ZrO ₂ catalysts by EISA method	160
Fig.A4: Preparation sulfonated carbon (-SO ₃ H/C)	161
Fig.A5: Preparation of hydrotalcite NiCu-Al catalysts.....	162
Fig.A6: GC-FID chromatograms a) before the reaction, b) reaction after 4 hours.....	163
Fig.A7: Calibration data w.r.t CCl ₄ solvent of A) FAL, B) BL, C) butanol, D) DBE.	164
Fig.A8: GC-FID chromatograms a) before the reaction, b) reaction after 2 hours.....	165
Fig.A9: Calibration data w.r.t methanol (MeOH) solvent of A) Furfural, B) FAL, C) THFA D) 2-butanol, E) 2-MF, F) MTHF.....	166

List of Tables

Table 1.1: Literature review of butanolysis of FAL	9
Table 1.2: Representative in literature on furfural hydrogenation to THFA	15
Table 2.1: Physical properties of $\text{WO}_3\text{-ZrO}_2$	34
Table 2.2: Peak temperature and acidity of the $\text{WO}_3\text{-ZrO}_2$ catalysts.	35
Table 2.3: Normalized peak areas w.r.t weight of the $\text{WO}_3\text{-ZrO}_2$ catalysts.	38
Table 2.4: Physical properties of sulfonated carbon catalysts.	40
Table 2.5: Normalized peak areas w.r.t weight of the sulfonated carbon catalysts.	43
Table 2.6: Catalytic activity of $\text{WO}_3\text{-ZrO}_2$ catalysts	48
Table 2.7: Comparison of this work with previous reports.	56
Table 3.1: Physical properties of the prepared catalysts	77
Table 3.2: Theoretical and measured elemental compositions of the catalysts	88
Table 3.3: H_2 -TPR studies of the prepared catalysts	91
Table 3.4: CO pulse chemisorption of reduced catalysts	93
Table 3.5: N_2O pulse chemisorption of reduced catalysts	93
Table 3.6: NH_3 -TPD studies of the prepared catalysts	97
Table 3.7: Elemental composition of calcined samples from XPS analysis	100
Table 3.8: Elemental composition of reduced samples from XPS analysis	101
Table 3.9: Reaction studies with calcined and reduced catalysts	102
Table 3.10: TOF values of hydrogenation of furfural for the reduced catalysts in 2- butanol	110
Table 3.11: The product distribution of furfural hydrogenation with different solvents	111
Table 3.12: Physical properties of the fresh and spent catalysts	115
Table 3.13: Elemental composition reduced samples from XPS analysis	118
Table 4.1: Gibbs free energy and standard cell potentials for the hydrogenation of furfural.	130

Table 4. 2: Experimental conditions	134
Table 5.2: Raw material and product costs.....	148
Table 5.3: Utility costs.....	148
Table 5 4: Summary of stream results	149
Table 5. 5: Cost of the equipment.....	150
Table 5.6: Operating cost summary	151
Table 5.7: Summary of the plant economics	152

List of Publications

1. **U.R. Thuppati**, S. Suchada, C. Choi, H. Machida, Z. Huo, and K. Norinaga, “Selective hydrogenation of furfural to tetrahydrofurfuryl alcohol in 2-butanol over an equimolar Ni-Cu-Al catalyst prepared by the co-precipitation method,” *Energy Convers. Manag.*, vol. 265, no. February, p. 115736, 2022.
<https://doi.org/10.1016/j.enconman.2022.115736>
2. **U. R. Thuppati**, **L. Zhang**, J. Wang, D. Ren, A review of thermal catalytic and electrochemical hydrogenation approaches for converting biomass-derived compounds to high-value chemicals and fuels, *Fuel Process. Technol.* 226 (2022) 107097. <https://doi.org/10.1016/j.fuproc.2021.107097>
3. **U. R. Thuppati**, C. Choi, H. Machida, and K. Norinaga, “A comprehensive study on butanolysis of furfuryl alcohol to butyl levulinate using tungstated zirconia and sulfonated carbon catalysts,” *Carbon Resour. Convers.*, vol. 4, 111–121, 2021.
<https://doi.org/10.1016/j.crcon.2021.03.003>

List of Conferences

1. **U. R. Thuppati**, Suchada S, Choi C, Machida H, Norinaga K, "The catalytic efficiency of Ni-Cu-Al catalysts on hydrogenation of furfural through thermo catalytic and electrocatalytic routes"., 9th Asian Conference on Biomass Science (ACBS2021), Japan Institute of Energy, January 21, 2022
2. **U. R. Thuppati**, C. Choi, H. Machida, and K. Norinaga, “V320 Production of butyl levulinate through butanolysis of furfuryl alcohol over acidic catalysts.” 2020, SCEJ 51st Autumn Meeting (2020).

Abstract

Interest in the generation of biofuels and green chemicals from biomass, particularly lignocellulosic biomass, which is a high-potential renewable feedstock, has grown significantly in recent years. This work focussed on the utilization of hemicellulose derived furfuryl alcohol (FAL) to produce a sustainable aviation fuel (SAF) or gasoline additive such as butyl levulinate (BL) through butanolysis reaction and furfural hydrogenation to obtain an industrial green solvent tetrahydrofurfuryl alcohol (THFA). Thus, making a good use of lignocellulosic biomass to contribute to the fuels and fine chemicals sectors to cope with the depleting fossil fuels. This work also aimed at developing process catalysts that can accommodate these reactions in achieving high yields of BL and THFA. It is highly advantageous and desirable to synthesize suitable catalysts that are efficient and versatile in chemical reactions.

The first part of the thesis discusses the butanolysis of FAL over a solid acid catalyst to produce BL. Considering butanolysis of furfuryl alcohol is a strong function of acidity, tungstated zirconia ($\text{WO}_3\text{-ZrO}_2$), a robust solid acid catalyst, and a sulfonated carbon catalyst were employed to achieve high yields BL while targeting a lower initial molar ratio of butanol to FAL. The catalytic activity of $\text{WO}_3\text{-ZrO}_2$ with respect to BL yield was optimized in calcination temperature (800 °C) and WO_3 loading (15 Wt.%). However, a maximum of 28 mol% of BL yield was achieved at a reaction temperature as high as 240 °C. At such high temperature, FAL polymerization was promoted rapidly resulting in low yield of BL. Using noble (Pd & Pt) and non-noble (Fe, Co, Ni, and Cu) promoters to increase the acidic strength also resulted in the same activity as neat $\text{WO}_3\text{-ZrO}_2$. As the acidity of the catalysts is a key factor for butanolysis of FAL, a carbon catalyst was synthesized by partial carbonation of biomass derived sucrose to obtain acidic carboxyl, phenolic, and hydrophilic groups in the carbon structure. This carbon structure was further enhanced with strong Bronsted $\text{-SO}_3\text{H}$ groups by sulfonation. Thus, prepared sulfonated carbon catalyst possessed an acidic strength of 2.357 mmol/g, resulting in 80 mol% of BL yield at as low as 8.5 initial mole ration of butanol: FAL.

The second part of the thesis focussed on developing a bi-metallic catalysts to employ for furfural hydrogenation to THFA. In this regard, Ni-Cu-Al hydrotalcite catalysts were prepared by dispersing equal moles of Ni and Cu on varying amount of Al by the co-precipitation method to synthesize Ni-Cu alloy particles. The nickel species were active for both the furan ring (C=C) and carbonyl group (C=O) of furfural molecule, while Cu species were highly active for only the carbonyl group of furfural molecule. Systematic characterization of the prepared catalysts by XRD, TPR, STEM-EDS, and XPS analysis revealed the formation of highly active Ni-Cu alloys and near-equal Ni/Cu surface contents were achieved for the equimolar catalyst, which showcased a maximum of 98 mol% yield of THFA at 140 °C, 30 bar, 4h. The reaction pressure and temperature showed a substantial effect on the product yield. The solvent selection also influenced the product selectivity, particularly with 2-butanol, which promoted the reaction with its hydrogen donor capacity and supported the ring hydrogenation of FAL to THFA. Moreover, the reduced Ni₁Cu₁-Al₁ catalyst displayed good recyclability for three runs and an equal activity to that of a fresh catalyst after the regeneration.

The next section of the thesis focussed on exploring the electrocatalytic hydrogenation (ECH) of furfural, which has a broad range of conversion to FAL, THFA, and 2-methyl furan (2-MF). In this work, furfural hydrogenation is carried out using Ni-Cu-Al mixed oxide catalysts in thermal catalytic conversion (TCH) and ECH to report the catalytic activity of these mixed oxides. The Ni-Cu-Al mixed oxide catalysts are prepared as working electrodes by depositing the catalyst ink on a Cu foam substrate. 98 mol% selectivity of THFA with complete conversion was observed in the TCH route using Ni₁-Cu₁-Al₁ R catalyst at 140 °C under 30 bar H₂ pressure after 4 hours of the reaction. However, the electrocatalyst (Ni₁-Cu₁-Al₁ R on Cu foam) through the ECH route displayed 89 mol% conversion of furfural with 58 % selectivity of 2-MF and 23.8 % selectivity of FAL. The pH (0.5) of the electrolyte used in the ECH process controlled the selectivity between 2-MF and FAL. Moreover, the formation of THFA was not observed in the ECH route.

The final section of the thesis aimed at developing a simulation model of furfural hydrogenation to evaluate the techno-economic analysis. In this work, an Aspen Plus model was developed using the PENG-ROB estimation method to hydrogenate furfural

to THFA and furfuryl alcohol (FAL) to estimate the economics and the energy scenario of the process. The best results obtained by Ni₁Cu₁-Al₁ R catalyst (100 mol% conversion and 98 mol% THFA yield, 1.5 mol% of FAL yield at 140 °C and 30 bar H₂ pressure) are used in the RSTOIC reactor to estimate its economic potential. As the reaction was exothermic, the liberated heat source was integrated to make use of the process heat.

Chapter 1: Introduction, literature review, and objectives

1.1 Introduction and background

Fossil fuels such as coal, oil, and natural gas are the primary energy resources in the development of human life and society. Fig.1.1 shows the world total primary energy supply 2019[1]. More than 80% of energy demand was contributed by natural gas, oil and coal which are non-renewable energy sources whereas the rest was by nuclear and renewable energies such as biomass, solar, hydro and wind energies. Regardless of the fossil fuels contribution, the emerging problems are associated with the greenhouse gas emissions, climate change and depletion of these fossil fuels. In response to these challenges, the sustainable energy sector has been focussed on utilizing renewable energy resources and introduced the concept of Net Zero Emissions (NZE) policy[2]. Among the renewable energy resources, biomass has contributed 9% and its contribution is expected in the future. According to the energy supply projections by International Energy Agency (IEA) for the year 2030[2], the consumption of fossil fuels would be reduced to 62% while increasing the energy supply by renewable sources to 28%. In 2019, the energy supply by biomass was 9.4% by utilizing the biofuels and solid waste to generate heat and electricity. The usage of biomass energy supply is expected to be more than 14 % by the year 2030. The sustainable wind and solar being zero-carbon emission renewable energies have developed significantly and are in rapid progression. However, the fine chemicals and high-performance liquid fuels remain produced from carbon-based feedstocks[3][4]. Moreover, the beginning of the pandemic COVID-19 in 2020 and Russia War on Ukraine in February 2022, the fossil fuels prices are increased drastically and has affected many countries by imposing a heavy toll on the global economy. The countries around the world have taken oath in the development strategies and policy measures concerning the energy sector as part of the economic recovery process, such as accelerating decarbonization processes and using clean sustainable energies. To minimize reliance on finite fossil fuels, it is important to produce energy, organic chemicals, fuels, and polymers from biomass.

Biomass is becoming an increasing commodity and can be classified into many types such as energy crops, agricultural residue & waste, forestry waste & residues, and industrial municipal waste[5][6][7]. The biomass further can be classified based on the chemical nature into Triglyceride feed stock (vegetable oils, animal fats, waste cooking oils and microalgal oils etc.), sugar and starchy feed stock (sugar beet, sweet sorghum, sugar cane etc.), and lignocellulosic feed stock (wood, straw, grasses etc.).

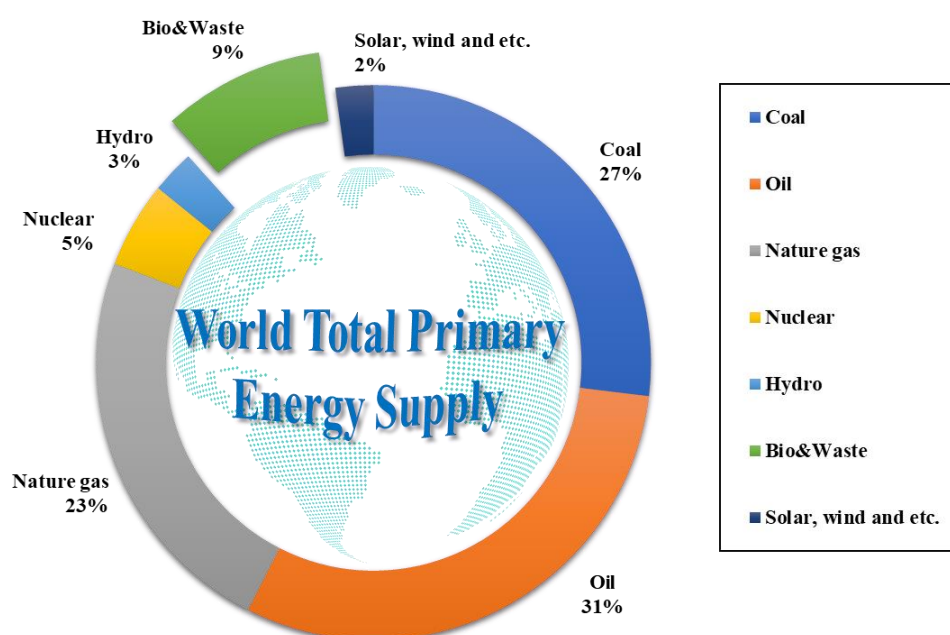


Fig.1.1: World Total primary energy supply 2019 (Source: IEA).

Lignocellulosic biomass is an abundant carbon-hydrogen-oxygen renewable resource that can produce fine chemicals, liquid fuels, olefins & aromatics, and heat energy. Lignocellulosic biomass primarily composed of cellulose (40-50%), hemicellulose (25-35%), and lignin (15-20%)[3] (Fig.1.2). The cellulose is a high molecular weight ($>10^6$ kg kmol⁻¹) composed of linear C₆ polymers of β - glycosidic units linked by β -1,4 glycosidic bonds. Moreover, Cellulose is highly crystalline, making it highly insoluble in aqueous solution. This crystalline nature makes it resistant to hydrolysis process. Hemicellulose is amorphous and composed of C₅ & C₆ D-xylose, D-galactose, D-arabinose, D-glucose, and D-mannose. The hemi-cellulose is highly soluble in aqueous solution due to its amorphous nature, thus makes the hydrolysis process much

easier than cellulose hydrolysis. The lignin is a high molecular weight aromatic polymer ($6 \times 10^6 - 15 \times 10^6 \text{ kg kmol}^{-1}$) and is amorphous. Cellulose and hemicellulose consisting of D- glycosidic monomer units which are the basic sources for the platform chemicals like 5-hydroxymethylfuran (HMF)[8], furfural[9], xylitol[10], sorbitol[10], and levulinic acid (LA)[11]. Furthermore, lignin is the source of cross-linked phenolic polymers which can be transformed into hydrocarbon compounds like olefins and polyaromatic hydrocarbons (Fig.1.2).

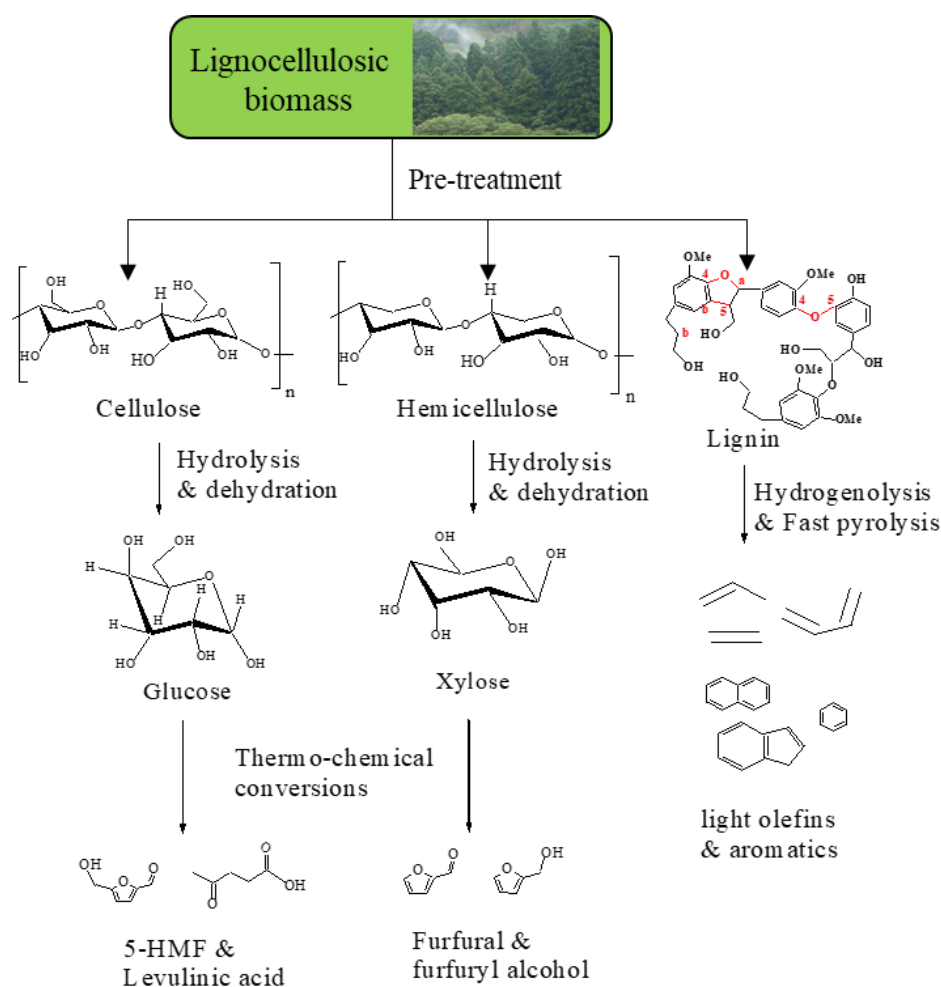


Fig.1.2: Lignocellulosic biomass fractionation and derived platform chemicals.

Currently, the three primary catalytic conversion routes of biomass are hydrolysis, gasification, and pyrolysis. Hydrolysis is employed to break biomass into its constituent cellulose, hemicellulose, and lignin while gasification and pyrolysis are used to obtain bio-oil, olefins, and aromatic hydrocarbons. The isolated constituents of biomass

(cellulose, hemicellulose, and lignin) after pre-treatment can undergo many transformative processes to obtain a group of biomass derivative molecules called platform chemicals [12][13]. The platform chemicals were selected by US department of energy (DOE)[14] based on several factors such as their potential to be converted into fine chemicals and liquid fuels, and the availability of technology for the commercial production etc. The cellulose fraction undergoes harsh treating conversion processes because of its rigid structure to produce D-glucose units. The hemicellulose fraction can be easily transformed to xylan polymers which can be depolymerized to xylose monomers by diluted acid hydrolysis (for example sulfuric acid). Thus, obtained xylose can be converted to a furan platform molecule called furfural, an important platform chemical with a wide range of transformative chemicals.

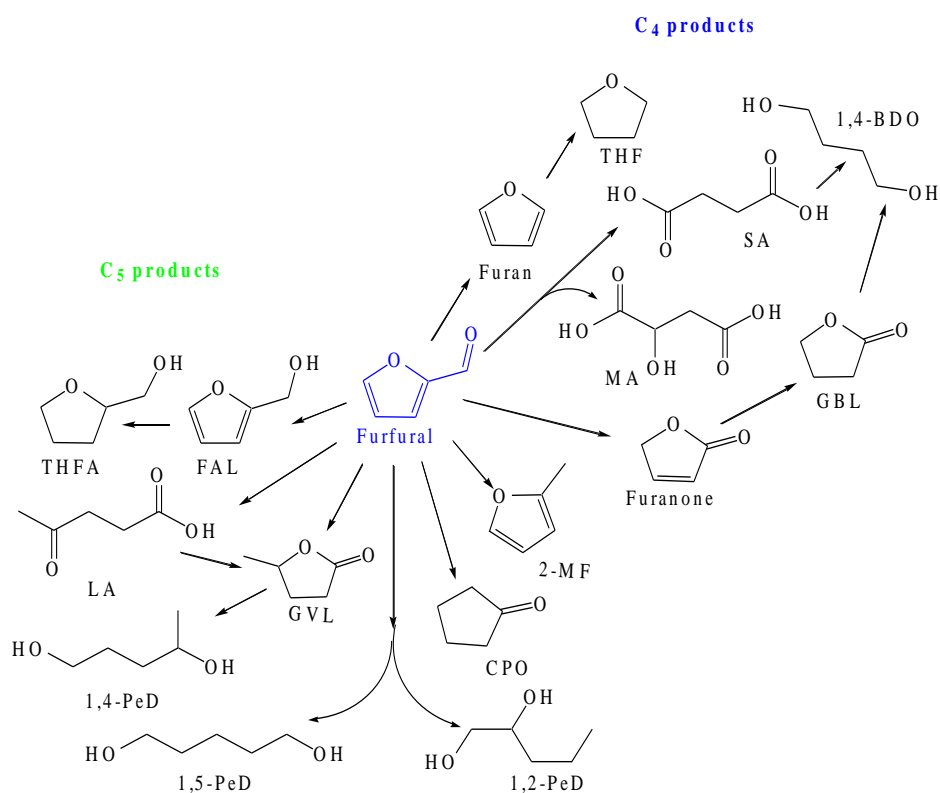
In contrast to chemicals derived from fossil feedstocks, which are already functionalized platform chemicals; a lower number of transformative steps are needed to produce fuels and industrial chemicals[15]. However, biomass is the only alternative renewable resource to fossil feedstocks to obtain fuels and chemicals. The production of liquid biofuels attracted much attention at first because of the importance of transport sector which depends mostly on petroleum feedstocks[16]. The biofuels such as biodiesel obtained by transesterification of triglycerides and bioethanol by fermentation of corn or sugarcane feedstocks were the first focussed liquid fuels derived from biomass. However, several drawbacks of these biofuels limited their application in transportation fuels. For instance, the main disadvantages were the cold flow properties, low oxidation stability, high molecular weight polymer impurities, and the corrosive nature of the biodiesel. In addition, the blended bioethanol with gasoline induced the water absorption by the fuel which could damage the engine and also corrosive nature of the bioethanol were regarded as the main drawbacks. These drawbacks influenced the development of advanced biofuels such as liquid hydrocarbon fuels through catalytic transformation of platform chemicals by hydrodeoxygenation to remove the oxygen from the molecules thereby promoting C-C coupling reactions (e.g., aldol-condensation, ketonization, and oligomerization) to obtain C₉-C₁₆ (jet fuel) and C₁₀-C₂₀ (diesel engine) fuels.

Another important aspect of the advanced biofuels is to convert the platform chemicals into fuel additives[17]. In general, a gasoline/diesel fuel additive is a chemical

compound which is being added in a known proportion to improve the fuel quality by acting as an oxidizing agent to reduce the particulate emissions (CO_x and NO_x emissions), to prevent corrosion, enhancing fuel cold flow properties, and improving the octane/cetane number of the fuels. The automobile engines are also been modified to suit the oxygenated gasoline since 1990, the research on fuel additives has ever been growing rapidly to meet the critical specifications of sulfur, olefins, vapor pressure, soot and smog reduction. Thus, the conversion of platform molecules into fuel additives and starting chemicals for producing hydrocarbon fuels to reduce the transformation steps has been cost competitive and a new approach in the transportation and petrochemical technologies. Therefore, the objectives of this research are focussed on transformation of platform chemicals to fuel additives and fine chemicals.

1.2 Hemicellulose derived furfural as a platform chemical for fuel additives, biofuels and fine chemicals

As discussed above, hydrolysis of hemicellulose is rather easy than cellulose because of its amorphous nature and solubility in aqueous solutions contrasted to the rigid crystalline structure of cellulose[18]. Hydrolysis of hemicellulose produces pentose sugars composed of xylose monomers. The dehydration of xylose units produces furfural, an important platform molecule[9]. Furfural has a numerous application in polymeric resins industry, however, is not an attractive fuel additive because of its stability and melting point. Perhaps, furfural as a starting chemical to obtain a variety of fine chemicals, liquid alkanes, fuel additives and value-added furan derivative makes strong validation as a platform molecule.



THFA-tetrahydrofurfuryl alcohol, GVL- gamma valerolactone, THF-tetrahydrofuran, PeD-pentane deols, GBL-gamma butyrolactone, SA-Succinic acid, MA-Malic acid, CPO-Cyclopentanone

Fig.1.3: Furfural as a platform chemical for a wide range of products.

In this regard, Fig.1.3 shows the conversion path of furfural into an array of C₄ and C₅ liquid biofuels and fine chemicals through various reactions such as hydrogenation, decarboxylation, deoxygenation, hydroxy alkylation, aldol condensation, and some optional combinations. The primary hydrogenation product of furfural is furfuryl alcohol (FAL), an intermediate chemical for fine chemistry and gasoline additives such as alkyl levulinates. 2-methylfuran (2-MF) which is an octane booster produced by hydrogenation followed by dehydration of furfural. Further down streamed hydrogenation products of furfural such as furan, furanone, tetrahydrofuran (THF), methyl tetrahydrofuran (MTHF), tetrahydrofurfuryl alcohol (THFA), lactones, cyclopentanones or pentane diols, and levulinates are other important value-added chemicals and biofuels from furfural. Furfural has been the centre of study in the field of biofuels and fuel additives in the past decade and a numerous studies have been published on effective utilization of furfural. Many kinds of noble (Pd, Pt, Ru, Rh etc.) and non-noble (Cu, Ni, Zn, Co, Zr etc.) catalysts have been employed for the furfural hydrogenation with a special emphasis on the

hydrogenation products such as FAL, 2-MF, THF, THFA, and MTHF[19]. Among these products, hydrogenation to FAL is the easy and commercial process accomplished industrially. However, the flow properties and the stability of furfural and FAL are not so diversified, making it necessary to upgrade to fuel additives and fine chemicals.

1.2. Research focus

1.2.1 Butyl levulinate from FAL

Alkyl levulinates are the promising candidates as a fuel additive to gasoline or diesel fuel considering their improved cold flow properties, high octane number, low sulfur content, and a stable flash point[20][21][22]. These properties make the alkyl levulinates ideal oxygenates for blending with gasoline and diesel fuels. Besides, alkyl levulinates are also important platform chemicals and have wide applications as solvents, flavouring and fragrance agents. Generally, Alcoholysis of furfuryl alcohol or levulinic acid with alcohols in the presence of an acidic catalyst produces alkyl levulinates such as methyl levulinate (ML), ethyl levulinate (EL), and butyl levulinate (BL). The anti-knocking index values of these levulinates are 106.5, 107.5, and 102.5 respectively which are suitable to enhance the octane number of a fuel[23]. The cold flow properties of ML are not primarily preferable due to the disadvantage of ML compared to other levulinates as it is miscible with water and hard to separate with gasoline. Joshi et al. have reported a significant decrease in pour point, cold filter plugging point, and cloud point of biodiesel when blended with EL[24]. EL is more suited to blend with diesel fuel than gasoline owing to the corrosive nature and lower energy density. BL as a high molecular weight oxygenate to control the oxidation of pollutants, BL is a suitable gasoline blend than EL. Moreover, BL as a food fragrant and solvent has numerous applications in food and chemical industries. Thus, making BL not only as a gasoline additive but also a more value-added chemical which gained much attention.

1.2.1.1 Literature review on butanolysis of FAL

Butyl levulinate can be synthesized from both cellulose and hemicellulose derived chemicals in the presence of an acidic catalyst. First, esterification of cellulose derived LA with n-butanol and the butanolysis of hemicellulose derived FAL produces BL. The butanolysis of FAL is favored over esterification of LA for the following reasons. First, LA itself is a platform molecule with numerous applications in fine chemistry. The LA is

expensive than FAL and production of LA from cellulose derived 5-HMF involves complicated processing. Moreover, FAL is the easily produced chemical from xylose. Therefore, utilizing a much easier and cheaper processes to produce BL from FAL over LA could make it a reasonably and economically feasible process. Table 1.1 represents the literature survey on butanolysis of FAL. BL synthesis has been carried out using a variety of homogeneous and heterogeneous catalysts in different reactors.

Gitis et al. have developed a graphite oxide (GO) and reduced graphite (rGO) oxide by modified Hummers and Offeman method to apply them for the conversion of FAL to BL[25]. The oxygen functionalities are incorporated onto the GO and rGO by treating them with KMnO_4 which were responsible for the acidic strength to lead to high selective formation of BL. B.S Rao et al. have employed $\text{Zn}_1\text{TPA}/\text{Nb}_2\text{O}_5$ catalyst at mild conditions to obtain 94 mol% of BL yield[26]. The use of KCC-1/Pr- SO_3H catalyst showed a maximum of 81.9 % BL yield because of the higher initial amounts of FAL, which was subsequently polymerized because of the strong acidity of the catalysts generated by strong bronsted $-\text{SO}_3\text{H}$ groups[27]. Using cation exchange resin catalysts such as Amberlyst39, DOW2, and DOW4 produced a maximum BL yield of 57 %, 46.9%, and 19.5% respectively at much higher FAL initial concentration[28]. However, the non-reusability and the deactivation at more than 130 °C of these catalysts hinder their wide applications. The acidity of the catalysts is a key factor in obtaining high amount of BL, which was stably achieved for SBA-15- SO_3H catalyst[29]. The SBA-15- SO_3H catalyst demonstrated good catalytic activity for this process, although catalyst reusability has not been reported. The critical catalyst preparation and the stability of this catalyst was main drawbacks of this system. Extremely low acidic H_2SO_4 was used as a homogeneous catalyst to accommodate butanolysis of FAL. Even though, the more than 97 % yield of BL was achieved, the inevitable difficulty in homogeneous catalyst separation and reactor corrosion are always a concern when employing homogeneous catalysts[30].

The catalysts prepared from waste paper, from biomass which generally contain the carboxylic and hydroxyl groups which can moderately produce BL. Incorporating the strong $-\text{SO}_3\text{H}$ groups onto these catalysts can dramatically improve the catalytic activity [31]. An array of metal chloride catalysts such as CrCl_3 , FeCl_3 , CuCl_3 , and AlCl_3 , and metal sulphides such as $\text{Cr}_2(\text{SO}_4)_3$, $\text{Fe}_2(\text{SO}_4)_3$, $\text{Cu}(\text{SO}_4)_3$, and $\text{Al}_2(\text{SO}_4)_3$ were also used as

catalysts for butanolysis of FAL reaction[32]. Ordered mesoporous Ti-KIT-6 acidic catalysts have shown high selectivity to BL with the conversion of FAL limited to around 90%[33]. Zeolite catalysts such as HY-Zeolite, HZSM-5, and Al-TUD-1 have shown moderate catalytic efficiency, yielding only 3%, 40%, and 60% of BL, respectively[33][34]. A variety of UiO-66(Hf)-SO₃H, AlCl₃ catalysts also exhibited 72 % and 96 % of BL yield, respectively [35] [36]. The catalyst Al₂O₃/SBA-15 exhibited substantial activity producing more than 94% yields of BL. However, to produce maximal yields of BL, the system needed a substantial quantity of the catalyst (0.4 g)[37]. Newly developed catalysts such as α -Fe₂O₃, Indium(III) triflate In(OTf)₃, and Cu(OTf)₂ catalysts have shown a good catalytic activity to produce 92%, 86% and 66% of BL yield respectively[38][39]. A series of ionic liquid catalysts like [BMIm-SH] [HSO₄][40], MIL-101(Cr)- SO₃H[41] and metal complex catalysts (organic-inorganic hybrid solid acid catalyst) such as Ti_{0.75}TPA[42], NKG-9, [MIMBS] H₃PW₁₂O₄₀ were also tested for butanolysis of FAL reaction with moderate to high BL yields[43].

Table 1.1: Literature review of butanolysis of FAL

Catalyst	Reaction Conditions	Initial mole ratio (FAL: butanol)	Conversion (%)	Yield (%)	Ref.
Graphite Oxide (GO)	383 K, 6h, 0.2g,	1:27	100	100	[25]
Reduced Graphite Oxide (rGO)			100	100	
Zn ₁ TPA/Nb ₂ O ₅	383 K, 5h, 0.3g	1:65	100	94	[26]
KCC-1/Pr-SO ₃ H	393 K, 3h, 0.1g	1:33	100	81.9	[27]
Amberlyst39	373 K, 6h, 1g	1:8	100	57.0	[28]
DOW2			100	46.9	
DOW4			100	19.5	

SBA-15-SO ₃ H	383 K, 4h, 0.05g	1:33	100	96	[29]
Extremely low acid H ₂ SO ₄	383 K, 8h, 0.005M		98	97	[30]
Magnetic waste paper (MWP)	393 K, 5h, 0.08g	1:50	5.4	0.3	[31]
Sulfonated magnetic waste paper (SMWP)			100	90.6	
HZSM-5			82.7	28.0	
Nafion-212			91	81.3	
CrCl ₃	383 K, 1h, 0.02M	1:35	47	28	[32]
FeCl ₃			95	24	
CuCl ₂			97	73	
AlCl ₃			97	61	
Cr ₂ (SO ₄) ₃			7	2	
Fe ₂ (SO ₄) ₃			62	10	
CuSO ₄			28	5	
Al ₂ (SO ₄) ₃			30	5	
KIT-6	383 K, 5h, 0.3g	1:60	8	100	[33]
Titanium (IV) isopropoxide			54	100	
100Ti-KIT-6			94	100	
100Ti-SBA-15			90	100	
100Ti-Si			60	100	
HZSM-5	383 K, 6h, 0.3g	1:60	100	40	
HY-zeolite	383 K, 12h, 0.3g	1:60	100	3	
Al-TUD-1	413 K, 24h, 10 gcat.dm ⁻³	0.3 M FAL, 1 mL butanol	100	60	[34]

UiO-66(Hf)-SO ₃ H	403 K, 4h, 0.1g	1mmol FAL 20 mL butanol	100	72	[35]
AlCl ₃	406 K, 2.7h, 0.021 mol/L	1:35	99	96	[36]
20Al ₂ O ₃ /SBA-15	383 K, 6h, 0.4g	1:65.5	100	94	[37]
20Al ₂ O ₃ /SBA-15	453 K, 6h, 0.4g		100	91	
α -Fe ₂ O ₃	523 K, 1.3h, 7.5 mmol α - Fe ₂ O ₃	0.23 mmol FAL, 10 mL butanol	100	86	[38]
In(OTf) ₃	391 K, 1.5h,0.028g	0.5 mmol FAL, 20 mL butanol	100	92	[39]
Cu(OTf) ₂			100	66	
[BMIm-SH] [HSO ₄] (Acidic Ionic liquid)	403 K, 2h 0.3g	5 wt% FAL, 95 ml butanol	99	85	[40]
MIL-101(Cr)- SO ₃ H	413 K, 2h 0.1g	60:1	99	55	[41]
Ti _{0.75} TPA	393 K, 0.5h, 2.25 wt%	44:1	100	92	[42]
NKG-9	383 K, 4h, 5mol%	48:1	100	73	[43]
H ₃ PW ₁₂ O ₄₀	383 K, 2h, 5mol%		100	58	
[BmimSO ₃ H]3PW ₁₂ O ₄₀	383 K, 12h, 5mol%		100	88	

1.2.1.2 Summary and gap analysis on butanolysis of FAL

The acidic strength of a catalyst, the initial concentration, and the reaction temperatures are the main parameters that influenced the yield of BL. Many kinds of catalysts were employed for the butanolysis of furfuryl alcohol starting from basic diluted

homogeneous catalysts such as H_2SO_4 , H_3PO_4 , and HCl . A wide range of heterogeneous acidic catalysts and ionic liquids were also extensively studied for this reaction to provide a pool of academic knowledge in obtaining the important gasoline additive (BL). The first parameter for this reaction specifically depended on the acidic catalyst. The catalyst has two primary functions in this reaction system. The first step is the protonation hydroxyl groups of the furfuryl alcohol molecule and butanol to form the reaction intermediate 2-butoxymethylfuran (2-BMF) releasing the water molecule. After that, the second step involves the ring opening mechanism of 2-BMF followed by the keto-enol isomerization to form BL. The formation of BL from 2-BMF is slower than the formation of 2-BMF from FAL, which makes the former step the rate determining step which is significantly governed by the acidic strength of the catalyst. The acidity generated by the metal oxide catalysts due to the transfer of outer band electrons which created the Lewis and Bronsted acidic sites was not adequate to accommodate the ring opening reaction mechanism. Additional sources of acidity were incorporated onto these metal oxide catalysts to provide high acidic strength. For instance, in the case of Al_2O_3 catalyst, the reaction with neat Al_2O_3 resulted in low conversion of FAL with low yield of BL. However, when incorporated with highly bronsted acidic $-\text{SO}_3\text{H}$ groups, 96 % of BL was obtained with complete conversion. Zeolite catalysts, non-sulphated highly acidic catalysts, resulted in below par yields (not more than 40 %) of BL, indicating the need for high acidic strength. Even though, the direct use of the metal chloride catalysts (e.g. AlCl_3) produced around 60 % BL yield, the corrosive nature of the catalysts hinders their efficient applications. The commercially available ion exchange resin catalysts also resulted in moderate BL yield given the temperature limitations of these catalysts. This catalyst summary induces the need of high acidic catalysts to obtain high yields of BL.

The other important parameter in this reaction system is the amount of initial FAL used in the reaction. FAL is furan ring molecule which can easily form the polymeric products under acidic conditions thereby reducing the selectivity of BL. The simultaneous protonation of the FAL molecules at different acidic sites and the nucleophilicity of the furan rings promote the polymerization process, producing the high molecular weight compounds called humins resulting in a brown thick black liquid. The reaction with neat FAL in acidic conditions resulted in this black thick liquid. This polymerization of FAL

can be controlled by using a reaction solvent. However, the possibility of polymerization cannot be taken out completely given the acidic reaction conditions. The FAL polymerization is the main reason for using high initial butanol to FAL mole ratios. The reaction temperature also influences the FAL polymerization under a certain limit. Therefore, it is important to find the optimized initial FAL concentration conditions to get high BL yields.

Another reaction parameter that has greatly affected the BL yield was reaction temperature. The literature review (Table 1.1) shows that the minimum reaction temperature used was 383 K, which is a slightly moderate temperature. The reaction temperature may change accordingly to the applied catalyst. Low reaction temperature with longer reaction times were employed for highly acidic catalysts. This indicates a minimum temperature requirement to accommodate this reaction. With increased reaction temperature, the selectivity of the BL was increased due to the enhancement of rate determining step, i.e., conversion of 2-BMF to BL. The reaction temperature also controls the FAL polymerization. The high reaction temperatures (>210 °C) greatly favour the nucleophilicity of furan rings thereby increasing the FAL polymerization rate. The solvent dehydration reaction also influenced by the temperature which could promote the ether products of the respective solvents. Moreover, the degradation of the BL can also occur at high temperatures (>230 °C). Thus, choosing an appropriate reaction temperature to produce high BL yield is a major factor in butanolysis of FAL. Therefore, the objectives of the study are determined considering these challenges in developing a better reaction system for butanolysis of FAL.

1.2.1.4 Objectives of butanolysis of FAL

The difficulties associated with the butanolysis of FAL such as no stable catalyst for high yield production of BL at lower initial mole ratios of butanol to FAL, optimization of reaction temperature, use of high initial butanol to FAL mole ratio, polymerization of FAL, the formation of unwanted products, dehydration of solvent to respective ethers. The following objectives are set for this study on butanolysis of FAL.

- I. Development of an acidic catalyst mainly focussed on acidic corresponding to metal oxides.** In this regard, a mesoporous tungstated zirconia ($\text{WO}_3\text{-ZrO}_2$)

prepared by evaporative induced self-assembly method owing to its excellent activity on alkane isomerization, trans-esterification of triglycerides, and esterification of LA to produce BL.

- II. A catalyst from biomass.** Pyrolyzed biomass or sugars contain the acidic groups in its structure such as carboxylic acid, hydrophilic, and phenolic groups which can act as active acidic sites. Moreover, incorporating $-\text{SO}_3\text{H}$ groups strengthens the acidity of the catalyst. In this regard, a sulfonated carbon catalyst prepared by the carbonation of biomass derived sucrose followed by sulfonation process. The details on catalysts activity, role of promoters, and their preparation methods are discussed in Chapter 2
- III. A systematic catalyst characterization.** The characterization of the prepared catalysts to study the activity parameters in detail. For example, the spectroscopic, acid-base titration and NH_3 -desorption studies essentially reveal the acidic strength of the catalysts.
- IV. Reducing the initial mole ratio of butanol to FAL.** Only a few studies have focussed on reducing the amount of butanol and increasing the initial FAL concentration. This study intended on this objective to provide more information of FAL polymerization provide more information on butanol as a reactant than of being a solvent. At high initial concentrations and high reaction temperature, more than 40% of FAL tends to form either furanic ethers or high molecular weight FAL humins. Thus, focussed on achieving higher BL yields in such difficult conditions.
- V. Optimizing the reaction parameters to facilitate a maximum yield of BL.** For example, to find the suitable reaction temperature that promotes the transformation of 2-BMF to BL and other parameters such as catalyst loading and the reaction time.

1.2.2 Hydrogenation of furfural to THFA

Hydrogenation is a primary reaction to transform furfural into fuel additives and liquid biofuels. As described in section 1.2, furfural can be converted to an array of chemical products. Its hydrogenation was carried out using non-noble and noble catalysts in gas and liquid phase reactors. Among the many products, the direct

hydrogenation to THFA is preferable as it involves the hydrogenation of C=O and the C=C groups and has numerous applications in various fields such as pharmaceutical, polymers, agricultural and is a versatile green solvent in the chemical industry. Moreover, it is an outstanding intermediate product to produce tetrahydrofuran, dihydropyran, pyridine, and pentane diols (Ref). THFA can be produced with high selectivity in gas and liquid phases by choosing an appropriate carbonyl group and furan ring hydrogenation catalysts. Over the past few years, a series of noble metal catalysts, especially Pd-containing catalysts with good metallic strength to hydrogenate furan ring, and non-noble catalysts containing mostly Cu and Ni were employed to get THFA product. Moreover, the solvent selection also influences the selectivity between THFA and FAL. Therefore, the present study focussed on hydrogenation of furfural to THFA. The following section describes the latest literature review on hydrogenation of FAL to THFA.

1.2.2.1 Literature review and gap analysis on furfural to THFA

The latest literature studies show that various types of catalysts were applied to facilitate hydrogenation of furfural to obtain high yields of THFA. More than 90 % of yields were achieved in different conditions. Noble metal Pd based catalysts reported higher yields (Table 1.2, entries 1-8). However, the cost and availability of noble metals limit their applicability. Jun Wu et al. have reported that the excellent catalytic activity towards the reaction with hydrotalcite CuNi/MgAlO catalysts (Table 1.2, entry 9) is involved in slightly higher temperature and pressure using ethanol as a solvent. Moreover, Ni and Cu metals were deposited on the hydrotalcite MgAlO support. Additionally, this catalytic system can selectively switch between the products FAL and THFA by changing the solvent to methanol. Cu and Ni active sites deposited on carbon nanotubes with the reaction at 150 °C produced 95% of THFA after 10 hours (Table 1.2, entry 10). Sunyol C et al. reported the furfural hydrogenation with Ni (40)/MgO (30)-M catalyst to produce 95% of THFA (Table 1.2, entry 11). However, more (600 mg) catalyst was used (Table 1.2, entry 11). Sánchez et al. reported the furfural hydrogenation using high catalyst loadings at slightly higher pressure (Table 1.2, entry 12).

Table 1.2: Representative in literature on furfural hydrogenation to THFA

Entr y	Catalyst	Reaction conditions	Conversion of furfural, (%)	THFA yield (%)	Ref.
1	Ni-Pd/SiO ₂	40 °C, 80 bar H ₂ , 8 h, water	99	95	[44]
2	Pd UiO	60 °C, 1 bar H ₂ , 4 h, water	100	100	[45]
3	Pd-Ir/SiO ₂	2 °C, 80 bar H ₂ , 6 h, water	>99	96	[46]
4	Ru/ZrO ₂ & Pd/Al ₂ O ₃	30 °C, 0.5 bar H ₂ , 4 h, water	100	100	[47]
5	Pd/MFI	220 °C, 35 bar H ₂ , 5 h, iso-propanol	93	62.3	[48]
6	RuO ₂	120 °C, 50 bar H ₂ , 2.5 h, methanol	100	76	[49]
7	5% Ru/C	120 °C, 50 bar H ₂ , 2.5 h, methanol	99	59	[49]
8	3% Pd/C	160 °C, 80 bar H ₂ , 0.5 h, water	98.4	62.1	[50]
9	CuNi/MgAlO	150 °C, 40 bar H ₂ , 3 h, ethanol	>99	95	[51]
10	Cu-Ni/CNTs	150 °C, 40 bar H ₂ , 10 h, ethanol	100	90.3	[52]
11	Ni (40)/MgO (30)-M	140 °C, 40 bar H ₂ , 4 h,	100	95	[53]
12	NiCu/delaminate dhectorite (DH)	140 °C, 40 bar H ₂ , 4 h	100	95	[54]

1.2.2.2 Objectives furfural to THFA

From the literature, it can be deduced the catalysts containing Ni and Cu metals can efficiently produce THFA at higher yields. However, the metal composition and the support material could play an important role in the catalytic activity. In this regard, hydrotalcite like structure catalysts are attracted much attention because of the development of the nano metal alloy particles on the support surface which could drive the synergy of the metals. Al as a support metal oxide could provide the required surface area, pore structure, and metal dispersion given the interaction between Ni or Cu and Al. Thus, the developed catalytic system (NiCu-Al) should have several advantages compared to the literature reports. First, a simple hydrotalcite structured catalyst preparation method should be employed to successfully synthesize Ni-Cu alloys which are crucial for the catalytic activity. Second, low reaction pressures and lower catalyst loadings are needed to achieve higher yields of THFA. Third, the catalyst should have a good thermal and recyclable efficiency. Additionally, the use of any solvent with no oxidation or dehydration products should display the characteristics of a good solvent. A complete study on hydrogenation of furfural using NiCu-Al catalysts including the economic importance of the processes would provide an overview of the implementation of the process in industrial scales. Based on these requirements, the following objectives are determined.

- I. **Development of a versatile, efficient, inexpensive and a non-noble metal catalyst.** In this regard, synthesis of inexpensive hydrotalcite NiCu-Al catalysts by co-precipitation method as Cu is highly active for hydrogenation of the carbonyl group of furfural molecule while Ni has remarkable interaction strength for both the carbonyl group and the furan ring of the furfural molecule. However, the activity drawn by the synergetic effect of Ni and Cu metal would be drawn from the composition of the metals. Therefore, to find out the best composition of the Ni,Cu and Al material based on THFA yield.
- II. **A systematic catalyst characterization.** The special characterization such as XRD, XPS, STEM-EDS should be conducted to determine the crystallinity nature, oxidation state of the metals, and elemental composition accompanied by the mapping. The study of other characterization including BET, TPR, pulse

chemisorption study, SEM, TEM, and TPD study to obtain more insights into the physicochemical properties of the prepared catalysts.

- III. **Optimizing the reaction parameters to facilitate a maximum yield of THFA.** The important reaction parameters including the effect of hydrogen pressure, temperature, time profile study, catalyst loading, solvent selection, and the catalyst reusability or spent analysis which would describe the complete understanding of this reaction with the developed NiCu-Al catalysts in achieving a maximum yield of THFA.
- IV. **Comparative study on thermal catalytic hydrogenation (TCH) and electrocatalytic hydrogenation (ECH).** A review study on TCH and ECH of biomass derivatives would provide the clear insights into the operating conditions and the understanding of both processes. The two versatile conversion techniques of furfural aiming to obtain different products using NiCu-Al catalysts. ECH has been ever growing since integrating renewable electricity could facilitate the current need for ECH process.
- V. **Techno economic evaluation of the hydrogenation of furfural process using ASPEN plus.** To realize the economic importance of this process, An ASPEN PLUS model would be developed based on the best catalytic results.

1.3. Thesis outline

The thesis has been divided into two main parts. The first part consists the study on butanolysis of FAL to obtain BL. The second part is on furfural hydrogenation to THFA. The thesis writing has been organized in 6 chapters followed by appendix. The background of the study, motivation, literature review, and objectives of the studies are discussed in **Chapter 1**

Chapter 2 illustrates the study on butanolysis of FAL. In this chapter, the activity of a mesoporous tungstated zirconia ($\text{WO}_3\text{-ZrO}_2$) catalyst prepared by evaporative induced self-assembly method and a sulfonated carbon catalyst prepared by carbonation of sucrose followed by the sulfonation process for butanolysis of FAL is described. The activity of the $\text{WO}_3\text{-ZrO}_2$ promoted by various metals also discussed. The catalysts characterization and the reaction parameters such as effect temperature, time profile,

effect of initial concentration of FAL, catalyst loading, and catalyst recyclability are reported. This chapter is concluded with the summary.

Chapter 3 describes the hydrogenation of furfural to THFA in 2-butanol solvent using NiCu-Al catalysts prepared by the co-precipitation method. The composition of Ni, Cu and Al are optimized with respect to THFA yield. Special emphasis is dedicated to catalyst characterization conducted by BET, XRD, SEM, TEM, STEM-EDS, H₂-TPR, CO & N₂O pulse chemisorption, NH₃-TPD, XPS, and TGA techniques. The reaction parameter optimization and spent analysis of the catalyst are also reported and concluded by the summary of the work.

Chapter 4 is about the review on furfural conversion using electrocatalytic hydrogenation (ECH) and reported the results of product selectivity of ECH and thermal catalytic hydrogenation (TCH) of furfural. The use of Ni foam, Cu foam, Cu foil, and NiCu-Al catalyst deposited on Cu foam as working electrodes are discussed.

Chapter 5 deals with the development of an ASPEN PLUS model of furfural hydrogenation based on the best catalytic results of NiCu-Al catalysts to estimate the cost and economic analysis of the process.

Chapter 6 concludes the summary of the thesis, suggestions, and prospects of the work.

Appendix describes the methodology such as schematics of catalyst preparation methods, reaction system (Parr reactor), calibration data of the reactants and products with respect to solvents, and product analysis.

1.4 References

- [1] International Energy Agency, “Total primary energy supply by fuel 2019,” 2019.
- [2] L. Cozzi and T. Gould, “World Energy Outlook 2021,” *IEA Publ.*, pp. 1–386, 2021.
- [3] S. K. Maity, “Opportunities, recent trends and challenges of integrated biorefinery: Part i,” *Renew. Sustain. Energy Rev.*, vol. 43, pp. 1427–1445, 2015.
- [4] S. K. Maity, “Opportunities, recent trends and challenges of integrated biorefinery: Part II,” *Renew. Sustain. Energy Rev.*, vol. 43, pp. 1446–1466, 2015.
- [5] J. P. Lange *et al.*, “Valeric biofuels: A platform of cellulosic transportation fuels,” *Angew. Chemie - Int. Ed.*, vol. 49, no. 26, pp. 4479–4483, 2010.
- [6] M. J. Climent, A. Corma, and S. Iborra, “Conversion of biomass platform molecules into fuel additives and liquid hydrocarbon fuels,” *Green Chem.*, vol. 16, no. 2, pp. 516–547, 2014.
- [7] N. Taufiqurrahmi and S. Bhatia, “Catalytic cracking of edible and non-edible oils for the production of biofuels,” *Energy Environ. Sci.*, vol. 4, no. 4, p. 1087, 2011.
- [8] A. Mukherjee, M. J. Dumont, and V. Raghavan, “Review: Sustainable production of hydroxymethylfurfural and levulinic acid: Challenges and opportunities,” *Biomass and Bioenergy*, vol. 72, pp. 143–183, 2015.
- [9] R. Mariscal, P. Maireles-Torres, M. Ojeda, I. Sádaba, and M. López Granados, “Furfural: A renewable and versatile platform molecule for the synthesis of chemicals and fuels,” *Energy Environ. Sci.*, vol. 9, no. 4, pp. 1144–1189, 2016.
- [10] M. J. Ahmed and B. H. Hameed, “Hydrogenation of glucose and fructose into hexitols over heterogeneous catalysts: A review,” *J. Taiwan Inst. Chem. Eng.*, vol. 96, pp. 341–352, 2019.
- [11] K. Yan, C. Jarvis, J. Gu, and Y. Yan, “Production and catalytic transformation of levulinic acid: A platform for speciality chemicals and fuels,” *Renew. Sustain. Energy Rev.*, vol. 51, pp. 986–997, 2015.
- [12] M. J. Climent, A. Corma, and S. Iborra, “additives and liquid hydrocarbon fuels,”

2013.

- [13] H. Shaghaleh, X. Xu, and S. Wang, “Current progress in production of biopolymeric materials based on cellulose, cellulose nanofibers, and cellulose derivatives,” *RSC Adv.*, vol. 8, no. 2, pp. 825–842, 2018.
- [14] T. Werpy and G. Petersen, “Top value added chemicals from biomass: Volume I- Results of screening for potential candidates from sugars and synthesis gas,” United States, 2004.
- [15] M. I. Alam and B. Saha, *Catalysis for the Production of Sustainable Chemicals and Fuels from Biomass*, no. Figure 1. Elsevier B.V., 2015.
- [16] G. W. Huber, S. Iborra, and A. Corma, “Synthesis of transportation fuels from biomass: Chemistry, catalysts, and engineering,” *Chem. Rev.*, vol. 106, no. 9, pp. 4044–4098, 2006.
- [17] M. J. Climent, A. Corma, and S. Iborra, “Conversion of biomass platform molecules into fuel additives and liquid hydrocarbon fuels,” *Green Chem.*, vol. 16, no. 2, pp. 516–547, 2014.
- [18] A. Fuente-Hernandez, P.-O. Corcos, R. Beauchet, and J.-M. Lavoie, “Biofuels and Co-Products Out of Hemicelluloses,” *Liq. Gaseous Solid Biofuels - Convers. Tech.*, pp. 3–46, 2013.
- [19] Y. Wang, D. Zhao, D. Rodríguez-Padrón, and C. Len, “Recent advances in catalytic hydrogenation of furfural,” *Catalysts*, vol. 9, no. 10, 2019.
- [20] A. Démolis, N. Essayem, and F. Rataboul, “Synthesis and applications of alkyl levulinates,” *ACS Sustain. Chem. Eng.*, vol. 2, no. 6, pp. 1338–1352, 2014.
- [21] S. S. R. Gupta and M. L. Kantam, “Catalytic conversion of furfuryl alcohol or levulinic acid into alkyl levulinates using a sulfonic acid-functionalized hafnium-based MOF,” *Catal. Commun.*, vol. 124, no. November 2018, pp. 62–66, 2019.
- [22] D. Zhao *et al.*, “Continuous Flow Alcoholysis of Furfuryl Alcohol to Alkyl Levulinates Using Zeolites,” *ACS Sustain. Chem. Eng.*, vol. 6, no. 5, pp. 6901–6909, 2018.

- [23] E. Ahmad, M. I. Alam, K. K. Pant, and M. A. Haider, "Catalytic and mechanistic insights into the production of ethyl levulinate from biorenewable feedstocks," *Green Chem.*, vol. 18, no. 18, pp. 4804–4823, 2016.
- [24] H. Joshi, B. R. Moser, J. Toler, W. F. Smith, and T. Walker, "Ethyl levulinate: A potential bio-based diluent for biodiesel which improves cold flow properties," *Biomass and Bioenergy*, vol. 35, no. 7, pp. 3262–3266, 2011.
- [25] V. Gitis, S. H. Chung, and N. Raveendran Shiju, "Conversion of furfuryl alcohol into butyl levulinate with graphite oxide and reduced graphite oxide," *FlatChem*, vol. 10, no. May, pp. 39–44, 2018.
- [26] B. S. Rao, P. K. Kumari, D. Dhanalakshmi, and N. Lingaiah, "Selective conversion of furfuryl alcohol into butyl levulinate over zinc exchanged heteropoly tungstate supported on niobia catalysts," *Mol. Catal.*, vol. 427, pp. 80–86, 2017.
- [27] Z. Mohammadbagheri and A. Najafi Chermahini, "KCC-1/Pr-SO₃H as an efficient heterogeneous catalyst for production of n-butyl levulinate from furfuryl alcohol," *J. Ind. Eng. Chem.*, vol. 62, pp. 401–408, 2018.
- [28] R. Bringué, E. Ramírez, M. Iborra, J. Tejero, and F. Cunill, "Esterification of furfuryl alcohol to butyl levulinate over ion-exchange resins," *Fuel*, vol. 257, no. June, p. 116010, 2019.
- [29] P. Demmacarà, R. Ciriminna, N. R. Shiju, G. Rothenberg, and M. Pagliaro, "Enhanced heterogeneous catalytic conversion of furfuryl alcohol into butyl levulinate," *ChemSusChem*, vol. 7, no. 3, pp. 835–840, 2014.
- [30] L. Peng, H. Li, L. Xi, K. Chen, and H. Chen, "Facile and efficient conversion of furfuryl alcohol into n-butyl levulinate catalyzed by extremely low acid concentration," *BioResources*, vol. 9, no. 3, pp. 3825–3834, 2014.
- [31] J. Yang *et al.*, "Waste paper-derived magnetic carbon composite: A novel eco-friendly solid acid for the synthesis of n-butyl levulinate from furfuryl alcohol," *Renew. Energy*, vol. 146, pp. 477–483, 2020.
- [32] L. Peng, R. Tao, and Y. Wu, "Catalytic upgrading of biomass-derived furfuryl

- alcohol to butyl levulinate biofuel over common metal salts,” *Catalysts*, vol. 6, no. 9, 2016.
- [33] J. N. Appaturi, M. R. Johan, R. J. Ramalingam, H. A. Al-Lohedan, and J. J. Vijaya, “Efficient synthesis of butyl levulinate from furfuryl alcohol over ordered mesoporous Ti-KIT-6 catalysts for green chemistry applications,” *RSC Adv.*, vol. 7, no. 87, pp. 55206–55214, 2017.
- [34] P. Neves *et al.*, “Production of biomass-derived furanic ethers and levulinate esters using heterogeneous acid catalysts,” *Green Chem.*, vol. 15, no. 12, pp. 3367–3376, 2013.
- [35] S. S. R. Gupta and M. L. Kantam, “Catalytic conversion of furfuryl alcohol or levulinic acid into alkyl levulinates using a sulfonic acid-functionalized hafnium-based MOF,” *Catal. Commun.*, vol. 124, no. March, pp. 62–66, 2019.
- [36] L. Peng, X. Gao, and K. Chen, “Catalytic upgrading of renewable furfuryl alcohol to alkyl levulinates using AlCl₃ as a facile, efficient, and reusable catalyst,” *Fuel*, vol. 160, pp. 123–131, 2015.
- [37] S. S. Enumula, K. S. Koppadi, V. R. Babu Gurram, D. R. Burri, and S. R. Rao Kamaraju, “Conversion of furfuryl alcohol to alkyl levulinate fuel additives over Al₂O₃/SBA-15 catalyst,” *Sustain. Energy Fuels*, vol. 1, no. 3, pp. 644–651, 2017.
- [38] D. Ren, J. Fu, L. Li, Y. Liu, F. Jin, and Z. Huo, “Efficient conversion of biomass-derived furfuryl alcohol to levulinate esters over commercial α -Fe₂O₃,” *RSC Adv.*, vol. 6, no. 26, pp. 22174–22178, 2016.
- [39] J. R. Kean and A. E. Graham, “Indium(III) triflate promoted synthesis of alkyl levulinates from furyl alcohols and furyl aldehydes,” *Catal. Commun.*, vol. 59, no. Iii, pp. 175–179, 2015.
- [40] A. M. Hengne, S. B. Kamble, and C. V. Rode, “Single pot conversion of furfuryl alcohol to levulinic esters and γ -valerolactone in the presence of sulfonic acid functionalized ILs and metal catalysts,” *Green Chem.*, vol. 15, no. 9, pp. 2540–2547, 2013.

- [41] X. F. Liu *et al.*, “Efficient conversion of furfuryl alcohol to ethyl levulinate with sulfonic acid-functionalized MIL-101(Cr),” *RSC Adv.*, vol. 6, no. 93, pp. 90232–90238, 2016.
- [42] S. R. B., K. K. P., D. L. D., and N. Lingaiah, “One pot selective transformation of biomass derived chemicals towards alkyl levulinates over titanium exchanged heteropoly tungstate catalysts,” *Catal. Today*, vol. 309, no. May, pp. 269–275, 2018.
- [43] Z. Zhang, K. Dong, and Z. Zhao, “Efficient conversion of furfuryl alcohol into alkyl levulinates catalyzed by an organic-inorganic hybrid solid acid catalyst,” *ChemSusChem*, vol. 4, no. 1, pp. 112–118, 2011.
- [44] Y. Nakagawa and K. Tomishige, “Total hydrogenation of furan derivatives over silica-supported Ni-Pd alloy catalyst,” *Catal. Commun.*, vol. 12, no. 3, pp. 154–156, 2010.
- [45] C. Wang *et al.*, “Aqueous phase hydrogenation of furfural to tetrahydrofurfuryl alcohol over Pd/UiO-66,” *Catal. Commun.*, vol. 148, p. 106178, 2021.
- [46] Y. Nakagawa, K. Takada, M. Tamura, and K. Tomishige, “Total Hydrogenation of Furfural and 5-Hydroxymethylfurfural over Supported Pd–Ir Alloy Catalyst,” *ACS Catal.*, vol. 4, no. 8, pp. 2718–2726, Aug. 2014.
- [47] R. Huang, Q. Cui, Q. Yuan, H. Wu, Y. Guan, and P. Wu, “Total Hydrogenation of Furfural over Pd/Al₂O₃ and Ru/ZrO₂ Mixture under Mild Conditions: Essential Role of Tetrahydrofurfural as an Intermediate and Support Effect,” *ACS Sustain. Chem. Eng.*, vol. 6, no. 5, pp. 6957–6964, 2018.
- [48] Narayan S. Biradar, Amol M. Hengne, Rode, “Single-Pot Formation of THFAL via Catalytic Hydrogenation of FFR Over Pd/MFI Catalyst,” *ACS Sustain. Chem. Eng.*, 2013.
- [49] N. Merat, C. Godawa, and A. Gaset, “High selective production of tetrahydrofurfuryl alcohol: Catalytic hydrogenation of furfural and furfuryl alcohol,” *J. Chem. Technol. Biotechnol.*, vol. 48, no. 2, pp. 145–159, 1990.

- [50] M. Hronec, K. Fulajtarová, and T. Liptaj, “Effect of catalyst and solvent on the furan ring rearrangement to cyclopentanone,” *Appl. Catal. A Gen.*, vol. 437–438, pp. 104–111, 2012.
- [51] J. Wu, G. Gao, J. Li, P. Sun, X. Long, and F. Li, “Efficient and versatile CuNi alloy nanocatalysts for the highly selective hydrogenation of furfural,” *Appl. Catal. B Environ.*, vol. 203, pp. 227–236, 2017.
- [52] L. Liu, H. Lou, and M. Chen, “Selective hydrogenation of furfural to tetrahydrofurfuryl alcohol over Ni/CNTs and bimetallic Cu[sbnd]Ni/CNTs catalysts,” *Int. J. Hydrogen Energy*, vol. 41, no. 33, pp. 14721–14731, 2016.
- [53] C. Sunyol, R. English Owen, M. D. González, P. Salagre, and Y. Cesteros, “Catalytic hydrogenation of furfural to tetrahydrofurfuryl alcohol using competitive nickel catalysts supported on mesoporous clays,” *Appl. Catal. A Gen.*, vol. 611, no. October 2020, 2021.
- [54] V. Sánchez, P. Salagre, M. D. González, J. Llorca, and Y. Cesteros, “Effect of the formation of NiCu alloy and use of biomass-derived furfural on the catalytic hydrogenation of furfural to THFA,” *Mol. Catal.*, vol. 490, no. December 2019, p. 110956, 2020.

Chapter 2: A comprehensive study on butanolysis of furfuryl alcohol to butyl levulinate using tungstated zirconia and sulfonated carbon catalysts

Abstract:

This work presents the formation of butyl levulinate (BL), a potential fuel additive and an excellent renewable chemical obtained by the butanolysis of furfuryl alcohol (FAL) over a solid acid catalyst. The butanolysis of FAL reaction is a strong function of acidity for which tungstated zirconia ($\text{WO}_3\text{-ZrO}_2$), a robust solid acid catalyst, and a sulfonated carbon catalyst were employed to produce high yields of BL while targeting a lower initial molar ratio of butanol to FAL. A maximum of 28 mol% yield of BL was obtained with a tungstated zirconia catalyst. Easily prepared sulfonated carbon catalyst at high reaction temperatures facilitated the complete conversion of reaction intermediate, 2-butoxymethylfuran (2-BMF), through which BL was formed, and as high as 80 mol% yield of BL was produced at an initial mole ratio of 8.5:1 of butanol to FAL. The good results of sulfonated carbon catalyst could be attributed to the presence of $-\text{SO}_3\text{H}$, carboxylic acid, and phenolic OH groups on the carbon surface.

Keywords: Butanolysis, tungstated zirconia, sulfonated carbon, and butyl levulinate.

2.1 Introduction

With recent changes in the energy-consuming sector's advancements and depleting fossil fuels, significant attention has been drawn to transforming renewable resources into transportation fuels and fine chemicals[1][2]. Selective chemical conversion of lignocellulosic biomass, especially cellulose and hemicellulose, provides platform chemicals such as 5-hydroxymethylfurfural, levulinic acid (LA), and furfural, which can be further down streamed to versatile alkyl levulinates[3][4]. Alkyl levulinates possess high lubricity, low toxicity, stable flashpoint, and moderate flow properties, making them suitable gasoline and diesel blends. Moreover, alkyl levulinates have numerous

applications as a solvent, plasticizer, and precursor to obtaining γ -valerolactone[5]. Among the alkyl levulinates, butyl levulinate (BL), an oxygenate fuel additive with high octane number, rich oxygen content, and low solubility in water, makes it a better fuel blend than ethyl levulinate and an alternative for the water-soluble carcinogen methyl tert-butyl ether (MTBE) [6].

The esterification of LA with alcohols and alcoholysis of furfuryl alcohol (FAL) in acid-catalyzed environments are the general methods to produce the alkyl levulinates. However, the production of butyl levulinate using LA as a raw material is an expensive process, with product water inhibiting the reaction from progressing effectively [7][8]. The other route via FAL's alcoholysis has gained much attention due to its smooth and cost-effective pathway for BL synthesis. The BL production was reported using various homogeneous acid catalysts such as H_2SO_4 , AlCl_3 [9], and a double $\text{SO}_3\text{-H}$ functionalized ionic liquids, sulfonic acid-functionalized ionic liquids[10], which surmises that the butanolysis of FAL is a function of strong acidity. To avoid the major drawbacks of homogeneous systems comprehended by potential reactor corrosion, recovery, and recyclability, several heterogeneous catalyst systems such as ion exchange resins[11], zeolites, SBA-16[6], metal oxides[12][13], mesoporous aluminosilicates[14], and zinc exchanged heteropoly acids[15] catalysts have been successfully employed for the alkyl levulinates production.

To accommodate butanolysis reaction, a facile, highly stable, and easily regenerable tungstated zirconia (WZr) catalyst[16] was first employed to test its activity. Hino and Arata first reported the WZr catalyst's synthesis to cope with the challenges posed by the desorption of active SO_4^{2-} ions from $\text{SO}_4^{2-}/\text{ZrO}_2$ catalysts[17]. W-O-Zr bonds' presence makes it strongly stable, which overcomes the detachment of active WO_x species from ZrO_2 support. WZr catalysts efficiently enhanced the alkanes isomerization[18], hydrogenolysis[19], dehydration[20], aqueous phase hydrolysis[21], selective catalytic NO_x reduction[22], cyclohexane hydration[23], in liquid phase Beckmann rearrangement[24], esterification and transesterification reactions[25]. Besides, LA's esterification with butanol was carried out to obtain BL with 97% selectivity[26]. Owing to the excellent catalytic activity of WZr, this study was interested in reporting the WZr activity for the butanolysis of FAL with lower initial butanol to FAL mole ratios.

Upon the WZr catalyst activity for butanolysis of FAL, with barely around 28% of the BL yield, the reaction was carried out using a sulfonated carbon catalyst. Carbon-based catalysts with low synthesis cost, high catalytic activity, and abundant carbon sources make them suitable heterogeneous catalytic systems[27]. The partially pyrolyzed carbon source is rich in oxygen content composed of several surface functional groups such as carboxylic acid, aromatic hydrocarbons, and phenolic hydroxyl groups[28]. Thus, obtained carbon black can easily be functionalized with $-SO_3H$ groups by sulfonation with various $-SO_3H$ group sources, for instance, conc. H_2SO_4 , fuming H_2SO_4 , and 4-Benzenediazoniumsulfonate. Literature reports were available to find the excellent catalytic activity of sulfonated carbon catalysts for a wide range of reactions like fatty acids (FFA) esterification[29][30], cellulose hydrolysis[31], transesterification of vegetable oils[32], glycerol conversion[33], and esterification reactions[34][35][36].

Most of the studies reported for the butanolysis of FAL were with high initial 1-butanol to FAL molar ratios to avoid the formation of FAL polymers. Bringué et al. performed the butanolysis of FAL over sulfonated polystyrene-divinylbenzene (PS-DVB) resins at low initial 1-butanol to FAL molar ratios (8:1) with a maximum of 63% BL yield at 110 °C. This study also reported that 2-BMF was still unconverted to BL at the end of the reaction time owing to the temperature. The Amberlyst catalysts are thermally challengeable above 120 °C, and the lower reaction temperature influenced obtaining the maximum yield [11]. Similarly, Enamula et al. also employed a high initial mole ratio of 16 at a high reaction temperature (180 °C) to obtain 63 mol% of BL yield using $Al_2O_3/SBA-15$ catalyst. The same catalyst at 110 °C resulted in 91 mol% of BL yield but at the initial mole ratio of 65[13]. Yang et al. reported the activity of a magnetic carbonaceous solid acid (SMWP) catalyst with 91 mol% of BL yield, operating at an initial mole ratio of 40 (BtOH: FAL)[8]. Thus, the present study focuses on increasing the BL yield to a maximum level at a possible lower initial molar (BtOH: FAL) ratio.

2.2 Materials and methods

2.2.1 Materials

Pluronic P-123, zirconium (IV) butoxide solution (80 wt.% in 1-butanol), ammonium metatungstate hydrate, Conc. HNO_3 (65%), n-Butanol (purity > 99.0%), carbon tetrachloride (CCl_4), and methanol were acquired from Sigma-Aldrich. Ethanol,

furfuryl alcohol, sucrose, and sulfuric acid were obtained from Fuji film Wako chemicals Ltd. n-Butyl levulinate and dibutyl ether were purchased from TCI chemicals. All the chemicals were used as received.

2.2.2 Catalyst synthesis

2.2.2.1 Preparation of Tungstated Zirconia ($\text{WO}_3\text{-ZrO}_2$)

The catalyst synthesis was carried out using the evaporation-induced self-assembly (EISA) method mentioned elsewhere to obtain a mesoporous structured catalyst[37]. Ammonium meta tungstate hydrate (0.05074 mmol) and zirconium (IV) butoxide solution (80 wt.% in 1-butanol) (68.982 mmol) were used as precursors for WO_3 and ZrO_2 , and pluronic P123 (1.724 mmol) was used as a structure directive agent. In a typical synthesis, Pluronic P123, tungsten, and zirconia precursors were dissolved in 250 ml of ethanol. To this solution, 2ml of H_2O and 8 ml of HNO_3 were added to promote the condensation during the synthesis and to maintain the pH of the solution below the electrostatic point of the tungsten and zirconia. The solution was aged for 12 hours with continuous stirring of 300 rpm. After that, the homogeneous mixture was dried in a hot air oven at 40 °C for 48 hours to facilitate the slow evaporation and then completely dried further at 70 °C for 12 hours. Finally, thus obtained solid was calcined in air at 800 °C for 6 hours with a ramping rate of 1 °C/min (25→200 °C, 1-hour stay at 200 °C, 200→400 °C, 1-hour stay at 400 °C, 400→800 °C, 6 hours stay 800 °C). The prepared catalysts were termed xWZrT (where x -wt.% of WO_3 & T-calcination temperature, °C). The promoted catalyst was prepared by the wet impregnation method with noble and novel metals and further calcined at respective reduction temperatures of the metals. The notation yM15WZr800 (M- Metal, y-wt.% of the metal) was used to represent the promoted catalysts.

2.2.2.2 Preparation of sulfonated carbon

The catalyst was synthesized by incomplete carbonization of the sucrose, followed by sulfonation at the designated temperature for a particular time under inert conditions[38][39][40]. The catalyst preparation was done in two steps. In the first step, 5g of sucrose was partially carbonized at 400 °C for 15 hours under constant N_2 flow (200 ml/min) to obtain a black solid. Thus, obtained carbon black was grounded to a fine powder. In the second step, 2g of carbon black was sulfonated using 40 ml of conc.

H₂SO₄(>98%) at 80 °C for 10 hours under inert conditions. After the sulfonation, the black mixture was washed with hot distilled water and then vacuum filtered until the neutral pH of the water was observed. Finally, the catalyst was dried at 100 °C for 12 hours before direct use. The prepared catalyst was denoted by SO₃H_C80S (Carbon black sulfonated at 80 °C) and the spent catalyst after 3 cycles by SO₃H_C80S Spent.

2.2.3 Catalyst characterization

The specific surface area and pore size distribution of the prepared catalysts were analyzed using nitrogen adsorption/desorption isotherms data obtained at 77 K using the BELSORP-Minix analyzer. The catalyst samples were first degassed under vacuum (10⁻⁵ torr) conditions at 573 K (Tungstated zirconia catalysts) and at 393 K (carbon catalysts) for 4 hours to remove the surface adsorbed species and moisture on the catalysts. The specific surface area was determined by the adsorption isotherm of nitrogen in the relative pressure range of $0.05 < p/p_0 < 0.3$ using the BET equation. The pore size distribution and pore volume were determined by the BJH desorption method using desorption isotherm.

Fourier-transform infrared spectroscopy (FTIR) was done using a Bruker ALPHA II. The samples were mixed with spectroscopic grade potassium bromide (KBr, 100 mg) and pressed to acquire a circular transparent disk with a hydraulic press. The spectra were collected from 4000 to 400 cm⁻¹ with a resolution of 4 cm⁻¹ for 16scans using KBr disks.

The pyridine probed FTIR was performed to distinguish the acidic sites present on the catalyst. Pyridine was added to the catalyst samples and allowed pyridine to adsorb on the samples' surface for 2 hours at room temperature. The unadsorbed pyridine was removed by keeping the samples in the oven at 383 K for 2 hours. 100 mg of KBr was added to the samples, and the transparent pellets were made using the hydraulic press. The IR spectra were recorded against the KBr background.

The acidic properties of the tungstaed zirconia and metal-promoted catalysts were estimated by the NH₃ adsorption and temperature-programmed desorption (NH₃-TPD) technique using BEL-CAT (MicrotracBEL corp.) automated chemisorption analyzer with a TCD detector. The samples were first pretreated with helium gas (50 ml/min) at 250 °C for 1 hour and cooled down to 100 °C. After that, ammonia adsorption was carried out

using a 5% NH₃ gas mixed with helium (95%) for 30 minutes at 100 °C. After completing ammonia adsorption, the samples were purged with pure He for 30 more minutes, allowing TCD stabilization. Finally, the ammonia desorption spectra were obtained by gradually increasing the temperature by 10 °C/min until the final temperature, followed by the calibration with a 5% NH₃-He mixture. The amount of ammonia adsorbed in mmol/g was automatically calculated by the ChemMaster software using the calibration curve and the amount of ammonia taken. The ammonia adsorption technique was not performed for carbon catalysts as the detachment of -SO₃H progressed at higher temperatures (>230 °C) during the analysis.

Thermogravimetric analysis (TGA) measurement was conducted using STA 2500 REGULUS apparatus in the temperature range of 25 °C-400 °C in a platinum crucible under 80 ml/min of N₂ flow. Before the analysis, all the samples were dried under vacuum at 110 °C for 24 hours. During the analysis, an isothermal state was maintained at 100 °C for 1 hour to remove the moisture completely. The temperature ramp rate of 2 °C/min was employed as the same heating rate was used during the partial carbonization of sucrose.

The acidic sites of the carbon catalysts were measured by the acid-base back titrations using an aqueous ion-exchange method using NaHCO₃ base solution followed by the titration against aqueous HCl solution[41]. In a typical process, 30 mg of catalyst was dispersed in 0.005 N NaHCO₃ solution and continuously stirred for 24 hours. After that, the resulting mixture was filtered, and the filtrate was titrated against 0.005 N HCl solution using a methyl orange indicator. The acid sites on the catalysts were quantified by the amount of NaHCO₃ consumed.

2.2.4 Butanolysis of FAL

The catalytic activity was tested for the butanolysis of FAL in a 100 ml high-pressure batch reactor (Parr Instruments). In a typical experiment, the specified amounts of reactants and the catalyst were charged into the reactor. The reactor was purged with nitrogen gas several times to ensure an inert environment and then pressurized. The reaction temperature and agitation speed were fixed, and the reaction was carried out for the specified times after reaching the set temperature. After the reaction, the reactor was

cooled down to room temperature, and the sample was collected. The liquid samples were centrifuged to remove the catalyst traces and diluted with internal calibration solvent carbon tetrachloride and dilutant methanol before analyzing with GC-FID (flame ionization detector) and GC-MS (mass spectroscopy). The following equations were used for the quantification calculations[33].

$$\text{Conversion (mol\%)} = \frac{(\text{Initial moles} - \text{Final moles}) \text{ of FAL}}{\text{Initial moles of FAL}} \times 100$$

$$\text{Selectivity (mol\%)} = \frac{\text{moles of a product obtained}}{\text{total moles of product}} \times 100$$

$$\text{Yield(mol\%)} = \frac{\text{moles of BL formed}}{\text{theoretical moles of BL expected}} \times 100$$

2.2.5 Catalyst reuse

The reuse test was conducted to determine the number of cycles that the catalyst can be used without requiring regeneration. Thus, three reaction cycles of the best-performing catalyst were performed for the spent analysis. After completing every reaction, the catalyst was separated from the reaction mixture by vacuum filtration and several washings with methanol followed by ethanol to remove the adsorbed organic compounds. Afterwards, the catalyst was dried at 100 °C for 12 hours before use.

2.3 Results and discussion on the characterization of WO₃-ZrO₂ catalyst

2.3.1 Textural properties

The N₂ physisorption illustrates the physical properties of the prepared WZr catalysts. The typical isotherms correspond to type IV isotherms and represent the mesoporous nature of the catalyst. Fig.2.1a and 2.1b further showed that for a 15 wt.% WO₃ loading, the incipient of the hysteresis loop shifted towards higher relative pressure with the increase in calcination temperature. On the contrary, for a fixed calcination temperature of 800 °C, the beginning of the hysteresis loop was observed at P/P₀ of 0.5 for 10WZr800 and shifted towards higher relative pressure with the increase in the WO₃

content in tungstated zirconia catalysts. These results exhibited the expansion and contraction of the pores with the increase in calcination temperature for fixed WO₃ content and WO₃ loading for a fixed calcination temperature, respectively. The pure zirconia's surface area was also relatively low, representing its non-porous nature at such a high calcination temperature. The pure zirconia and pure WO₃ have a poor surface area (Table 2.1, entries 1,2), which explains the integration of W-O-Zr bonds needed to stabilize this catalyst, which is responsible for its strong thermal and mechanical strength[42]. An increase in calcination temperature at constant metal oxide loading increases the surface density of the metal on the support oxide, which triggers the mobility of support metal atoms[43]. In the case of tungstated zirconia catalyst, calcination at higher temperature promotes Zr atoms mobility, which triggers the sintering of Zr atoms along with the augmentation of pore size[26]. These phenomena were observed for 15WZr900. The specific surface area of the catalyst was reduced to 17.5 m²/g with widened pores (Table 2.1, entry 5). The surface density of the W dispersion on the ZrO₂ support was calculated by the following equation, which measures the tungsten monolayer coverage[44].

$$\text{Surface density of W} = \frac{(\text{WO}_3 \text{ Loading(wt.\%)/100}) \times 6.023 \times 10^{23}}{231.8 (\text{formula weight of WO}_3) \times \text{BET Surface area(m}^2\text{g}^{-1}) \times 10^{18}}$$

The increase in the WO₃ loading increased the surface area to 79 m²/g for 15 wt.% calcined at 800 °C (Table 2.1, entry 4), for which the surface density was around 4.9 W-atom/nm², which is in the range for a typical value of the surface monolayer coverage[45][46]. The pore size distribution measured by the BJH desorption method was also represented in Fig.1b. The 15WZr800 catalyst has a pore diameter of 10.6 nm compared to 8.3 nm of 10WZr800, and the depth of the pores for the 15 Wt.% is longer than 10 Wt.%, which was clearly shown by the increased pore volume for the 15 Wt.% loadings (Table 2.1, entries 3,4). The further increase in the calcination temperature to 900 °C profoundly affected the pore structure of the catalyst, resulting in the widening of the pores caused by the sintering of the Zr atoms (Table 2.1, entry 5) [16].

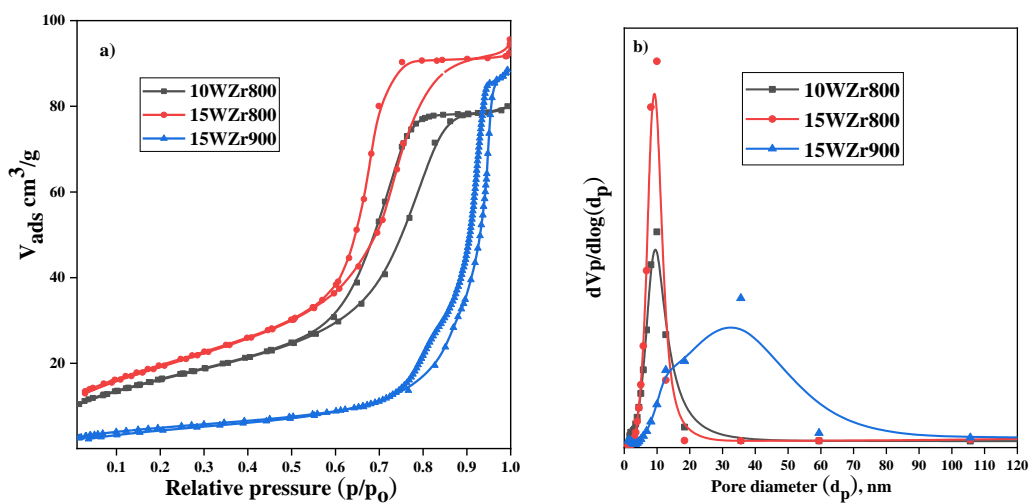


Fig.2.1: BET analysis of tungstated zirconia catalysts a) N₂ physisorption isotherms (b) BJH Pore size distribution

Table 2.1: Physical properties of WO₃-ZrO₂

Catalyst	BET Surface area (m ² /g)	Pore volume (cm ³ /g)	Pore diameter (nm)	Surface density (W-atoms/nm ²)
WO ₃ 800	0.47	0.00573	49.06	NA
ZrO ₂ 800	19	0.013	19	0.0
10WZr800	59.42	0.124	8.316	4.37
15WZr800	79.2	0.157	10.63	4.92
15WZr900	17.5	0.136	31.098	22.2

2.3.2 NH₃-TPD analysis

NH₃-TPD study was implemented to understand the surface acidic properties of the tungstated zirconia catalysts and the metal-promoted catalysts. The NH₃-TPD spectra are shown in Fig.2.2a and 2.2b. The total surface acidity and the peak temperatures are summarized in Table 3. The ammonia desorption was obtained in a broad range from 100

°C to 800 °C to understand the acid strength of the catalysts. The peak temperatures below 350 °C were assigned to the weaker acidic sites to comprehend and quantify the surface acidity. The peaks above 350 °C correspond to the stronger acidic sites [26][25]. However, the intensity of more substantial acidic strength peaks was very low compared to the lower temperature peaks.

The surface acidity was affected by WO₃ loading and the calcination temperature (Table 2.2, entries 1,2 &3). The increase in the WO₃ loading from 10 wt.% to 15 wt.% induced a hike in the surface acidity from 0.143 mmol/g to 0.201 mmol/g (Table 2.2, entries 1,2). For 15 wt.% WO₃ loading, the surface density was 4.9 W-atoms/nm² (Table 2.1, entry 4), which generally corresponds to the monolayer coverage of the W-atoms, thereby increasing the surface acidity[46]. The collapse of the pore structure (BET results, Fig. 2.1b) at such a higher calcination temperature (900 °C) probably caused the drop in the total acidity to 0.122 mmol/g.

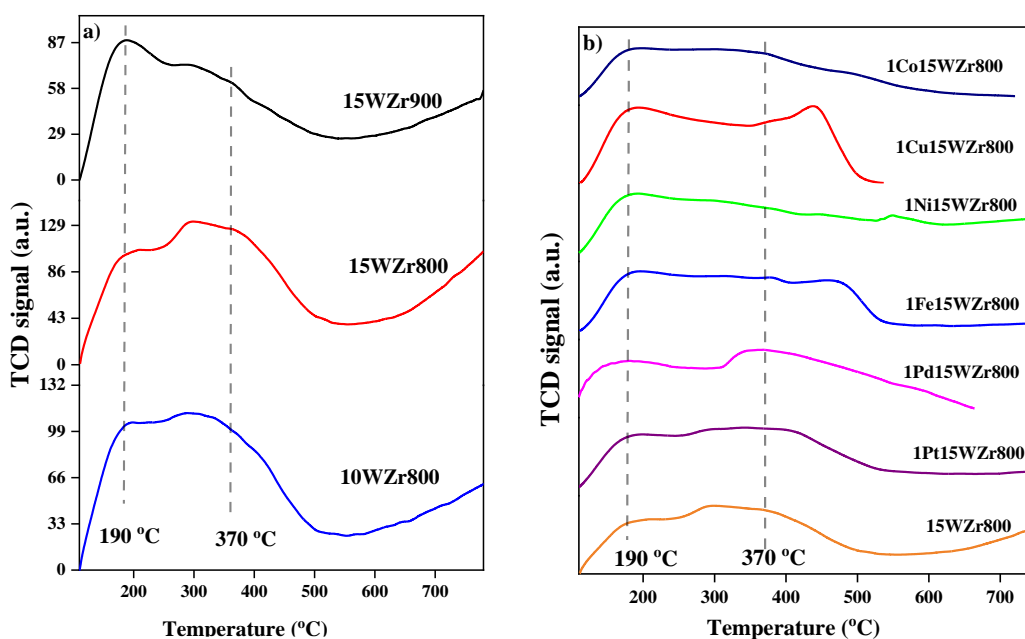


Fig.2.2: NH₃-TPD spectra of a) Tungstated zirconia catalysts b) Metal promoted catalysts

Table 2.2: Peak temperature and acidity of the WO₃-ZrO₂ catalysts.

Catalyst	Peak temperature ($^{\circ}\text{C}$)		Total Acidity (mmol/g)	BL yield
10WZr800	188	360	0.143	5.58
15WZr800	188	370	0.201	14.43
15WZr900	198	294	0.122	3.7
1Pt15WZr800	187	394	0.203	13.5
1Pd15WZr800	174	352	0.209	14.2
1Ni15WZr800	185	335	0.199	12.5
1Fe15WZr800	190	465	0.207	11.2
1Cu15WZr800	185	432	0.199	10.73
1Co15WZr800	180	370	0.203	10.72

The peak corresponding to weaker acidic strength was observed at 175-198 $^{\circ}\text{C}$ for all the catalysts. This indicates that the metal promotion influenced the strong acidic sites upon interaction with the W atoms. The surface acidity of all metal-promoted catalysts is constrained to a narrow range from 0.199 to 0.209 mmol/g (Table 2.2, entries 4-9). The yield of BL was also restricted to a narrow range of 10.7 mol% to 14.2 mol% (Table 2.2, entries 4-9). Even though the enhancement in terms of the acidity of the tungstated catalyst was achieved very slightly by the metal promotion, it has not led to a significant difference in the activity towards increasing the BL yield.

2.3.3 Pyridine-FTIR analysis

To distinguish the nature of the surface acidity of the tungstated zirconia catalyst, Pyridine-FTIR analysis was studied and represented in Fig.3.3a & 3.3b and the peak areas were reported in Table 2.3. The band at 1440 cm^{-1} corresponds to the interaction of pyridine Bronsted molecules with H^+ electron-accepting molecules corresponding to Lewis acidity. The band at 1540 cm^{-1} was attributed to the presence of Bronsted acidic molecules. The band at 1490 cm^{-1} represents the combined acidic strength of Lewis and Bronsted. The intensity of the bands progressed with WO_3 loading from 10 wt.% to 15

wt.% (Table 2.3, entries 1 & 2). Increasing the WO_3 content led to the development of polytungstate species and the formation of Zr- WO_x clusters[51][52]. At 15 wt.% of WO_3 loading, the monolayer coverage was accomplished by progressing the condensation of monotungstate to polytungstate species by enhancing the surface acidity. The tungsten atom in the polytungstate can delocalize the adjacent zirconia electrons, thereby generating the proton development to compensate the delocalized electrons, enhancing the growth of the Bronsted acidity[42][52]. At a higher calcination temperature of 900 °C, the band intensity corresponding to Lewis acidity weakened, and other peak intensities reduced considerably. The basic reason is the pore structure collapse at elevated temperatures, accompanied by the sintering of Zr atoms [16][53].

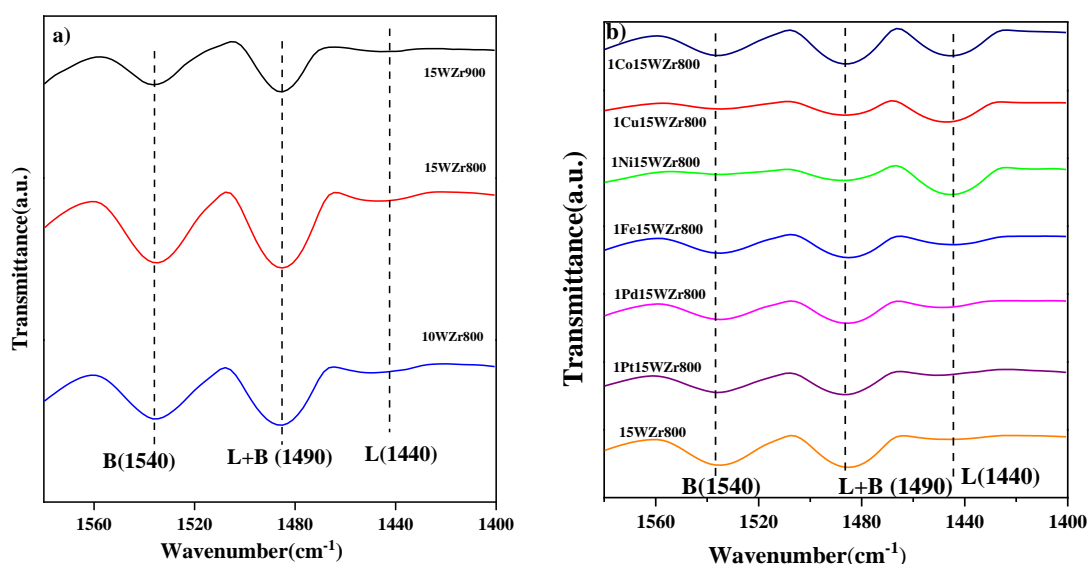


Fig.2.3: Pyridine-FTIR spectra of a) Tungstated zirconia catalysts b) Metal promoted catalysts

As described in the NH_3 -TPD analysis section, the metal promotion slightly altered the surface acidic properties of the catalysts. The incorporation with Pt and Pd metals resulted in close Bronsted to Lewis acidic sites that of neat tungstated zirconia (Table 2.3, entries 2, 4 & 5). The BL yield obtained for these catalysts is also in the close range from 13.5 to 14.42 mol% (Table 2.3, entries 2, 4 & 5). The Ni and Cu up-gradation remarkably increased the intensity of the Lewis acidity compared to other novel metals (Table 2.3, entries 7 & 8). This change is probably surmised to be the interaction between metals (Ni, Cu) and ZrO_2 surface, thereby revoking the $\text{Zr}^{+4}\text{O}^{2-}$ activation, which induces the Lewis

acidity and simultaneously makes unavailability of electrons for polytungstate to develop the Bronsted acidic sites. The modification with Fe and Co metals also induced the Lewis acidity hike compared to the neat and noble (Pt, Pd) metal incorporation (Table 2.3, entries 6,9). Despite all these structural and physicochemical improvements by metal incorporation on the tungstated catalysts, the yield of BL was not improved significantly. Thus, making this catalyst low selective for the butanolysis of FAL.

Table 2.3: Normalized peak areas w.r.t weight of the $\text{WO}_3\text{-ZrO}_2$ catalysts.

Catalyst	Lewis	Lewis +Bronsted	Bronsted	Bronsted/Lewis
10WZr800	0.148	1.213	1.126	7.574
15WZr800	0.293	1.426	1.383	4.718
15WZr900	0.003	0.035	0.032	12.402
1Pt15WZr800	0.208	0.625	0.896	4.354
1Pd15WZr800	0.211	0.799	0.926	3.388
1Fe15WZr800	0.453	1.151	0.963	2.125
1Ni15WZr800	1.445	0.681	0.203	0.141
1Cu15WZr800	1.058	0.721	0.374	0.354
1Co15WZr800	0.567	0.742	0.528	0.939

2.4 Results and discussion on the characterization of sulfonated carbon catalysts

2.4.1 Textural properties

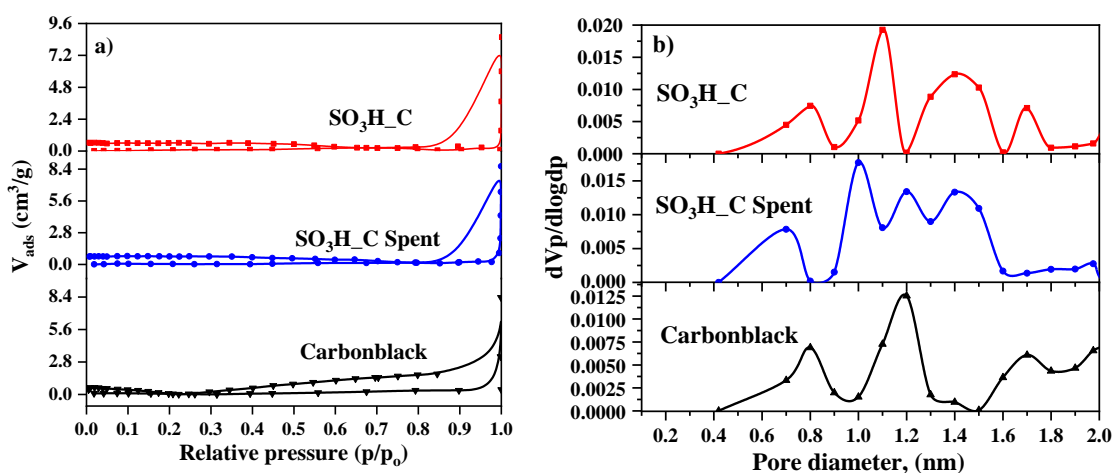


Fig.2.4: BET analysis of carbon catalysts a) N₂ physisorption isotherms of sulfonated carbon catalysts b) Micropore distribution

Fig.2.4a and 2.4b exemplify N₂ adsorption isotherms and micropore analysis of the carbon catalysts. The carbonation and sulfonation temperatures relatively influence the specific surface area of the catalysts. The isotherms of the sulfonated carbon catalyst and the spent catalysts are adequately similar to the carbon black isotherm except for the amount of nitrogen adsorbed on the surface. Umar et al. reported a similar trend of isotherms for sulfonated waste biomass catalysts[5]. This excess N₂ adsorption transpired because of the deep pores compared to the spent one (Fig.2.4b). The sulfonation of the carbon black resulted in the oxidation of functional groups and developed a deeper micropore than the carbon black (Fig.2.4b). The sulfonation of the carbon black deepened micropores of the carbon black and showed an average of 1.12 nm micropore diameter (Fig.2.4b). The spent catalyst showed a similar trend to the fresh except for the reduced micropore of 1nm. Finally, the carbon black showed a 1.2nm wide micropore, modified during the sulfonation process.

The specific surface area of the prepared carbon-based catalysts measured by the N₂ adsorption technique at 77 K was reported in Table 2.4. The specific surface area of the catalysts is relatively influenced by the carbonation and sulfonation temperatures[47]. The carbon catalysts have a specific surface area <1 m²/g (Table 2.4, entries 1-3), primarily because of the formation of amorphous carbon by incomplete carbonization of

the sucrose, which resulted in the dispersion of large phenol hydrophilic and carboxylic acid functional groups[29][36]. There was no significant change in the surface area of the carbon black after the sulfonation with conc. H₂SO₄ indicates that the –SO₃H groups were incorporated into the carbon structure by bonding with the existing functional groups. The pore volume and pore diameter of the catalysts were very low, caused by no surface area development and the pore structure. N₂ adsorption isotherms and micropore analysis are shown in the supporting information (Fig.2.4a &2.4b).

Table 2.4: Physical properties of sulfonated carbon catalysts.

Catalyst	BET Surface area (m²/g)	Pore volume (cm³/g)	Pore diameter (nm)
Carbon black	0.28	0.0061	1.2
SO ₃ H_C80S	0.29	0.0078	1.12
SO ₃ H_C80S Spent	0.23	0.0059	1.0

2.4.2 FTIR analysis

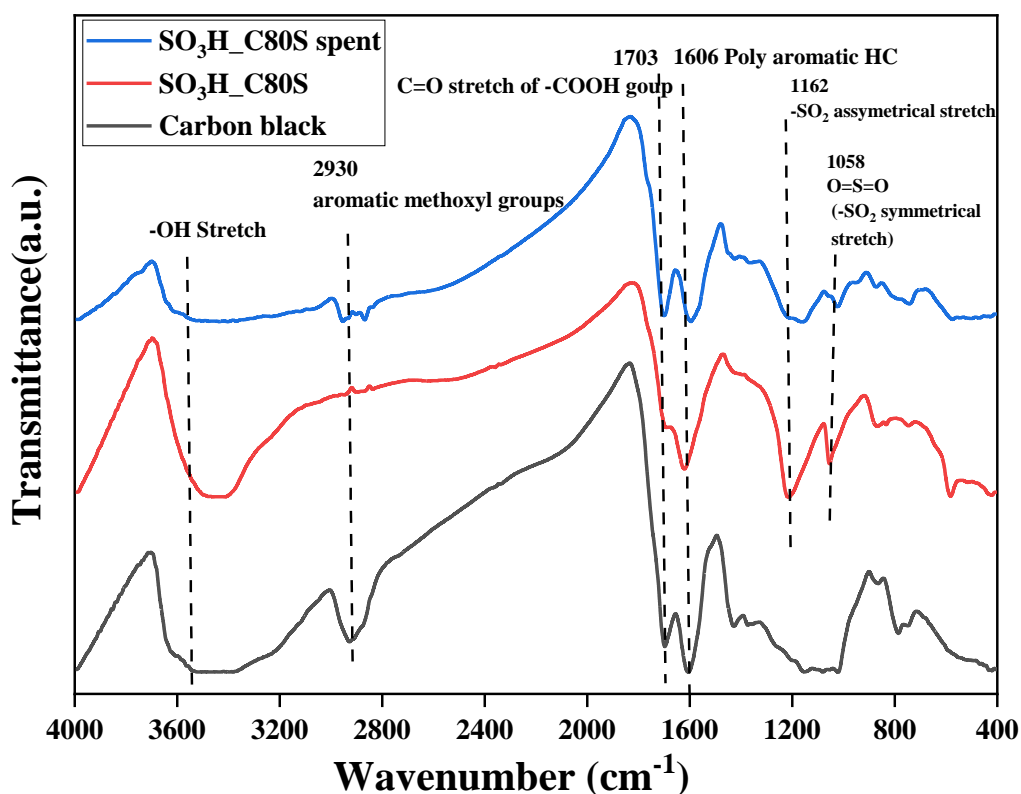


Fig.2.5: FTIR analysis of the sulfonated carbon catalysts

Fig.2.5 demonstrates the FTIR spectra of sulfonated carbon catalysts and carbon black at 298 K in the range of 4000 to 400 cm⁻¹, indicating the functional groups present on the catalyst's surface and their interaction. The band at 1058 cm⁻¹ correlated to the symmetrical stretching of O=S=O in SO₂ bonding and the band at 1162 cm⁻¹ to the asymmetrical stretching of SO₂, which were not observed in the carbon black compared to sulfonated catalysts[40][48][41]. These functional groups indicate the incorporation of -SO₃H groups onto the carbon black. The reduction in the intensity of the peaks at 1162 cm⁻¹ and 1058 cm⁻¹, which corresponds to asymmetrical and symmetrical stretching of -SO₃H, supports the desorption of -SO₃H groups after the reaction. The polyaromatic hydrocarbon of C=C stretching was due to the vibration band at 1606 cm⁻¹[34][41]. The carboxylic acid groups, one of the major functional groups formed by the partial carbonization of the carbon source, were attributed to the presence of a vibration band at 1700 cm⁻¹, which represents the stretching of a C=O of a -COOH group[32]. The band at 2930 cm⁻¹ illustrates aromatic methoxyl groups, which were subsequently suppressed

during the sulfonation process. Finally, the band at 3600 cm^{-1} corresponds to the -OH stretch phenolic functional groups[49]. Thus, FTIR analysis provided insights into the surface functional groups of the carbon catalysts and the desorption of $\text{-SO}_3\text{H}$ groups.

2.4.4 Pyridine FTIR analysis

Fig.2.6 and Table 2.5 represent the Pyridine-FTIR spectrum, the normalized peak areas corresponding to the acidic sites present on the catalyst, and the amount of acidity possessed by the catalyst. The strong Bronsted acidic band was due to SO_3H groups and some other functional groups such as phenolic and carboxylic acid groups present on the carbon black represented by the FTIR analysis. Incorporating $\text{-SO}_3\text{H}$ groups onto carbon black enhanced the Lewis acid groups and the combination of Lewis + Bronsted acidic groups (Table 2.5, entry 2). The reason is that the sulfonation oxidizes the functional groups present in the carbon network, especially carboxyl and methoxyl groups (Bands at 1703 cm^{-1} & 2930 cm^{-1} in Fig.2.5). The decrease in the spent catalyst's acidic nature was ascribed to the detachment of $\text{-SO}_3\text{H}$ groups that are weakly bonded to the polycyclic aromatic carbon network[30][54]. Konwar et al. reviewed biodiesel production using various carbon-based catalysts, in which the sulfonated carbon-based catalysts exhibited the leaching of $\text{-SO}_3\text{H}$ groups during the reaction[27]. Due to the surface and textural properties of the carbon catalysts observed from the BET results, the pyridine FTIR spectrums were different compared to tungstated zirconia catalysts. Table 2.5 compares the presence of Lewis and Bronsted acidic sites of the carbon catalysts. The Lewis acidic sites were reduced for the spent catalyst (Table 2.5, entry 3). This was surmised to be the detachment of weakly bonded functional groups caused by the affinity between the reactants and the hydroxyl groups of the carbon network[55]. The total surface acidity values of the catalysts were measured by the acid-base back titration (Table 2.5, entry 1,2,3) and are in alignment with the reported literature [34][56][57]. The carbon black acidity of 1.12 mmol/g comprises multiple surface functional groups. The sulfonated catalyst enhanced by SO_3H groups, which were building blocks for the strong acidity, displayed 2.357 mmol/g of surface acidity. The spent catalyst after 3 cycles of use and the leaching of the surface functional groups possessed 1.658 mmol/g of acidity contributed by the strong $\text{-SO}_3\text{H}$ groups. The acidity and activity for butanolysis of FAL

were in the order of $\text{SO}_3\text{H}/\text{C} > \text{SO}_3\text{H}/\text{C spent} > \text{Carbon black}$, which complied with the pyridine FTIR results.

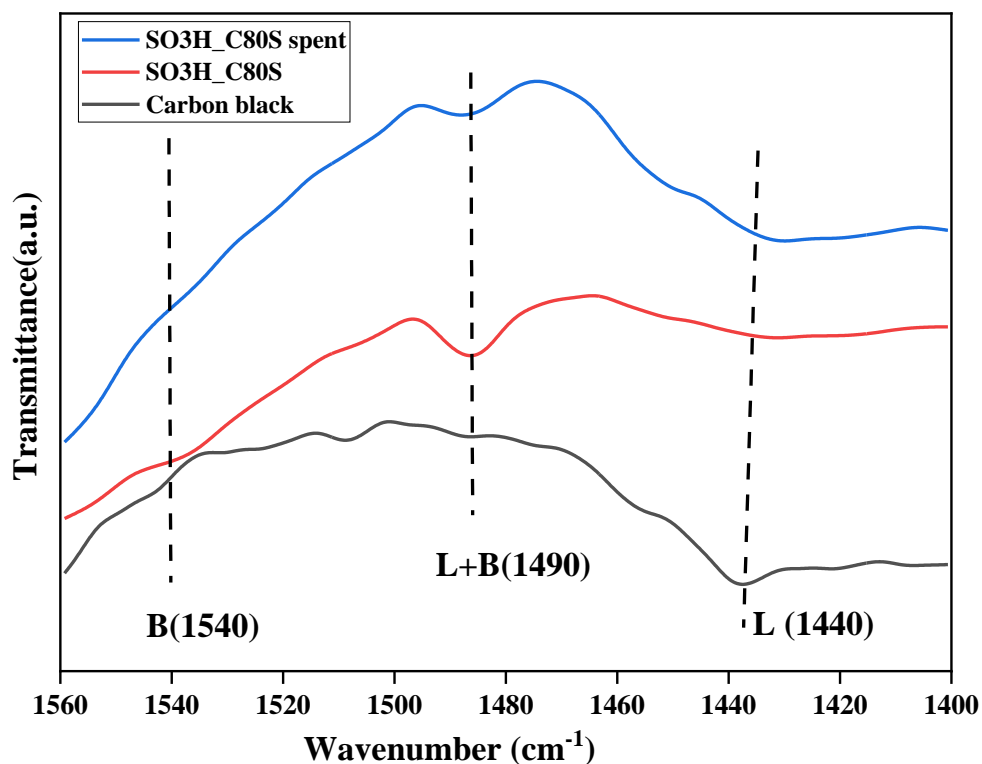


Fig.2.6: Pyridine-FTIR analysis of the sulfonated carbon catalysts

Table 2.5: Normalized peak areas w.r.t weight of the sulfonated carbon catalysts.

Catalyst	Lewis	Lewis +Bronsted	Bronsted	Bronsted/Lewis	Acidity ^a (mmol/g)
Carbon black	0.055	0.0052	0.0019	0.04	1.12
SO3H_C80S	0.029	0.062	0.0046	0.16	2.357
SO3H_C80S Spent	0.021	0.025	0.0032	0.15	1.658

a: Measured by acid-base back titration.

2.4.5 TGA analysis carbon catalysts

Fig.2.7 demonstrates the thermal stability of the carbon catalysts from 100 °C-400 °C. Carbon black, which was carbonized at 400 °C for 15 hours, showed excellent thermal stability, and a slight mass loss of 1.4 wt% occurred from 350 °C to 400 °C. This signifies the pyrolysis of unburnt carbon during carbonization at a meagre scale. Sulfonated carbon catalysts showed strong thermal stability in the reaction temperature range up to 220 °C. The mass loss for the sulfonated carbon catalysts occurred over 220 °C to 400 °C interpreting the significant leaching of the surface sulfonic groups and oxygenated functional groups[34][36][48]. Thus, the catalyst mass loss for the fresh sulfonated carbon catalyst (17.7%) is relatively higher than the fourth recycled catalyst (13.5%). However, the mass loss for the spent catalyst specifies that the strong sulfonic acid groups remained, even after the 3 reaction cycles. The decomposition of the surface sulfonic functional groups did not determine the acidic strength using the NH₃-TPD study. Umar et al. [47] and Konwar et al.[56] also observed the same phenomena of desorption of SO_x species along with NH₃ molecules, making it overestimate the acidity of the catalyst. A conventional ion exchange method of acid-base back titration was employed to determine the acidic strength of these catalysts.

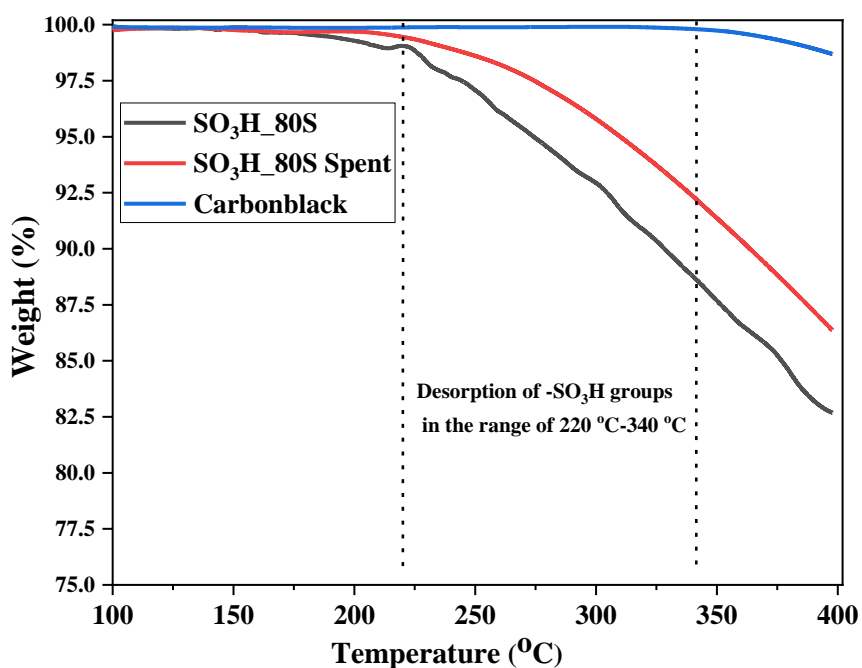
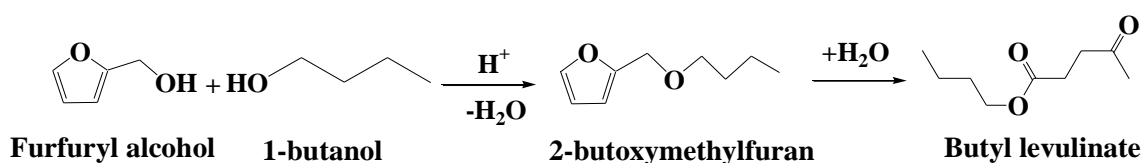


Fig.2.7: TGA analysis of sulfonated carbon catalysts

2.5 Butanolysis of FAL reaction study

The butanolysis of FAL was carried out using the tungstated zirconia and sulfonated carbon catalysts. Scheme.1 represents the conversion of FAL to BL through the reaction intermediate 2-BMF over the solid acid catalysts[7][57][58]. The catalyst protonated the hydroxyl groups of the FAL molecule. Then the attack of 1-butanol on this conjugated FAL molecule to form the reaction intermediate was the initial step of butanolysis of FAL. The reaction intermediate was identified through the GC-MS (GCMS-QP2020 NX) analysis. Further conversion of 2-BMF to BL was a prolonged step, which can be regarded as the rate-determining step of butanolysis of FAL[6][8][59]. The polymerization of FAL molecules in the acidic media is a significant concern to using the lower initial BtOH: FAL ratios, and the dehydration of n-butanol to the di-butyl ether was a non-consuming FAL byproduct of this reaction system. Fig.2.8 describes a typical GC-MS chromatogram of the product formation of the butanolysis reaction. Butanolysis chromatogram shows reactants butanol and FAL, and the products 2-BMF, BL, and FAL polymers.



Scheme.1. Butanolysis of FAL to BL

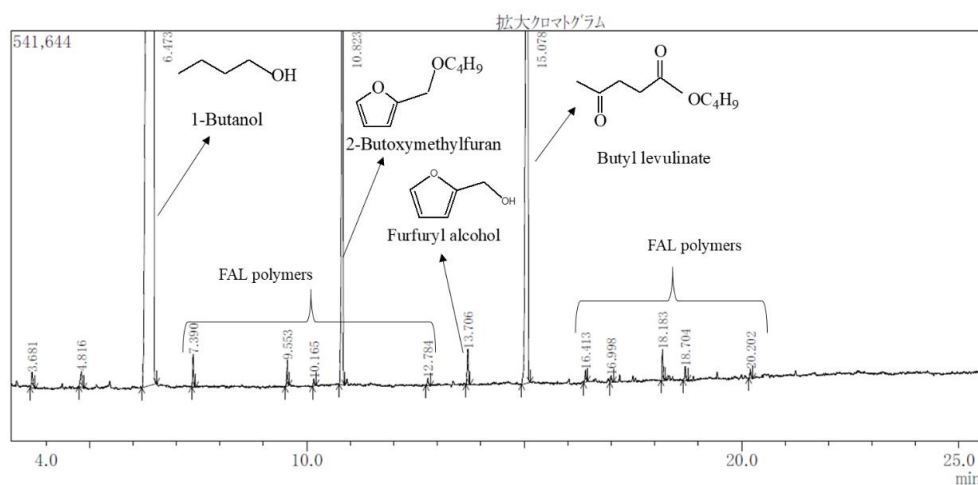


Fig.2.8: GC-MS spectra of butanolysis of FAL reaction

30 bar N₂, 190°C, 400 rpm, 0.5 g SO₃H-C catalyst, 1 h, 8.5:1 molar ratio (BtOH: FAL)

2.6 Butanolysis of FAL with WO₃-ZrO₂

Fig.2.9 explains the reaction temperature effect on FAL conversion, 2-BMF yield, and BL yield. At 150 °C, 75% of FAL was converted to 15 mol% yield of 2-BMF and 6 mol% yield of BL. As the reaction temperature reached 170 °C, the conversion of FAL increased to 95 mol%, whereas the 2-BMF yield reached its maximum and decreased with the temperature by converting to BL. Further increase in the reaction temperature resulted in the complete conversion of FAL at 190 °C, the yield of 2-BMF was decreased, and the yield of BL was increased to 17 mol%. BL yield reached a maximum of 28 mol% at 240 °C, at which complete transformation of 2-BMF to BL was attained after 2 hours. High reaction temperature induced the complete conversion of FAL and complete transformation of 2-BMF to BL.

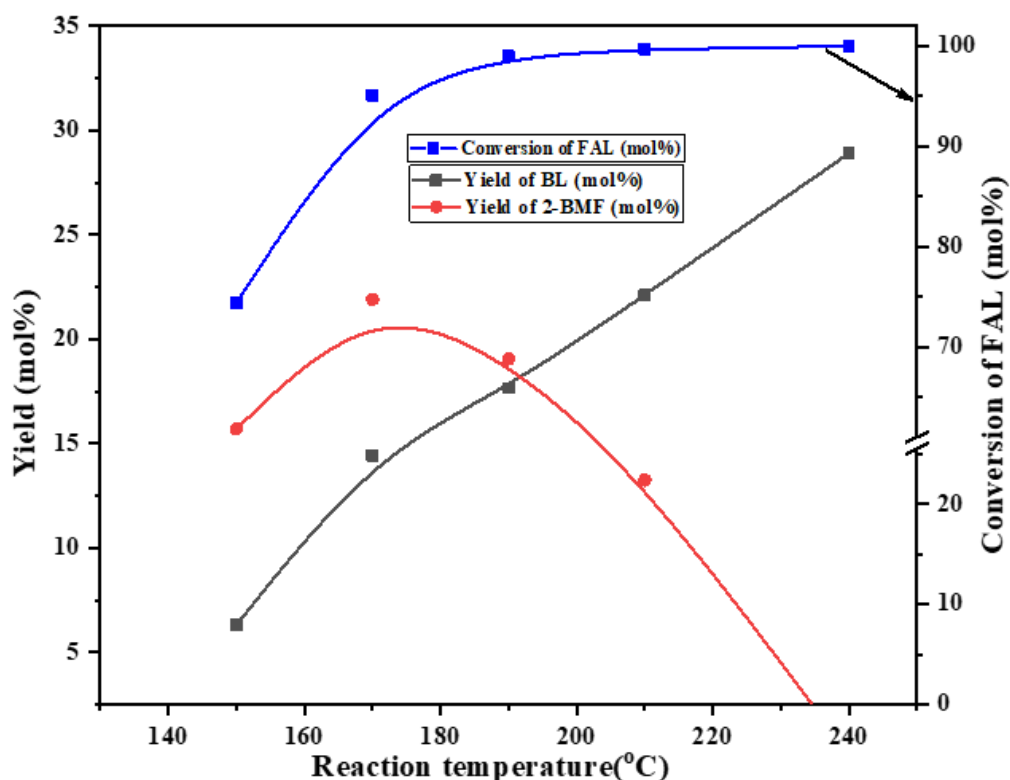


Fig.2.9: Effect reaction temperature with $\text{WO}_3\text{-ZrO}_2$ catalyst

Reaction conditions: 30 bar N_2 , 400 rpm, 0.5 g 15WZr800, 6 h, 8.5:1 molar ratio (BtOH: FAL)

*Reaction time for 240 °C is 2 hours

Table 2.6 shows the activity of the tungstated zirconia catalysts for FAL butanolysis, which indicates the selectivity and yield of 2-BMF & BL. The metal oxide loading and calcination temperature parameters were applied for this catalyst with 10&15 wt.% of WO_3 and 800 °C & 900 °C calcination temperature. An increase in the WO_3 loading enhanced its activity in terms of the FAL conversion from 77% to 95 mol% with 5.5 % to 14 mol% BL yield (Table 2.6, entries 1,2). As discussed in the NH_3 -TPD analysis (Fig. 2.2a, Table 2.2, entries 1,2), the increase in the acidity of the catalyst enhanced the FAL conversion and the BL yield. Further increase in the calcination temperature for 15 wt.% from 800 to 900 °C resulted in the collapse of the pore structure with widened pores, and a drop in the acidity caused the decrease in the catalytic activity to 50.5 mol% FAL conversion (Table 2.6, entry 3). The catalyst activity for this reaction was minimal as only around 14.43 mol% of BL yield was observed after 6 hours of the reaction (Table 2.6,

entries 2). In contrast, the same catalyst showed excellent catalytic activity for other reactions mentioned in the introduction. The same catalyst was tested for dehydration 1-butanol resulted in 72.5 mol% 1-butanol conversions with around 35 mol% of di-butyl ether yield after 1 hour of the reaction.

The incorporation of metals onto the tungstated zirconia catalyst enhanced its catalytic activity for various reactions [22][60][61]. Promoting noble and novel metals such as Pt, Pd & Ni, Fe, Cu, and Co also resulted in the similar catalytic activity of fresh catalysts (Table 2.6, entries: 4-9). The acidity of the catalysts slightly changed and more or less remained in the order of neat 15WZr800 catalyst (Table 2.2, entry 4-9). The FAL conversion has reached a maximum for all the catalysts. In contrast, the BL yield was varied in the range of 10-14 mol% with a 25-32% yield range of 2-BMF, indicating that the FAL molecules polymerization and unconverted intermediates were progressed. The reaction temperature was also studied for this catalyst in the range of 130-240 °C with an interval of 20 °C, and a maximum of 28 mol% BL yield was observed at 240 °C after 2 hours of the reaction (Fig.2.9). The reaction was also studied with a high initial BtOH to FAL mole ratio, such as 60:1, which resulted in only 11.2 mol% of BL yield with 26 mol% of 2-BMF yield (Table 2.6, entry10). Due to the lack of sufficient acidity (0.201 mmol/g) of the catalyst, the conversion of 2-BMF to BL was not progressed to obtain higher yields.

Table 2.6: Catalytic activity of WO₃-ZrO₂ catalysts

Catalyst	Mole ratio (BtOH: FAL)	X _{FAL}	S _{2-BMF}	S _{BL}	Y _{2-BMF}	Y _{BL}
10WZr800	8.5:1	77.5	40.6	16.1	19.9	5.58
15WZr800	8.5:1	95.1	53.2	42.8	21.9	14.43
15WZr900	8.5:1	50.5	59.08	15.89	6.14	3.77
1Pt15WZr800	8.5:1	100	62.82	28.25	30.1	13.5
1Pd15WZr800	8.5:1	100	63.59	27.52	30.4	14.2
1Ni15WZr800	8.5:1	100	65.42	26.1	29.2	12.5

1Fe15WZr800	8.5:1	100	67.19	21.36	33.86	11.2
1Cu15WZr800	8.5:1	98.3	57.9	32.65	19.91	10.72
1Co15WZr800	8.5:1	100	60.4	33.23	28.38	10.73
15WZr800	60.0:1	100	69.12	26.05	28.8	11.42

X- conversion, S- selectivity, Y- yield, respectively

Reaction conditions: 30 bar N₂, 170 °C, 400 rpm, 0.5 g catalyst, 6 h, 8.5:1 molar ratio (BtOH: FAL)

2.7 Reaction with sulfonated carbon catalysts

2.7.1 Effect of reaction temperature

To study the effect of reaction temperature, the butanolysis reaction was carried out in the range of 130-210 °C. Fig.2.10 explains the impact of reaction temperature on FAL butanolysis for sulfonated carbon catalyst on the selectivity and yield of reaction products. The previous studies have reported that the reaction temperature favours the butanolysis reaction by converting the reaction intermediate 2-BMF to BL via a furan ring-opening mechanism[6][8][12][15]. The FAL oligomers tend to form FAL polymers in acidic conditions at higher reaction temperatures, which is the primary concern for high-temperature reactions. A reaction with neat FAL in the tetralin solvent at 190 °C is also conducted to understand the formation of FAL polymers in acidic conditions. However, Milan et al. reported that the activation energies for forming FAL polymers are identical to that of the primary reaction concluding that high reaction temperatures can be favourable under optimized conditions[62]. At the reaction temperature of 130 °C, though the FAL conversion was near completion, the yield of BL was 49 mol%, accompanied by the unconverted reaction intermediates after 6 hours of the reaction. Further increase in the temperature to 150 °C, there was a slight increase in the BL yield with a reduced yield of others, including FAL polymers. As the reaction temperature progressed, there was a significant change in the BL yield, indicating that higher reaction temperatures are needed for this catalyst system to convert the reaction intermediate 2-BMF to BL. Almost a similar BL yield of around 80 mol% was observed for 190 °C & 210 °C, indicating that

the reaction temperature reached its threshold value, thus optimizing the reaction temperature at 190 °C.

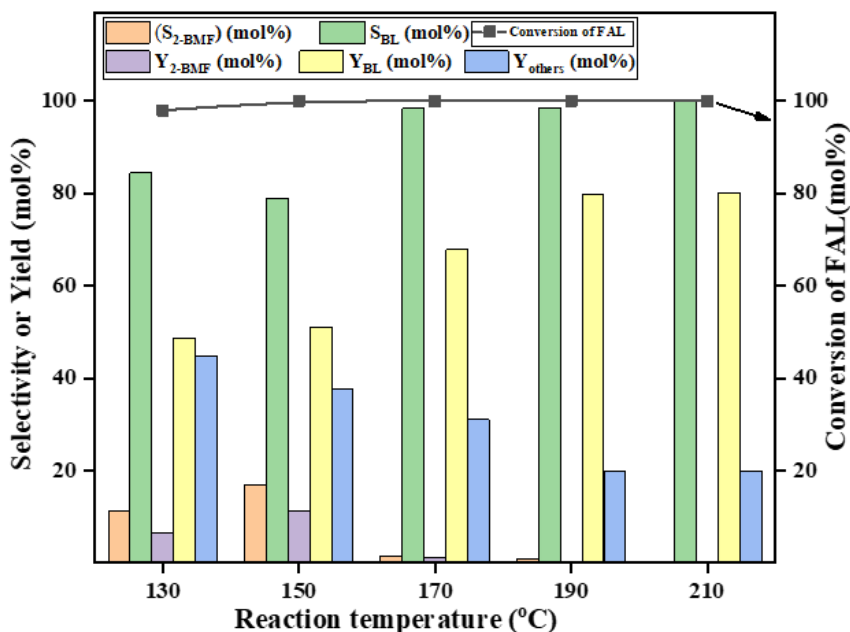


Fig.2.10: Effect of reaction temperature, S- Selectivity, Y- Yield

30 bar N₂, 400 rpm, 0.5 g catalyst, 6 h, 8.5:1 molar ratio (BtOH: FAL)

The selectivity of the BL was steadily increasing with reaction temperature, whereas the 2-BMF selectivity was gradually decreased, and there was no 2-BMF at 210 °C left to convert to BL. The yield of others, including FAL polymers, was on a declining trend with the reaction temperature and kept constant for 190 °C and 210 °C temperatures. Designating that higher reaction temperatures favour the product formation. The total surface acidity of the sulfonated carbon catalyst was way higher (2.357 mmol/g) than the 15WZr800 (0.201 mmol/g) catalyst, which facilitated the transformation of 2-BMF to BL towards higher yields.

2.7.2 Effect of reaction time

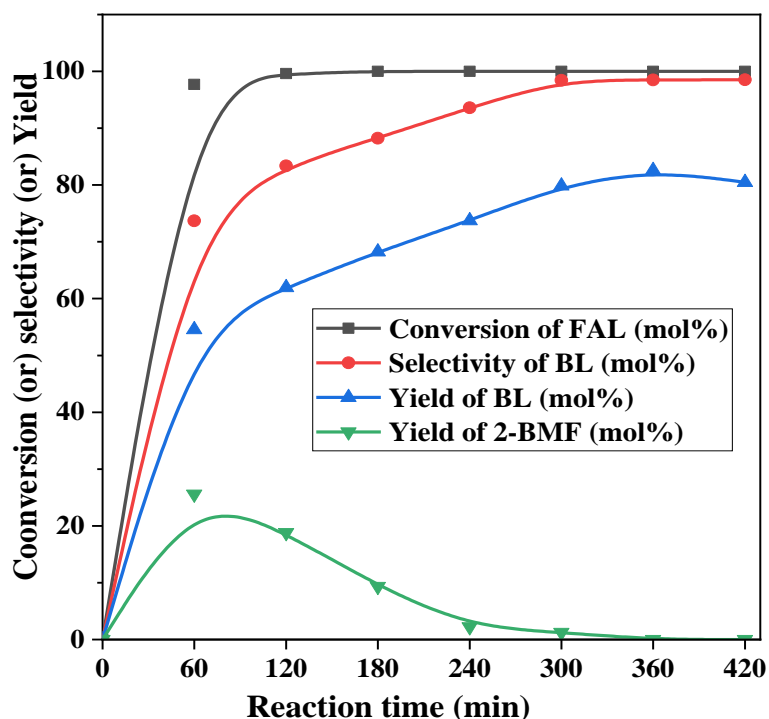


Fig.2.11: Effect of reaction time

30 bar N₂, 190 °C, 400 rpm, 0.5 g catalyst, 8.5:1 molar ratio (BtOH: FAL)

The butanolysis of FAL was studied at 190 °C with a sulfonated carbon catalyst for the reaction time profile with an 8.5:1 butanol to FAL mole ratio. Fig.2.11 represents the selectivity and yield of BL along with the yield of 2-BMF as a function of time. FAL conversion proceeded rapidly and almost completely converted after 1 hour while 54 mol% BL yield and 26 mol% of 2-BMF were observed. The temperature significantly affects this reaction, which accelerates the conversion of 2-BMF to BL via furan ring-opening (Fig.2.10). The BL yield increased sharply to 80 mol% after 6 hours as time progressed. The selectivity of the BL also kept on increasing with time and reached a maximum of 98 mol% after 6 hours. Meanwhile, the yield of 2-BMF was decreased over time and completely converted to BL after 6 hours. However, after the complete conversion of 2-BMF, the BL yield has slightly reduced to 80 mol% at 7 hours, implying the beginning of the BL degradation. Though the complete conversion of FAL was observed after one hour, the formation of BL progressed up on time to achieve the maximum value and settled at 6 hours, thereby optimizing the reaction time to 6 hours.

2.7.3 Effect of initial FAL concentration

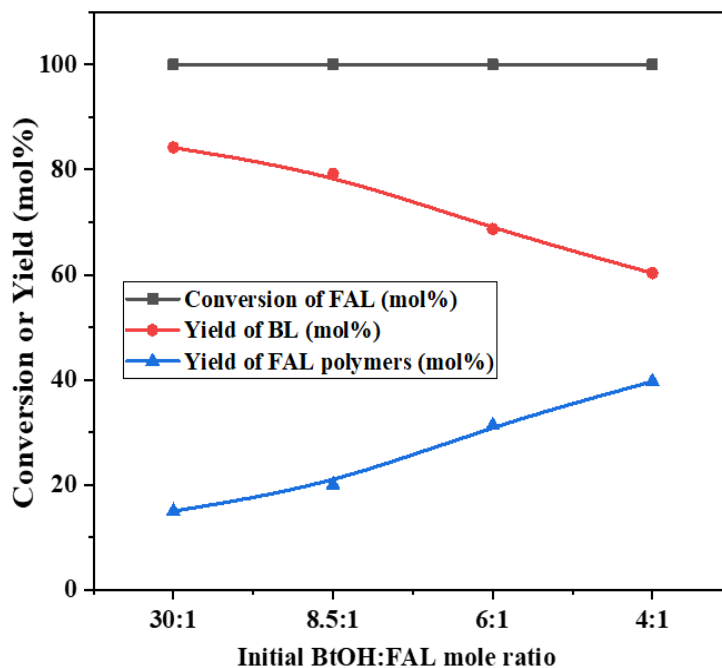


Fig.2.12: Effect of initial FAL concentration

30 bar N₂, 190 °C, 400 rpm, 0.5 g catalyst, 6 h

As described in the introduction, most studies for butanolysis of FAL were reported at a higher initial molar ratio of butanol to FAL (>30) with higher selectivities. This study intended to reduce the initial mole ratio to a maximum achievable range. The effect of initial FAL concentration was studied in the range of 30:1 to 4:1 at 190 °C for 6 hours using sulfonated carbon catalyst, and results are reported in Fig.2.12. The results depicted that increase in the initial FAL concentration resulted in the decreasing trend of BL yield, and increasing the FAL polymers yield replicates that the formation of FAL polymers was favoured upon high FAL concentration. The yield of BL reduced from 84 mol% to 57 mol% from 30:1 to 4:1 initial molar ratio of BtOH to FAL. The complete conversion was obtained even at lower mole ratios because of the high activity of the catalyst, but the respective yields of BL were decreased. Almost no intermediates are left to convert at such high temperatures, as evident from the reaction temperature optimization. Moreover, a decrease in the BL yield was obvious because of the unavailability of FAL conjugates due to FAL polymerization. Higher initial concentrations of FAL led to the

polymerization under acidic conditions, thereby decreasing the product formation[11][12][13]. Therefore, a maximum of 80 mol% of BL yield was achieved at a much lower initial molar ratio of 8.5:1, whereas for a 6:1 initial molar ratio, the BL yield was limited to 68 mol% only. The yield of FAL polymers inclined with increasing initial FAL concentration and relatively increased to 33 mol% for a 4:1 initial molar ratio. Therefore, feasible and economic studies are needed to find suitable initial conditions for this reaction to obtain maximum yields of BL.

2.7.4 Optimization of catalyst loading

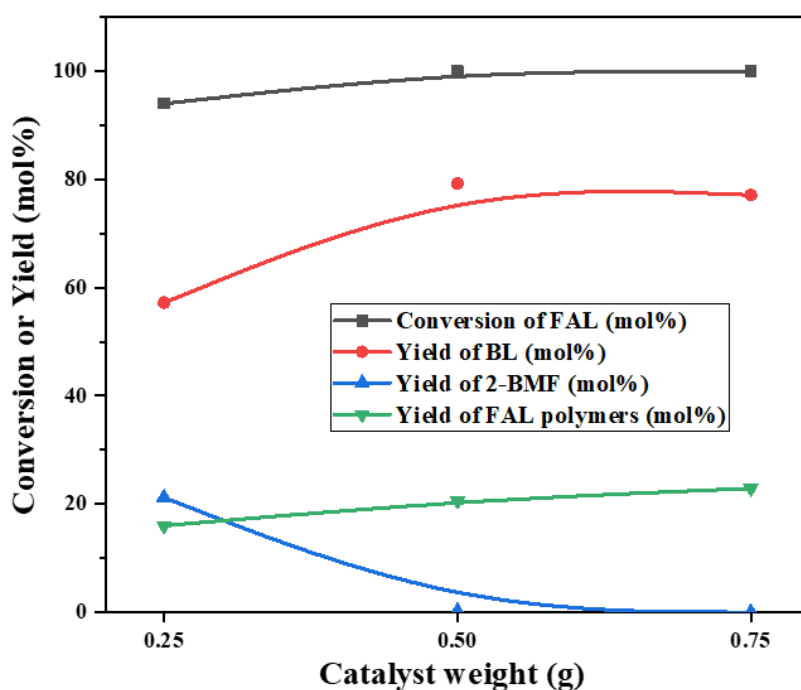


Fig.2.13: Catalyst loading

30 bar N₂, 190 °C, 400 rpm, 6 h, 8.5:1 molar ratio (BtOH: FAL)

Fig.2.13 exemplifies the variation of BL yield with respect to the amount of catalyst loaded at a reaction temperature of 190 °C for 6 hours. The reaction was first performed without the catalyst, which resulted in no conversion of FAL, indicating that a minimum amount of a catalyst is needed to enhance the FAL conversion. Starting with a 4.5 wt.% of catalyst loading (0.25g), 94% of FAL conversion was achieved with most of the unconverted reaction intermediates (around 20 mol% of 2-BMF) left to convert to BL.

With an increase in the catalyst amount from 0.25 to 0.5g, the complete conversion of FAL was achieved along with a significant increase in BL yield from 57 to 80 mol%. An increase in the catalyst amount provided more acidity in the reaction, which boosted the FAL conversion and completely transformed the intermediate 2-BMF to BL. Upon further increase in the catalyst loading to 0.75g, a slight decrease in the BL yield, around 77 mol%, was observed. The yield of FAL polymers increased from 15% to 23 mol% with the catalyst amount. This was bounded to happen in acidic conditions at higher temperatures and was probably caused by the presence of the more active sites, which promoted the initial conversion of FAL molecules to polymerize, thereby increasing the yield of FAL polymers[62]. Thus, a minimum of 9 wt.% of catalyst loading was sufficient for the complete conversion of FAL with a maximum of 80 mol% BL yield.

2.7.5 Comparison with various acid catalysts

In comparing study, the butanolysis reaction was first studied at 190 °C using dilute H₂SO₄ (Fig.2.14). Because reactor corrosion occurs at a higher temperature using conc. H₂SO₄, the reaction was studied at various concentrations from 0.001M to 0.1M to elucidate the role of acidity in the butanolysis of FAL. At a low acid concentration of 0.001M, only 35% conversion of FAL led to 12 mol% of 2-BMF with 8 mol% of BL yield after 6 hours. This infers that the formation of 2-BMF is more rapid than the conversion of 2-BMF to BL. When the acid concentration was significant enough (0.005M), complete conversion of FAL was observed, and only 39 mol% of BL formed with more than 35 mol% of 2-BMF still left to convert to BL. It implies the role of acidity in accommodating the conversion of 2-BMF to BL. Further increase in the H₂SO₄ concentration to 0.1M facilitated the nearly complete conversion of 2-BMF with 78 mol% of BL. 1M concentration of H₂SO₄ has led to the formation of 85 mol% of BL. Higher acid concentration complemented the BL formation even at higher initial butanol to FAL mole ratio.

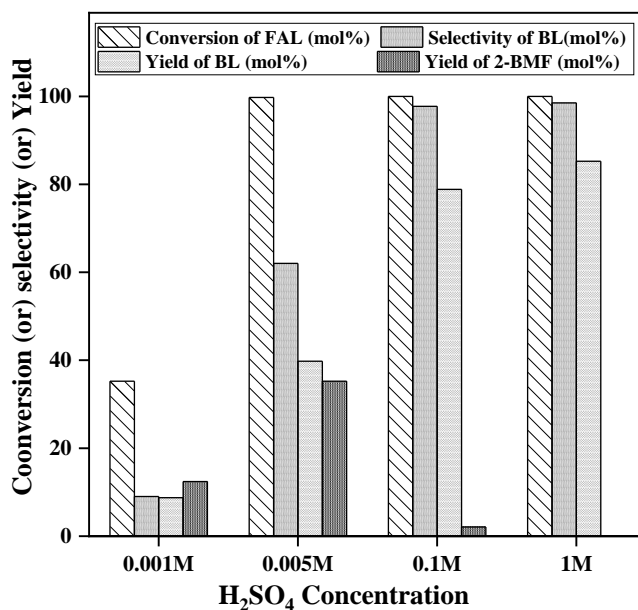


Fig.2.14: Reaction with dilute H₂SO₄

30 bar N₂, 190 °C, 400 rpm, 0.5 g catalyst, 6 h, 8.5:1 molar ratio (BtOH: FAL)

The sulfonated carbon catalyst activity was compared with some typical previously reported solid acid catalysts, metal salts such as AlCl₃ and dilute H₂SO₄. The results are summarized in Table 2.7. The reaction with AlCl₃.6H₂O at 123 °C yielded 92 mol% of BL at very high butanol to FAL mole ratio (Table 2.7, entry 1). This study depicts that the BL formation not only correlated to Bronsted acidic sites of Al salts but also with the Lewis acidic sites from Al³⁺ ions. An optimal combination of both Bronstedic and Lewis sites would proceed with a unique selectivity towards the BL. In the present work, the reaction was performed with anhydrous AlCl₃ at 190 °C for 2 hours at a lower initial mole ratio of 8.5:1, and 73 mol% of BL yield was observed with 6 mol% of 2-BMF yield (Table 2.7, entry 8). The reaction was carried out only for 2 hours because of the fact that chloride ion corrodes the reactor at such a high temperature and might affect the reaction results[68][69]. Alumina-supported SBA-15 catalyst showed 91% of BL yield for 6 hours at 180 °C but at the initial mole ratio of 65, remarking the FAL polymerization to 9% at high temperature even at a high initial mole ratio of butanol to FAL (Table 2.7, entry2). Waste paper-derived magnetic carbonaceous (SMWP) catalyst also showed 91 % BL yield at a reduced initial mole ratio of 41 with consistent activity (table 2.7, entry 3).

Sulfonated SBA-15 catalyst at a much reduced initial molar ratio of 16 gave 63 % of BL after 4 hours but at a much lower temperature of 100 °C (Table 2.7, entry 4). The Amberlyst 39 catalyst displayed 63 % BL yield at 110 °C after 6 hours (Table 72., entry 5). The authors have mentioned that unconverted intermediates such as 2-BMF and 4,5,5-tributoxy-2-pentanone at low-temperature reaction caused the 63% yield of BL. Moreover, the ionic resin Amberlyst catalysts are thermally unstable above 120 °C. The reaction with 1M H₂SO₄ showed a maximum yield of 85% after 6 hours (Table 2.77, entry 7).

Table 2.7: Comparison of this work with previous reports.

Entry	Initial mole ratio (BtOH:FAL)	Reaction conditions	Catalyst and its dosage	BL yield (mol%)	Ref.
1	109:1	123 °C, 2.7 h	AlCl ₃ .6H ₂ O, 0.1g (0.021 mol/L)	92	[9]
2	65.5	180 °C, 6 h	Al ₂ O ₃ /SBA-15 ,0.4g	91	[13]
3	40.5	120 °C, 5 h	Waste paper-derived magnetic carbonaceous solid acid (SMWP), 0.08g	90.6	[8]
4	16:1	110 °C, 4 h	SBA-15-SO ₃ H, 0.05g	63	[65]
5	8:1	110 °C, 6 h	Amberlyst 39, 1g	63	[11]
6	8.5:1	190 °C, 6 h	SO ₃ H_C, 0.5g	80	P
7	8.5:1	190 °C, 6 h	1M H ₂ SO ₄ , 0.5g	85	P
8	8.5:1	190 °C, 2 h	AlCl ₃ , 0.5g	73	P

P: Present work

2.7.6 Hot filtration test

The hot filtration test was carried out to check the heterogeneity of the reaction[65][66]. As observed in the time profile results (Fig.2.11), the conversion of FAL reached its maximum after 1 hour of the reaction time. Therefore, two samples at 15 minutes and 30 minutes of reaction time were collected before removing the catalyst. After 30 minutes of the reaction time, the reaction mixture was quenched, and the catalyst was filtered out. After that, the filtrate was reloaded into the reactor and carried out for 4 hours under the same conditions. Again, the reaction mixture was quenched, and the catalyst was added to the reaction mixture. The reaction was further continued for 2 hours before cooling down the reactor. The result (Fig.2.15) shows the reaction slightly progressed after removing the catalyst (3 mol% conversion of FAL increased after 2 hours of the reaction time). The slight increase in the conversion is possibly caused by the leaching of weak -SO₃H groups. However, the FAL conversion and the yields of 2-BMF and BL remain unchanged until 4 hours of the reaction time, indicating no reaction has proceeded without the catalyst. Adding the catalyst again and continuing for 2 more hours resulted in complete FAL conversion and an increase in BL yield. From the hot filtration test results, it can be assumed that the desorption could happen because of the affinity between the functional groups and FAL butanol molecules during the reaction.

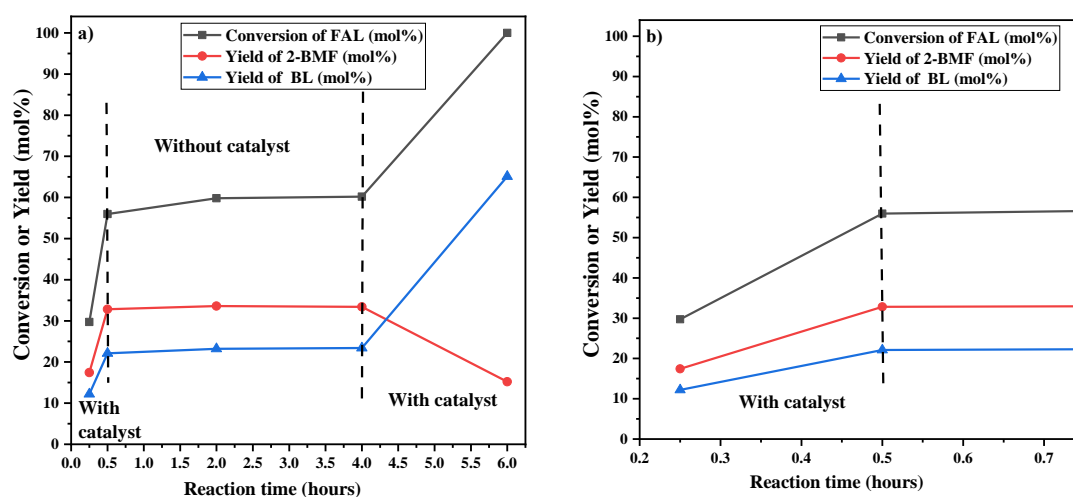


Fig.2.15: Butanolysis reaction results of a) hot filtration test, b) Hot filtration test in the interval of 15 to 30 minutes.

30 bar N₂, 190°C, 400 rpm, 0.5 g SO₃H_C catalyst, 8.5:1 molar ratio (BtOH: FAL)

2.7.7 Spent analysis

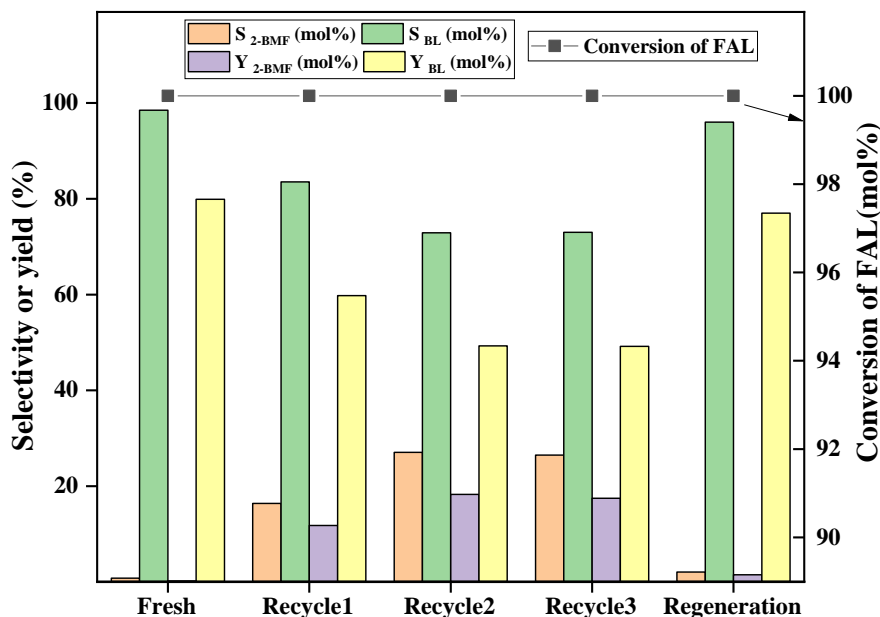


Fig.2.16: Spent analysis of sulfonated carbon catalyst

S- Selectivity, Y- Yield

30 bar N₂, 400 rpm, 190 °C, 6 h, 8.5:1 molar ratio (BtOH: FAL)

The deactivation study (Fig.2.16) of the sulfonated carbon catalyst was performed for three recycles. After every reaction, the catalyst was recovered by vacuum filtration and dried for 12 hours at 120 °C for subsequent use. The heterogeneity of the reaction was reported in Fig.2.15, which indicated slight leaching of the -SO₃H groups. Moreover, based on the heterogeneity test results, the reaction was mainly catalyzed by the acid sites on the surface of the sulfonated carbon catalyst instead of the leached -SO₃H groups. After three recycles, the BL yield was reduced to 49 mol%, indicating that the -SO₃H groups bonded to weakly functional groups of the carbon network were desorbed during the reaction. Though the FAL was fully converted after 6 hours for all the recycles, the 2-BMF was left unconverted to BL, attributing the need for acidity for the conversion. This problem can be overcome by regenerating the activity of the catalyst by sulfonation.

The catalyst, after three cycles, was regenerated by sulfonation at 80 °C under inert conditions. It replicated the results of the fresh catalyst with 78 mol% of BL yield compared to 80 mol% with fresh catalyst.

2.8 Reaction with carbon black catalyst

The carbon black showed the optimal activity for the reaction with 34 mol% of BL yield (Fig.2.17). The selectivity and the yield of both 2-BMF & BL were identical and settled at 48 mol% selectivity and 34 mol% yield. The carboxylic acid and phenolic groups formed during the incomplete carbonization of sucrose were responsible for the carbon black's optimal activity. The fig. illustrates the reaction results with the carbon black. Upon the results with 0.5 g of catalyst, the loading was increased to 1 g, which resulted in a similar outcome. The product distribution indicated that a maximum of 0.5 g of catalyst loading was enough to convert the FAL to the products.

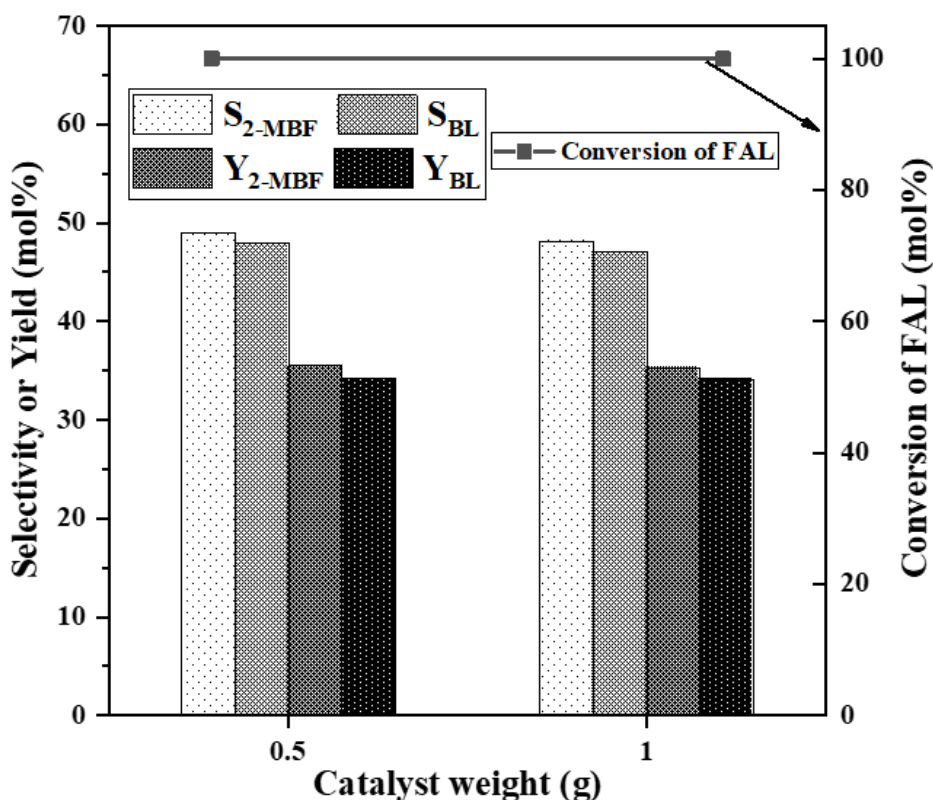


Fig.2.17: Effect of carbon black catalyst loading

S- Selectivity, Y- Yield

30 bar N₂, 400 rpm, 190 °C, 6 h, 8.5:1 molar ratio (BtOH: FAL)

2.9 Conclusions

In conclusion, the butanolysis of FAL at a lower initial mole ratio was conducted using two different catalysts. The tungstated zirconia catalyst and the metal-promoted catalysts resulted in a maximum of 28 mol% of BL yield, signifying the need for high catalytic activity for butanolysis reaction. The sulfonated carbon catalyst (surface acidity 2.357 mmol/g) resulting in 80 mol% of BL yield showed superior activity caused by the strong Bronstedic –SO₃H groups and the aided acidic carbon groups. The partially carbonized sucrose to carbon black showed better catalytic activity than the tungstated zirconia catalyst caused by the presence of phenolic, hydroxyl, and carboxylic acid functional groups. Thus, this work demonstrated that the high BL yields as high as more than 80 mol% with sulfonated carbon catalyst even at low butanol: FAL ratio as low as 8.5. Further decreasing the initial mole ratio decreased the BL yield accompanied by FAL polymerization. The deactivation study reveals that the weakly bonded –SO₃H groups were detached from the carbon network, resulting in the catalytic activity to 49 mol% of BL yield after three recycles with 100% FAL conversion and regained the activity to 78 mol% BL yield upon regeneration.

2.10 References

- [1] SK. Maity, Opportunities, recent trends and challenges of integrated biorefinery: Part i, *Renew. Sustain. Energy Rev.* 43 (2015) 1427–1445. <https://doi.org/10.1016/j.rser.2014.11.092>.
- [2] D.M. Alonso, J.Q. Bond, J.A. Dumesic, Catalytic conversion of biomass to biofuels, *Green Chem.* 12 (2010) 1493–1513. <https://doi.org/10.1039/c004654j>.
- [3] A. Démolis, N. Essayem, F. Rataboul, Synthesis and applications of alkyl levulinates, *ACS Sustain. Chem. Eng.* 2 (2014) 1338–1352. <https://doi.org/10.1021/sc500082n>.
- [4] E. Ahmad, M.I. Alam, K.K. Pant, M.A. Haider, Catalytic and mechanistic insights into the production of ethyl levulinate from biorenewable feedstocks, *Green Chem.* 18 (2016) 4804–4823. <https://doi.org/10.1039/c6gc01523a>.
- [5] C. Li, G. Xu, Y. Zhai, X. Liu, Y. Ma, Y. Zhang, Hydrogenation of biomass-derived ethyl levulinate into Γ -valerolactone by activated carbon supported bimetallic Ni and Fe catalysts, *Fuel.* 203 (2017) 23–31. <https://doi.org/10.1016/j.fuel.2017.04.082>.
- [6] E. Siva Sankar, K. Saidulu Reddy, Y. Jyothi, B. David Raju, K.S. Rama Rao, Alcoholysis of Furfuryl Alcohol into n-Butyl Levulinate Over SBA-16 Supported Heteropoly Acid Catalyst, *Catal. Letters.* 147 (2017) 2807–2816. <https://doi.org/10.1007/s10562-017-2155-9>.
- [7] D. Song, S. An, B. Lu, Y. Guo, J. Leng, Arylsulfonic acid functionalized hollow mesoporous carbon spheres for efficient conversion of levulinic acid or furfuryl alcohol to ethyl levulinate, *Appl. Catal. B Environ.* 179 (2015) 445–457. <https://doi.org/10.1016/j.apcatb.2015.05.047>.
- [8] J. Yang, Z. Ao, H. Wu, S. Zhang, C. Chi, C. Hou, L. Qian, Waste paper-derived magnetic carbon composite: A novel eco-friendly solid acid for the synthesis of n-butyl levulinate from furfuryl alcohol, *Renew. Energy.* 146 (2020) 477–483. <https://doi.org/10.1016/j.renene.2019.06.167>.

- [9] L. Peng, X. Gao, K. Chen, Catalytic upgrading of renewable furfuryl alcohol to alkyl levulinates using AlCl₃ as a facile, efficient, and reusable catalyst, *Fuel*. 160 (2015) 123–131. <https://doi.org/10.1016/j.fuel.2015.07.086>.
- [10] S.S.R. Gupta, M.L. Kantam, Catalytic conversion of furfuryl alcohol or levulinic acid into alkyl levulinates using a sulfonic acid-functionalized hafnium-based MOF, *Catal. Commun.* 124 (2019) 62–66. <https://doi.org/10.1016/j.catcom.2019.03.003>.
- [11] R. Bringué, E. Ramírez, M. Iborra, J. Tejero, F. Cunill, Esterification of furfuryl alcohol to butyl levulinate over ion-exchange resins, *Fuel*. 257 (2019) 116010. <https://doi.org/10.1016/j.fuel.2019.116010>.
- [12] D. Ren, J. Fu, L. Li, Y. Liu, F. Jin, Z. Huo, Efficient conversion of biomass-derived furfuryl alcohol to levulinate esters over commercial α -Fe₂O₃, *RSC Adv.* 6 (2016) 22174–22178. <https://doi.org/10.1039/c5ra24319j>.
- [13] S.S. Enumula, K.S. Koppadi, V.R. Babu Gurram, D.R. Burri, S.R. Rao Kamaraju, Conversion of furfuryl alcohol to alkyl levulinate fuel additives over Al₂O₃/SBA-15 catalyst, *Sustain. Energy Fuels*. 1 (2017) 644–651. <https://doi.org/10.1039/c6se00103c>.
- [14] J.N. Appaturi, M.R. Johan, R.J. Ramalingam, H.A. Al-Lohedan, J.J. Vijaya, Efficient synthesis of butyl levulinate from furfuryl alcohol over ordered mesoporous Ti-KIT-6 catalysts for green chemistry applications, *RSC Adv.* 7 (2017) 55206–55214. <https://doi.org/10.1039/c7ra10289e>.
- [15] BS. Rao, P.K. Kumari, D. Dhanalakshmi, N. Lingaiah, Selective conversion of furfuryl alcohol into butyl levulinate over zinc exchanged heteropoly tungstate supported on niobia catalysts, *Mol. Catal.* 427 (2017) 80–86. <https://doi.org/10.1016/j.molcata.2016.11.032>.
- [16] W. Zhou, N. Soultanidis, H. Xu, M.S. Wong, M. Neurock, C.J. Kiely, I.E. Wachs, Nature of Catalytically Active Sites in the Supported WO₃/ZrO₂ Solid Acid System: A Current Perspective, *ACS Catal.* 7 (2017) 2181–2198. <https://doi.org/10.1021/acscatal.6b03697>.

- [17] M. Hino, K. Arata, Synthesis of solid superacid of tungsten oxide supported on zirconia and its catalytic action for reactions of butane and pentane, *J. Chem. Soc. Chem. Commun.* (1988) 1259–1260. <https://doi.org/10.1039/C39880001259>.
- [18] A.H. Karim, S. Triwahyono, A.A. Jalil, H. Hattori, WO₃ monolayer loaded on ZrO₂: Property-activity relationship in n-butane isomerization evidenced by hydrogen adsorption and IR studies, *Appl. Catal. A Gen.* 433–434 (2012) 49–57. <https://doi.org/10.1016/j.apcata.2012.04.039>.
- [19] S. Feng, A. Nagao, T. Aihara, H. Miura, T. Shishido, Selective hydrogenolysis of tetrahydrofurfuryl alcohol on Pt/WO₃/ZrO₂ catalysts: Effect of WO₃ loading amount on activity, *Catal. Today.* 303 (2018) 207–212. <https://doi.org/10.1016/j.cattod.2017.08.058>.
- [20] C.D. Baertsch, K.T. Komala, Y.H. Chua, E. Iglesia, Genesis of Brønsted acid sites during dehydration of 2-butanol on tungsten oxide catalysts, *J. Catal.* 205 (2002) 44–57. <https://doi.org/10.1006/jcat.2001.3426>.
- [21] R. Kourieh, S. Bennici, M. Marzo, A. Gervasini, A. Auroux, Investigation of the WO₃/ZrO₂ surface acidic properties for the aqueous hydrolysis of cellobiose, *Catal. Commun.* 19 (2012) 119–126. <https://doi.org/10.1016/j.catcom.2011.12.030>.
- [22] R. Foo, T. Vazhnova, D.B. Lukyanov, P. Millington, J. Collier, R. Rajaram, S. Golunski, Formation of reactive Lewis acid sites on Fe/WO₃-ZrO₂ catalysts for higher temperature SCR applications, *Appl. Catal. B Environ.* 162 (2015) 174–179. <https://doi.org/10.1016/j.apcatb.2014.06.034>.
- [23] P.Q. Yuan, Y. Liu, F. Bai, L. Xu, Z.M. Cheng, W.K. Yuan, Hydration of cyclohexene in sub-critical water over WO_x-ZrO₂ catalysts, *Catal. Commun.* 12 (2011) 753–756. <https://doi.org/10.1016/j.catcom.2011.01.009>.
- [24] NR. Shiju, M. Anilkumar, W.F. Hoelderich, D.R. Brown, Tungstated zirconia catalysts for liquid-phase Beckmann rearrangement of cyclohexanone oxime: Structure-activity relationship, *J. Phys. Chem. C.* 113 (2009) 7735–7742. <https://doi.org/10.1021/jp810542t>.

- [25] Y.M. Park, S.H. Chung, H.J. Eom, J.S. Lee, K.Y. Lee, Tungsten oxide zirconia as solid superacid catalyst for esterification of waste acid oil (dark oil), *Bioresour. Technol.* 101 (2010) 6589–6593. <https://doi.org/10.1016/j.biortech.2010.03.109>.
- [26] W. Ciptonugroho, M.G. Al-Shaal, J.B. Mensah, R. Palkovits, One pot synthesis of WO_x/mesoporous-ZrO₂ catalysts for the production of levulinic-acid esters, *J. Catal.* 340 (2016) 17–29. <https://doi.org/10.1016/j.jcat.2016.05.001>.
- [27] L.J. Konwar, J. Boro, D. Deka, Review on latest developments in biodiesel production using carbon-based catalysts, *Renew. Sustain. Energy Rev.* 29 (2014) 546–564. <https://doi.org/10.1016/j.rser.2013.09.003>.
- [28] H.P. Boehm, Some aspects of the surface chemistry of carbon blacks and other carbons, *Carbon N. Y.* 32 (1994) 759–769. [https://doi.org/10.1016/0008-6223\(94\)90031-0](https://doi.org/10.1016/0008-6223(94)90031-0).
- [29] WW Mar, E. Somsook, Sulfonic-functionalized carbon catalyst for esterification of high free fatty acid, *Procedia Eng.* 32 (2012) 212–218. <https://doi.org/10.1016/j.proeng.2012.01.1259>.
- [30] X. Tang, S. Niu, Preparation of carbon-based solid acid with large surface area to catalyze esterification for biodiesel production, *J. Ind. Eng. Chem.* 69 (2019) 187–195. <https://doi.org/10.1016/j.jiec.2018.09.016>.
- [31] S. Suganuma, K. Nakajima, M. Kitano, D. Yamaguchi, H. Kato, S. Hayashi, M. Hara, Hydrolysis of cellulose by amorphous carbon bearing SO₃H, COOH, and OH groups, *J. Am. Chem. Soc.* 130 (2008) 12787–12793. <https://doi.org/10.1021/ja803983h>.
- [32] AB Fadhil, A.M. Aziz, M.H. Al-Tamer, Biodiesel production from *Silybum marianum* L. seed oil with high FFA content using sulfonated carbon catalyst for esterification and base catalyst for transesterification, *Energy Convers. Manag.* 108 (2016) 255–265. <https://doi.org/10.1016/j.enconman.2015.11.013>.
- [33] TS Galhardo, N. Simone, M. Gonçalves, F.C.A. Figueiredo, D. Mandelli, W.A. Carvalho, Preparation of sulfonated carbons from rice husk and their application in catalytic conversion of glycerol, *ACS Sustain. Chem. Eng.* 1 (2013) 1381–1389.

<https://doi.org/10.1021/sc400117t>.

- [34] AP da Luz Corrêa, R.R.C. Bastos, G.N. da Rocha Filho, J.R. Zamian, L.R.V. da Conceição, Preparation of sulfonated carbon-based catalysts from murumuru kernel shell and their performance in the esterification reaction, *RSC Adv.* 10 (2020) 20245–20256. <https://doi.org/10.1039/d0ra03217d>.
- [35] L. Geng, Y. Wang, G. Yu, Y. Zhu, Efficient carbon-based solid acid catalysts for the esterification of oleic acid, *Catal. Commun.* 13 (2011) 26–30. <https://doi.org/10.1016/j.catcom.2011.06.014>.
- [36] S. Kang, J. Chang, J. Fan, One step preparation of Sulfonated solid catalyst and its effect in esterification reaction, *Chinese J. Chem. Eng.* 22 (2014) 392–397. [https://doi.org/10.1016/S1004-9541\(14\)60058-6](https://doi.org/10.1016/S1004-9541(14)60058-6).
- [37] L. Mahoney, R.T. Koodali, Versatility of Evaporation-Induced Self-Assembly (EISA) method for preparation of mesoporous TiO₂ for energy and environmental applications, *Materials (Basel)*. 7 (2014) 2697–2746. <https://doi.org/10.3390/ma7042697>.
- [38] K. Nakajima, M. Hara, Amorphous carbon with SO₃H groups as a solid brønsted acid catalyst, *ACS Catal.* 2 (2012) 1296–1304. <https://doi.org/10.1021/cs300103k>.
- [39] X. Mo, DE López, K. Suwannakarn, Y. Liu, E. Lotero, J.G. Goodwin, C. Lu, Activation and deactivation characteristics of sulfonated carbon catalysts, *J. Catal.* 254 (2008) 332–338. <https://doi.org/10.1016/j.jcat.2008.01.011>.
- [40] BVSK. Rao, K. Chandra Mouli, N. Rambabu, AK Dalai, R.B.N. Prasad, Carbon-based solid acid catalyst from de-oiled canola meal for biodiesel production, *Catal. Commun.* 14 (2011) 20–26. <https://doi.org/10.1016/j.catcom.2011.07.011>.
- [41] G. Chen, B. Fang, Preparation of solid acid catalyst from glucose-starch mixture for biodiesel production, *Bioresour. Technol.* 102 (2011) 2635–2640. <https://doi.org/10.1016/j.biortech.2010.10.099>.
- [42] A. Galano, G. Rodriguez-Gattorno, E. Torres-García, A combined theoretical-experimental study on the acidity of WO_x-ZrO₂ systems, *Phys. Chem. Chem.*

- Phys. 10 (2008) 4181–4188. <https://doi.org/10.1039/b802934b>.
- [43] J. Regalbuto, Catalyst Preparation: Science and Engineering, Focus Catal. 2007 (2007) 8. [https://doi.org/10.1016/s1351-4180\(07\)70051-x](https://doi.org/10.1016/s1351-4180(07)70051-x).
- [44] A. Kumar, A. Ali, K.N. Vinod, A.K. Mondal, H. Hegde, A. Menon, B.H.S. Thimmappa, WO_x/ZrO_2 : A highly efficient catalyst for alkylation of catechol with tert-butyl alcohol, J. Mol. Catal. A Chem. 378 (2013) 22–29. <https://doi.org/10.1016/j.molcata.2013.05.010>.
- [45] E.I. Ross-medgaarden, W. V Knowles, T. Kim, M.S. Wong, W. Zhou, C.J. Kiely, I.E. Wachs, New insights into the nature of the acidic catalytic active sites present in ZrO_2 -supported tungsten oxide catalysts, 256 (2008) 108–125. <https://doi.org/10.1016/j.jcat.2008.03.003>.
- [46] D.G. Barton, M. Shtein, R.D. Wilson, S.L. Soled, E. Iglesia, Structure and electronic properties of solid acids based on tungsten oxide nanostructures, J. Phys. Chem. B. 103 (1999) 630–640. <https://doi.org/10.1021/jp983555d>.
- [47] U.I. Nda-Umar, I. Ramli, EN Muhamad, Y.H. Taufiq-Yap, N. Azri, Synthesis and characterization of sulfonated carbon catalysts derived from biomass waste and its evaluation in glycerol acetylation, Biomass Convers. Biorefinery. (2020). <https://doi.org/10.1007/s13399-020-00784-0>.
- [48] L.J. Konwar, R. Das, A.J. Thakur, E. Salminen, P. Mäki-Arvela, N. Kumar, J.P. Mikkola, D. Deka, Biodiesel production from acid oils using sulfonated carbon catalyst derived from oil-cake waste, J. Mol. Catal. A Chem. 388–389 (2014) 167–176. <https://doi.org/10.1016/j.molcata.2013.09.031>.
- [49] S. Na, Z. Minhua, D. Xiuqin, W. Lingtao, Preparation of sulfonated ordered mesoporous carbon catalyst and its catalytic performance for esterification of free fatty acids in waste cooking oils, RSC Adv. 9 (2019) 15941–15948. <https://doi.org/10.1039/c9ra02546d>.
- [50] W. Zhou, E.I. Ross-Medgaarden, W. V. Knowles, M.S. Wong, I.E. Wachs, C.J. Kiely, Identification of active Zr- WO_x clusters on a ZrO_2 support for solid acid catalysts, Nat. Chem. 1 (2009) 722–728. <https://doi.org/10.1038/nchem.433>.

- [51] M. Scheithauer, R.K. Grasselli, H. Knözinger, Genesis and structure of WO_x/ZrO₂ solid acid catalysts, *Langmuir*. 14 (1998) 3019–3029. <https://doi.org/10.1021/la971399g>.
- [52] G.K. Chuah, S. Jaenicke, T.H. Xu, Acidity of high-surface-area zirconia prepared from different precipitants, *Surf. Interface Anal.* 28 (1999) 131–134. [https://doi.org/10.1002/\(SICI\)1096-9918\(199908\)28:1<131::AID-SIA634>3.0.CO;2-5](https://doi.org/10.1002/(SICI)1096-9918(199908)28:1<131::AID-SIA634>3.0.CO;2-5).
- [53] J.R. Sohn, M.Y. Park, Characterization of zirconia-supported tungsten oxide catalyst, *Langmuir*. 14 (1998) 6140–6145. <https://doi.org/10.1021/la980222z>.
- [54] L.H. Tamborini, ME Casco, M.P. Militello, J. Silvestre-Albero, C.A. Barbero, D.F. Acevedo, Sulfonated porous carbon catalysts for biodiesel production: Clear effect of the carbon particle size on the catalyst synthesis and properties, *Fuel Process. Technol.* 149 (2016) 209–217. <https://doi.org/10.1016/j.fuproc.2016.04.006>.
- [55] H.P. Boehm, Surface oxides on carbon and their analysis: A critical assessment, *Carbon N. Y.* 40 (2002) 145–149. [https://doi.org/10.1016/S0008-6223\(01\)00165-8](https://doi.org/10.1016/S0008-6223(01)00165-8).
- [56] L.J. Konwar, P. Mäki-Arvela, E. Salminen, N. Kumar, A.J. Thakur, J.P. Mikkola, D. Deka, Towards carbon efficient biorefining: Multifunctional mesoporous solid acids obtained from biodiesel production wastes for biomass conversion, *Appl. Catal. B Environ.* 176–177 (2015) 20–35. <https://doi.org/10.1016/j.apcatb.2015.03.005>.
- [57] SR B., KK. P., DL D., N. Lingaiah, One pot selective transformation of biomass derived chemicals towards alkyl levulinates over titanium exchanged heteropoly tungstate catalysts, *Catal. Today*. 309 (2018) 269–275. <https://doi.org/10.1016/j.cattod.2017.05.040>.
- [58] D. Song, S. An, Y. Sun, Y. Guo, Efficient conversion of levulinic acid or furfuryl alcohol into alkyl levulinates catalyzed by heteropoly acid and ZrO₂ bifunctionalized organosilica nanotubes, *J. Catal.* 333 (2016) 184–199. <https://doi.org/10.1016/j.jcat.2015.10.018>.

- [59] L. Peng, H. Li, L. Xi, K. Chen, H. Chen, Facile and efficient conversion of furfuryl alcohol into n-butyl levulinate catalyzed by extremely low acid concentration, *BioResources*. 9 (2014) 3825–3834. <https://doi.org/10.15376/biores.9.3.3825-3834>.
- [60] S. Canavese, Z. Finelli, M. Busto, V.M. Benitez, C.R. Vera, J.C. Yori, Poisoning and regeneration of Pt-Pd/WO₃-ZrO₂ short paraffin isomerization catalysts, *Quim. Nova*. 33 (2010) 508–513. <https://doi.org/10.1590/S0100-40422010000300003>.
- [61] L. Wang, S. Xu, W. Chu, W. Yang, Influence of noble metals on the direct oxidation of ethylene to acetic acid over NM/WO₃-ZrO₂ (NM = Ru, Rh, and Pd) catalysts, *Cuihua Xuebao/Chinese J. Catal.* 30 (2009) 1281–1286. [https://doi.org/10.1016/s1872-2067\(08\)60144-8](https://doi.org/10.1016/s1872-2067(08)60144-8).
- [62] M. Hronec, K. Fulajtárová, T. Soták, Kinetics of high temperature conversion of furfuryl alcohol in water, *J. Ind. Eng. Chem.* 20 (2014) 650–655. <https://doi.org/10.1016/j.jiec.2013.05.029>.
- [63] P.M. Natishan, W.E. O'Grady, Chloride Ion Interactions with Oxide-Covered Aluminum Leading to Pitting Corrosion: A Review, *J. Electrochem. Soc.* 161 (2014) C421–C432. <https://doi.org/10.1149/2.1011409jes>.
- [64] J.-H. Wang, C.C. Su, Z. Szklarska-Smialowska, Effects of Cl⁻ Concentration and Temperature on Pitting of AISI 304 Stainless Steel, *Corrosion*. 44 (1988) 732–737. <https://doi.org/10.5006/1.3584938>.
- [65] P. Demmacarà, R. Ciriminna, N.R. Shiju, G. Rothenberg, M. Pagliaro, Enhanced heterogeneous catalytic conversion of furfuryl alcohol into butyl levulinate, *ChemSusChem*. 7 (2014) 835–840. <https://doi.org/10.1002/cssc.201301027>.
- [66] J. Yang, H. Zhang, Z. Ao, S. Zhang, Hydrothermal carbon enriched with sulfonic and carboxyl groups as an efficient solid acid catalyst for butanolysis of furfuryl alcohol, *Catal. Commun.* 123 (2019) 109–113. <https://doi.org/10.1016/j.catcom.2019.02.016>.

Chapter 3: Selective hydrogenation of furfural to tetrahydrofurfuryl alcohol in 2-butanol over an equimolar Ni-Cu-Al catalyst prepared by the coprecipitation method

Abstract

In order to upgrade biomass-derived platform chemicals to high value-added chemicals and liquid fuels, it is highly advantageous and desirable to synthesize suitable non-precious bimetallic catalysts that are efficient and versatile in chemical reactions. Equal moles of Ni and Cu were dispersed on varying mole ratios of Al by the coprecipitation method to synthesize Ni-Cu alloy particles to obtain a maximum yield of tetrahydrofurfuryl alcohol (THFA) by the liquid phase hydrogenation of furfural. The nickel species were active for the furan ring (C=C) and the carbonyl group (C=O) of furfural molecule, while Cu species were highly active for only the carbonyl group of furfural molecule. Systematic characterization of the prepared catalysts by XRD, TPR, STEM-EDS, and XPS analysis revealed the formation of highly active Ni-Cu alloys and near-equal Ni/Cu surface contents were achieved for the equimolar catalyst, which showcased a maximum of 98 mol% yield of THFA at 140 °C, 30 bar, 4h. The reaction pressure and temperature showed a substantial effect on the product yield. The solvent selection also influenced the product selectivity, particularly with 2-butanol, which promoted the reaction with its hydrogen donor capacity and supported the ring hydrogenation of FAL to THFA. Moreover, the reduced Ni₁Cu₁-Al₁ catalyst displayed good recyclability for three runs and an equal activity to that of a fresh catalyst after the regeneration.

Keywords:

Biomass, bimetallic NiCu-Al catalysts, hydrogenation of furfural, tetrahydrofurfuryl alcohol.

3.1 Introduction

The sustainable energy sector has been exploring renewable resources for energy and chemical production to negate the active adverse effects of depletion of fossil fuels and climate change[1][2]. In this regard, biomass-derived oxygen-containing chemicals are more attractive targets due to their higher added value and could be the hydrogen energy carriers[3]. Moreover, the effective use of hemicellulose remains a challenge in biorefinery. The hydrolysis of hemicellulose is an easy step compared to cellulose hydrolysis or lignin removal in biomass fractionation[4]. Thus, can be easily hydrolysed hemicellulose roots for an important platform chemical such as furfural, which has a broad range of conversion to synthetic chemicals and liquid fuels[5][6]. Furfural molecule has a furan ring and a carbonyl group in its structure, which contains two C=C double bonds and one cyclic ether bond; therefore, it is highly reactive and can be transformed into many synthetic chemicals and liquid fuels such as furfuryl alcohol (FAL)[7][8], tetrahydrofurfuryl alcohol (THFA)[9][10][11], 2-methyl furan (2-MF)[12][13], cyclopentanone and furan via hydrogenation, hydrogenation-hydrogenolysis, and decarbonylation reactions. Among these formations, the selective hydrogenation of furfural to THFA through aldehyde hydrogenation followed by ring hydrogenation is of great importance in producing the environmentally benign solvent, which has numerous applications in pharmaceutical solvents, industrial resins, and fuel additives[6][14][15].

Furfural hydrogenation could effectively and efficiently take place in both gas and liquid phases due to its high vapour pressure. Cu-Cr catalysts have been extensively employed for hydrogenation of furfural to FAL in large-scale production[16]. A variety of Cu-based catalysts are comprehensively studied for furfural hydrogenation because of their excellent activity toward the aldehyde group of furfural [17][18]. Furfural hydrogenation reaction is also studied with noble metal catalysts, especially with Pd, Pt, Rh, and Ru[19][20][21][22]. The direct hydrogenation of furfural to THFA, or FAL to THFA, was accomplished with high yields and recyclability, mainly with Pd and its bimetallic compositions[9][10]. Notably, the catalytic performances of bimetallic Ni-Pd or Ir-Pd alloys supported on SiO₂ were enhanced to form THFA compared to monometallic catalysts, possibly ascribing to the synergy between the Pd and the other metal as well as the interaction strength towards the carbonyl group and furan ring of the

furfural molecule[23][24]. Although the noble metal catalysts showed excellent catalytic activity, the apparent limitations such as high cost and limited availability hinder their wide application. Many efforts have been put into developing an efficient and non-precious metal catalyst for furfural hydrogenation, especially with Ni and Cu metals[14][24][25]. Moreover, the furfural molecule is open for reactions such as hydrogenation, hydrodeoxygenation, ring-opening reaction, hydrogenolysis reaction, and decarbonylation reaction; thus, the onus is on the selection of suitable metals for a particular reaction to obtain the target product[1][2]. The bimetallic catalysts could provide more electron density and different active sites at similar conditions to enhance the simultaneous hydrogenation of carbonyl group and furan ring. Henceforth, it would be more economical and desirable to develop a versatile, efficient, stable, and non-corrosive bi-metallic catalysts to facilitate the hydrogenation of furfural to THFA.

The Ni-Cu bimetallic catalysts have been widely used in many significant reactions such as ethanol steam reforming[26], CO methanation reaction[27][28], CO hydrogenation[27], and the selective hydrogenation of unsaturated aldehydes[24][29]. The composition of the metals, the support effect, metal dispersion, and the synergetic effect between the metals at a particular reaction condition drive the enhanced catalytic activity to selectively tune the target product[30][31]. Furthermore, the catalytic performance of NiCu-Al catalysts usually depends on the homogeneous metal composition and the high metal particle dispersion, which could be determined by the preparation method. The usual catalysts preparation methods such as the impregnation method, co-precipitation, and microemulsion methods have been extensively used to prepare the NiCu-Al catalysts. However, the mole ratio of Ni, Cu, and Al could determine the particle dispersion and available active sites, especially when using high metal loadings. The optimal mole ratio of these transition metals could be vital to inducing the high catalytic activity. Cu has an excellent affinity for furfural conversion to FAL, and Ni has shown remarkable selectivity towards THFA from FAL. Dezhang et al. have recently reported the activity of Ni-Al hydrotalcite catalyst which was very effective for the hydrogenation of FAL to THFA under mild conditions[32]. In this regard, we have applied the co-precipitated method followed by constant temperature ageing to develop crystal-like structures to obtain the NiCu-Al catalysts. Moreover, we synthesized a non-

noble transition bimetallic NiCu supported on Al catalysts that could promote the highly efficient production of THFA in 2-butanol. Additionally, this research obviously explained the influence of surface chemical composition, Al content, reaction pressure, temperature, and mechanistic pathway of the catalyst towards achieving high yields of THFA.

3.2 Methodology

3.2.1 Chemicals

Nickel(II) nitrate hexahydrate, aluminium nitrate nonahydrate, Copper(II) chloride dihydrate, 2-butanol (purity > 99.0%), furfural, and methanol were acquired from Sigma-Aldrich. 2-propanol, acetone, ethanol, sodium carbonate, and sodium hydroxide were purchased from Wako chemicals. Furfuryl alcohol, tetrahydrofurfuryl alcohol, 2-methyl furan, and 2-methyl tetrahydrofuran were obtained from TCI chemicals. All the chemicals were used as received.

3.2.2 Catalysts preparation

A series of monometallic (2:1 mole ratio of metal to support) and bimetallic catalysts (equal mole ratios of Ni or Cu on different Al molar ratios) were prepared by the co-precipitation method mentioned elsewhere[28]. In a typical procedure, the aqueous metal precursor solutions were added dropwise to a precipitating solution of Na₂CO₃ and NaOH at vigorous stirring conditions. The resulting solution was stirred for 1 hour, maintaining the pH at 10 by adding 3M NaOH solution. After that, the precipitated mixture was aged at 65 °C in a Parr reactor for 18 hours to promote the crystallization of metals on the Al surface. Finally, the solid precipitate was filtered out before multiple washes with ultrapure water to bring down the pH of the mixture to neutral. Thus, obtained solid was dried at 110 °C overnight, and further calcination and reduction were carried out at 500 °C in air and 5% H₂/N₂ gas, respectively. The monometallic catalysts are denoted as M-Al (M= Ni or Cu) with calcined samples as M-Al C and reduced samples as M-Al R. The mole ratio of metal to Al was maintained as 2:1. The bi-metallic catalysts are represented as Ni_xCu_y-Al_z C or R, where x, y, and z represent the molar ratio of Ni, Cu, Al, and C/R represents calcination or reduction, respectively.

3.2.3 Catalyst characterization

The textural properties of the prepared catalysts were analyzed by nitrogen adsorption/desorption isotherms data obtained at 77 K using the BELSORP-Max analyzer. The catalyst samples were first degassed under vacuum (10⁻⁵ torr) conditions at 573 K for 4 hours, and then N₂ physisorption measurements were carried out.

Powder X-ray diffraction (XRD) analysis was performed using the Rigaku ATX-G instrument with Cu-K α as the radiation source ($\lambda=0.154051$ nm) at 50 kV and 300 mA in the range of $2\theta = 10^\circ$ to 80° with a scan speed of 10 $^\circ$ /min.

Scanning electron microscope (SEM) images were recorded in a field emission scanning electron microscope, Hitachi S4300 instruments with an acceleration voltage of 0.5 kV ~ 15 kV.

Transmission electron microscope (TEM) and scanning transmission electron microscopy coupled with energy-dispersive X-ray spectroscopy (STEM-EDS) analysis were conducted in a transmission electron microscope system JEM-2100 plus with an acceleration voltage of 80 kV ~ 200 kV using carbon-coated Mo grids.

H₂ Temperature-programmed reduction (H₂-TPR) studies were carried out in BEL-CAT (MicrotracBEL corp.) instrument. The samples were first pre-treated under Argon flow (50 ml/min) at 400 $^\circ$ C for 1 hour, followed by the treatment with O₂ for 30 mins (Treatment with O₂ was excluded for reduced catalysts). After that, the temperature was cooled down to 50 $^\circ$ C in Ar flow. After this step, TCD was allowed for stabilization for 1 hour. Finally, the temperature was increased from 50 $^\circ$ C to 800 $^\circ$ C (10 $^\circ$ C/min) under a continuous 5% H₂/Ar flow (30 ml/min). The amount of H₂ consumed in mmol/g was automatically calculated by the ChemMaster software using calibration data of H₂ in Argon flow.

The metal dispersion and the active metal surface area were calculated by pulse chemisorption (CO and N₂O pulses) studies using BEL-CAT (MicrotracBEL corp.) instruments. The samples were first pre-treated under helium flow (50 ml/min) at 400 $^\circ$ C for 1 hour, followed by the treatment with O₂ and H₂ for 30 mins, respectively. After that, the temperature was cooled down to 50 $^\circ$ C, and the pulse gas was introduced for 30

minutes, followed by TCD stabilization. Finally, the pulse gas was injected through loop volumes, and the TCD spectra and the calibration were measured.

The acidic properties were estimated by the NH₃-TPD technique using BEL-CAT (MicrotracBEL corp.) automated chemisorption analyzer with a TCD detector. The samples were first pre-treated under helium flow (50 ml/min) at 400 °C for 1 hour and cooled to 100 °C. After that, ammonia adsorption was carried out using a 5% NH₃ gas mixed with helium (95%) for 30 minutes at 100 °C. After completing ammonia adsorption, the samples were purged with pure He for 30 more minutes, allowing TCD stabilization. Finally, the ammonia desorption spectra were obtained by gradually increasing the temperature by 10 °C /min until the final temperature, followed by the calibration with a 5% NH₃-He mixture. The amount of ammonia adsorbed in mmol/g was automatically calculated by the ChemMaster software using the calibration curve.

X-ray photoelectron spectra (XPS) of the prepared catalysts were investigated using ESCA Lab 250 (XPS only, Avantage, Ver.11) with an Al K α excitation source in twin anode mode. First, a survey spectrum was recorded with an energy step size of 0.5 eV in the range of 0-1200 eV of binding energy, followed by the individual elemental spectra record with a much-reduced energy step size of 0.05 eV for C (275- 305 eV), O (520-540 eV), Ni (835-900 eV) and Cu (925-975) respectively. The peak shifts of all spectra were calibrated with the true carbon peak at 284.8 eV.

TGA analysis was performed using the STA 2500 regulus (NETZSCH) equipment in N₂ flow with a 5 K/min temperature rate from 30 °C to 800 °C. Before the analysis, the samples were vacuum dried at 80 °C for 36 hours to remove the moisture content from the sample.

3.2.4 Catalytic hydrogenation of furfural

The furfural hydrogenation was carried out in a 100 mL stainless steel high-pressure batch reactor (parr instruments) at a stirring speed of 600 rpm. In a typical experiment, 5 mmol of furfural, 30 mol of 2-butanol, and 100 mg of catalyst were charged into the reactor and then purged with pure H₂ several times to completely remove the air inside the reactor. After that, the reactor was pressurized with pure H₂ to 2-3 MPa and heated to the designated temperature. After 4 h of reaction, the reactor was cooled down to room

temperature, and the liquid product sample was collected, followed by centrifugation to remove the catalyst particles. The product samples were first mixed with internal solvent methanol and then diluted with acetone to quantify using GC-FID equipped with a DB-WAX column (30m×0.25mm×0.25μm) and identified by GC-MS (DB-WAX column-30m×0.25mm×0.25μm). The following theoretical equations were used in evaluating the reaction data.

$$\text{Conversion of furfural (mol \%)} = \frac{\text{Initial moles of furfural} - \text{final moles of furfural}}{\text{Initial moles of furfural}}$$

$$\text{Yield of the product (mol \%)} = \frac{\text{moles of product formed}}{\text{Theoretical moles of product expected}}$$

3.3 Results and discussions on catalysts characterization

3.3.1 Textural properties

Fig.3.1a and 3.1b show the N₂ adsorption-desorption isotherms at 77 K of calcined and reduced catalysts. According to IUPAC classification, all the obtained isotherms except for Cu-Al catalysts correspond to type IV with H3 hysteresis indicating mesoporous materials. The isotherm of Cu-Al catalysts corresponds to type II isotherm suggesting non-porous or macroporous materials. The type of isotherms has not changed even after the reduction indicating the structural stability of the catalysts under thermal treatment. However, the hysteresis loops shifted towards higher relative pressure indicating a widening of the pores during reduction mainly because of thermal treatment[33]. Upon introducing the Cu content at equal molar ratios of Ni and Al, the amount of N₂ adsorbed was decreased because of bimetallic content and the formed Ni-Cu alloys[34]. Decreasing the Al content to maintain more active sites on the Al surface further decreased the N₂ intake, and the width of the hysteresis loop was contracted, indicating the transformation of cylindrical type pores to slit type pores. The dispersion of Cu on Al resulted in surface coverage forming large particles. Sharma et al. reported a similar isotherm and textural properties for the Cu-ZrO₂ catalyst prepared by the co-precipitation method[35]. Introducing Cu and changing the mole ratios of Ni and Al caused the changes in the location and slope of the hysteresis loop, surmising that the order and regularity of the pore structure have been altered, which could be attributed to the dispersion of Ni and Cu on Al and their spatial confinement on Al surface [34][36].

The physical properties of the prepared catalysts are reported in Table 3.1. The specific surface area of calcined and reduced Ni-Al and Ni₁Cu₁-Al₁ catalysts is higher than that of other catalysts (Table 3.1, entries 1-4). The high dispersion of Ni on the Al surface and the spatial confinement of Ni into the Al surface probably caused the high surface areas. The dispersion of Ni and Cu metals, including the formation of Ni-Cu alloys on the Al surface in the Ni₁Cu₁-Al₁ R catalyst, has driven the high surface area [33][37]. However, with the decrease in Al content and without Ni component, the specific surface area and pore volume are decreased, and Cu-Al catalysts showed a minimum value (30.6 m²/g). Interestingly the total surface area of the Cu-Al catalysts has not changed much before and after reduction, indicating the total surface coverage of Cu on Al surface. Fig.3.2a and 3.2b display the BJH pore size distribution (BJH-PSD) of the prepared catalysts to determine the pore size from N₂ desorption isotherms measured at 77 K. All the catalysts displayed a monomodal pore size distribution apart from Cu-Al catalysts. The average pore size of the catalysts has been concentered in the range of 5-10 nm except for Cu-Al catalysts (Table 3.1, entries 1-6). From Fig. 3.2b, it can be seen that the Ni-Al and Ni₁Cu₁-Al₁ catalysts have deep pores in the range of 5-8 nm and the pores were widened after the reduction attributing to the thermal treatment and probably caused the reduction in specific surface area and pore volume. For the Ni₂Cu₂-Al₁ catalysts, the average pore size (Table 3.1, entries 5,6) was slightly increased with much widened pores than Ni₁Cu₁-Al₁ Catalysts. The pores of the Cu-Al catalysts were significantly widened, and the pore structure was not developed properly because of the surface coverage and pore blockage of the Cu component. The higher specific surface area and pore volume of the catalysts provide maximum possible active sites for the reaction system, including the adsorption and migration of the substrate and the product molecules. Thus, the requirement of high dispersion of Ni and Cu on Al was achieved with an equimolar ratio catalyst (Ni₁Cu₁-Al₁ R) to expose active sites and increase the adsorption rate of the substrate molecules.

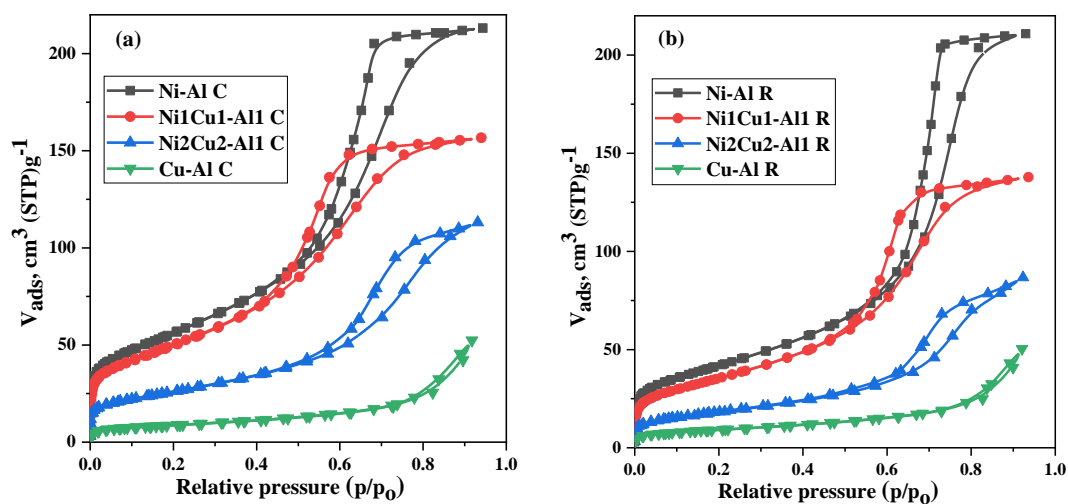


Fig.3.1: N₂ adsorption-desorption isotherms: a) calcined catalysts and b) reduced catalysts

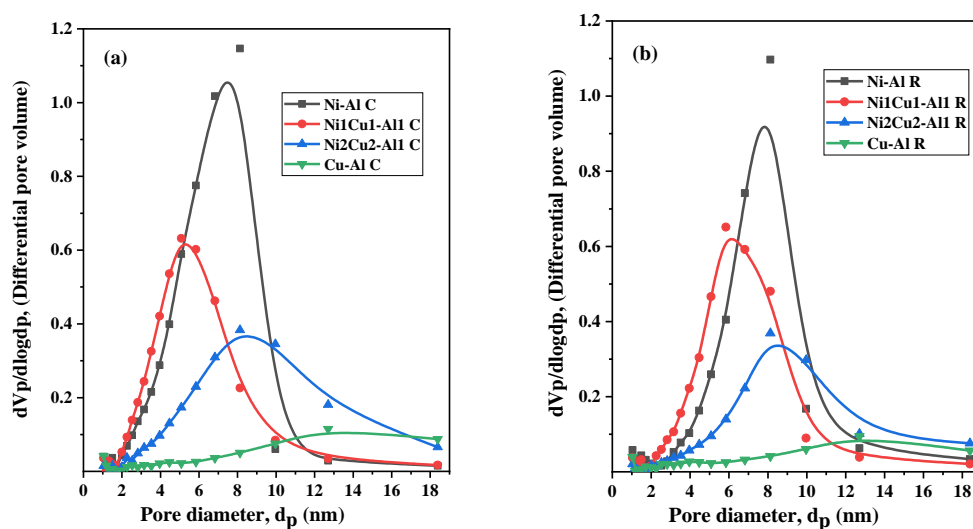


Fig.3.2: BJH pore size distribution: a) calcined catalysts and b) reduced catalysts

Table 3.1: Physical properties of the prepared catalysts

Entry	Catalyst	BET Surface area (m ² /g)	Pore volume (cm ³ /g)	Pore diameter (nm) ^x	Lattice parameter, a (Å) ^y	Particle size (nm) ^z
1	Ni-Al C	206	0.33	7.4	3.58	3.8

2	Ni-Al R	152	0.326	7.8	3.56	4.7
3	Ni1Cu1-Al1 C	183	0.242	5.2	4.01	13.1
4	Ni1Cu1-Al1 R	131	0.213	6.1	3.61	5.3
5	Ni2Cu2-Al1 C	93	0.18	8.4	4.03	16.6
6	Ni2Cu2-Al1 R	65	0.134	8.5	3.59	8.5
7	Cu-Al C	31	0.081	13.8	4.01	14.5
8	Cu-Al R	32	0.077	13.2	3.62	21.8

x: reported from BJH-PSD data, y: calculated from XRD analysis using Bragg's law, z: calculated using the Scherrer's equation.

3.3.2 XRD characterization

The crystallization phase properties of the prepared catalysts have been studied using XRD analysis. As shown in Fig.3.3a, the diffraction peaks of the calcined catalysts indicated the presence of NiO, CuO, and spinel phases of CuAl_2O_4 and NiAl_2O_4 phases. The XRD pattern of the Al_2O_3 synthesized by the co-precipitation method (calcined at 500°C) prompted slight sharp diffraction at $2\theta = 21^\circ$ and two broad diffraction peaks at $2\theta = 30^\circ$ and 63.2° , respectively. These broad peaks indicate the amorphous nature of the Al support. However, with the introduction of metals, the diffraction peaks at $2\theta = 21^\circ$ and 30° were suppressed by the formation of metal particles on the surface. It can be observed that all the catalysts showed a characteristic diffraction peak at $2\theta = 63.2^\circ$ representing the Al_2O_3 phase. A series of characteristic diffraction peaks of NiO phase at $2\theta = 37.1^\circ$, 43.6° , and 76.5° were assigned to the $\{111\}$, $\{200\}$, and $\{220\}$ lattice planes of face-centred cubic (fcc) structure[14][34]. Calcined Cu-Al catalyst has displayed multi diffraction peaks at $2\theta = 35.6^\circ$, 38.9° , 48.7° , 58.8° , and 75.3° , respectively, corresponding to the CuO phase, which can be assigned to the crystal planes of $\{111\}$ and $\{200\}$. The bi-metallic catalysts showed the diffraction peaks of both NiO and CuO phases in the range of $2\theta = 35.6^\circ \sim 48.7^\circ$. These diffraction peaks could be ascribed to the formed Ni-Cu alloys in the oxide form during the calcination process. It is generally stated that the intensity of the diffraction peak can be varied with the particle dispersion to some

extent[14]. The calcined Ni₂Cu₂-Al₁ and Ni₁Cu₁-Al₁ catalysts have shown indistinct behaviour similar to Cu-Al C and Ni-Al C catalysts. It can be observed from BET results that the Ni₁Cu₁-Al₁ catalyst possessed a high surface area compared to Ni₂Cu₂-Al₁, which indicates the high dispersion of small particles over the support surface. The Al content instigated the dispersion of Ni, Cu, and Ni-Cu alloys on the surface. Notably, the change in Al ratio in the bimetallic catalysts depicted the XRD behaviour analogous to Cu-Al catalyst when a low amount of Al was used in contrast to Ni-Al catalyst behaviour with high Al content. The reduction of the catalysts resulted in the respective metallic forms of Ni and Cu catalysts on the Al surface. Fig.3.3b represents the XRD patterns of the reduced catalysts. The diffraction peaks corresponding to CuO ($2\theta = 35.6^\circ$ & 38.9°) and NiO ($2\theta = 37.1^\circ$) phases were also observed with reduced peak intensity indicating the room for further reduction of the samples (reduction degree is reported in Table 2). It also confirms that the presence of metal oxides can enhance the catalytic activity because of the different oxidation states of the metals.

The diffraction peaks corresponding to metallic Ni, Cu, and Ni-Cu crystallites shifted slightly towards the higher diffraction angles than calcined catalysts. As per the monometallic Ni-Al R & Cu-Al R catalysts, the diffraction peaks at 2θ of 44.2° and 43.3° indexed to Ni {111} and Cu {111} were observed, respectively (JCPDS: 87-0712, JCPDS: 89-2838). The other diffraction peaks that were observed for the Ni-Al R catalyst at $2\theta = 51.6^\circ$ and 75.5° are assigned to the metallic Ni attributed to the {200} and {220} crystal planes, respectively. The characteristic peaks at $2\theta = 50.3^\circ$ and 74.1° are assigned to the metallic Cu crystal phases for the Cu-Al R catalyst. Furthermore, the reduction of Cu-Al catalysts resulted in the suppression of various diffraction peaks, particularly in the 2θ range of 55° - 71° that were observed in calcined catalysts due to the reduction of CuO and Cu₂O crystal phases[33]. However, the bi-metallic Ni₂Cu₂-Al₁ and Ni₁Cu₁-Al₁ catalysts showed the diffraction peaks of {111} plane positioned at the intermediary of monometallic Ni and Cu catalysts, indicating that the Ni-Cu alloys were synthesized successfully (Fig. S3). Besides, the broad diffraction peaks indicate the formation of mixed oxides with small crystallites[38]. Moreover, the presence of CuAl₂O₄ and NiAl₂O₄ spinel phases were observed for the Ni₂Cu₂-Al₁ catalyst by the indicated

diffraction peaks at 2θ of 32.3° , 58.3° , and 66.3° (highlighted with sky-blue colour)[34][36].

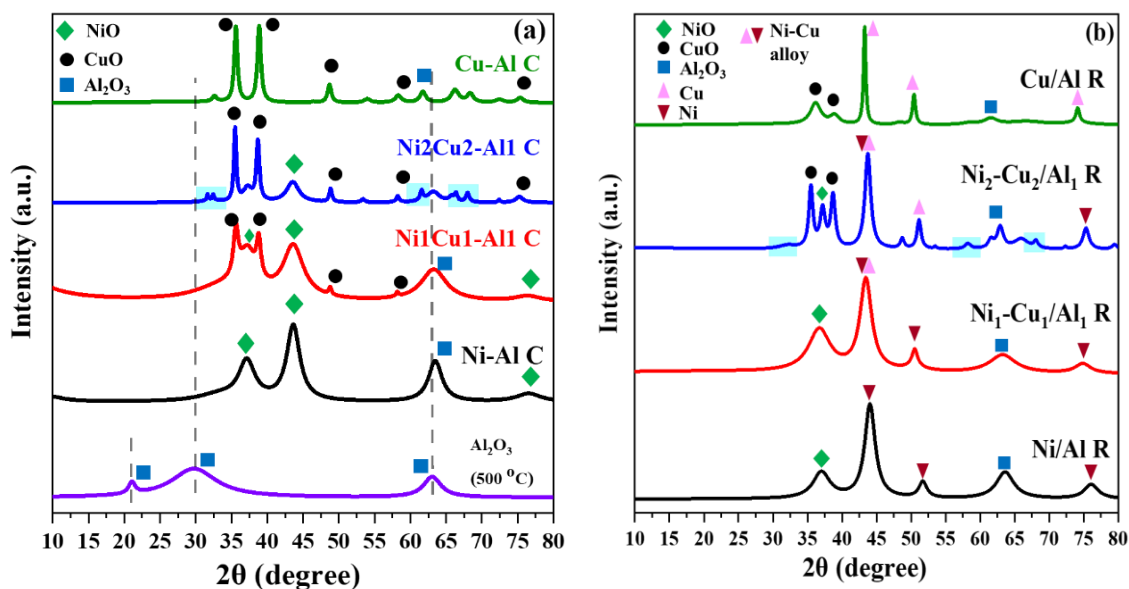


Fig.3. 3: XRD patterns of a) calcined catalysts and b) reduced catalysts

The mean diameter of the Ni, Cu, and Ni-Cu crystallites was calculated by the Scherrer equation using the full width at half maxima (β) and half of the diffraction angle (θ) of the highest peak intensity, which corresponds to the $\{111\}$ plane. Nickel and copper possess an FCC structure with lattice parameters $a = 3.52 \text{ \AA}$ (JCPDS 04-0850) and 3.62 \AA (JCPDS 04-0836), respectively. Table 3.1 shows the lattice parameter and particle size of the Ni, Cu, and Ni-Cu alloy phases using Bragg's law. The Ni and Cu samples showed the lattice parameters 3.56 \AA and 3.62 \AA , respectively, which are in accordance with the JCPDS data mentioned above. However, for the bimetallic catalysts, the lattice parameters (Table 3.1, entries 4 & 6) lay in the range of Ni-Al R and Cu-Al R catalysts. The particle size of the monometallic catalysts (Table 3.1, entries 1,2 & 7,8) increased after reduction, attributed to the reduction process and the thermal treatment, which results in the formation of large crystals through the reduction of spinal phase metals. Leontyev et al. have well explained the dependence of the lattice parameter as a function of inverse average particle size, which was observed for Ni-Al and Cu-Al catalysts[39]. On the other hand, the complete opposite behaviour was observed for the bimetallic catalysts. The lattice parameter and particle size were reduced after the reduction. This could be due to the formation of Ni-Cu alloys which can be reduced at a larger scale

because of the cluster formations. The Al content also instigated the particle size. It can be observed that the Ni₂Cu₂-Al₁ catalysts have a larger particle size compared to Ni₁Cu₁-Al₁ catalysts. This could be because of the lack of support material, which resulted in close dispersion of metal particles, and also the presence of closely dispersed copper, which does not promote the reduction of Ni-Cu alloy. Furthermore, the formation of Ni-Cu alloy could enhance the electric effect between the Ni and Cu active species, thus increasing the adsorption properties of bimetallic catalysts for the reactant molecules.

3.3.3 Structure and morphology characterization (SEM, TEM, and STEM-EDS)

Fig.3.4 shows the SEM images of reduced catalysts at a 10 μm magnification scale to study the microscopic structure. The images revealed the non-uniform aggregated textural distribution of metals on the support. It can be seen that, for the monometallic catalysts, the dispersion of Ni and Cu on the Al surface contrasts each other where Ni has been widely dispersed over the Al surface with smaller particles while Cu covered the Al surface to form large particles. This wide dispersion for Ni and surface coverage for Cu resulted in higher surface area for Ni-Al catalysts and lower surface area for Cu-Al catalysts, which are in good agreement with the literature [35]. It is apparent that the higher surface areas of the metal-supported catalysts are provided by the surface chemistry of the support material. In this regard, alumina possesses high academic and industrial significance because of its great and benign surface chemistry. The effect of Al content on Ni-Cu-Al catalysts morphology showed in Fig.3.4c and 3.4d. For the bimetallic catalysts, the amount of Al instigated the surface morphology. When equal amounts of Ni, Cu, and Al were used (Ni₁Cu₁-Al₁ R), the non-uniform dispersion of Ni, Cu, and Ni-Cu alloys was observed with a well-developed pore structure. For the Ni₂Cu₂-Al₁ R catalyst, the insufficient amount of Al resulted in close dispersion of Ni, Cu, and Ni-Cu alloys and the cluster formation, thereby hindering the structural properties. Furthermore, TEM analysis was conducted for more topographical information.

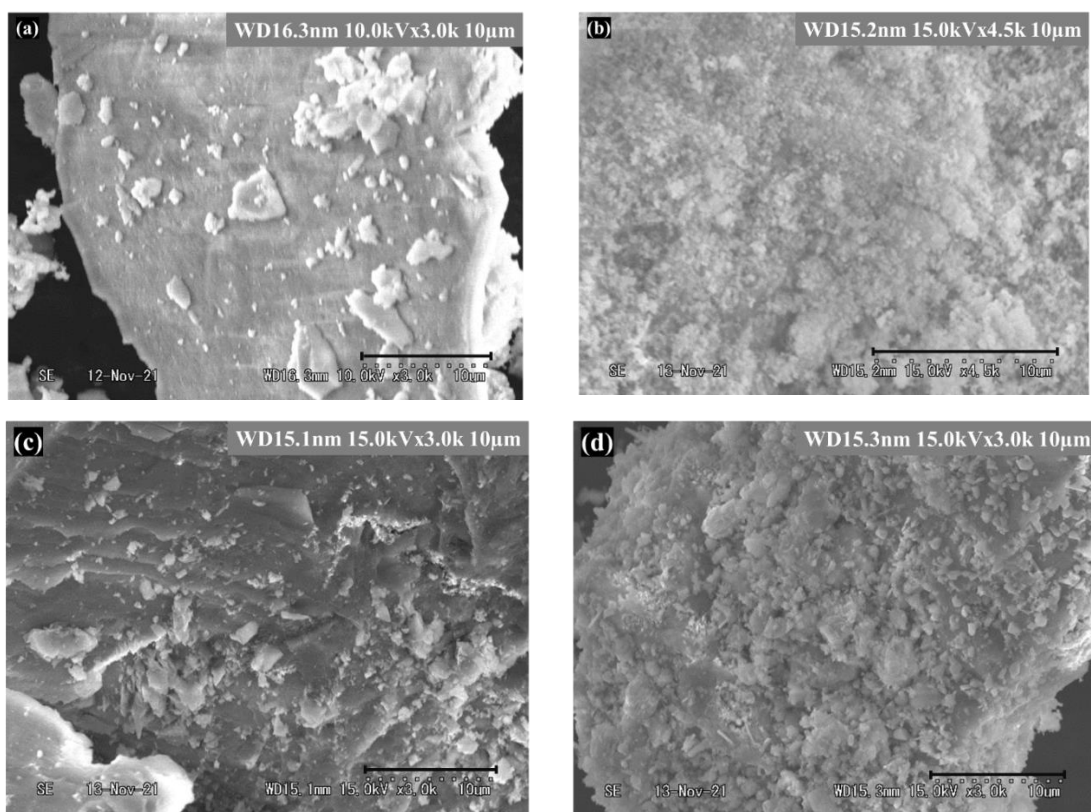


Fig.3.4: SEM images of (a) Ni-Al R, (b) Cu-Al R, (c) Ni1Cu1-Al1 R, (d) Ni2Cu2-Al1 R

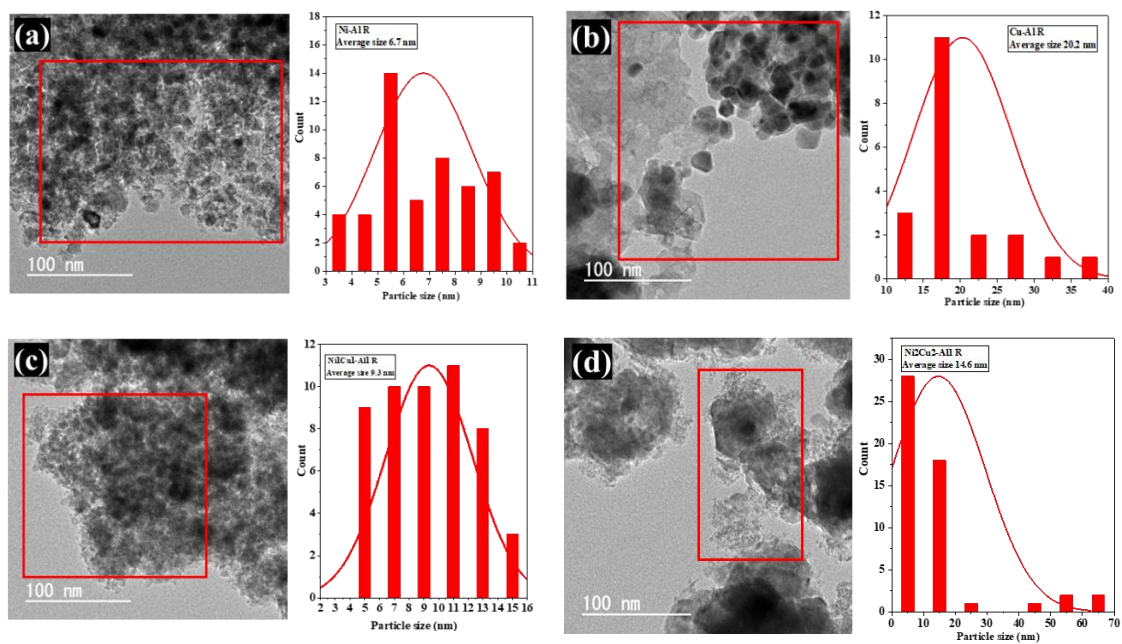


Fig.3.5: TEM images and the corresponding particle size distribution of (a) Ni-Al R, (b) Cu-Al R, (c) Ni₁Cu₁-Al₁ R, (d) Ni₂Cu₂-Al₁ R

TEM images showed the overlaid crystals surrounded by amorphous particles indicating the dispersion and embedment of Ni and Cu into the Al surface. (Fig. 3.5). From Fig. 3.5a and 3.5b, it can be seen that different particle structures were observed for the monometallic Ni-Al R and Cu-Al R catalysts. Ni-Al R catalyst resulted in the formation of small particles with an average particle size of 6.7 nm. In comparison, the Cu-Al R catalyst displayed relatively large particles with an average particle size of 20.2 nm. The results are in good agreement with that reported by S. Das et al.[40]. The effect of the introduction of Cu on the particle size and structure of the catalyst depended on Al content. For instance, in the case of the Ni₁Cu₁-Al₁ R catalyst (Fig.3.5c), small particles with an average size of 9.3 nm similar to Ni-Al R are formed, whereas, for the Ni₂Cu₂-Al₁ R catalyst (Fig.3.5d), the combination of small and large particles with an average particle size of 14.6 nm was observed. These results are in accordance with BET and XRD analysis. TEM images of the Al support prepared by the as-synthesized method are shown in Fig. 3.6, which showed an amorphous nature with large particles of plate-type structure.

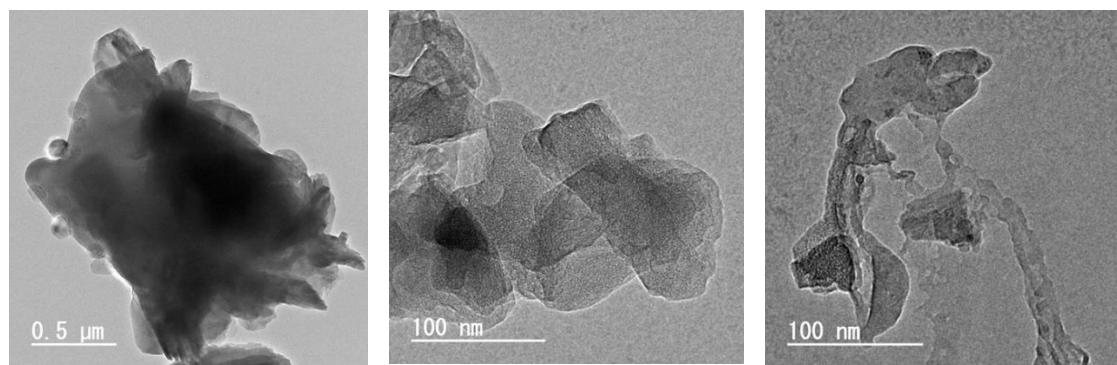


Fig.3.6: TEM images of Al₂O₃ support prepared by the co-precipitation method

In order to investigate the dispersion of Ni and Cu, visual representation of the elements, and the formation of Ni-Cu alloys, STEM-EDS analysis was performed. The STEM-EDS images of the monometallic Ni-Al R and Cu-Al R catalysts are shown in Fig.3.7, and 3.8, respectively. Since high metal loadings were (Table 3.2) used, highly dispersed metal mapping on the Al surface was observed for the monometallic catalysts.

In addition, the mapping of individual elements (Fig.3.7d~f, & Fig.3.8d~f), overlaid metal and support elements (Fig.3.7b & Fig.3.8b), and the map sum spectrum are reported to understand the visual representation of the surface elements and their compositions.

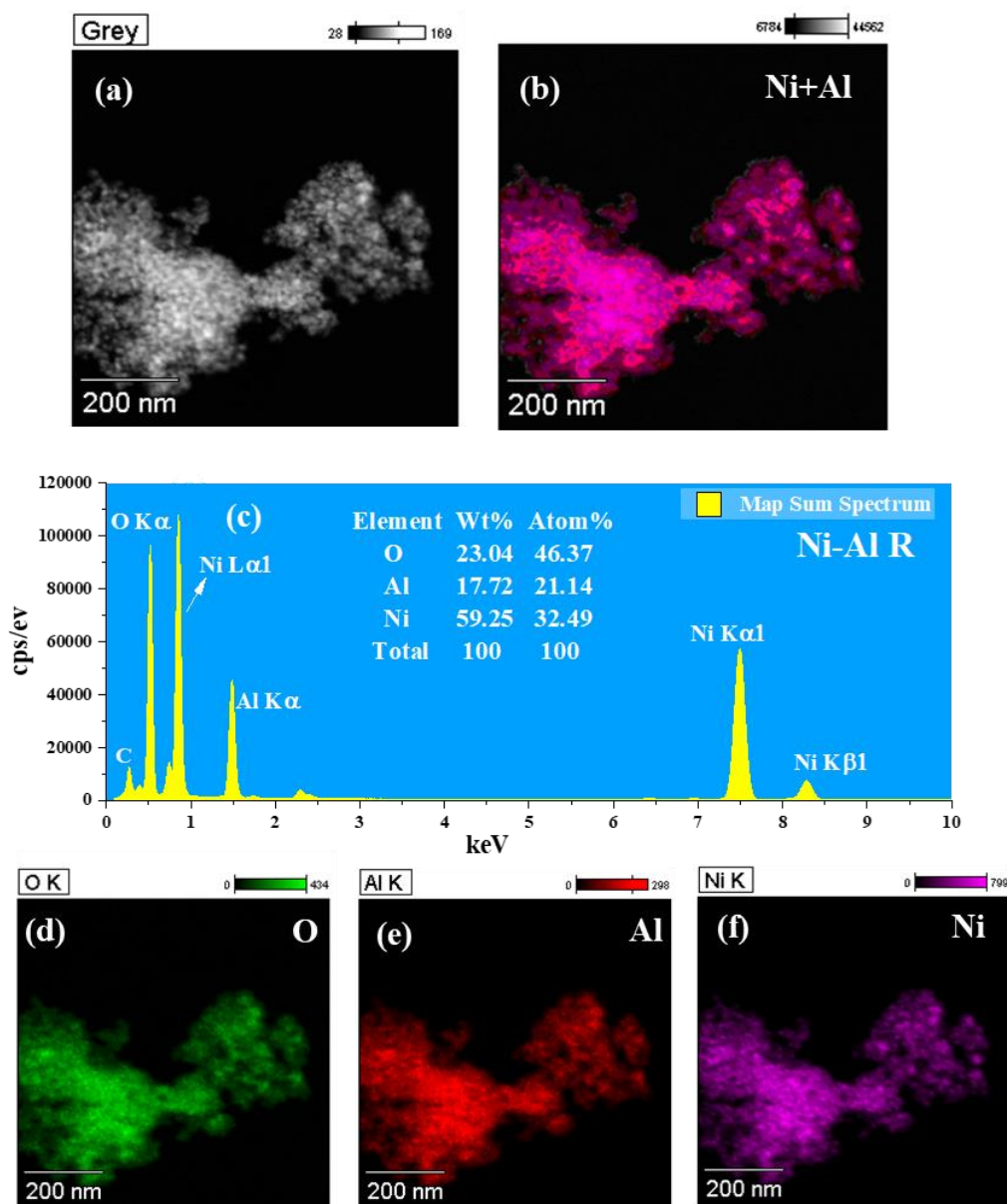


Fig.3.7: STEM-EDS mapping of the corresponding elements of the catalyst Ni-Al R

(a) grey image selected for elemental mapping, (b) overlay image of Ni and Al elements, (c) map sum spectrum representing elemental composition, (d)~(f) individual element mapping of O, Al, and Ni, respectively.

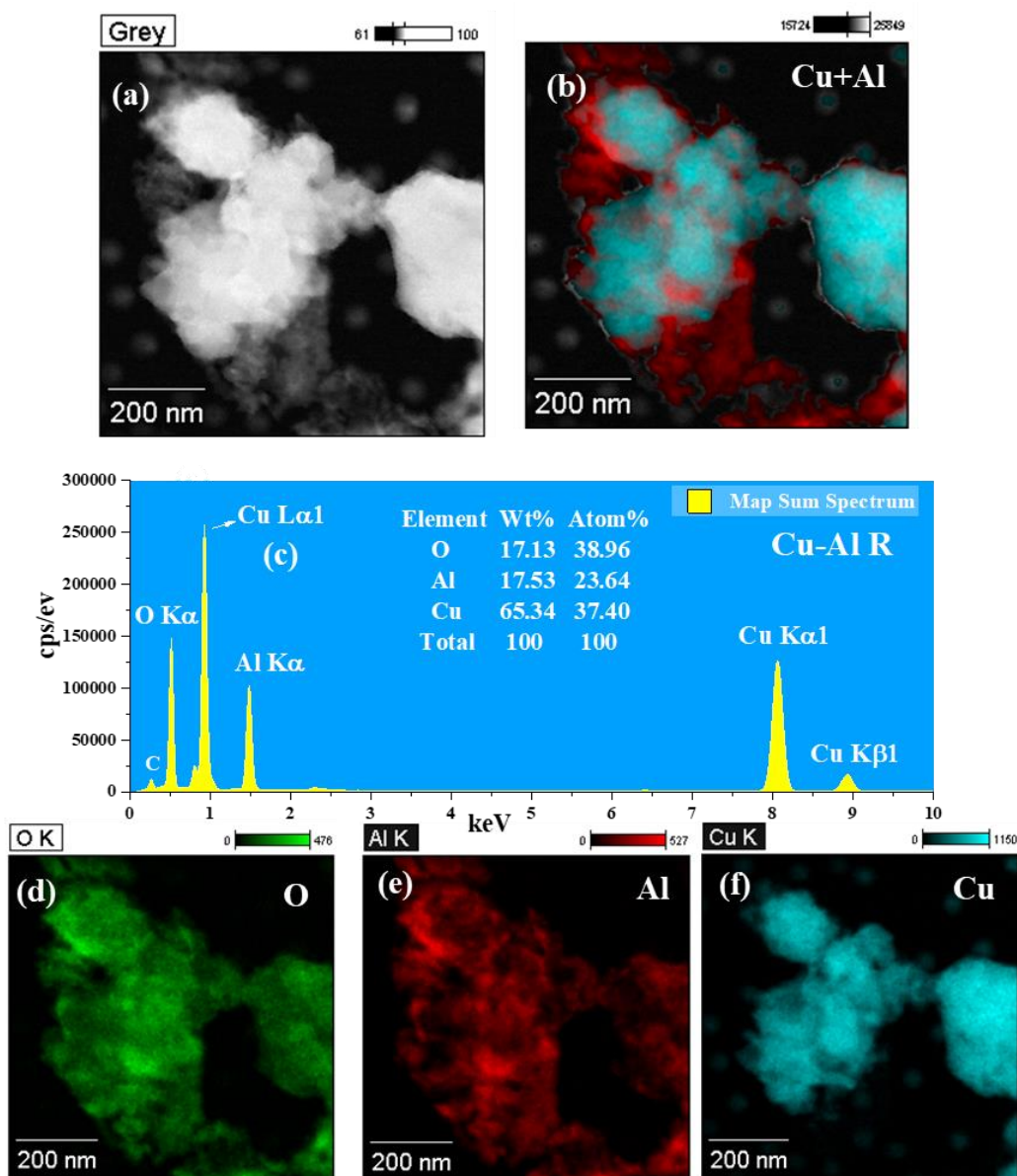


Fig.3. 8: STEM-EDS mapping of the corresponding elements of the catalyst Cu-Al R

(a) grey image selected for elemental mapping, (b) overlay image of Cu and Al elements, (c) map sum spectrum representing elemental composition, (d)~(f) individual element mapping of O, Al, and Cu, respectively.

Fig.3.9 shows the presence of various constituent elements of the equimolar bi-metallic catalyst (Ni1Cu1-Al1 R). Fig.3.9b is the overlaid image of Ni, Cu, and Al elements, exhibiting the close dispersion of Ni and Cu elements. It can be seen that there are more Ni sites than Cu, indicating the more Ni active sites and also confirming the formation of Ni-Cu alloys (combination colour of Ni and Cu element colours) which are

very crucial for the synergetic catalytic activity. Fig.3.9d presents the elemental composition and the presence of shell electrons (L&K) of various constituent elements of the Ni₁Cu₁-Al₁ R. The first small peak corresponds to carbon, which arose because of carbon coated-Mo grids. The ratio of element wt.% of Ni and Cu on Al is more than 1 specifying the presence of more surface Ni than Cu.

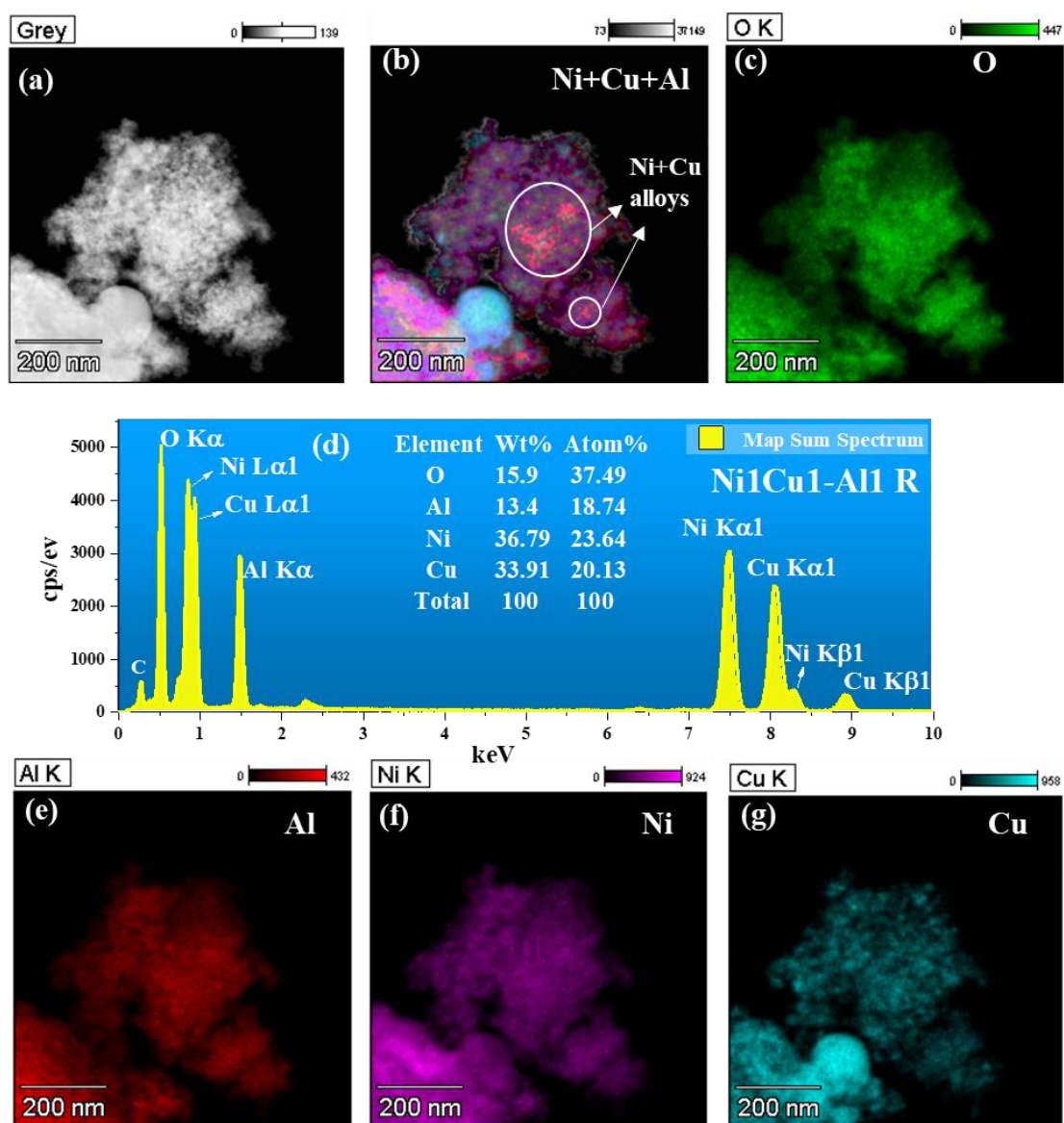


Fig.3.9: STEM-EDS mapping of the corresponding elements of the catalyst Ni₁Cu₁-Al₁ R

(a) grey image selected for elemental mapping, (b) overlay image of Ni, Cu, and Al elements showing the Ni-Cu alloys, (c) mapping of O, (d) map sum spectrum

representing elemental composition, (e)~(g) individual element mapping of Al, Ni, and Cu, respectively.

Fig.3.10 displays the STEM-EDS images of Ni₂Cu₂-Al₁ R for which more surface Cu dispersion with large particles than Ni was observed. The formation of Ni-Cu alloys was also confirmed for this catalyst. However, the dominance of surface Cu (Fig.3.10d) led to fewer Ni-Cu alloys than the Ni₁Cu₁-Al₁ R catalyst.

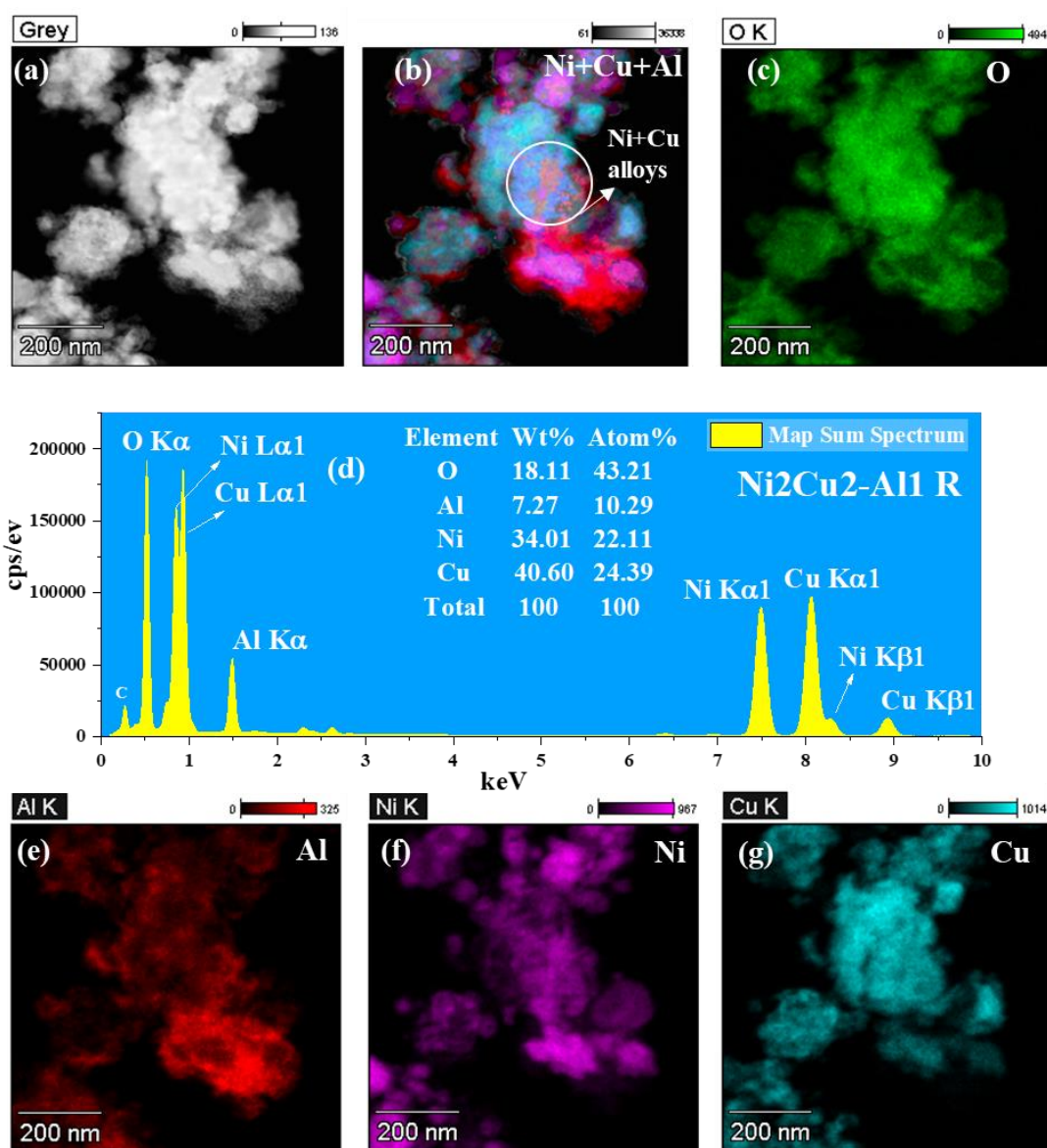


Fig.3.10: STEM-EDS mapping of the corresponding elements of the catalyst Ni₂Cu₂-Al₁ R

(a) grey image selected for elemental mapping, (b) overlay image of Ni, Cu, and Al elements showing the Ni-Cu alloys, (c) mapping of O, (d) map sum spectrum representing elemental composition, (e)~(g) individual element mapping of Al, Ni, and Cu respectively.

The theoretical elemental composition and the determined elemental composition by STEM-EDS of the reduced samples are reported in Table 3.2. Due to high metal loadings, the composition of the monometallic catalysts was slightly varied from that of the theoretical composition (Table 3.2, entries 1-4). For the bimetallic catalysts, the determined compositions (Table 3.2, entries 5-10) are close to that of theoretical values (Table 3.2, columns 5). The elemental composition was decreased for the spent catalyst (Table 3.2, entries 11-13) due to slight leaching and carbon deposition.

Table 3.2: Theoretical and measured elemental compositions of the catalysts

Entry	Catalyst	Element	Theoretical Wt.%	STEM-EDS analysis Wt.%
1	Ni-Al	Ni	69.73	59.25
2		Al	18.69	17.72
3	Cu-Al	Cu	71.2	65.34
4		Al	17.6	17.53
5	Ni1Cu1-Al1	Ni	33.98	36.79
6		Cu	36.51	33.91
7		Al	18.12	13.4
8	Ni2Cu2-Al1	Ni	39.86	34.01
9		Cu	42.8	40.6
10		Al	9.96	7.27
11		Ni	33.98	32.03

12	Ni1-Cu1-Al1	Cu	36.51	31.32
13	Spent	Al	18.12	16.18

3.3.4 H₂-Temperature programmed reduction study (H₂-TPR)

To understand the reducibility of the calcined samples and to calculate the reduction degree of the reduced catalysts, H₂-TPR studies were conducted. Fig.3.11a & 3.11b and Table 3.3 display the TPR profiles and the quantitative H₂ consumption of calcined and reduced samples. Since the Al₂O₃ cannot be reduced in the studied reduction temperature range, the reduction peaks corresponded to the reducible species of Ni and Cu dispersed on the support and inside the pores of the support[41]. The apparent monomodal peak of Ni-Al C suggested high interaction of active metal species with support and displayed a strong reduction peak after 400 °C, particularly at 620 °C. This assertive reduction behaviour of Ni-Al C catalyst at 620 °C ascribed to the reduction of highly dispersed NiO species to metallic Ni on Al [14]. The higher surface area of Ni-Al C catalyst from BET results explains the wide dispersion of NiO species on the surface of the Al as well as inside the pores, which were reduced at a higher temperature. The absence of any reduction peak in the range of 280-380 °C corresponds to the NiO species that were unbound to any support indicating no such unbound species [37]. The long shift of the reduction peak for Ni-Al C catalyst describes the increase of the mobility of Ni²⁺ species on the Al surface and the reduction of spinel NiAl₂O₄ species making the reduction more difficult caused by the increasing polarization effect of aluminium ions[37]. However, for the Cu-Al C catalyst, a rising peak at 270 °C and a substantial reduction peak at 423 °C represent the probable reduction of Cu₂O and CuO species. The reduction peak corresponding to the pure CuO sample (Fig. 3.12) obtained at 335 °C represents an unbound CuO species. However, this reduction peak was not observed for the Cu-Al C catalyst indicating a strong interaction between CuO species and Al. This reduction behavior of the Cu-Al catalyst could be attributed to the reduction of CuO and Cu₂O species that were dispersed on Al, including spinel CuAl₂O₄ species[36].

The bimetallic catalysts (Ni1Cu1-Al1 C and Ni2Cu2-Al1 C) contained the various reducible species on the support, resulting in several peaks due to the presence of different

metals on the Al surface in different states. For the equimolar ratio catalyst (Ni1Cu1-Al1 C), CuO and Cu₂O species reduction happened below 300 °C. This pattern can be explained by the strong support and metal interaction between Ni and Al compared to Cu and Al. The catalyst with reduced Al content (Ni₂Cu₂-Al₁ C) displayed a strong peak at 391 °C, similar to the Cu-Al C catalyst. A rising peak obtained at 328 °C could be due to unbound CuO species. For these catalysts, the reduction temperature of NiO species to metallic Ni shifted towards low temperature, particularly near 500 °C from 620 °C, signifying that the presence of Cu metal improves the reduction of NiO species, thereby generating the strong synergy between Ni and Cu components. The CuO species on Al are more accessible to be reduced by H₂ than the NiO species on Al having similar physicochemical properties. The overflow of the formed reactive hydrogen by reducing CuO species onto the NiO species creates a more conducive environment to reduce NiO species to metallic Ni. Thus, NiO species can be reduced for bimetallic catalysts at lower reduction temperatures[33]. Furthermore, the formation of metallic Cu before metallic Ni could form the Ni-Cu alloy, effectively lowering the reduction difficulty. However, some high valence state NiO species are hard to be reduced completely.

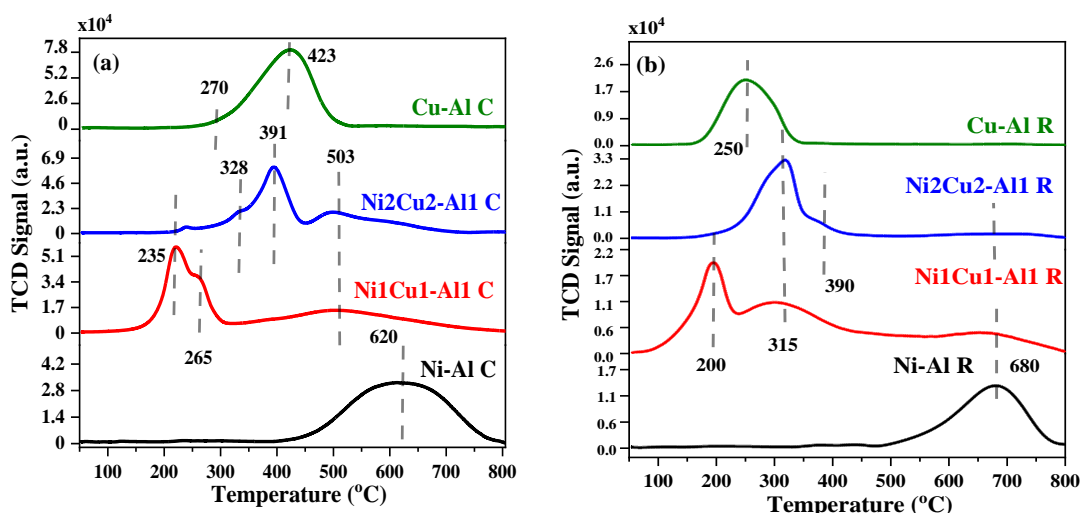


Fig.3.11: H₂-TPR profiles of a) calcined catalysts and b) reduced catalysts

Fig. 3.11b shows the reduction behaviour of reduced catalysts. Since the reduction was conducted in a horizontal tubular reactor, the reduced catalysts showed reduced behaviour with low H₂ consumption. Interestingly, the reduction peak shifted towards

lower temperatures than calcined samples, whereas for the Ni-Al R catalyst, the reduction happened at 680 °C. Zhang et al. have observed the reducible species of Ni-Cu alloys on Al catalysts well below 250 °C [42].

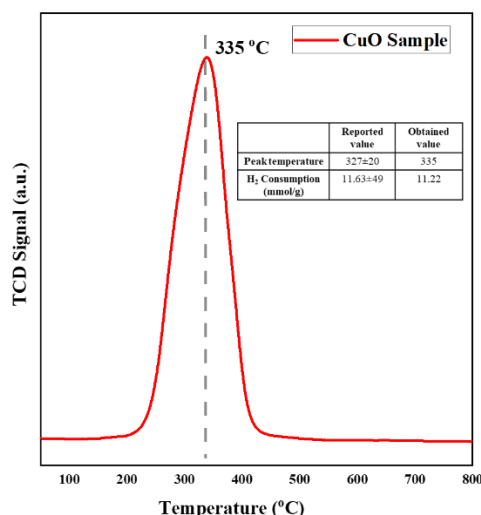


Fig.3.12: H₂-TPR profile of CuO sample

The reduction degree of the catalysts was calculated based on the amount of H₂ consumed before and after reduction, and the results are shown in Table 3.3. More than 70 % reduction was achieved for all the catalysts. The oxygen content in the STEM-EDS results could be derived from the metal oxide species present after the reduction. From H₂-TPR studies, the catalysts, which were reduced at 500 °C for 5 hours in 10 % H₂/N₂ flow, have possessed co-existed metal oxide species and metals on Al surface, especially NiO species along with metallic Ni and metallic Cu components, which can enhance the catalytic activity of the equimolar catalyst.

Table 3.3: H₂-TPR studies of the prepared catalysts

E nt ry	Catalyst	Calcined samples		Reduced samples		Reduct ion degree ^a
		Peak temperat ure (°C)	Amount of H ₂ consumed (mmol/g of catalyst)	Peak temperat ure (°C)	Amount of H ₂ consumed (mmol/g of catalyst)	
1	Ni-Al	620	8.13	685	2.02	75.1

2	Ni1Cu1- Al1	231	2.63	315	1.01	75.3
		265	1.43	680	1.2	
		503	4.91			
3	Ni2Cu2- Al1	235	0.13	350	0.66	71.1
		391	4.53	680	1.5	
		516	2.82			
4	Cu-Al	423	8.07	250	2.08	74.2

$$^a \text{Reduction degree} = \frac{\text{Amount of H}_2 \text{ consumed after(calcination-reduction),mmol/g}}{\text{Amount of H}_2 \text{ consumed after calcination,mmol/g}} \times 100$$

3.3.5 CO and N₂O chemisorption

As the catalysts contain two different metals (Ni and Cu) on the Al surface which are active to adsorb CO and N₂O probe molecules at different active sites, the two CO and N₂O pulse chemisorption techniques were employed to determine the metal dispersion, active metal surface area and the active particle size of the reduced catalysts. The electron-accepting and electron-donating sites on the surface of a catalyst can be explored with a probe molecule. Based on probe molecule consumption, the active metal surface area, metal dispersion, and the active particle size can be calculated. CO pulse chemisorption can accurately determine the chemisorption properties of Ni containing catalysts because of its irreversible interaction with Ni metal sites. In contrast, N₂O chemisorption can determine chemisorption properties of Cu containing catalysts because of the effective adsorption of oxygen atoms on Cu surfaces from N₂O gas driven by the free energy change in N₂O adsorption caused by a change in electronic energy during adsorption[43]. Tada et al. reported the applicability of N₂O chemisorption by investigating N₂O chemisorption studies on Ni/ α -Al₂O₃ catalysts combined with the results of CO pulse and transmission electron microscopy studies. [44]. The adsorption of either CO or N₂O probe molecules by NiO or CuO surface-active species is negligible at the temperature range of 50-100 °C during the chemisorption. Therefore, Ni and Cu metal active sites adsorb the probe molecules during the chemisorption study. Thus, the

reliability of the chemisorption data of NiCu-Al catalysts can be obtained through both CO and N₂O techniques[44,45].

Table 3.4: CO pulse chemisorption of reduced catalysts

Entry	Catalyst	Metal dispersion, Dm (%)	Active metal surface area		Active particle diameter (nm)	Amount of CO adsorbed (cm ³ /g of catalyst)
			m ² /g of sample	m ² /g of metal		
1	Ni-Al R	3.67	17	24.4	27	4.88
2	Cu-Al R	0.51	2.3	3.3	205	0.64
3	Ni ₂ Cu ₂ -Al ₁ R	0.15	0.56	0.64	1060	0.15
4	Ni ₁ Cu ₁ -Al ₁ R	1.48	6.8	9.7	70	1.9
5	Ni ₁ Cu ₁ -Al ₁ R	1.21	5.6	7.9	85	1.57

Spent

Table 3.5: N₂O pulse chemisorption of reduced catalysts

Entry	Catalyst	Metal dispersion, Dm (%)	Active metal surface area		Active particle diameter (nm)	Amount of N ₂ O adsorbed (cm ³ /g of catalyst)
			m ² /g of sample	m ² /g of metal		
1	Ni-Al R	3.28	15.3	21.9	31	4.37
2	Cu-Al R	0.72	3.3	4.6	145	0.91
3	Ni ₂ Cu ₂ -Al ₁ R	0.09	0.5	0.6	1186	0.13
4	Ni ₁ Cu ₁ -Al ₁ R	1.36	6.3	8.9	76	1.76
5	Ni ₁ Cu ₁ -Al ₁ R	0.76	3.5	5.0	137	0.97

Spent

Tables 3.4 and 3.5 represent the CO pulse and N₂O pulse chemisorption details of the reduced catalysts, respectively. Among all the catalysts Ni-Al R catalyst has shown more metal dispersion and the active metal surface area on the Al surface (Tables 3.4 & 3.5, entry 1), which signifies the presence of active sites all over the Al surface, attributing to the formation of small Ni crystals on the Al surface, as evidenced by STEM-EDS images. The strong metal and support interactions can influence the amount of probe molecule adsorption. Furthermore, from the TPR results, the co-existence of metal and oxide phases also caused the low adsorption amount of CO and N₂O as probe molecules, leading to a relatively low dispersion degree of the active metallic sites. Ni-Al R showed a maximum of 4.88 cm³/g of catalyst of CO adsorption due to the strong Ni and Al interaction. Despite the subpar pore structural properties, the metal dispersion was around 0.72% for the Cu-Al R catalyst (Tables 3.5, entry 2). The TEM and XRD analysis evidenced the formation of Cu clusters with large particles and spinel CuAl₂O₄ species during the catalyst preparation. Because of this, the N₂O adsorption resulted in a low value of 0.91 cm³/g of catalyst. The Ni₂Cu₂-Al₁ R catalyst showed a minimum metal dispersion of only about 0.1 % among all the catalysts (Tables 3.4 & 3.5, entry 3). This might be due to the formation of both NiAl₂O₄ and CuAl₂O₄ spinel phases in small and large particles (TEM images, Fig.5d). The Ni-Al R catalyst has shown good metal dispersion than the Ni₁Cu₁-Al₁ R catalyst (Tables 3.4 & 3.5, entry 4). The amount of Al in bi-metallic catalysts instigated the contrasting outcome between wide and close dispersion of both metals and the alloy species.

The formation of Ni-Cu alloys and the cluster formations on the Al surface determined the amount of gas adsorption because the synergy between Ni and Cu can also affect gas adsorption[14]. Moreover, the active sites occupied by hydrogen during the reduction process can also affect gas adsorption capacity. For the spent catalyst, the metal dispersion decreased, and active particle size was increased after three reaction cycles. It is surmised to be due to the carbon deposition, leaching of active surface Ni and Cu sites during the reaction, and the thermal treatment during the reactions. The increase in the active metal surface area per gram of sample to the per gram metal is apparent because the catalyst sample includes support material. Although the active sites for pulse chemisorption are different from acidic sites, which can adsorb NH₃, the adsorption

capacity of all the catalysts showed by the chemisorption technique followed the order of ammonia adsorption by NH_3 -TPD (Fig. 3.13 and Table 3.6) analysis except for the Cu-Al R catalyst.

The active particle size acquired through chemisorption data contrasts with the data obtained by XRD analysis (Table 3.1) but can be supported by TEM analysis. For example, the average crystalline size reported by XRD analysis for the Ni-Al R catalyst was 4.73 nm. In contrast, TEM results showed a minimum of 6.7 nm to 27.62 nm by the chemisorption study. For the Cu-Al R catalyst, the particle sizes were 3.6 nm and 144 nm by XRD and N_2O chemisorption analysis, respectively, while an average of 20.2 nm particles were observed in TEM analysis. The data obtained in XRD corresponds to the average crystal particle on the Al surface by which the X-ray beam was diffracted in a particular plane. In contrast, the particle size obtained by chemisorption corresponds to the surface-active Ni species or a group of small Ni or Cu active crystals. The Ni₂Cu₂-Al₁ R catalysts showed an active particle size of more than 1000 nm by both CO and N_2O chemisorption (Tables 3.4 & 3.5, entry 3). As seen in the TEM images, the Ni₂Cu₂-Al₁ catalyst showed a combination of large and small particles, which explains the larger active particle size by chemisorption analysis.

Furthermore, Larmier et al. stated that the determination of particle size of Cu-containing catalysts was not possible due to the strong metal-support interaction between Cu and the support[45]. Nonetheless, the particle size data obtained through chemisorption and XRD analysis was not comparable in this study; however, TEM results are partially supporting the chemisorption studies. Furthermore, the chemisorption data was used to find out the number of surface-active sites using the metal dispersion, which is the ratio of moles of metal on the surface of the sample to the moles of total metal present in the sample. The number of active sites on the surface data was used to calculate the turnover frequency (TOF) [46]. However, chemisorption data does not accurately determine a true active site since the catalytically active sites and the surface-active sites calculated by the chemisorption may not be the same. Instead, it can give a relative comparison of the measured catalysts.

3.3.6 NH₃-TPD study

NH₃-TPD profiles of the calcined and reduced catalysts are shown in Fig.3.13a and 3.13b, respectively. The calcined catalysts exhibited only one broader desorption peak in the temperature range of 180-270 °C, which could be attributed to the weak and moderate acidic sites (Lewis sites). Table 3.6 displays the amount of NH₃ desorbed, and it can be seen that the Ni-Al C catalyst (Table 3.6, entries 1-4) has adsorbed more amount of NH₃ compared to other catalysts. This could be due to the wide dispersion of NiO active species over the Al surface because of its higher surface area, which is favourable to the exposure of the acidic sites[47]. Furthermore, the SEM images clearly show the dispersion of NiO and CuO species over the Al surface. The surface coverage by CuO and Cu₂O species on the Al surface of Cu-Al C catalyst provided lower active sites, which resulted in only 0.113 mmol of NH₃ adsorption/g of catalyst (Table 3.6, entry 4). The possibility of the acidity generated from Al_xO_x surface adsorption was not the case for the Cu-Al C catalyst because of the surface coverage by CuO and Cu₂O species. The presence of both NiO and CuO species with good dispersion for Ni₁Cu₁-Al₁ C catalyst resulted in 1.88 mmol of NH₃ adsorption/g of catalyst (Table 3.6, entry 2), whereas for Ni₂Cu₂-Al₁ C catalyst, a relatively lower amount of NH₃ was adsorbed on the surface-active sites. NH₃-TPD study described the acidic properties of the catalysts and explained the surface-active sites.

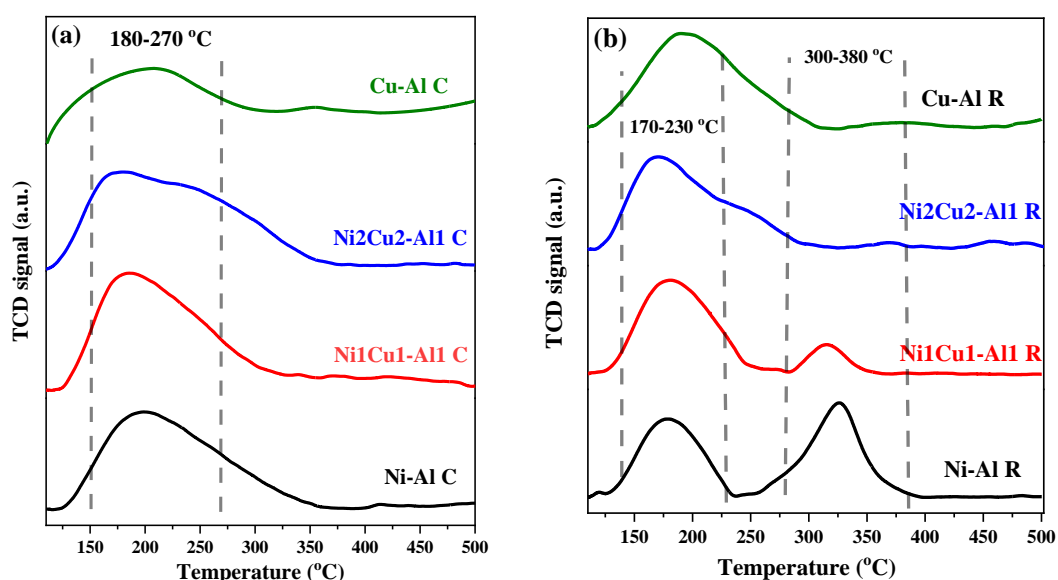


Fig.3.13: NH₃-TPD profiles of a) calcined catalysts and b) reduced catalysts

The reduction of the catalysts resulted in the formation of stronger acidic sites along with moderate acidic sites represented by the sharper peaks in the range of 315-380 °C and broader peaks in the range of 170-230 °C for all the reduced catalysts (Fig. 3.13b). However, the total amount of NH₃ adsorbed was decreased for the reduced catalysts except the Cu-Al Catalyst (Table S3.6, entries 5-8). The decrement in the acidity could be related to the occupation of Ni and Ni-Cu alloys on acidic sites[48]. The increase in the acidity for Cu-Al R catalyst could be to the plausible exposure of Al surface after the reduction and the spinal phase CuAl₂O₄ species.

Table 3. 6: NH₃-TPD studies of the prepared catalysts

Entry	Catalyst	Peak temperature (°C)	Amount of NH ₃ desorbed (mmol/g of catalyst)
1	Ni-Al C	198	2.15
2	Ni1Cu1-Al1 C	180	1.88
3	Ni2Cu2-Al1 C	183	0.63
4	Cu-Al C	194	0.11
5	Ni-Al R	180	0.61
		325	0.33
6	Ni1Cu1-Al1 R	180	0.76
		315	0.11
7	Ni2Cu2-Al1 R	170	0.4
		366	0.11
8	Cu-Al R	190	0.37
		377	0.11

3.3.7 XPS analysis

In-situ XPS analysis was conducted to investigate the chemical state and the surface composition of the corresponding elements present on the surface of the catalysts. The results are shown in Fig.3.14 (a-d). Fig. 3.14a shows the Ni2p spectra of the calcined catalysts. Two sharp peaks were observed at a binding energy of 855.94 eV and 873.44

eV, along with the shakeup peaks assigned to Ni 2p_{3/2} and Ni 2p_{1/2} surface states, respectively. These were attributed to the presence of Ni²⁺ species of NiO state on the catalyst surface. The peak shifts, surface metal oxide content, and the surface NiO/CuO ratio details are mentioned in Table 3.7. For the bimetallic catalysts, the electron energy corresponding to Ni 2p_{3/2} and Ni 2p_{1/2} surface states slightly moved towards the lower values caused by the strong electronic effect between Ni and Cu metal oxides. For the catalyst Ni₂Cu₂-Al₁ C, the shift was more than Ni₁Cu₁-Al₁ C because of more CuO and Cu₂O content on the Al surface, which caused the transfer of more electrons from Cu to Ni species.

Fig. 3.14c shows the XPS spectra of the reduced catalysts. The reduction of the catalysts resulted in broadened peaks due to the formation of Ni²⁺ and Ni⁰ species of metallic Ni. The peaks at the binding energies of 873.44 eV and 856.4 eV correspond to the Ni²⁺ species of Ni 2p_{1/2} and Ni 2p_{3/2} states, respectively. While the emerged peaks after the reduction at the binding energies of 870.17 eV and 852.4 eV represent the formation of Ni⁰ species on the catalyst surface. The low amount of the Ni⁰ species was inferred from the low calcination temperature (500 °C). Further increase in the calcination temperature could enhance the formation of metallic Ni⁰ species. The peak shifts, surface metal content, and the surface Ni/Cu ratio are mentioned in Table 3.8. The peak shifts of Ni²⁺ and Ni⁰ are moved towards lower binding energies for the bimetallic catalysts mainly due to the formation of Ni-Cu alloys, and Ni-Cu clusters can be seen by STEM-EDS images. Furthermore, Miao et al. reported the shakeup peak at 880.5 eV, which signifies the strong interaction between Ni²⁺ species and Al, demonstrating the XRD results indicating the formation of spinel NiAl₂O₄ species[33]. From the H₂-TPR study, the reduction of the monometallic Ni catalyst happened above 500 °C. However, the reducible NiO species were reduced to Ni²⁺ and Ni⁰ for the bimetallic catalysts at 500 °C. Combining with the TPR results, the presence of low-temperature reducible Cu species improved the reducibility of NiO species which can also cause the decrease in electronic energy of Ni²⁺ and Ni⁰ peaks of Ni2p spectra.

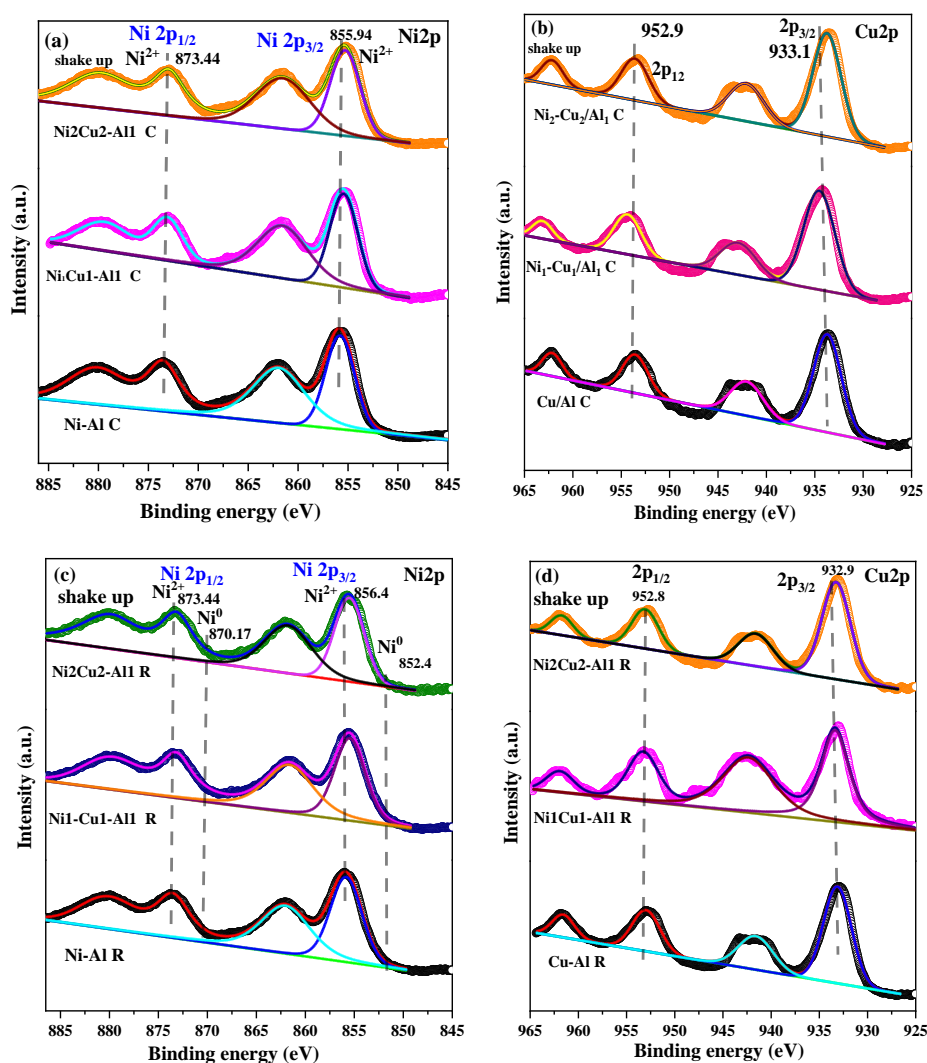


Fig.3. 14: XPS spectra of a) Ni2p of calcined catalysts, b) Cu2p of calcined catalysts, c) Ni2p of reduced catalysts, d) Cu2p of reduced catalysts

Fig. 3.14b shows the Cu2p XPS spectra of calcined catalysts. The sharp peaks at binding energies of 933.1 eV and 952.9 eV represent the Cu 2p_{3/2} and Cu 2p_{1/2} oxidation states of cu²⁺ species in the calcined catalysts. The spin-orbital splitting binding energy ($\Delta E = BE_{Cu\ 2p_{1/2}} - BE_{Cu\ 2p_{3/2}}$) values of the calcined samples are 20.05 eV (Cu-Al C), 19.87 eV (Ni1Cu1-Al1 C), and 19.97 eV (Ni2Cu2-Al1 C), respectively. The spin-orbital splitting binding energy values of Cu-Al C and Ni2Cu2-Al1 C are very close, representing the similar dispersion of surface-active species as evidenced by STEM-EDS results. The binding energies of Cu 2p_{3/2} XPS peak for Cu₂O and CuO species are 932.5 ± 0.4 and 933.6 ± 0.4 , respectively[43]. As described in the TPR study, the reducibility of CuO and

Cu₂O species could be reduced entirely below 300 °C in an ideal condition. In comparison, the reduction of spinel CuAl₂O₄ species occurs at a reduction temperature of more than 450 °C.

Fig. 14d shows the Cu 2p spectra of reduced samples. As the reduction of the samples was performed at 500 °C, the XPS peaks of Cu 2p_{3/2} and Cu 2p_{1/2} at the binding energies of 932.9 eV and 952.8 eV, respectively, are belonged to metallic Cu⁰ species. The broadened peaks resulted from the reduction of both CuO and Cu₂O species. The shakeup peak represents the strong interaction between Cu and Al in the CuAl₂O₄ spinel species. The spin-orbital splitting binding energy ($\Delta E = BE_{Cu\ 2p_{1/2}} - BE_{Cu\ 2p_{3/2}}$) values of the reduced catalysts are 19.95 (Cu-Al R), 19.77 (Ni1Cu1-Al1 R), and 19.92 (Ni2Cu2-Al1 R), respectively. For the bimetallic catalysts, the slight shift in the peak towards lower binding energy could be caused by the presence of Ni-Cu alloy species which enhances the electronic effect between metallic Ni and Cu species. During the reduction process, because of the presence of Cu metals, the reduction temperature of NiO species comes down significantly, as depicted in the TPR study, thus creating the metallic Ni⁰ and Cu⁰ species on the Al surface. Metallic Ni possesses more d band holes than Cu, which creates a more substantial electronic effect between Ni and Cu alloy species by allowing the transfer of d electrons of Cu⁰ to occupy the vacant d band holes of Ni⁰. Thus, this phenomenon explains the shift of the XPS peak of Cu⁰ towards the lower binding energy.

Table 3.7: Elemental composition of calcined samples from XPS analysis

Catalyst	Ni2p (BE)		Cu2p(BE)		NiO (%)	(CuO+Cu ₂ O) (%)	Surface NiO/(CuO+Cu ₂ O) ratio (XPS)
	Ni2p _{3/2}	Ni2p _{1/2}	Cu2p _{3/2}	Cu2p _{1/2}			
Ni-Al C	855.94	873.44	-	-	17.6	-	-
Cu-Al C	-	-	933.1	952.9	-	5.52	-
Ni1Cu1-Al1 C	855.84	873.34	933.94	953.92	9.09	8.79	1.034
Ni2Cu2-Al1 C	855.05	873.12	933.55	953.45	6.22	6.58	0.9452

Table 3.7 shows the atomic surface composition of the calcined catalysts determined by the XPS analysis. Ni-Al C catalyst showed 17.6 % of NiO surface content derived from the wide dispersion of NiO species on the Al surface. In contrast, for the Cu-Al C catalyst, the surface CuO and Cu₂O content was only 5.5%, mainly due to the spinel CuAl₂O₄ species formation, which resulted in surface coverage with subpar pore structure. Meanwhile, more amounts of NiO and CuO are dispersed on the Ni₁Cu₁-Al₁ C catalyst than Ni₂Cu₂-Al₁ C because of the more Al content. However, the surface NiO/(CuO+Cu₂O) ratio remained intact at one before reduction for both the catalysts. The peak shift for Ni2p and Cu2p spectra happened towards lower binding energies.

Table 3.8 displays the atomic surface composition of the reduced catalysts determined by the XPS analysis. Ni-Al R catalyst showed 12.78 % surface Ni content after reduction out of 17.6% NiO species on Al surface, whereas only 4.79 % of Cu content was observed for Cu-Al R catalyst. After the reduction, the surface ratio of Ni/Cu for Ni₁Cu₁-Al₁ R catalyst resulted in 0.979 because of the more Al content, which accommodated the fine dispersion of both Ni and Cu metal species along with Ni-Cu alloy species. On the other hand, after the reduction, For Ni-Cu-Al 221 R catalyst, the surface Ni/Cu ratio was dropped to 0.571 because of the lack of Al content. Cu metal species dominantly occupied more Al surface than Ni, resulting in Ni-Cu cluster species with more Cu content. The peaks shift for both Ni2p and Cu2p spectra happened towards lower binding energies. The surface metal content determined the shift length.

Table 3.8: Elemental composition of reduced samples from XPS analysis

Catalyst	Ni2p (BE)		Cu2p(BE)		Ni%	Cu %	Surface Ni/Cu ratio (XPS)
	Ni2p _{3/2}	Ni2p _{1/2}	Cu2p _{3/2}	Cu2p _{1/2}			
	2	2	2				
Ni-Al R	856.4	873.44	-	-	12.78	-	-
Cu-Al R	-	-	932.9	9552.8	-	4.79	-
Ni ₁ Cu ₁ -Al ₁ R	854.83	872.33	932.83	952.33	5.84	5.96	0.979

Ni ₂ Cu ₂ -	853.71	871.51	931.71	951.21	4.12	7.21	0.571
Al ₁ R							

3.4 Results and discussion on hydrogenation of furfural

3.4.1 Catalytic performances

The catalytic efficiency of the prepared catalysts and the optimization of Ni, Cu, and Al to obtain a maximum yield of THFA are reported in Table 3.9. A blank test and a reaction with as-synthesized Al₂O₃ provided only 11 mol% and 12 mol% furfural conversion, respectively, indicating the catalytic transfer hydrogenation by 2-butanol and no activity derived from the Al₂O₃ support. A blank test was conducted with 2-butanol as solvent. The transfer catalytic hydrogenation took place, which showed around 11 % of furfural conversion to furfuryl alcohol and a similar result with pure as-synthesized Al₂O₃ indicating no activity with the support (Table 3.9, entries 1&2). The calcined catalysts showed the formation of only FAL, indicating that NiO or CuO species are active in the hydrogenation of the carbonyl group of the furfural molecule. Interestingly, monometallic catalysts have not shown the formation of THFA (Table 3.9, entries 2&4), illustrating that NiO species are not active for ring hydrogenation of furfural. However, in the case of bi-metallic calcined catalysts, complete conversion of furfural was observed with the formation of THFA (Table 3.9, entries 7&9), indicating the combination of both NiO and CuO active species could convert furfural completely. Additionally, the formation of THFA signifies the catalytic activity that could be drawn by developing Ni-Cu alloy, which could be active for the ring hydrogenation.

Table 3.9: Reaction studies with calcined and reduced catalysts

Entry	Catalyst	Furfural conversion (mol%)	FAL yield (mol%)	THFA yield (mol%)
1	-	11	9	0
2	Al ₂ O ₃	12	8.7	0

3	Ni-Al C	43.31	40.1	0
4	Ni-Al R	87.2	50.66	35.46
5	Cu-Al C	58	54.9	0
6	Cu-Al R	100	100	0
7	Ni1Cu1-Al1 C	100	82	16.84
8	Ni1Cu1-Al1 R	100	29.39	67.87
9	Ni2Cu2-Al1 C	100	85	11
10	Ni2Cu2-Al1 R	100	60	39.1
11	Ni1Cu1-Al2 R	100	56.4	40.3

Reaction conditions: 5 mmol furfural, 30 ml 2-butanol, catalyst 100 mg, 140 °C, 20 bar H₂, 4 h.

Fig. 10a presents the catalytic activity of the reduced monometallic and bimetallic catalysts for the hydrogenation of furfural in 2-butanol. After that, mono-metallic (Ni-Al and Cu/Al) catalysts were tested for the hydrogenation of furfural. It was observed that the Ni-Al R catalyst was active for the hydrogenation of both C=O and C=C of furfural, while the Cu-Al R catalyst was highly active for only C=O in furfural. Mono metallic Ni-Al R catalyst showed a maximum of 87% conversion of furfural which distributed in 50 mol% yield for FAL and 35 mol% for THFA. This might be attributed to the presence of both NiO and Ni active species as evidenced in TPR studies which were widely dispersed on the Al surface. However, the subsequent hydrogenation of formed FAL was not completely converted to THFA. The presence of furfural in the reaction indicated all three components well occupied the active sites in the reaction, which led to the incomplete conversion of furfural. Notably, the monometallic Cu-Al R catalyst resulted in a 100% yield of FAL with complete conversion, which revealed that the Cu could selectively hydrogenate C=O in furfural [18][25].

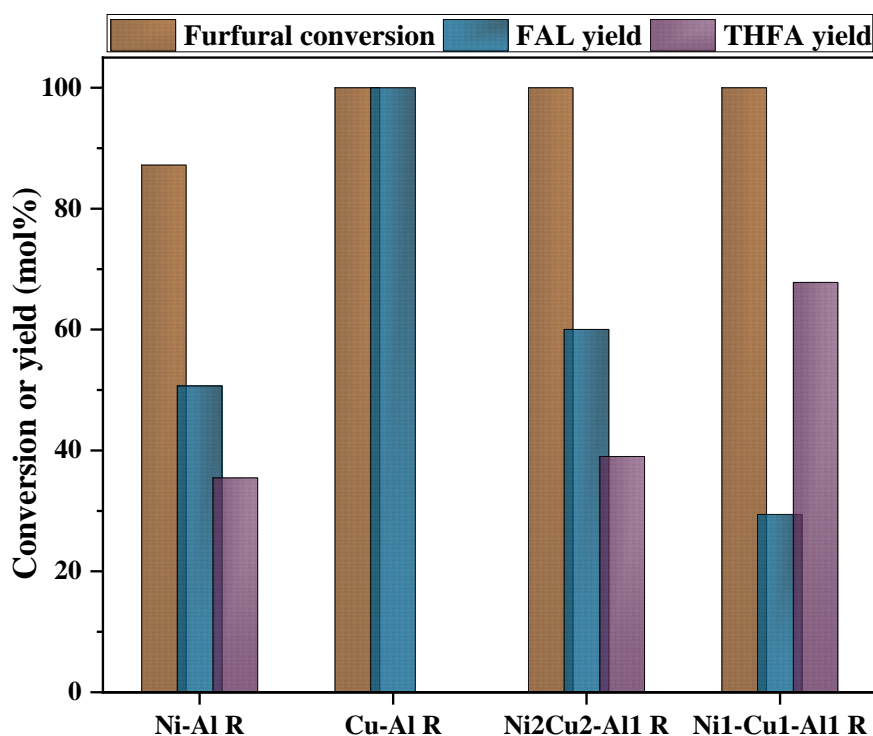


Fig.3.15: Catalytic performances of the reduced catalysts

Reaction conditions: 5 mmol furfural, 30 ml 2-butanol, catalyst 100 mg, 140 °C, 20 bar H₂, 4 h

BET and XRD studies revealed that Ni-Al R and Cu-Al R catalysts have contrasting textural properties. However, the dominant factor in the hydrogenation of the C=O bond turned out to be the metal component. In addition, Cu metal was inactive for the C=C bond of furfural since the interaction between Cu and C=C is very weak, whereas Ni has a dominant activity for C=C in furfural because of the strong surface interaction with the furan ring, which is in good agreement with the study by Sittisha et al. [14] and Jun wu et al. [25]. Interestingly, a recent study by Sanchez et al. reported Cu active sites showed higher conversion and selectivity to THFA than Ni active sites attributing to the structural and higher amounts of metallic Cu phase [49]. From the results of monometallic catalysts, it can be seen that the generation of THFA progressed through the formation of FAL for the Ni-Al R catalyst, whereas for the Cu-Al R catalyst, only FAL was formed. Fig.3.16 represents the conversion path for furfural hydrogenation using monometallic and bimetallic Ni-Cu-Al catalysts reported in this study.

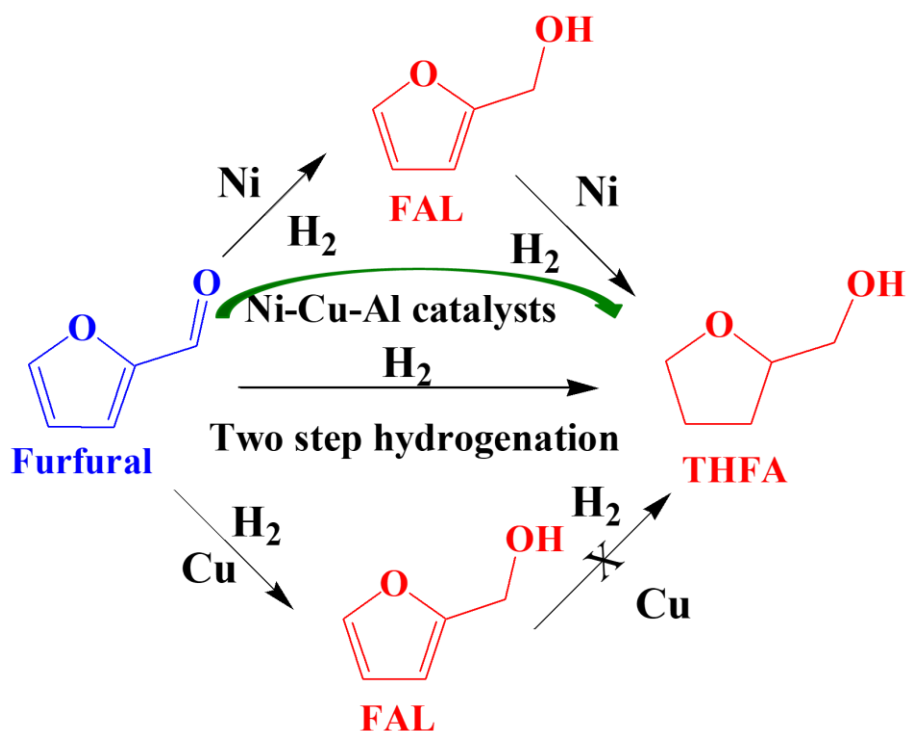


Fig.3.16: Furfural conversion pathway for monometallic and bimetallic catalysts in 2-butanol

The bimetallic catalysts showed the complete conversion of furfural. However, they displayed the different THFA yields through a two-step hydrogenation process. For the Ni₂Cu₂-Al₁ R catalyst, equal moles (2 moles) of Ni and Cu were dispersed on one mole of Al to provide a high number of Ni and Cu active sites to accommodate the formation of FAL at higher conversion rates which can be further hydrogenated to THFA. However, the textural and surface properties of this catalyst were developed as close to Cu-Al R catalysts caused by the dominance Cu component, resulting in more surface Cu active sites than Ni. As a result of Cu dominance in the Ni₂Cu₂-Al₁ R catalyst, only around 39 mol% of THFA was observed after 4 hours of the reaction. On the other hand, providing more Al content in equal amounts with the metals for the catalyst Ni₁Cu₁-Al₁ R showed the THFA yield of 67.8 mol%. In addition, this catalyst observed a well-developed pore structure and surface properties similar to the Ni-Al R catalyst. The more amount of Al provided the required space for developing individual Ni and Cu active species and Ni-Cu alloy species on the surface.

In addition, the increased dispersion of metals has promoted hydrogen activation and adsorption ability. The geometry of Ni-Cu sites and the close dispersion of active sites, as observed in STEM-EDS analysis, can enhance the adsorption configuration and strength of the reaction intermediate species such as FAL. The proportional presence of the required active species in the form of Ni, Cu, NiO, and Ni-Cu alloys which were active for the furan ring and the carbonyl group, produced more THFA. Fig.3.17 shows the plausible reaction mechanism of THFA formation through FAL intermediate by hydrogenation of furfural on the active sites of Ni1Cu1-Al1 R catalyst. Zhang et al. [50] and Kumar et al.[51] have illustrated the formation of THFA through FAL on active metallic sites. The hydrogenation of the carbonyl group of furfural molecule can be possible on all-active species of Ni1Cu1-Al1 R catalyst to form FAL. The subsequent hydrogenation of formed FAL could occur on either Ni or Ni-Cu alloy active sites by parallel hydrogenation of furan ring by adsorbed hydrogen to form THFA.

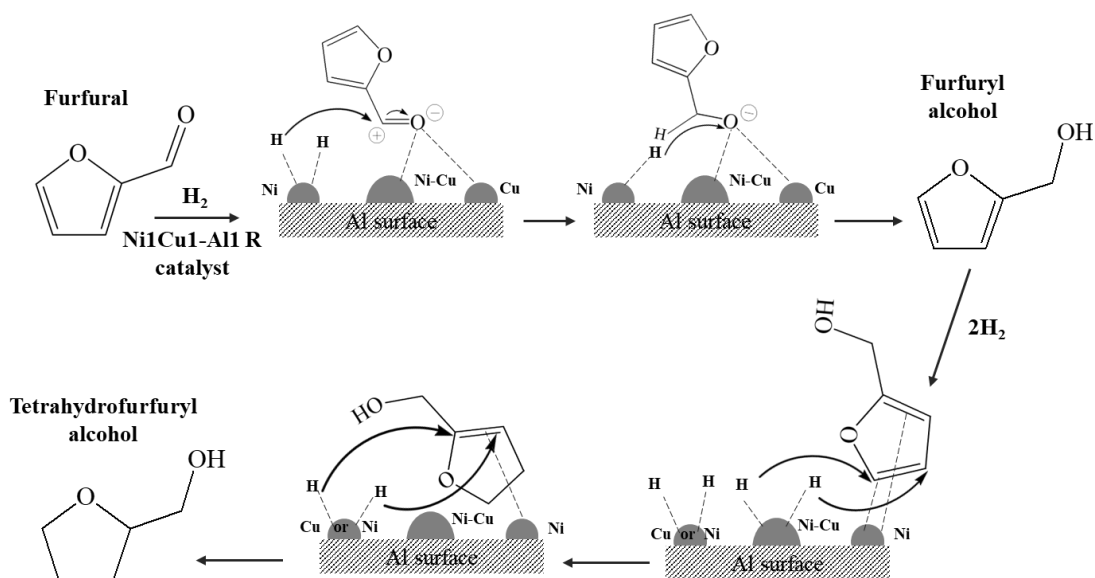
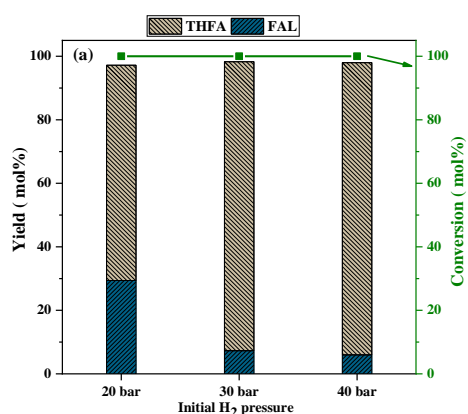


Fig.3.17: Plausible reaction mechanism of hydrogenation of furfural over Ni1Cu1-Al1 R catalyst

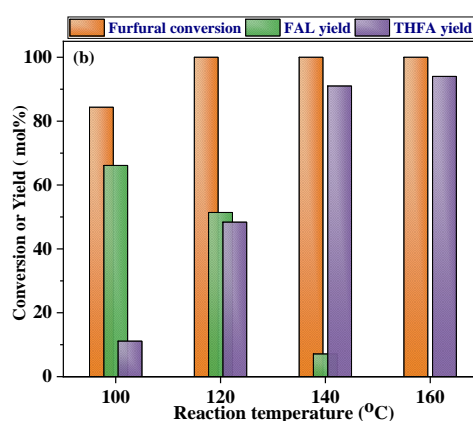
3.4.2 Optimization of reaction parameters

After achieving a maximum possible yield of THFA through the tested catalysts, the reaction parameters such as reaction pressure, reaction temperature, and reaction time

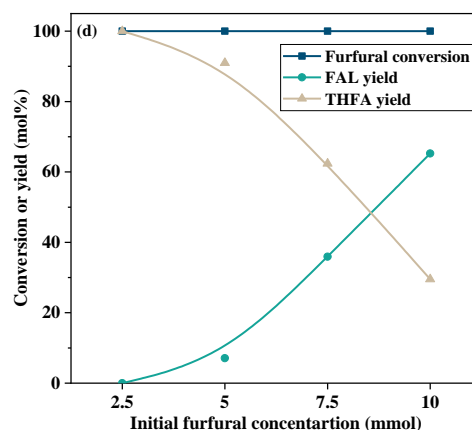
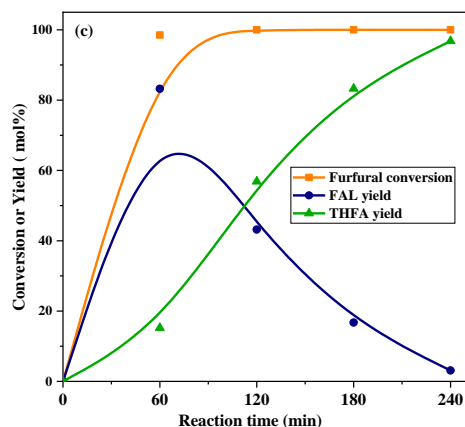
were studied under controlled experiments using the Ni1Cu1-Al1 R catalyst 3.18a shows the influence of initial H₂ pressure on THFA yield. The reaction pressure has a significant influence on the THFA yield. The yield of THFA has increased sharply from 67.8 mol% to 92 mol%, with an increase in reaction pressure from 20 bar to 30 bar. The increase in the pressure promoted hydrogen diffusion into the liquid phase and enhanced the adsorption capacity on active catalytic sites. Carsten et al. explained the competitive adsorption of substrates and the hydrogen molecules on the catalyst active sites by increasing the reaction pressure[52]. Moreover, Tike et al.[53] and Chen et al.[54] have reported that the high hydrogen pressure promoted the FAL hydrogenation to produce THFA. However, a further increase in the H₂ pressure to 40 bar resulted in 94 mol% of THFA yield, indicating that the diffusional limitations of H₂ into the liquid phase are reached.



Reaction conditions: 5 mmol furfural, 30 ml 2-butanol, Ni1Cu1-Al1 R = 100 mg, 140 °C, 4 h



Reaction conditions: 5 mmol furfural, 30 ml 2-butanol, Ni1Cu1-Al1 R = 100 mg, 30 bar H₂, 4 h.



Reaction conditions: 5 mmol furfural, 30 ml 2-butanol, Ni1Cu1-Al1 R = 100 mg, 30 bar H₂, 140 °C

Reaction conditions: 30 ml 2-butanol, Ni1Cu1-Al1 R = 100 mg, 30 bar H₂, 4 h 140 °C, 4 h

Fig.3.18: Influence of reaction parameters on hydrogenation of furfural

a) Initial H₂ pressure, b) Effect of temperature, c) Reaction time, d) Effect of initial furfural concentration

Fig.3.18b displays the effect of reaction temperature on furfural using Ni1Cu1-Al1 R catalyst at 30 bar reaction pressure after 4 hours of the reaction. The reaction temperature is important for choosing an end product for furfural hydrogenation. At high temperatures (>230°C), the furfural undergoes a decarbonylation reaction to produce tetrahydrofuran using noble-metal-based catalysts (Pt, Pd, and Ru)[52]. In contrast, under mild reaction conditions (150-200 °C), transition metal-based catalysts like Cu, Ni, and Co promote the furfural hydrogenation to produce FAL, THFA, and pentanediols[25]. To avoid the formation of pentanediols and decarbonylation products, the reaction temperature was tested in the range of 100-160 °C to observe the temperature effect on THFA yield using our bimetallic Ni1Cu1-Al1 R catalyst. At 100 °C reaction temperature, the complete conversion of furfural has not occurred but increasing to 120 °C showed the complete conversion with similar yields of THFA and FAL. The increase in reaction temperature from 100 °C to 140 °C resulted in a sharp increase in the THFA yield from 11 % to 92 mol%. The yield of FAL followed the opposite trend. The increase in reaction temperature promotes the activation energy of the substrate molecules to get adsorbed on the active sites of the catalysts and also promotes the desorption of product molecules from the catalyst surface. However, further increase in the reaction temperature resulted

in 94 mol% of THFA yield with no amount of FAL left in the reaction system. This phenomenon indicating that FAL was completely transformed to THFA and the formed THFA started to transform into the 1,2-pentanediol and 1,5-pentanediol which caused the THFA yield limited to 94 mol%. Similar observation was reported by Wu et al. at a reaction temperature of 170 °C[14]. This catalytic system showed that a minimum of 140 °C reaction temperature is sufficient for producing more than 90 mol% yield of THFA after 4 hours of the reaction.

Fig.3.18c presents the time profile of the furfural conversion and yield of the hydrogenation products FAL and THFA at the specified reaction conditions during a reaction time of 4 hours. As it can be seen, the volcano trend was observed for FAL yield, while the steep increasing trend of THFA yield specifies that THFA was formed through FAL. The complete conversion of furfural was achieved after 2 hours of the reaction, and further reaction time was needed to obtain THFA from FAL. The TOF study (Table 5) reported that the formation of FAL from furfural is faster than the formation of THFA from FAL, which signifies the later step to be the rate-determining step that involves the hydrogenation of the rigid furan ring of furfural. A minimum reaction time of 4 hours provided more than 90 mol% of THFA yield for this catalytic system.

The influence of the initial furfural amount was also studied, and the results are reported in Fig.3.18d. The increase in the initial furfural amount showed two distinct trends: increasing in yield of FAL and decreasing in yield of THFA. This phenomenon implies that, within a controlled reaction time, the catalytically active sites were occupied by both furfural and FAL, which are undergoing the hydrogenation of the carbonyl group and furan ring of the furfural molecule.

3.4.3 Turnover frequency (TOF) study

After the reaction parameter optimization, the turnover frequency (TOF) study was conducted to understand the hydrogenation capacity of the reduced catalysts towards the carbonyl group and the furan ring. Table 3.10 presents the TOF values of the hydrogenation of C=O and C=C of furfural, respectively. In order to determine the TOF values of the catalysts, the hydrogenation of furfural and FAL were conducted separately under similar conditions for 0.5h. Jun Wu et al. followed a similar procedure to determine

the TOF values of the catalysts reported in the study [14]. The results show that the $TOF_{C=O}$ is higher than $TOF_{C=C}$, signifying that the formation of THFA from FAL may be the rate-determining step compared to FAL formation from furfural. It is apparent that the formation of FAL from furfural involves the hydrogenation of the outer carbonyl group of furfural, while the formation of THFA involves the hydrogenation of a rigid furan ring whose interaction strength varies with the metal provided[25]. Significantly, the $TOF_{C=O}$ of Cu-Al R (Table 3.10, entry 2) catalyst is higher than Ni-Al R (Table 3.10, entry 1) and is close to that of bimetallic catalysts (Table 5, entry 3-4) attributed to its strong interaction with C=O bond of furfural. Notably, the synergetic effect generated by forming Ni-Cu alloys for the bimetallic catalysts showed more $TOF_{C=O}$ than monometallic catalysts. However, for the Ni₂Cu₂-Al₁ R catalyst, the $TOF_{C=C}$ was lower than that of the Ni-Al R catalyst caused by the more surface Cu content, evidenced in XPS analysis (Surface Ni/Cu ratio 0.57). For the Ni₁Cu₁-Al₁ R catalyst, both $TOF_{C=O}$ and $TOF_{C=C}$ are higher than the monometallic counterparts, showing the maximum yield of THFA. XPS results showed that the surface Ni/Cu ratio for the catalyst Ni₁Cu₁-Al₁ R is 0.98 indicating the near equal amounts of Ni and Cu were present on the Al surface in different alloy and mono metallic forms which were active to produce higher amount of THFA. Clearly, the correlation between THFA yield and the catalytic activity was well followed the corroboration of catalyst characterization data and the reaction data.

Table 3.10: TOF values of hydrogenation of furfural for the reduced catalysts in 2-butanol

Entry	Catalyst	$TOF_{C=O}$ (h^{-1}) ^a	$TOF_{C=C}$ (h^{-1}) ^b
1	Ni-Al R	14.25	11.9
2	Cu-Al R	20.23	0
3	Ni ₁ Cu ₁ -Al ₁ R	23.09	15.65
4	Ni ₂ Cu ₂ -Al ₁ R	20.85	9.9

Reaction conditions: ^a 5 mmol furfural, 30 ml 2-butanol, catalyst 100 mg, 140 °C, 30 bar H₂, 0.5 h, ^b 5 mmol FAL. TOF is the mole of FAL or THFA formed per metal site per hour. The number of metal site data was obtained by the chemisorption studies[46].

3.4.4 Influence of the solvent

Solvents play an essential role in a heterogeneous catalytic system and can significantly affect product selectivity and catalytic activity for many reasons. Herein, we report the solvents tested in this study using our Ni1Cu1-Al1 R catalyst at optimized reaction conditions, and the results are summarized in Table 3.11. Notably, a change in the yield of THFA and FAL was observed with various solvents, especially in the case of n-butanol, where only 35.2 mol% of THFA yield (Table 3.11, entry 4) was observed compared to only 91.7 mol% in 2-butanol. In addition, the hydrogen donor capability of 2-butanol enhanced the formation of more THFA by promoting the ring hydrogenation of furfural compared to n-butanol, where n-butanol acted as a non-reactive solvent. Finally, 2-propanol, a suitable hydrogen donor solvent in catalytic transfer hydrogenation reactions, produced only 52 mol% of THFA with more than 45 mol% of FAL still to be converted. The slight dehydration and strong adsorption of 2-propanol on active sites of the bimetallic catalyst, which suppressed the furan ring hydrogenation, resulted in a low yield of THFA. In the case of ethanol, no dehydration of products was observed and showed a similar effect as n-butanol, which was in agreement with the literature [60][61]. The insistent adsorption between the substrate molecules and solvents on the available catalytically active sites influenced the selectivity of the products and influenced the furan ring hydrogenation. Solvent selection controlled the targeted product yield in upgrading the biomass-derived platform chemical.

Table 3.11: The product distribution of furfural hydrogenation with different solvents

Entry	Solvent	Furfural conversion (mol%)	FAL yield (mol%)	THFA Yield (mol%)
1	2-butanol	100	7.1	91.7
2	2-Propanol	100	45.48	52.32
3	Ethanol	100	53.6	40.12
4	n-butanol	100	60.21	35.2

Reaction conditions: 5 mmol furfural, 30 ml solvent, catalyst Ni1Cu1-Al1 R, 100 mg, 140 °C, 20 bar H₂, 4 h.

3.2.2 Catalyst loading and reusability analysis

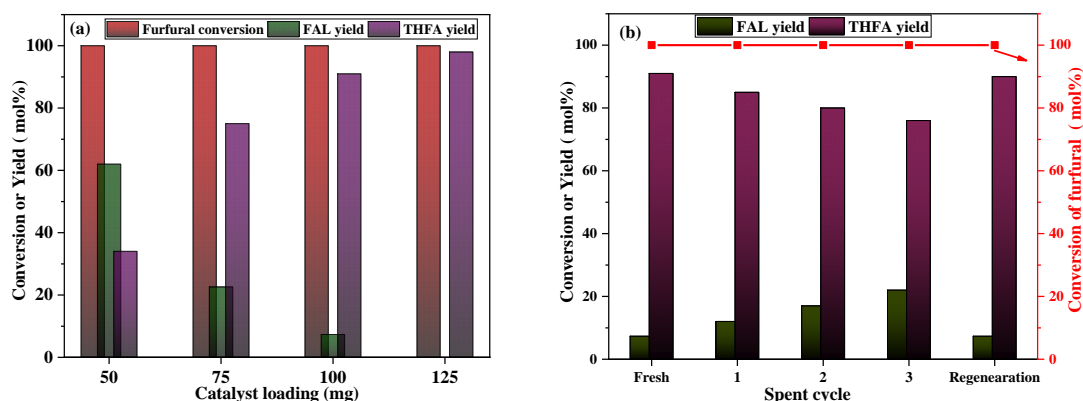


Fig.3.19: Study of a) Catalyst loading, b) reusability analysis

Reaction conditions: 5 mmol furfural, 30 ml 2-butanol, Ni1Cu1-Al1 R, 30 bar H₂, 4 h 140 °C

Fig.3.19a shows the effect of catalyst amount on THFA yield. Though the complete conversion of furfural was achieved with 50 mg, more than 60 mol% of FAL yield with only 35 mol% of THFA was formed, indicating the insufficient active sites that can accommodate the furan ring hydrogenation. Increasing the amount of catalyst to 75 mg sharply increased the THFA yield to 75 mol%. Further increasing the amount to 100 mg resulted in more than 90 mol% of THFA yield signifying the minimum amount of catalyst needed for obtaining higher yields of THFA. Providing more amounts of catalyst resulted in 98 mol% of THFA yield.

Interestingly, the availability of more active sites has not promoted any other side reactions or solvent dehydration reactions, indicating that our catalyst was highly selective towards THFA. Fig.3.19b displays the reusability and regeneration activity of the Ni1Cu1-Al1 R catalyst. After the reaction with a fresh catalyst, the reaction mixture was centrifuged, washed with the solvent, and allowed for drying at room temperature, which could be readily used for the subsequent cyclic reactions. The complete conversion

of furfural was observed for the three cycles of reusability with a gradual decrease in the hydrogenation ability of the catalyst.

3.5 Spent analysis

Systematic characterization techniques were employed to analyse the spent catalyst after three cycles of reuse to understand the reduction in the activity. First, the TGA technique addresses the plausible carbon deposition and weight loss during a linear thermal treatment. Next, BET and XRD analysis to determine the structural changes after the reuse. After that, SEM and STEM-EDS analysis to observe the surface leaching phenomena and the metal composition of the catalysts. Finally, XPS analysis was performed to determine the surface Ni/Cu composition and to assist the STEM-EDS analysis.

3.5.1 TGA analysis

TGA results showed the weight loss of the sample of about 6 Wt.% in the range of 100 °C-400 °C, indicating the possible decomposition of the deposited reaction organic carbons, which hinders the catalytic activity (Fig.3.20). Additionally, the STEM-EDS map sum spectrum showed an increased carbon peak supporting the carbon deposits after a reaction (Fig.3.23).

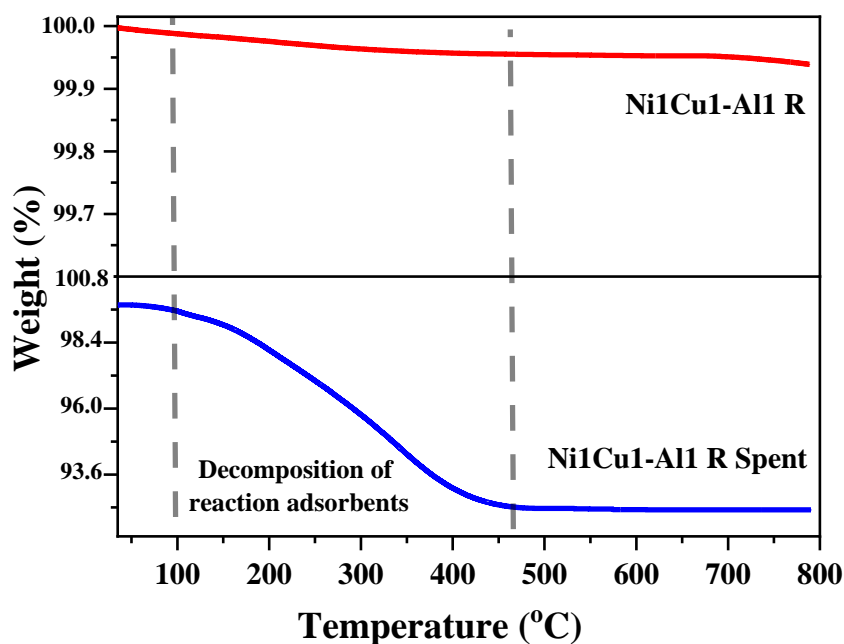


Fig.3.20: TGA analysis of the fresh and spent catalyst

3.5.2 Textural properties

The spent catalyst was pre-treated only a 100 °C under vacuum conditions not to remove the surface adsorbents during the reaction. Fig.3.21a shows the N₂ adsorption isotherms, which indicate the shift in the isotherm of the spent catalyst to the lower relative pressure. The amount of N₂ adsorbed decreased slightly, indicating the obvious surface impurities deposited during the reaction. The BJH pore size distribution (Fig.3.21b) of the spent catalyst illustrates a decrease in the pore volume and depth. This could be due to the enlargement of the pores caused by the heat treatment during the three cycles of reuse. The carbon deposition is also the other reason for the slight changes in the textural properties as depicted in the TGA results about the weight loss due to the carbon deposition. Moreover, the XRD results provided that the crystal size increased after the use with slightly reduced peak intensities (Table 3.12). However, no significant changes were transpired during the three cycles of the reaction indicating the thermal strength of the catalysts.

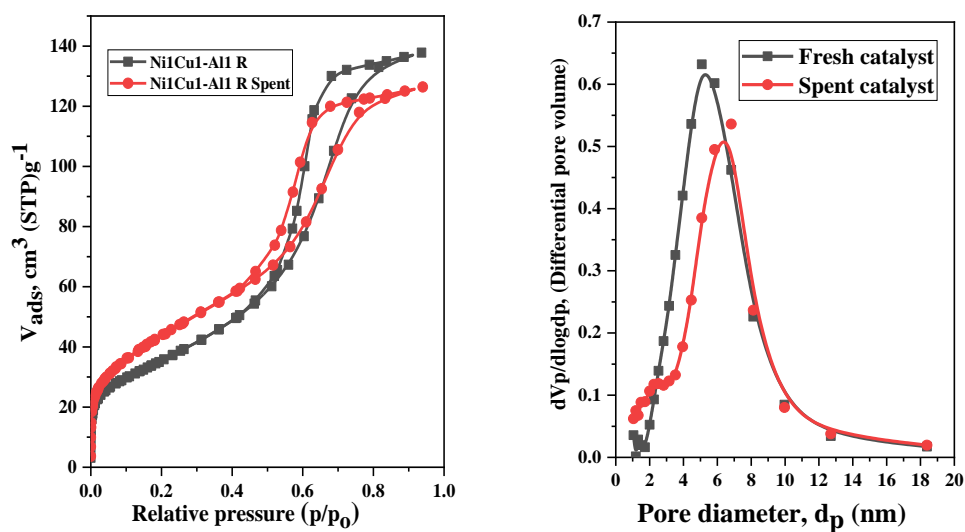


Fig.3.21: Textural properties a) N₂ adsorption isotherms, b) BJH pore size distribution

Table 3.12: Physical properties of the fresh and spent catalysts

Entry	Catalyst	BET Surface area (m ² /g)	Pore volume (cm ³ /g)	Pore diameter (nm) ^x	Lattice parameter, a (Å) ^y	Particle size (nm) ^z
1	Ni1Cu1-Al1 R	130.8	0.2132	6.52	3.6075	5.34
2	Ni1Cu1-Al1 R Spent	134.5	0.1955	7.26	3.6058	6.31

x: reported from BJH-PSD data, y: calculated from XRD analysis using Bragg's law, z: calculated using the Scherrer's equation.

3.5.3 SEM, STEM-EDS, and XPS analysis

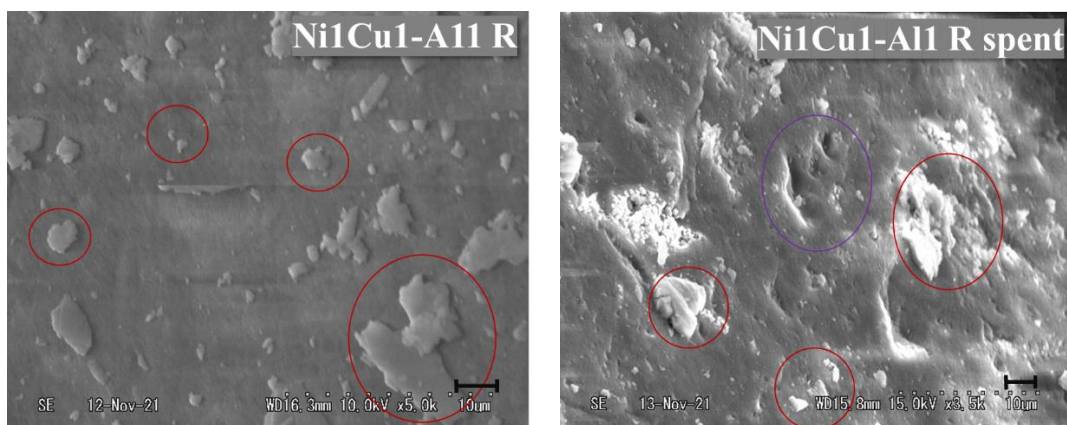


Fig.3.22: SEM images of the fresh and spent catalysts

The SEM images of the spent catalyst showed aggregation of metal particles and some vacant leached spots on the Al surface, as shown in Fig.3.22. This illustrates the leaching of the active metals during the reaction. Furthermore, the elemental composition by STEM-EDS (Fig.3.23d) of the spent catalyst revealed a decrease in surface Ni and Cu content, specifying slight leaching of surface Ni and Cu metals. To further confirm the surface metals composition, XPS analysis was performed (Fig.3.24). Fig.3.24a and 3.24b show the Ni2p and Cu2p spectra of the fresh and spent catalysts, respectively, to evaluate the surface metal content described in Table 3.13. The surface Ni/Cu ratio decreased for the spent catalyst from 0.979 to 0.892 compared to the fresh catalyst (Table 3.13, entries 1&2). As shown in the SEM images, slight leaching of active metal species happened during the reaction, which was corroborated by STEM-EDS and XPS analysis.

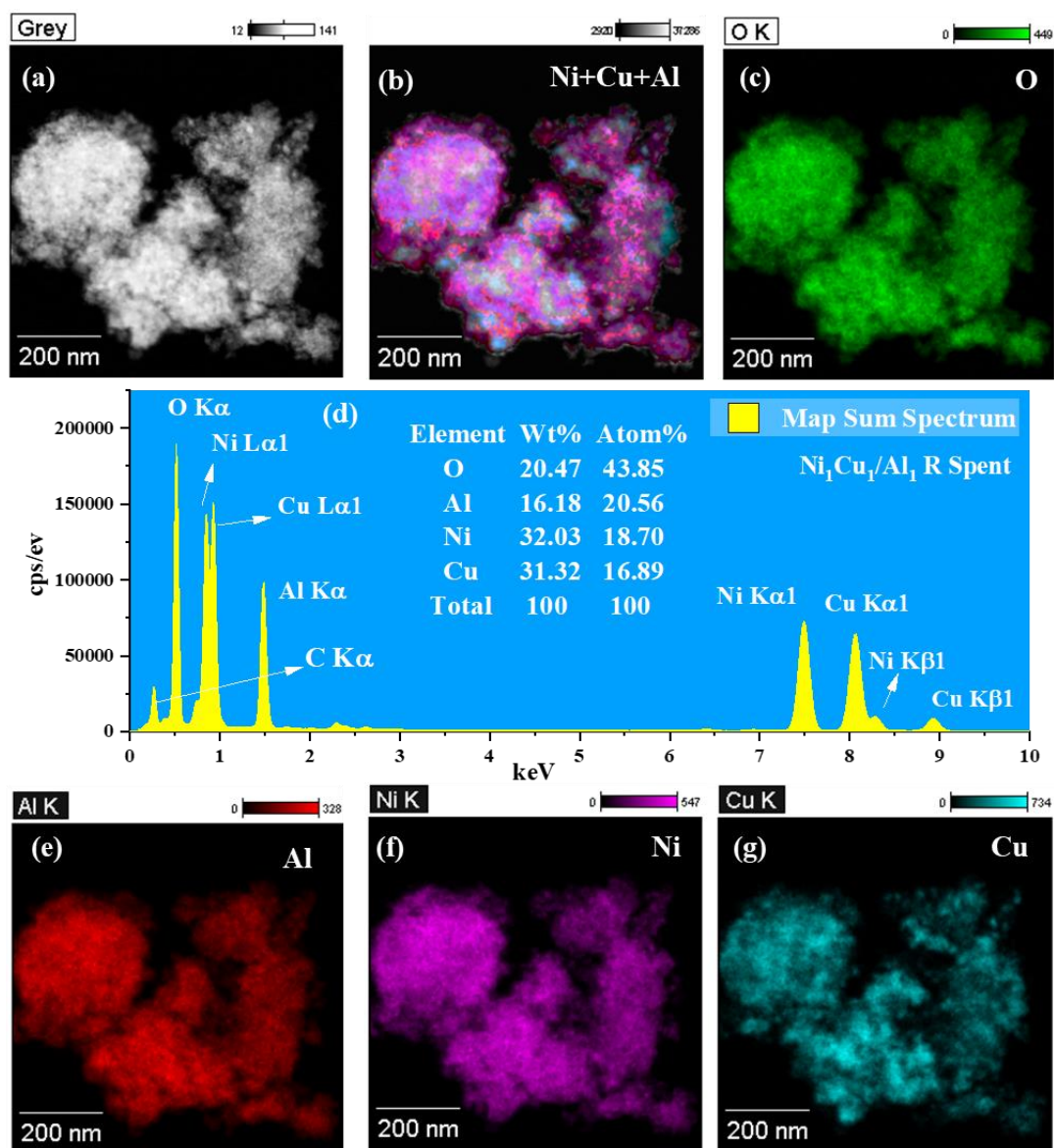


Fig.3.23: STEM-EDS mapping of the corresponding elements of the catalyst Ni₁Cu₁-Al₁ R Spent

(a) grey image selected for elemental mapping, (b) overlay image of Ni, Cu and Al elements showing the Ni-Cu alloys, (c) mapping of O, (d) map sum spectrum representing elemental composition, (e)~(g) individual element mapping of Al, Ni, and Cu, respectively.

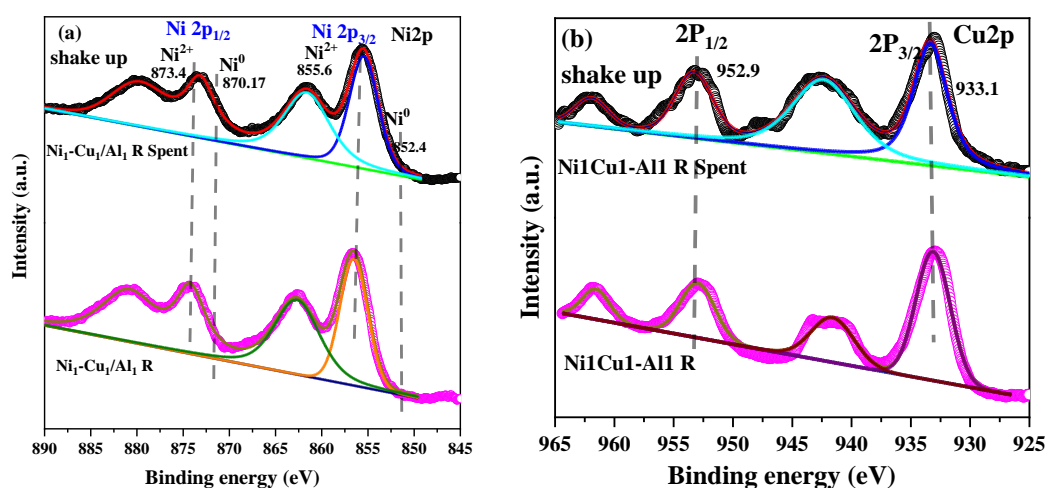


Fig.3.24: XPS analysis, a) Ni2p spectra and b) Cu2p spectra

Table 3.13: Elemental composition reduced samples from XPS analysis

Catalyst	Ni2p (BE)		Cu2p(BE)		Ni %	Cu %	Surface Ni/Cu ratio (XPS)
	Ni2p _{3/2}	Ni2p _{1/2}	Cu2p _{3/2}	Cu2p _{1/2}			
Ni ₁ Cu ₁ -Al ₁ R	854.83	872.33	932.83	952.33	5.84	5.96	0.979
Ni ₁ Cu ₁ -Al ₁ R Spent	855.94	872.84	933.41	953.32	4.83	5.41	0.892

In addition, a hot filtration test was conducted to understand the role of leached metals. After 1 hour of the reaction with the fresh catalyst under specified conditions, the reaction mixture was filtered to remove the catalyst. Then, the filtrate was reintroduced into the reactor to continue the reaction under identical conditions. No further conversion of furfural and FAL was observed, implying the leached active species could be removed as the catalytically active species. The spent catalyst, after three cycles, was regenerated at 500 °C in 5% H₂/N₂ gas which reproduced the result of a fresh catalyst indicating the regeneration and thermal stability of the catalyst.

3.6 Conclusions

In summary, the synthesized equimolar Ni₁Cu₁-Al₁ catalyst by coprecipitation method, which was calcined and reduced at 500 °C, developed stable Ni-Cu alloys on the Al surface with near equal Ni/Cu surface ratio. This bimetallic catalyst showcased an excellent physicochemical properties, which intensified the catalytic activity in producing high yields of THFA under mild conditions compared to the monometallic catalysts. In particular, the Al content in bi-metallic catalysts instigated a specific dispersion of Ni and Cu active species on the Al surface. Systematic characterization of the catalysts by XRD, STEM-EDS, TPR and XPS analysis inferred the successful synthesis of Ni-Cu alloys which have driven the high catalytic activity due to the synergetic effect caused by the electronic exchange energy between Ni and Cu metals. The hydrogenation of furfural with monometallic catalysts revealed that Ni had shown catalytic activity for both carbonyl and furan ring of the furfural while Cu was highly active for only the carbonyl group. The reaction pressure showed a substantial effect on THFA yield, which was attributed to increased adsorption capacity with increased pressure. In addition, the time profile study revealed that THFA has formed through FAL. Furthermore, the selectivity of THFA and FAL was changed by the solvent selection, and 2-butanol showed good solvent characteristics and functioned as a hydrogen donor solvent. The equimolar bimetallic catalyst could be used for several runs and has shown good regeneration and thermal stability. This efficient and versatile equimolar Ni₁Cu₁-Al₁ R catalyst provides clear insights into the direct hydrogenation of furfural to tetrahydrofurfuryl alcohol and the efficiency of non-noble bimetallic catalysts. In addition, comprehensive knowledge from this research will benefit in further hydrogenation applicability to other transformative reactions and efficient processes for industrial applications.

3.7 References

- [1] K. Yan, G. Wu, T. Lafleur, C. Jarvis, Production, properties and catalytic hydrogenation of furfural to fuel additives and value-added chemicals, *Renew. Sustain. Energy Rev.* 38 (2014) 663–676. <https://doi.org/10.1016/j.rser.2014.07.003>.
- [2] Y. Wang, D. Zhao, D. Rodríguez-Padrón, C. Len, Recent advances in catalytic hydrogenation of furfural, *Catalysts.* 9 (2019). <https://doi.org/10.3390/catal9100796>.
- [3] L. Zhang, T.U. Rao, J. Wang, D. Ren, A review of thermal catalytic and electrochemical hydrogenation approaches for converting biomass-derived compounds to high-value chemicals and fuels, *Fuel Process. Technol.* 226 (2022) 107097. <https://doi.org/10.1016/j.fuproc.2021.107097>.
- [4] L.J. Jönsson, C. Martín, Pretreatment of lignocellulose: Formation of inhibitory by-products and strategies for minimizing their effects, *Bioresour. Technol.* 199 (2016) 103–112. <https://doi.org/10.1016/j.biortech.2015.10.009>.
- [5] X.H. Chadderdon, D.J. Chadderdon, J.E. Matthiesen, Y. Qiu, J.M. Carraher, J.P. Tessonnier, W. Li, Mechanisms of Furfural Reduction on Metal Electrodes: Distinguishing Pathways for Selective Hydrogenation of Bioderived Oxygenates, *J. Am. Chem. Soc.* 139 (2017) 14120–14128. <https://doi.org/10.1021/jacs.7b06331>.
- [6] R. Mariscal, P. Maireles-Torres, M. Ojeda, I. Sádaba, M. López Granados, Furfural: A renewable and versatile platform molecule for the synthesis of chemicals and fuels, *Energy Environ. Sci.* 9 (2016) 1144–1189. <https://doi.org/10.1039/c5ee02666k>.
- [7] U.R. Thuppati, C. Choi, H. Machida, K. Norinaga, A comprehensive study on butanolysis of furfuryl alcohol to butyl levulinate using tungstated zirconia and sulfonated carbon catalysts, *Carbon Resour. Convers.* 4 (2021) 111–121. <https://doi.org/10.1016/j.crcon.2021.03.003>.
- [8] J. Li, J.L. Liu, H.J. Zhou, Y. Fu, Catalytic Transfer Hydrogenation of Furfural to Furfuryl Alcohol over Nitrogen-Doped Carbon-Supported Iron Catalysts,

- ChemSusChem. 9 (2016) 1339–1347. <https://doi.org/10.1002/cssc.201600089>.
- [9] C. Wang, A. Wang, Z. Yu, Y. Wang, Z. Sun, V.M. Kogan, Y.-Y. Liu, Aqueous phase hydrogenation of furfural to tetrahydrofurfuryl alcohol over Pd/UiO-66, *Catal. Commun.* 148 (2021) 106178. <https://doi.org/https://doi.org/10.1016/j.catcom.2020.106178>.
- [10] and C. V. Narayan S. Biradar, Amol M. Hengne, Rode, Single-Pot Formation of THFAL via Catalytic Hydrogenation of FFR Over Pd/MFI Catalyst, *ACS Sustain. Chem. Eng.* (2013).
- [11] R. Huang, Q. Cui, Q. Yuan, H. Wu, Y. Guan, P. Wu, Total Hydrogenation of Furfural over Pd/Al₂O₃ and Ru/ZrO₂ Mixture under Mild Conditions: Essential Role of Tetrahydrofurfural as an Intermediate and Support Effect, *ACS Sustain. Chem. Eng.* 6 (2018) 6957–6964. <https://doi.org/10.1021/acssuschemeng.8b00801>.
- [12] Z.X. Li, X.Y. Wei, Z. Yang, J. Li, W.W. Yan, L.L. Bie, Y.Y. Zhang, S. Li, Z.M. Zong, Selective hydrogenation of bio-based furfural over Co-based catalysts derived from zeolitic imidazolate frame materials, *Mol. Catal.* 492 (2020) 111007. <https://doi.org/10.1016/j.mcat.2020.111007>.
- [13] M. Kalong, P. Hongmanorom, S. Ratchahat, W. Koo-amornpattana, K. Faungnawakij, S. Assabumrungrat, A. Srifa, S. Kawi, Hydrogen-free hydrogenation of furfural to furfuryl alcohol and 2-methylfuran over Ni and Co-promoted Cu/ γ -Al₂O₃ catalysts, *Fuel Process. Technol.* 214 (2021) 106721. <https://doi.org/10.1016/j.fuproc.2020.106721>.
- [14] J. Wu, G. Gao, J. Li, P. Sun, X. Long, F. Li, Efficient and versatile CuNi alloy nanocatalysts for the highly selective hydrogenation of furfural, *Appl. Catal. B Environ.* 203 (2017) 227–236. <https://doi.org/10.1016/j.apcatb.2016.10.038>.
- [15] T. Mizugaki, T. Yamakawa, Y. Nagatsu, Z. Maeno, T. Mitsudome, K. Jitsukawa, K. Kaneda, Direct transformation of furfural to 1,2-pentanediol using a hydrotalcite-supported platinum nanoparticle catalyst, *ACS Sustain. Chem. Eng.* 2 (2014) 2243–2247. <https://doi.org/10.1021/sc500325g>.
- [16] H. Adkins, R. Connor, The catalytic hydrogenation of organic compounds over

- copper chromite, *J. Am. Chem. Soc.* 53 (1931) 1091–1095. <https://doi.org/10.1021/ja01354a041>.
- [17] M.M. Villaverde, N.M. Bertero, T.F. Garetto, A.J. Marchi, Selective liquid-phase hydrogenation of furfural to furfuryl alcohol over Cu-based catalysts, *Catal. Today*. 213 (2013) 87–92. <https://doi.org/10.1016/j.cattod.2013.02.031>.
- [18] K. Yan, J. Liao, X. Wu, X. Xie, A noble-metal free Cu-catalyst derived from hydrotalcite for highly efficient hydrogenation of biomass-derived furfural and levulinic acid, *RSC Adv.* 3 (2013) 3853–3856. <https://doi.org/10.1039/c3ra22158j>.
- [19] M.J. Taylor, L.J. Durndell, M.A. Isaacs, C.M.A. Parlett, K. Wilson, A.F. Lee, G. Kyriakou, Highly selective hydrogenation of furfural over supported Pt nanoparticles under mild conditions, *Appl. Catal. B Environ.* 180 (2016) 580–585. <https://doi.org/10.1016/j.apcatb.2015.07.006>.
- [20] K. Yan, C. Jarvis, T. Lafleur, Y. Qiao, X. Xie, Novel synthesis of Pd nanoparticles for hydrogenation of biomass-derived platform chemicals showing enhanced catalytic performance, *RSC Adv.* 3 (2013) 25865–25871. <https://doi.org/10.1039/c3ra43619e>.
- [21] B.M. Matsagar, C.Y. Hsu, S.S. Chen, T. Ahamad, S.M. Alshehri, D.C.W. Tsang, K.C.W. Wu, Selective hydrogenation of furfural to tetrahydrofurfuryl alcohol over a Rh-loaded carbon catalyst in aqueous solution under mild conditions, *Sustain. Energy Fuels*. 4 (2019) 293–301. <https://doi.org/10.1039/c9se00681h>.
- [22] Q. Yuan, D. Zhang, L. Van Haandel, F. Ye, T. Xue, E.J.M. Hensen, Y. Guan, Selective liquid phase hydrogenation of furfural to furfuryl alcohol by Ru/Zr-MOFs, *J. Mol. Catal. A Chem.* 406 (2015) 58–64. <https://doi.org/10.1016/j.molcata.2015.05.015>.
- [23] Y. Nakagawa, K. Tomishige, Total hydrogenation of furan derivatives over silica-supported Ni-Pd alloy catalyst, *Catal. Commun.* 12 (2010) 154–156. <https://doi.org/10.1016/j.catcom.2010.09.003>.
- [24] B. Chen, F. Li, Z. Huang, G. Yuan, Tuning catalytic selectivity of liquid-phase hydrogenation of furfural via synergistic effects of supported bimetallic catalysts,

- Appl. Catal. A Gen. 500 (2015) 23–29.
<https://doi.org/https://doi.org/10.1016/j.apcata.2015.05.006>.
- [25] S. Sitthisa, D.E. Resasco, Hydrodeoxygenation of furfural over supported metal catalysts: A comparative study of Cu, Pd and Ni, *Catal. Letters*. 141 (2011) 784–791. <https://doi.org/10.1007/s10562-011-0581-7>.
- [26] L.C. Chen, S.D. Lin, The ethanol steam reforming over Cu-Ni/SiO₂ catalysts: Effect of Cu/Ni ratio, *Appl. Catal. B Environ.* 106 (2011) 639–649. <https://doi.org/10.1016/j.apcatb.2011.06.028>.
- [27] F. Studt, F. Abild-Pedersen, Q. Wu, A.D. Jensen, B. Temel, J.D. Grunwaldt, J.K. Norskov, CO hydrogenation to methanol on Cu-Ni catalysts: Theory and experiment, *J. Catal.* 293 (2012) 51–60. <https://doi.org/10.1016/j.jcat.2012.06.004>.
- [28] H.L. Huynh, Z. Yu, CO₂ Methanation on Hydrotalcite-Derived Catalysts and Structured Reactors: A Review, *Energy Technol.* 8 (2020). <https://doi.org/10.1002/ente.201901475>.
- [29] S.H. Pang, N.E. Love, J.W. Medlin, Synergistic effects of alloying and thiolate modification in furfural hydrogenation over Cu-based catalysts, *J. Phys. Chem. Lett.* 5 (2014) 4110–4114. <https://doi.org/10.1021/jz502153q>.
- [30] R.L. Manfro, T.P.M.D. Pires, N.F.P. Ribeiro, M.M.V.M. Souza, Aqueous-phase reforming of glycerol using Ni-Cu catalysts prepared from hydrotalcite-like precursors, *Catal. Sci. Technol.* 3 (2013) 1278–1287. <https://doi.org/10.1039/c3cy20770f>.
- [31] D. Li, M. Lu, K. Aragaki, M. Koike, Y. Nakagawa, K. Tomishige, Characterization and catalytic performance of hydrotalcite-derived Ni-Cu alloy nanoparticles catalysts for steam reforming of 1-methylnaphthalene, *Appl. Catal. B Environ.* 192 (2016) 171–181. <https://doi.org/10.1016/j.apcatb.2016.03.052>.
- [32] D. Ren, J. Wang, X. Jiang, Z. Song, K. Norinaga, Z. Huo, A Supported Ni Catalyst Produced from Ni-Al Hydrotalcite-Like Precursor for Reduction of Furfuryl Alcohol to Tetrahydrofurfuryl Alcohol by NaBH₄ in Water, *ChemistrySelect*. 6 (2021) 551–556. <https://doi.org/10.1002/slct.202003543>.

- [33] C. Miao, G. Zhou, S. Chen, H. Xie, X. Zhang, Synergistic effects between Cu and Ni species in NiCu/ γ -Al₂O₃ catalysts for hydrodeoxygenation of methyl laurate, *Renew. Energy*. 153 (2020) 1439–1454. <https://doi.org/10.1016/j.renene.2020.02.099>.
- [34] N.F.P.R. and M.M.V.M.S. Robinson L. Manfro, Thaí's P. M. D. Pires, Aqueous-phase reforming of glycerol using Ni-Cu catalysts prepared from hydrotalcite-like precursors, *Catal. Sci. Technol.* 3 (2013) 1278–1287. <https://doi.org/10.1039/c3cy20770f>.
- [35] P.K. Sharma, N. Saxena, A. Bhatt, C. Rajagopal, P.K. Roy, Synthesis of mesoporous bimetallic Ni-Cu catalysts supported over ZrO₂ by a homogenous urea coprecipitation method for catalytic steam reforming of ethanol, *Catal. Sci. Technol.* 3 (2013) 1017–1026. <https://doi.org/10.1039/c2cy20563g>.
- [36] A.M. Bahmanpour, F. Héroguel, M. Kılıç, C.J. Baranowski, L. Artiglia, U. Röthlisberger, J.S. Luterbacher, O. Kröcher, Cu-Al Spinel as a Highly Active and Stable Catalyst for the Reverse Water Gas Shift Reaction, *ACS Catal.* 9 (2019) 6243–6251. <https://doi.org/10.1021/acscatal.9b01822>.
- [37] S. Abate, K. Barbera, E. Giglio, F. Deorsola, S. Bensaid, S. Perathoner, R. Pirone, G. Centi, Synthesis, Characterization, and Activity Pattern of Ni-Al Hydrotalcite Catalysts in CO₂ Methanation, *Ind. Eng. Chem. Res.* 55 (2016) 8299–8308. <https://doi.org/10.1021/acs.iecr.6b01581>.
- [38] D. Li, L. Wang, M. Koike, Y. Nakagawa, K. Tomishige, Steam reforming of tar from pyrolysis of biomass over Ni/Mg/Al catalysts prepared from hydrotalcite-like precursors, *Appl. Catal. B Environ.* 102 (2011) 528–538. <https://doi.org/10.1016/j.apcatb.2010.12.035>.
- [39] N.V. I.N. Leontyev, A.B. Kuriganova, d N.G. Leontyev, e L. Henet, A. Rakhmatullin, dand V.D. Smirnova, Size dependence of the lattice parameter of carbon supported platinum nanoparticles: X-ray diffraction analysis and theoretical considerations, *R. Soc. Chem.* 3 (2010). <https://doi.org/10.1039/b000000x>.
- [40] S.K. Das, A. Das, M. Gaboardi, S. Pollastri, G.D. Dhamale, C. Balasubramanian,

- B. Joseph, Large scale synthesis of copper nickel alloy nanoparticles with reduced compressibility using arc thermal plasma process, *Sci. Rep.* 11 (2021) 1–9. <https://doi.org/10.1038/s41598-021-86776-0>.
- [41] V. Rives, M.A. Ulibarri, A. Montero, Application of temperature-programmed reduction to the characterization of anionic clays, *Appl. Clay Sci.* 10 (1995) 83–93. [https://doi.org/10.1016/0169-1317\(95\)00009-S](https://doi.org/10.1016/0169-1317(95)00009-S).
- [42] Z. Zhang, Q. Yang, H. Chen, K. Chen, X. Lu, P. Ouyang, J. Fu, J.G. Chen, In situ hydrogenation and decarboxylation of oleic acid into heptadecane over a Cu-Ni alloy catalyst using methanol as a hydrogen carrier, *Green Chem.* 20 (2018) 197–206. <https://doi.org/10.1039/c7gc02774e>.
- [43] J. Morales, L. Sánchez, F. Martín, J.R. Ramos-Barrado, M. Sánchez, Use of low-temperature nanostructured CuO thin films deposited by spray-pyrolysis in lithium cells, *Thin Solid Films.* 474 (2005) 133–140. <https://doi.org/10.1016/j.tsf.2004.08.071>.
- [44] S. Tada, M. Yokoyama, R. Kikuchi, T. Haneda, H. Kameyama, N₂O pulse titration of Ni/ α -Al₂O₃ catalysts: A new technique applicable to nickel surface-area determination of nickel-based catalysts, *J. Phys. Chem. C.* 117 (2013) 14652–14658. <https://doi.org/10.1021/jp404291k>.
- [45] K. Larmier, S. Tada, A. Comas-Vives, C. Copéret, Surface Sites in Cu-Nanoparticles: Chemical Reactivity or Microscopy?, *J. Phys. Chem. Lett.* 7 (2016) 3259–3263. <https://doi.org/10.1021/acs.jpcclett.6b01328>.
- [46] J.G.G. Jr., S. Kim, W.D. Rhodes, Turnover frequencies in metal catalysis: Meanings, functionalities and relationships, *R. Soc. Chem.* 17 (2007) 320–348. <https://doi.org/10.1039/9781847553294-00320>.
- [47] M.N. Gebresillase, R.Q. Raguindin, H. Kim, J.G. Seo, Supported bimetallic catalysts for the solvent-free hydrogenation of levulinic acid to γ -valerolactone: Effect of metal combination (ni-cu, ni-co, cu-co), *Catalysts.* 10 (2020) 1–20. <https://doi.org/10.3390/catal10111354>.
- [48] I. Gandarias, J. Requies, P.L. Arias, U. Armbruster, A. Martin, Liquid-phase

- glycerol hydrogenolysis by formic acid over Ni-Cu/Al₂O₃ catalysts, *J. Catal.* 290 (2012) 79–89. <https://doi.org/10.1016/j.jcat.2012.03.004>.
- [49] V. Sánchez, P. Salagre, M.D. González, J. Llorca, Y. Cesteros, Effect of the formation of NiCu alloy and use of biomass-derived furfural on the catalytic hydrogenation of furfural to THFA, *Mol. Catal.* 490 (2020) 110956. <https://doi.org/10.1016/j.mcat.2020.110956>.
- [50] B. Zhang, Y. Zhu, G. Ding, H. Zheng, Y. Li, Selective conversion of furfuryl alcohol to 1,2-pentanediol over a Ru/MnO_x catalyst in aqueous phase, *Green Chem.* 14 (2012) 3402–3409. <https://doi.org/10.1039/c2gc36270h>.
- [51] A. Kumar, A. Shivhare, R. Bal, R. Srivastava, Metal and solvent-dependent activity of spinel-based catalysts for the selective hydrogenation and rearrangement of furfural, *Sustain. Energy Fuels.* 5 (2021) 3191–3204. <https://doi.org/10.1039/d1se00439e>.
- [52] C. Sievers, S.L. Scott, Y. Noda, L. Qi, E.M. Albuquerque, R.M. Rioux, Phenomena affecting catalytic reactions at solid–Liquid interfaces, *ACS Catal.* 6 (2016) 8286–8307. <https://doi.org/10.1021/acscatal.6b02532>.
- [53] M.A. Tike, V. V. Mahajani, Kinetics of liquid-phase hydrogenation of furfuryl alcohol to tetrahydrofurfuryl alcohol over a Ru/TiO₂ Catalyst, *Ind. Eng. Chem. Res.* 46 (2007) 3275–3282. <https://doi.org/10.1021/ie061137m>.
- [54] X. Chen, W. Sun, N. Xiao, Y. Yan, S. Liu, Experimental study for liquid phase selective hydrogenation of furfuryl alcohol to tetrahydrofurfuryl alcohol on supported Ni catalysts, *Chem. Eng. J.* 126 (2007) 5–11. <https://doi.org/https://doi.org/10.1016/j.cej.2006.08.019>.
- [55] Y. Nakagawa, K. Takada, M. Tamura, K. Tomishige, Total Hydrogenation of Furfural and 5-Hydroxymethylfurfural over Supported Pd–Ir Alloy Catalyst, *ACS Catal.* 4 (2014) 2718–2726. <https://doi.org/10.1021/cs500620b>.
- [56] N. Merat, C. Godawa, A. Gaset, High selective production of tetrahydrofurfuryl alcohol: Catalytic hydrogenation of furfural and furfuryl alcohol, *J. Chem. Technol. Biotechnol.* 48 (1990) 145–159. <https://doi.org/10.1002/jctb.280480205>.

- [57] M. Hronec, K. Fulajtarová, T. Liptaj, Effect of catalyst and solvent on the furan ring rearrangement to cyclopentanone, *Appl. Catal. A Gen.* 437–438 (2012) 104–111. <https://doi.org/10.1016/j.apcata.2012.06.018>.
- [58] L. Liu, H. Lou, M. Chen, Selective hydrogenation of furfural to tetrahydrofurfuryl alcohol over Ni/CNTs and bimetallic Cu[sbnd]Ni/CNTs catalysts, *Int. J. Hydrogen Energy.* 41 (2016) 14721–14731. <https://doi.org/10.1016/j.ijhydene.2016.05.188>.
- [59] C. Sunyol, R. English Owen, M.D. González, P. Salagre, Y. Cesteros, Catalytic hydrogenation of furfural to tetrahydrofurfuryl alcohol using competitive nickel catalysts supported on mesoporous clays, *Appl. Catal. A Gen.* 611 (2021). <https://doi.org/10.1016/j.apcata.2020.117903>.
- [60] I. McManus, H. Daly, J.M. Thompson, E. Connor, C. Hardacre, S.K. Wilkinson, N. Sedaie Bonab, J. Ten Dam, M.J.H. Simmons, E.H. Stitt, C. D’Agostino, J. McGregor, L.F. Gladden, J.J. Delgado, Effect of solvent on the hydrogenation of 4-phenyl-2-butanone over Pt based catalysts, *J. Catal.* 330 (2015) 344–353. <https://doi.org/10.1016/j.jcat.2015.06.008>.
- [61] X. Wang, R. Rinaldi, Solvent effects on the hydrogenolysis of diphenyl ether with raney nickel and their implications for the conversion of lignin, *ChemSusChem.* 5 (2012) 1455–1466. <https://doi.org/10.1002/cssc.201200040>.

Chapter 4: The catalytic performance of Ni-Cu-Al catalysts on hydrogenation of furfural through thermo catalytic and electrocatalytic routes

Abstract: Furfural is one of the important platform chemicals and its conversion has a broad range of synthetic chemicals and liquid fuels, including furfuryl alcohol (FAL), tetrahydro furfuryl alcohol (THFA), and 2-methyl furan (2-MF). In this work, furfural hydrogenation is carried out using Ni-Cu-Al mixed oxide catalysts in thermal catalytic conversion (TCH) and electrocatalytic hydrogenation (ECH) to report the catalytic activity of these mixed oxides. The Ni-Cu-Al mixed oxide catalysts are prepared as working electrodes by depositing the catalyst ink on a Cu foam substrate. 98 mol% selectivity of THFA with complete conversion was observed in the TCH route using Ni₁-Cu₁-Al₁ R catalyst at 140 °C under 30 bar H₂ pressure after 4 hours of the reaction. However, the electrocatalyst (Ni₁-Cu₁-Al₁ R on Cu foam) through the ECH route displayed 89 mol% conversion of furfural with 58 % selectivity of 2-MF and 23.8 % selectivity of FAL. The pH (0.5) of the electrolyte used in the ECH process controlled the selectivity between 2-MF and FAL. Moreover, the formation of THFA was not observed in the ECH route.

4.1. Introduction

Biomass is an abundant resource that resembles actual fossil feedstocks with carbon, hydrogen and oxygen in its structure. The futuristic possibility of integrating electricity generation from renewable sources and converting biomass-based carbon sources could make it feasible for energy and fine chemicals production from biomass[1]–[3]. However, the traditional conversion processes of biomass-derived components, such as thermal catalytic hydrogenation (TCH) and catalytic transfer hydrogenation (CTH), involve harsh treating conditions and energy-intensive processes. Hence, the immanent path forward is to use electrochemistry charged by renewable electricity to accommodate electrocatalytic hydrogenation (ECH). Electrochemistry provides a smooth technology for chemical processing and offers much-needed insights into the electron transfer mechanism,

including new reaction pathways. Despite the fascinating interest, widespread challenges of adopting this technology are driven by extra knowledge and the equipment setup. Nonetheless, the ECH process offers the following prospects (1) simple operating conditions, (2) requirement of no external H₂ source, (3) cleaner process, and easy product separation (higher carbon recovery and improved H/C ratios). In this regard, ECH of biomass-derived oxygen-containing compounds, especially furfural, are more appealing candidates since they have a greater added value and could be alternative feedstock for the fine chemicals and liquid fuels.

4.1.1 Furfural conversion pathway

Furfural is a product of acid-catalyzed hydrolysis of xylose and building blocks for producing a wide range of fuels and chemicals by hydrogenation, as described in Fig.4.1[4]. The furfural molecule has a furan ring and carbonyl group in its structure, which contains two C=C double bonds and one cyclic ether bond; therefore, it is highly reactive and can be transformed into many synthetic chemicals and liquid fuels. The hydrogenation products such as furfuryl alcohol (FAL), 2-methyl furan (2-MF), tetrahydrofurfuryl alcohol (THFA), and 2-methyl tetrahydrofuran (2-MTHF) have various applications as solvents and fuel blends, especially 2-MTHF with an octane number of 74 and can readily be blended with p-series gasoline fuel. Moreover, THFA as a green solvent has its potential applications in pesticides, coatings, and stripping formulations. At high temperatures (>230°C), the furfural decarbonylation can occur on noble-metal-based catalysts (Pt, Pd, and Ru)[5] to produce tetrahydrofuran, while under mild reaction conditions (150-200 °C), transition metal-based catalysts like Cu, Ni, and Co promote the furfural hydrogenation route[6]. This work aimed at the hydrogenation of furfural using the ECH process to produce FAL and 2-MF.

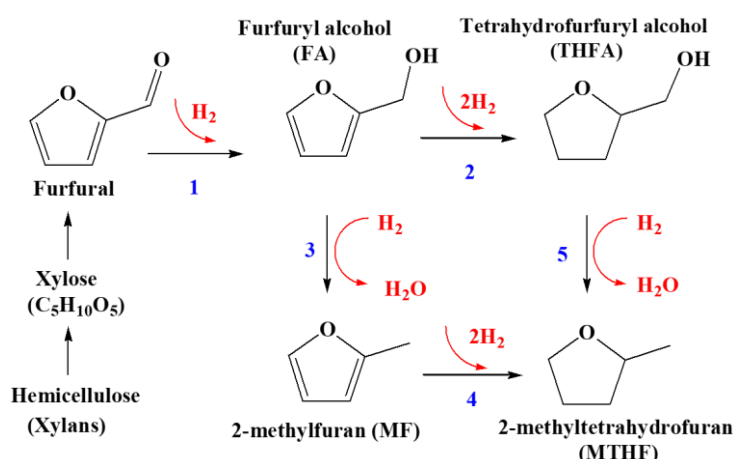


Fig.4.1: Conversion of furfural into fine chemicals.

The corresponding Gibbs free energies and standard cell potentials for the hydrogenation of furfural to FAL and the subsequent reduction reactions are mentioned in **Table 4.1**. It is apparent that water electrolysis reduction needs higher cell potential than hydrogen gas; thus, more significant power input is required. The formation of THFA from FAL involves the hydrogenation of the furan ring, whereas the formation of 2-MF involves the hydrogenolysis of the non-conjugated hydroxyl group of FA. The cell potentials required for the formation of THFA and 2-MF from FAL are 1.01 and 1.09 V, respectively, indicating that the formation of THFA is marginally favoured over the 2-MF. A similar pattern can be observed for forming 2-MTHF from 2-MF (1.5 V) by furan ring hydrogenation and from THFA (2.06 V) by hydrogenolysis of non-conjugated hydroxyl group, respectively. In fact, the formation of 2-MTHF from THFA is highly unlikely possible as the cell the potential required for the hydrogen gas is 1.23 V, and it is thermodynamically favourable and subsequently faster[7].

Table 4.1: Gibbs free energy and standard cell potentials for the hydrogenation of furfural.

Reaction	Hydrogen gas		Water electrolysis	
	ΔG (KJ mol ⁻¹)	E_{cell} (V)	ΔG (KJ mol ⁻¹)	E_{cell} (V)
1. Furfural \rightarrow FAL	35.95	0.19	200.38	-1.04
2. FA \rightarrow THFA	-80.97	0.21	391.69	-1.01
3. FA \rightarrow 2-MF	-25.27	0.13	211.06	-1.09

4. 2-MF → 2-MTHF	-104.78	-0.27	577.44	-1.50
5. THFA → 2-MTHF	160.48	-0.83	396.81	-2.06

4.1.2 Parameter selection for the design of ECH of furfural experiment

In order to attain maximum yields of furfural products, various reaction parameters such as various electrocatalysts, electrolytes, and reactors (Batch & Flow cells) were studied. The effect of several transition metals on the product selectivity of ECH of furfural was also investigated in the literature.

Although selecting an electrocatalyst is crucial in achieving the high selectivity and yield of desired products and high faradaic efficiency (FE), other reaction parameters have a significant influence, such as the pH of the electrolyte, the applied potential, and the initial concentration of the substrate. The other parameters, such as reaction time which the equivalent charge transfer could attain and the solvent ratio, were found to slightly influence the targeted product distribution. The experimental setup, which could be vital for the reaction performance, selectivity, and the mass balance of the substrate and the products, also an important parameter, needs to be considered. The three types of reactors: Continuous, batch, and semi-batch, have been implemented in various studies. In addition, the continuous flow reactors are efficacious for scaleup and challenging mass transport limitations. The batch and semi-batch reactors could investigate the fundamental studies and the kinetic parameter evaluation.

The challenging task of the ECH of the furfural is to account for the 2-MF, which tends to evaporate quickly due to its high vapor pressure[8]. Z. Li et al. [9] used an octane trap and have performed controlled experiments to account for the mole balance of a mixture of substrate and the products: furfural, FAL, and 2-MF in an undivided cell without performing ECH. The experiment resulted in a reduced evaporation loss of MF due to the octane layer on the top, yet a considerable, i.e., 35 % of 2-MF still evaporated from the system. Nilges and Schroder attached a cold trap reflux condenser to the catholyte outlet that flowed N₂ gas through catholyte to trap the evaporated 2-MF in the condenser using an acetonitrile coolant cooled to -15 °C[10].

The important parameter that determines the product selectivity between 2-MF and FAL is the pH of the electrolyte [10][11][12]. Jung S et al. reported the effect of electrolyte pH on the product selectivity at a constant current density of -10 mA/cm^2 using Cu flags in 20 vol.% acetonitrile and 80 vol.% water solvent[11]. The three electrolytes in the pH range of 0 to 3.4 were: 0.5 M H_2SO_4 (pH 0), 0.1 M H_2SO_4 (pH 1.1), and 0.2 M NH_4Cl (pH 3.4) tested. The most significant observation was the increasing trend of 2-MF selectivity with decreasing pH of the electrolyte. The 2-MF selectivity followed the pH order of 0.5 M H_2SO_4 (30 %) > 0.1 M H_2SO_4 (20 %) > 0.2 M NH_4Cl (less than 2 %). A similar trend was observed with HCl electrolyte instead of H_2SO_4 , depicting the pH effect rather than the anion effect[11]. In contrast to 2-MF, the FAL selectivity was increased with increasing pH from 0 to 3.4 and was observed to be dominant in the pH range of 6 to 10. Andrew S et al. clearly mentioned the pH of electrolyte effect on 2-MF and FAL selectivity in their brief review[13]. Although the formation of furans and hydrofurans above pH 10 has happened, FA was the major product[9][14]. The low selectivities of the furanics and hydrofurans above pH 10 were likely due to the instability of the furanics[15][16]. In summary, both 2-MF and FAL have been formed in a strong acidic electrolyte. 2-MF was the primary product, while FAL was dominant in mild acidic and high basic electrolytes.

Another important aspect of ECH of furfural is the faradaic efficiency (FE). The amount of electrons passed over the half-cell potential determines the FE, which is crucial in determining the efficiency of ECH over hydrogen evolution reaction (HER) reaction [12][17][18] [19]. The half-cell potential can be a determining factor in the reactions that occur on the catalyst surface. Both ECH and HER involve Volmer reactions (Eq. 7a and 7b) where the hydrogen would be chemisorbed on the electrode surface and then proceeding to ECH and HER simultaneously. In order to increase the ECH efficiency and FE, the chemisorbed hydrogen should react with the organic substrate to produce the respective products, thereby suppressing the protons to promote HER reaction. Increasing applied voltage increases the ECH rate and HER, thereby affecting the total efficiency of the reaction. Jung S et al. observed the increasing rate of HER at an applied voltage of -950 mV compared to -800 mV with Cu electrode using a 0.5 M H_2SO_4 electrolyte[11]. The combined FE of both FAL and 2-MF reached 100 % at -500 mV , whereas it was

dropped to 76 % at -600 mV. However, this drop was not caused by increasing HER but happened due to the progression of side reaction at -650 mV that resulted in the drop of FE of FAL. At -800 mV, the combined FE further dropped to 56 %, and the authors mentioned that about 27 % of FE was neither accounted for the furanic products nor the HER. The provision of excess applied potential necessarily makes it an inefficient use of produced electrons, thereby leading to a drop in the overall efficiency of the ECH system. In addition, FE was greatly influenced by the electrode used, as observed by the reports in which more than 80 % was achieved[20][21]. The applied potential should be chosen accordingly to the electrocatalyst, electrolyte, and substrate applied in the ECH system, which could be in a typical range of -500 to -650 mV[13].

The initial substrate concentration has a substantial effect on the FE and ECH of furfural. Zhao B et al. used the initial furfural concentration in the range of 40-120 mM over Pt supported on activated carbon fibres using 0.1 M HCl electrolyte at a constant applied voltage of -500 mV[15]. The FAL yield and current efficiency were maximized at 80 mM concentration, while below 80 mM HER dominated the ECH. Due to a lack of furfural concentration, the active catalyst sites were preoccupied with chemisorbed hydrogen instead of furfural. Increasing the furfural concentration over 80 mM led to forming an organic layer around the electrode, which decreased both furfural and current efficiencies[15]. Also, the mole balance and production rates were affected by the low initial concentration of 20 mM, a significant challenge to the ECH of furfural[9][17]. Jung S et al. also reported forming a thick organic layer around the electrode when 200 mM of initial furfural concentration was used, which inflicted the imbalance in production rate and mole balance[11].

Additionally, the H₂ production rate dropped by 60 % when 200 mM of furfural concentration was used due to the saturation of organic compounds on the electrode not providing active sites for H₂ adsorption[11]. The initial furfural concentration should be maintained in a range (typically from 20 mM to 100 mM) such that enough active sites should be occupied by furfural and hydrogen to promote ECH more than HER and should not be exceeded so that the electrode would mop up by the substrate to form a fouling layer on the electrode surface. The solvent ratio and the reaction time have shown the slightest concern effect on the product distribution and could be selected based on the

other defining parameters. Thus, parameter selection needs to be defined to design an effective ECH of the furfural system.

4.2 Methodology

4.2.1 Materials and Chemicals

Cu foam was obtained from Xiamen Tob New Energy Technology Co., ltd, and Cu foil was purchased from Sigma-Aldrich. Ni foam was bought from MTI Japan. Nafion N117 (Proton exchange membrane) was obtained from Chemours. The reference electrode (Ag/AgCl in 3M NaCl) was bought from BAS Inc. Pt mesh was purchased from EC-frontier Co., Ltd. 5 wt% Nafion solution in ethanol, 2-butanol, furfural, and methanol were acquired from Sigma-Aldrich. Conc. H₂SO₄, Acetonitrile, sodium carbonate, and sodium hydroxide were purchased from Wako chemicals. Furfuryl alcohol, tetrahydrofurfuryl alcohol, 2-methyl furan, and 2-methyl tetrahydrofuran were obtained from TCI chemicals; all the chemicals were used as received.

4.2.2 Electrocatalyst preparation

The equimolar catalyst (Ni₁Cu₁-Al₁ R) was prepared by the co-precipitation method (discussed in Chapter 3) [22]. The working electrode was prepared by the method mentioned elsewhere[23]. In a typical preparation, 20 mg of Ni₁Cu₁-Al₁ R catalyst was dispersed in a mixed solution of 475 μL of water, 475 μL of ethanol, and 50 μL of 5 wt % Nafion. Then, the resulted catalyst ink was sonicated for 2 hours. Afterwards, the working electrode was synthesized by depositing 50 μL of a catalyst ink onto the Cu foam with an area of 1 cm². Finally, thus obtained Ni₁Cu₁-Al₁ R on Cu foam was allowed for overnight drying at room temperature to obtain the working electrode.

4.2.3 Experimental

Table 4. 2: Experimental conditions

Thermal catalytic hydrogenation (TCH)	Electrocatalytic hydrogenation (ECH)
Catalyst	Working electrode
Ni-Cu-Al 111 R	Ni-Cu-Al 111 R on Cu foam

Substrate loading	5 mmol furfural	Counter electrode	Pt mesh
Solvent	30 ml 2-butanol	Reference electrode	Ag/AgCl
Reaction temperature	140 °C	Catholyte	50 ml of 100mM FF in 0.5M H ₂ SO ₄ with water/acetonitrile (4/1 by volume) cosolvent
Reaction pressure	30 bars (Hydrogen)	Anolyte	0.5M H ₂ SO ₄ in DI water
Reaction time	240 min	Membrane	Proton exchange membrane (Nafion117)
Catalyst loading	100 mg	Applied voltage	-0.8V vs RHE
Stirring speed	600 rpm	Electrolyte pH	0.5
		Reaction time	90 min

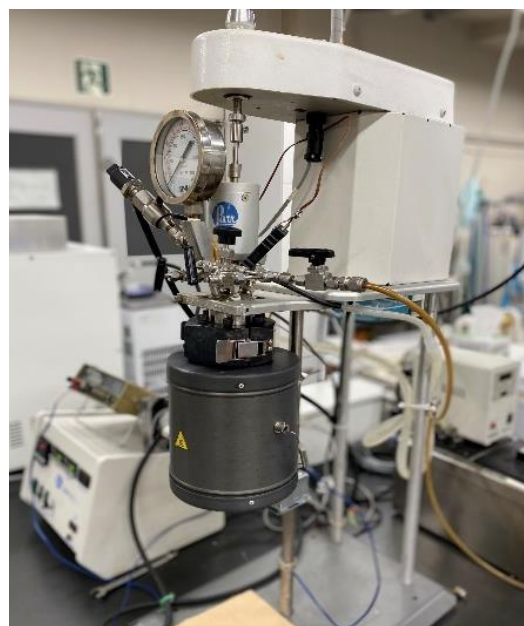
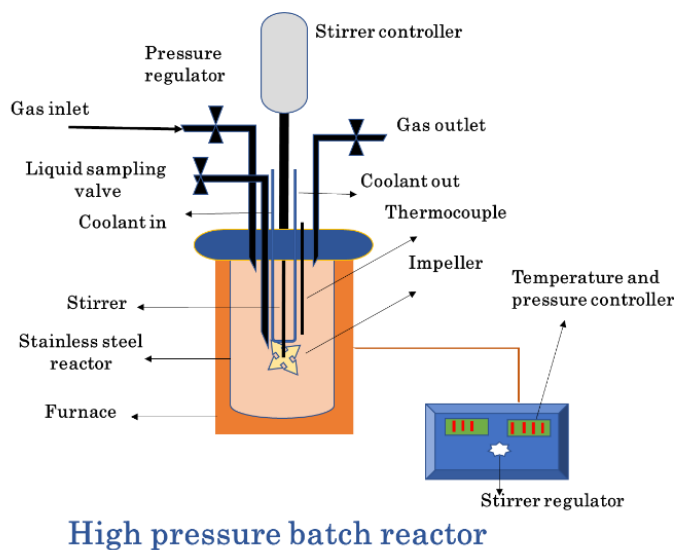


Fig.4.2: Schematic (left) and photograph (right) of high-pressure batch reactor

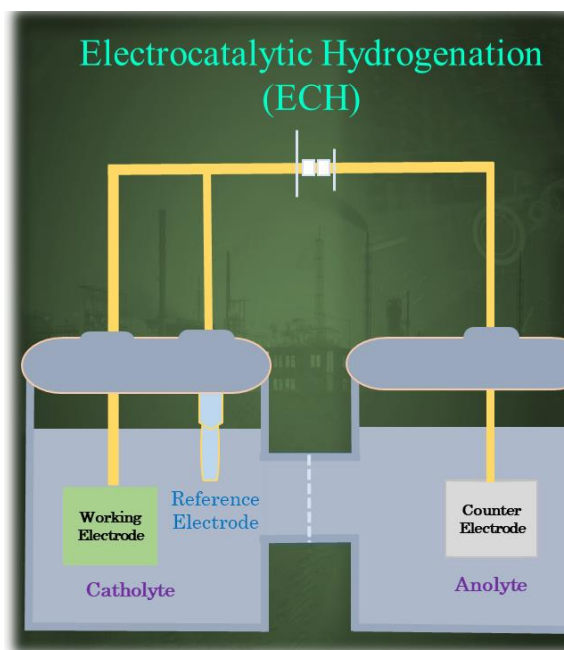


Fig.4. 3 Schematic (left) and photograph (right) of electrochemical reactor

Fig.4.2 and Fig.4.3 show the schematics and photographs of the high-pressure batch reactor and electrochemical setup, respectively. Thermal catalytic hydrogenation of furfural was investigated in a 100 ml high-pressure Parr reactor equipped with a pressure and a temperature controller. The reactions were conducted at a specific reaction

condition (140 °C, 30 bar H₂, 4 hours). Electrocatalytic hydrogenation was carried out using a three-electrode system in an electrochemical H-cell type connected to the Versa STAT instrument. A Pt mesh was used as a counter electrode and an Ag/AgCl as a reference electrode. 50 ml of catholyte and anolyte were added to the electrochemical setup, and nitrogen flowed through the catholyte chamber. The experimental conditions of TCH and ECH are mentioned in Table 4.2, respectively. The product samples were collected and quantified by GC-FID (DB-WAX column-30mx0.25mmx0.25um) and identified by GC-MS (DB-WAX column-30mx0.25mmx0.25um). The following equations were used in the calculations.

$$\text{Conversion} = \frac{\text{moles of furfural reacted}}{\text{Initial moles of furfural}} \times 100 \text{ (\%)}$$

$$\text{Selectivity} = \frac{\text{moles of the product}}{\text{Total moles of the product}} \times 100 \text{ (\%)}$$

4.3 Results and Discussion

4.3.1 Cyclic voltammetry study

The cyclic voltammetry experiments were performed to determine the reduction and oxidation behaviour of furfural molecule species and the applied potential range. **Fig. 4.3** represents voltammograms or cyclic voltammograms which is the current response of the working electrodes against a specific range of applied voltage. Oxidation behaviour of the furfural molecules was observed for the Ni foam electrocatalyst (**Fig. 4.3a**). In contrast, the reduction behaviour of the furfural molecules was noticed for the rest of the electrocatalysts (Fig. 4.3b-d). This study focused on the furfural reduction process instead of the oxidation process. Although Cu foil, Cu foam, and Ni₁Cu₁-Al₁ R/Cu foam have shown the reduction behaviour, the applied potential became more negative because of the elaborated rate of furfural molecules reduction to yield more of the products.

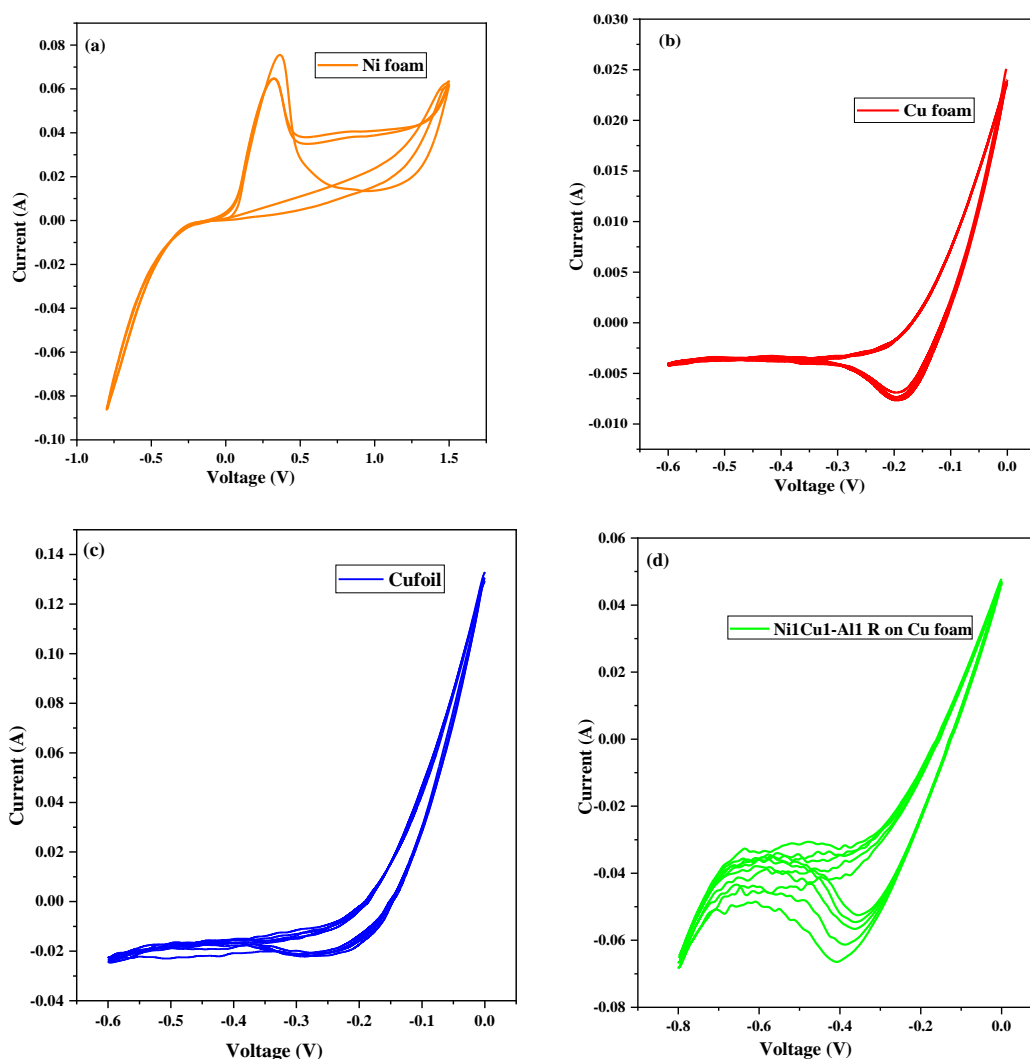


Fig.4.4: Cyclic voltammograms of the working electrodes (a) Ni foam, (b) Cu foam, (c) Cu foil, (d) Ni1Cu1-Al1 R on Cu foam

4.3.2 Electrocatalytic hydrogenation

From the literature, the best suitable conditions were selected to carry out the electrochemical hydrogenation of furfural[13] and are mentioned in **Table 4.2**. Fig. 4.4 shows the electrocatalytic reduction of furfural (50 ml of 100mM FF in 0.5M H₂SO₄ with water/acetonitrile (4/1 by volume) cosolvent) using the working electrodes. Cu foil resulted in only 31.2 mol% conversion with 22 mol% selectivity of 2-MF and 9 mol% of FAL. Although the Ni foam has the oxidation response, 26 mol% of furfural conversion was achieved, attributing to a minimum reduction capacity and free-electron reduction of furfural, which resulted in 25 mol% selectivity of the FAL. In the case of Ni foam, electrolyte pH has no prominent effect as the reduction process was free-electron process

which mostly produced FAL. The reaction with Cu foam showed a maximum furfural conversion of 86 mol% with moderately high selectivity for 2-MF (41 mol%) compared to FAL (24 mol%). Cu foam also was active in forming other compounds than 2-MF and FAL, such as furoic acid, 2-MTHF, and furfural polymers. The structural difference between Cu as a foil and as a foam significantly influenced the reaction results due to the adsorption properties of Cu as a foam structure.

Additionally, the introduction of Ni1Cu1-Al1 R active sites resulted in the suppression of the other products with increasing selectivity of 2-MF to 57 mol% by enhanced furfural conversion (89 mol%). Additionally, the selectivity of FAL more or less remained similar to that of Cu foam. Moreover, Ni and Cu on Al active species on Cu foam acted as an additional active phase to convert furfural into 2-MF while suppressing the formation of undesired products.

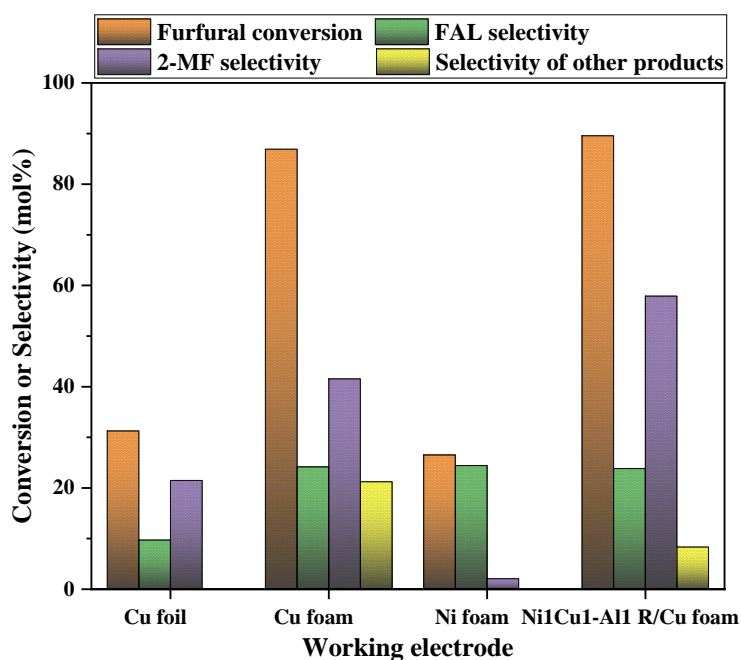


Fig.4.5 ECH of furfural

Reaction conditions are reported in Table 4.1

4.3.3 Performance of Ni1Cu1-Al1 R in TCH and ECH processes

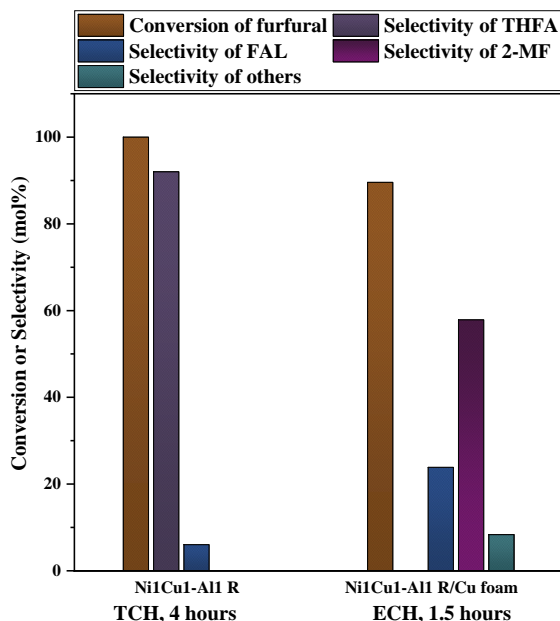


Fig.4.6: Catalytic activity of Ni-Cu-Al 111 R through TCH and ECH routes.

Reaction conditions are reported in Table 4.1

Ni and Cu electrodes are extensively used in the electrochemical hydrogenation to produce mostly either 2-MF or FAL, whose selectivity was majorly dependent on the pH of the electrolyte. In our effort to use Ni-Cu mixed oxide as a working electrode to observe its activity. In thermal catalytic hydrogenation (discussed in Chapter 3), the formation of THFA progressed through FAL formation. Cu species were highly active towards the carbonyl group of furfural molecule, while Ni species were active towards both the carbonyl group and furan ring of furfural molecule. Thus, the catalyst prepared with equal molar ratios of Ni, Cu, and Al yielded a maximum of 92 mol% selectivity of THFA at a reaction temperature of 140 °C and a hydrogen pressure of 30 bars after 4 hours of reaction. Fig.4.5 displays the catalytic activity of Ni1Cu1-Al1 R through thermal catalytic hydrogenation and electrochemical hydrogenation of furfural. Although carbonyl group reduction happened in both processes to produce FAL, the end products were different given the conditions. In TCH processes, further ring hydrogenation of FAL proceeded to form THFA at high yields. In contrast, simultaneous reduction of furfural to FAL and furfural to 2-MF was observed in the ECH process. In the ECH process, the possibility of direct reduction of furfural to 2-MF can also happen with the low pH of the electrolyte.

As a result of these observations, the TCH process produced high selectivity of THFA (92 mol%) with complete conversion, whereas the ECH process produced 2-MF (57 mol% selectivity) with 89 mol% furfural conversion.

4.4 Conclusions

In summary, ECH of furfural was studied using Ni and Cu material as working electrodes under the best conditions from the literature. Cyclic voltammetry study revealed that Ni foam had shown the oxidation response whereas the reduction response was noticed for other electrodes. The foil and foam structure of Cu has significantly affected the reaction results attributing to the structure dependency adsorption phenomena. The deposition of Ni₁Cu₁-Al₁ R catalyst on Cu foam enhanced the results and also suppressed the undesired products. TCH of furfural led to the formation of THFA (92 mol%), whereas ECH resulted in 2-MF (57 mol%). As a result, through TCH and ECH processes, the end product can be chosen selectively by utilizing Ni and Cu active phases. TCH of furfural fills in with high energy demand and harsh treating conditions. To reduce the energy demand and harsh conditions, ECH serves as a promising conversion technology of furfural integrated with renewable electricity can make ECH a promising route. However, the challenges of electrochemical setup, product separation and analysis are critical to competing with the existing TCH infrastructure. Nevertheless, the scaleup and the industrial applicability of ECH of furfural remain leading-edge research.

4.5 References

- [1] S. A. Akhade *et al.*, “Electrocatalytic hydrogenation of biomass-derived organics: A review,” *Chem. Rev.*, vol. 120, no. 20, pp. 11370–11419, 2020.
- [2] K. Li and Y. Sun, “Electrocatalytic Upgrading of Biomass-Derived Intermediate Compounds to Value-Added Products,” *Chem. - A Eur. J.*, vol. 24, no. 69, pp. 18258–18270, 2018.
- [3] Y. P. Wijaya, K. J. Smith, C. S. Kim, and E. L. Gyenge, “Electrocatalytic hydrogenation and depolymerization pathways for lignin valorization: Toward mild synthesis of chemicals and fuels from biomass,” *Green Chemistry*, vol. 22, no. 21, pp. 7233–7264, 2020.
- [4] Z. Yang *et al.*, “Process design and economics for the conversion of lignocellulosic biomass into jet fuel range cycloalkanes,” *Energy*, vol. 154, pp. 289–297, 2018.
- [5] V. Vorotnikov, G. Mpourmpakis, and D. G. Vlachos, “DFT study of furfural conversion to furan, furfuryl alcohol, and 2-methylfuran on Pd(111),” *ACS Catal.*, vol. 2, no. 12, pp. 2496–2504, 2012.
- [6] S. Sitthisa and D. E. Resasco, “Hydrodeoxygenation of furfural over supported metal catalysts: A comparative study of Cu, Pd and Ni,” *Catal. Letters*, vol. 141, no. 6, pp. 784–791, 2011.
- [7] L. Zhang, T. U. Rao, J. Wang, and D. Ren, “A review of thermal catalytic and electrochemical hydrogenation approaches for converting biomass-derived compounds to high-value chemicals and fuels,” *Fuel Process. Technol.*, vol. 226, no. August 2021, p. 107097, 2022.
- [8] R. F. Holdren and R. M. Hixon, “Vapor Pressure and Vapor-Liquid Equilibria in the System Furfural–2-Methylfuran,” *Ind. Eng. Chem.*, vol. 38, no. 10, pp. 1061–1062, 1946.
- [9] Z. Li *et al.*, “Aqueous electrocatalytic hydrogenation of furfural using a sacrificial anode,” *Electrochim. Acta*, vol. 64, pp. 87–93, 2012.

- [10] P. Nilges and U. Schröder, “Electrochemistry for biofuel generation: Production of furans by electrocatalytic hydrogenation of furfurals,” *Energy Environ. Sci.*, vol. 6, no. 10, pp. 2925–2931, 2013.
- [11] S. Jung and E. J. Biddinger, “Controlling Competitive Side Reactions in the Electrochemical Upgrading of Furfural to Biofuel,” *Energy Technol.*, vol. 6, no. 7, pp. 1370–1379, 2018.
- [12] X. H. Chadderdon *et al.*, “Mechanisms of Furfural Reduction on Metal Electrodes: Distinguishing Pathways for Selective Hydrogenation of Bioderived Oxygenates,” *J. Am. Chem. Soc.*, vol. 139, no. 40, pp. 14120–14128, 2017.
- [13] A. S. May and E. J. Biddinger, “Strategies to Control Electrochemical Hydrogenation and Hydrogenolysis of Furfural and Minimize Undesired Side Reactions,” *ACS Catal.*, vol. 10, no. 5, pp. 3212–3221, 2020.
- [14] W. C. Albert and A. Lowy, “The Electrochemical Reduction of Furfural,” *Trans. Electrochem. Soc.*, vol. 75, no. 1, p. 367, 1939.
- [15] B. Zhao, M. Chen, Q. Guo, and Y. Fu, “Electrocatalytic hydrogenation of furfural to furfuryl alcohol using platinum supported on activated carbon fibers,” *Electrochim. Acta*, vol. 135, pp. 139–146, 2014.
- [16] P. Parpot, A. P. Bettencourt, G. Chamoulaud, K. B. Kokoh, and E. M. Belgsir, “Electrochemical investigations of the oxidation-reduction of furfural in aqueous medium - Application to electrosynthesis,” *Electrochim. Acta*, vol. 49, no. 3, pp. 397–403, 2004.
- [17] S. Jung and E. J. Biddinger, “Electrocatalytic Hydrogenation and Hydrogenolysis of Furfural and the Impact of Homogeneous Side Reactions of Furanic Compounds in Acidic Electrolytes,” *ACS Sustain. Chem. Eng.*, vol. 4, no. 12, pp. 6500–6508, 2016.
- [18] S. Jung, A. N. Karaiskakis, and E. J. Biddinger, “Enhanced activity for electrochemical hydrogenation and hydrogenolysis of furfural to biofuel using electrodeposited Cu catalysts,” *Catal. Today*, vol. 323, no. September 2018, pp. 26–34, 2019.

- [19] Y. Feng *et al.*, “CuI-Cu₀ bicomponent CuNPs@ZIF-8 for highly selective hydrogenation of biomass derived 5-hydroxymethylfurfural,” *Green Chem.*, vol. 21, no. 16, pp. 4319–4323, 2019.
- [20] F. Wang *et al.*, “Fabrication of La-doped TiO₂ Film Electrode and investigation of its electrocatalytic activity for furfural reduction,” *Electrochim. Acta*, vol. 153, pp. 170–174, 2015.
- [21] X. Zhang *et al.*, “Simultaneously high-rate furfural hydrogenation and oxidation upgrading on nanostructured transition metal phosphides through electrocatalytic conversion at ambient conditions,” *Appl. Catal. B Environ.*, vol. 244, no. December 2018, pp. 899–908, 2019.
- [22] H. L. Huynh and Z. Yu, “CO₂ Methanation on Hydrotalcite-Derived Catalysts and Structured Reactors: A Review,” *Energy Technol.*, vol. 8, no. 5, 2020.
- [23] X. Hao *et al.*, “Biomass-Derived N-Doped Carbon for Efficient Electrocatalytic CO₂ Reduction to CO and Zn-CO₂ Batteries,” *ACS Appl. Mater. Interfaces*, vol. 13, no. 3, pp. 3738–3747, 2021.

Chapter 5: Economic potential of tetrahydrofurfuryl alcohol (THFA) from the hydrogenation of furfural in 2-butanol

Abstract

Pentose sugars derived from hemicellulose biomass, especially xylose, can produce furfural by dehydration which has numerous applications primarily in the polymer and lubricant industries. However, it is an important platform chemical to produce an array of fuel additives such as butyl levulinate (BL), a gasoline additive and fine chemicals like tetrahydrofurfuryl alcohol (THFA). In this work, an Aspen Plus model was developed using the PENG-ROB estimation method for the hydrogenation of furfural to THFA and furfuryl alcohol (FAL) to estimate the economic analysis of the process. The best results obtained by Ni1Cu1-Al1 R catalyst (100 mol% conversion and 98 mol% THFA yield, 1.5 mol% of FAL yield at 140 °C and 30 bar H₂ pressure) are used in the RSTOIC reactor to estimate its economic potential. As the reaction was exothermic, the liberated heat source was integrated with the process to make use of the process heat.

5.1 Introduction

The efficient utilization of hemicellulose remains a challenge in the biorefinery process. The hemicellulose composition of pentose and hexose sugars would vary depending on the plant species and produce the sugars accordingly after hydrolysis [1]. Due to the presence of acids during the pre-treatment of hemicellulose biomass, the pentose sugars undergo dehydration to produce furfural[2]. Production of furfural from xylose has technical and market advantages. From a technical point of view, xylose conversion to furfural can happen under moderate conditions[3]. Although the furfural yield is low, its recovery from water is easy as it forms a heterogeneous azeotrope with high relative volatility.

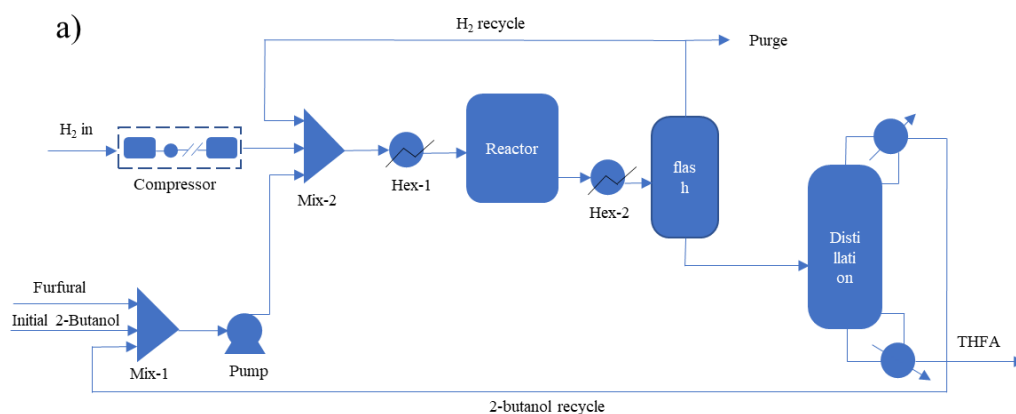
On the other hand, furfural has a good market in the polymer industry to produce resins and aromatic extract. Moreover, it is a platform chemical for low-cost chemicals and fuel additives[4][5]. However, to date, only a few studies have been reported on the techno-economic analysis of the furfural conversion to fuel additives and liquid fuels[6][7][8].

This work aimed to provide the economic and energy scenario analysis of the hydrogenation of furfural to THFA in 2-butanol solvent using the Ni1Cu1-Al1 catalytic system results reported in chapter 3.

5.2 Methodology

5.2.1 Process simulation

The hydrogenation of furfural to THFA was simulated in Aspen Plus V11 based on the results obtained using Ni1Cu1-Al1 R catalyst (100 mol% conversion and 98 mol% THFA yield at 140 °C and 30 bar H₂ pressure). The thermodynamic model was chosen based on the specific requirements. Furan compounds present assertive non-ideal behaviour, particularly with no binary data available to use more prolific activity coefficient models for the individual chemicals[6]. Therefore, the Peng-Robinson base method was used to simulate the hydrogenation of furfural. Fig.5.1 describes the basic schematic of the furfural hydrogenation process. The basic process includes the input of furfural, hydrogen gas and 2-butanol solvent. After the reaction, the flash operation separates the hydrogen from the product stream and a recycle stream could be connected to the input. The solvent and the product stream can be separated in a single distillation column based on the boiling point difference in 2-butanol (100 °C) to THFA (178°C) & FAL (170 °C). THFA (98 mol%) and FAL (2 mol%) form an inseparable azeotrope at very low concentrations estimated by the binary analysis in Aspen Plus. Therefore, the product stream contains 98 % THFA with FAL as an impurity.



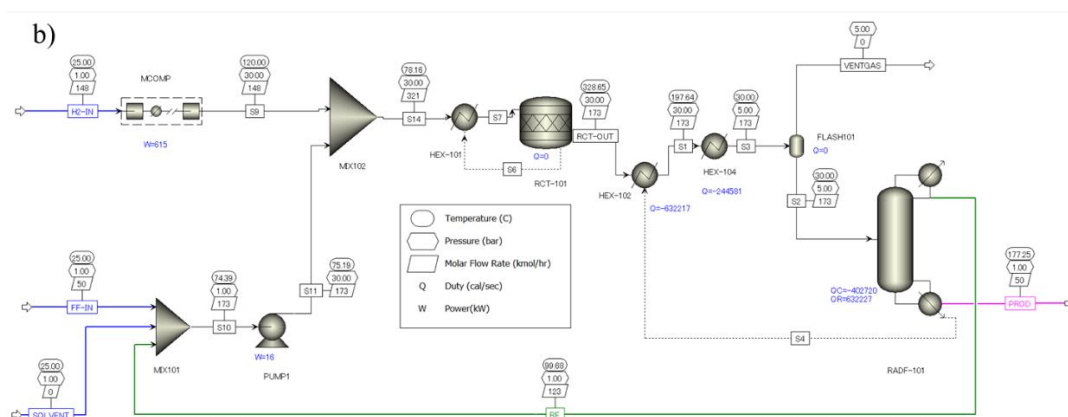


Fig.5.1: a) Schematic and b) Aspen plus flowsheet of furfural hydrogenation to THFA

5.2.2 Details of process simulation

First, furfural and solvent 2-butanol were mixed in Mix-101 to pump to Mix-102 at 30 bar pressure. The hydrogen was first compressed to 30 bars in a compressor which was mixed with the incoming furfural and 2-butanol stream. After that, the reactant stream was heated to the reaction temperature (140 °C) in a heat exchanger (Hex-101). The heated reaction mixer was sent to the stoichiometric reactor (RCT-101). The temperature of the product stream was increased because of the exothermic reaction. The product stream was first cooled in the second heat exchanger to a temperature of 197 °C from 320 °C using cooling water as a utility. This heat was utilized to generate process steam which can be used in the reboiler of the distillation column. After that, the product stream temperature was brought down to room temperature using a first-generation refrigerant. Next, the left-over hydrogen was separated from the flash, either recycled back or vented through the purge. The downstream products from the flash were sent to a distillation column (RADF-101) to separate the 2-butanol from the product stream. The distillation column was operated under total condenser condition with 18 stages with feeding above at stage 10 to obtain a product stream composed of THFA, FAL and a very low amount of 2-butanol. The solvent 2-butanol was recovered (98.95%), which was recycled back to the feed stream. At first, 2-butanol was supplied through the solvent stream to make the first run in an open-loop mode. After that, a free stream with the output specifications of the recycle stream was added to the Mix-101. Finally, the loop was closed by reconnecting the added free stream to the distil output of the RADF-101 column,

completing the loop process. Finally, the makeover solvent flow was added to the input stream to cover the loss of the solvent.

5.2.3 Economic analysis

The economic analysis was simulated in Aspen Energy Economic Analyzer (APEA). First, the stream prices based on the data available were entered and then economic analysis was processed. Table 5.1 lists the prices of the raw materials. Biomass-derived furfural was considered as a raw material for this process. Zang et al. have reported techno-economic analysis of integrated furfural production from biomass and set a minimum furfural selling price of 6.25 \$/kg, which is 37% lower than the current furfural market price[7]. Hydrogen supply was considered from the methane pyrolysis reported in Hydrogen Economy 2020, which reported a minimum hydrogen selling price of 5.4 \$/kg[9][10]. The cheapest available 2-butanol sources were considered from Antera Agro Chem, India. Dalvand et al. have mentioned a minimum product (THFA) selling price of 17.37 \$/kg [8]. However, recent reports on the production of THFA from China indicate the minimum selling price at 23.2 \$/kg [11]. Table 5.2 displays the cost of utilities used in this process to heat up and cool down the process streams mentioned in the literature [8].

Table 5.1: Raw material and product costs

Raw material	Price \$/kg	Ref.
Furfural from biomass	6.25	[7]
Hydrogen	5.4	[9]
2-butanol	2	Antera Agro Chem, India
THFA	17.37	[8]

Table 5.2:Utility costs

Utilities	Cost
Electricity	0.06 \$/kWhr
HPSTEAM	17.7 \$/GJ
MPSTEAM	14.19 \$/GJ
LPSTEAM	13.28 \$/GJ

REF1	27.4 \$/GJ
WATER	0.2 \$/metric ton

5.3 Results and discussions

5.3.1 Stream results

After a successful simulation run, the results were available without any errors or warnings, and the stream results summary is mentioned in Table 5.3. Table 5.3 shows the raw material input streams such as FF-IN, H₂-IN, and SOLVENT specified at a temperature of 25°C, the pressure of 1 bar, and the existing phase. Assuming the complete conversion of furfural to yield 98 % of THFA and 2% of FAL, the product stream (PROD) is composed of 49 kmol/hr of THFA and 1 kmol/hr of FAL, which could not be separated by rigorous distillation because of the formation of azeotrope boiling mixture at such very high and low concentrations with the specified flowrate. However, the product stream is considered 98% purity, and the plant's selling price was set for this purity. After the successful separation of the solvent, it is recycled (RE stream) back to the input stream with 99% purity.

Table 5 3: Summary of stream results

Description	Units	FF-IN	H ₂ -IN	PROD	SOLVEN T	RE
Temperature	°C	25	25	177.25	25	99.68
Pressure	bar	1	1	1	1	1
Phase		Liquid	Vapor	Liquid	Liquid	Liquid
Mole Flows	kmol/hr	50	148	50	0.002278	122.53
Furfural		50	0	0	0	0
FAL		0	0	0.999	0	0.0060
THFA		0	0	49	0	1.269
H ₂		0	148	0	0	0
2-butanol		0	0	6.85E-06	0.002278	121.25
Mole Fractions						
Furfural		1	0	0	0	0

FAL	0	0	0.02	0	4.91E-05
THFA	0	0	0.98	0	0.0103
H ₂	0	1	0	0	0
2-butanol	0	0	1.37E-07	1	0.9895

5.3.2 Cost flow analysis

Table 5.4 describes the cost of the equipment and installation cost. The cost includes purchasing and installing various unit operation blocks such as flash, heat exchangers, reactor, and the distillation column. It can be seen that the MCOMP has a high cost compared to other equipment, given the compression pressure duty from 1 bar to 30 bar, which essentially needs a minimum of 3 stages (compresses the pressure in the order of 3^3). It also can be observed that the installation costs are more than equipment costs considering the plant construction and the stream connection. The equipment and installation costs are about 80% of the capital costs. The rest of the cost was assigned to initial raw material, utility and operational costs.

Table 5. 4: Cost of the equipment

Name	Equipment Cost [USD]	Installed Cost [USD]
FLASH1-flash vessel	20200	116400
MCOMP	1961200	2111800
RADF-101-cond	14600	85600
RADF-101-cond acc	12900	94200
RADF-101-reb	31500	112300
RADF-101-reflux pump	5800	36900
RCT-101	93300	310400
PUMP1	52400	87600
HEX-101	16100	94700
HEX-102	12500	119700
HEX-103	24400	197400

Table 5.5 explains the operation of the plant and its cost flow. As the formation of THFA from furfural is an exothermic reaction, the heat generated in the reactor could be

used to free heat the products and also can be supplied to the reboiler by making heat integration of the process. This heat generation in the process makes the required total heat duties negligible. To cool down the liberated heat, a cooling duty of 4.98×10^6 KJ/hr should be provided using a first-generation refrigerant. This determined the cost flow of the utilities, which were basically the purchase cost of cooling utilities throughout the year. The inclusion of initial heat flow cost was added to the net cost, due to which net was increased from the cooling cost flow. The overall net cost flow indicates (4.09×10^8) is on the profit side, which can determine the payback period of the capital investment.

Table 5.5: Operating cost summary

Total heating duty (kJ/hr)	0
Total cooling duty (kJ/hr)	4.98×10^6
Net duty (Total heating duty - Total cooling duty) (kJ/hr)	-4.98×10^6
Total heating cost flow (\$/year)	0
Total cooling cost flow(\$/year)	9.09×10^4
Net cost (Total heating cost + Total cooling cost) (\$/year)	5.9×10^5
Electric power (kWh)	558.13
Electric power cost (\$/year)	2.9×10^5
Total utility cost (\$/year)	3.8×10^5
Stream cost	
Net cost flow of feeds (\$/year)	3.5×10^8
Net cost flow of products (\$/year)	7.6×10^8
Overall net cost flow (\$/year)	4.09×10^8

The summary of the plant economics is shown in Table 5.6. It shows the capital investment needs to start the plant. The costs are reported yearly to understand the plant data cumulatively. The primary cost of the plant arises from the raw material, operations, and utilities. Considering a typical plant life of 30 years, the desired rate of return life of the plant takes 20 years and the rest of the time (10 years) would make the plant go into fully profit mode. Considering the capital investment, the payback period is only 1.4 years, which means the plant can run on the profits made from the returns on the product. In other words, after 1.4 years, the cost of the plant is basically operating and utility costs

which the product could cover returns. Thus, the economics of the furfural process of hydrogenation could make the plant's breakeven point after 1.4 years of operation.

Table 5.6: Summary of the plant economics

Total Capital Cost [USD]	7665180
Total Operating Cost [USD/Year]	383416000
Total Raw Materials Cost [USD/Year]	350974000
Total Product Sales [USD/Year]	760261000
Total Utilities Cost [USD/Year]	2113680
Desired Rate of Return [Percent/Year]	20
Plant life [Year]	30
P.O. Period [Year]	1.3559
Equipment Cost [USD]	2387900
Total Installed Cost [USD]	3742700

5.4 Conclusions

In summary, hydrogenation of furfural to THFA using the catalytic activity results of Ni1Cu1-Al1 R catalysts studied in this thesis was simulated in Aspen plus V11 using a PENG-ROB thermodynamic model. The simulation model was built using an RTSOIC reactor based on the conversion of furfural. The product stream is composed of 98% THFA and 2% FAL. The formation of an azeotrope at such high THFA and low FAL concentrations limited the product stream to the above-mentioned composition. Since the formation of THFA was an exothermic reaction, the liberated heat was used in the process, which could be sufficient to provide the heat for heating the feed stream and has aided the reboiler heat supply. The economics of the plant were calculated based on the current prices of the hydrogen, 2-butanol, and furfural from a biomass process plant and the selling price of the THFA. The economic analysis signified the capital investment to start the plant, which could be covered within 1.4 years, reaching the breakeven point of the plant. However, given the operational and utility costs, it takes a minimum of 20 years to run the plant entirely on a profit basis. Further information on the kinetics of the reaction would provide an actual batch reactor process simulation which could be compared to the existing THFA production process and could be an attractive process for implementing this catalytic system industrially.

5.5 References

- [1] L. Z. Huang, M. G. Ma, X. X. Ji, S. E. Choi, and C. Si, "Recent Developments and Applications of Hemicellulose From Wheat Straw: A Review," *Front. Bioeng. Biotechnol.*, vol. 9, no. June, pp. 1–14, 2021.
- [2] A. Fuente-Hernandez, P.-O. Corcos, R. Beauchet, and J.-M. Lavoie, "Biofuels and Co-Products Out of Hemicelluloses," *Liq. Gaseous Solid Biofuels - Convers. Tech.*, pp. 3–46, 2013.
- [3] S. Peleteiro, S. Rivas, J. L. Alonso, V. Santos, and J. C. Parajó, "Furfural production using ionic liquids: A review," *Bioresour. Technol.*, vol. 202, pp. 181–191, 2016.
- [4] M. J. Climent, A. Corma, and S. Iborra, "Conversion of biomass platform molecules into fuel additives and liquid hydrocarbon fuels," *Green Chem.*, vol. 16, no. 2, pp. 516–547, 2014.
- [5] Z. Yang *et al.*, "Process design and economics for the conversion of lignocellulosic biomass into jet fuel range cycloalkanes," *Energy*, vol. 154, pp. 289–297, 2018.
- [6] J. F. Leal Silva, A. P. Mariano, and R. Maciel Filho, "Economic potential of 2-methyltetrahydrofuran (MTHF) and ethyl levulinate (EL) produced from hemicelluloses-derived furfural," *Biomass and Bioenergy*, vol. 119, no. March, pp. 492–502, 2018.
- [7] G. Zang, A. Shah, and C. Wan, "Techno-economic analysis of an integrated biorefinery strategy based on one-pot biomass fractionation and furfural production," *J. Clean. Prod.*, vol. 260, p. 120837, 2020.
- [8] K. Dalvand, J. Rubin, S. Gunukula, M. Clayton Wheeler, and G. Hunt, "Economics of biofuels: Market potential of furfural and its derivatives," *Biomass and Bioenergy*, vol. 115, no. August 2017, pp. 56–63, 2018.
- [9] "Hydrogen Economy 2020." [Online]. Available: https://en.wikipedia.org/wiki/Hydrogen_economy.
- [10] D. Kim and J. Han, "Comprehensive analysis of two catalytic processes to produce formic acid from carbon dioxide," *Appl. Energy*, vol. 264, no. February, p. 114711, 2020.
- [11] R. K. Schmidlein, "Tetrahydrofurfuryl Alcohol from China October 2020 U . S . International Trade Commission," vol. 1046, no. 731, 2020.

Chapter 6: Summary and future prospects

In summary, this thesis work is focused on upgrading the hemicellulose-derived furfural and furfuryl alcohol (FAL) to fine chemicals and fuel additives to make good use of biomass in finding alternative renewable sources to the ever-depleting fossil fuels. This work also focussed on developing new, non-noble, and inexpensive catalysts to accommodate the up-gradation of furfural and FAL. Although furfural and FAL have a good market in the polymer and adhesive industry, the low energy value and cold flow properties hinder their application in the transportation sector. Instead, they can be upgraded to low-cost fuel additives and fine chemicals, making them suitable candidates as starting chemicals in the fuels sector. Therefore, in upgrading FAL and furfural to butyl levulinate (BL) and tetrahydrofurfuryl alcohol (THFA), respectively, which serve as a gasoline additive and a green industrial solvent, the following conclusions and prospects are derived from this study.

6.1 butanolysis of FAL to BL

6.1.1 Summary

In conclusion, to upgrade FAL to BL, the acidic strength of the catalyst is a key factor in achieving high yields of BL. In this regard, first, mesoporous $\text{WO}_3\text{-ZrO}_2$ catalysts prepared by evaporative induced self-assembly method were employed. The calcination temperature (800 °C) and the WO_3 loadings (15 Wt.%) were optimized based on BL yield to induce the best catalytic activity. The catalysts were characterized by BET, FTIR, pyridine-FTIR, and $\text{NH}_3\text{-TPD}$ techniques to study the physicochemical properties and the catalytic activity. The electron transfers of tungsten to oxygen and vice versa in the octahedral phase derived the acidity of the catalyst. This acidic strength activated the outer hydroxyl group of the FAL molecule to produce the reaction intermediate 2-butoxymethylfuran (2-BMF) with complete conversion and was moderate in the ring-opening of 2-BMF to yield low results of BL (28 mol%). To further activate the acidic strength of $\text{WO}_3\text{-ZrO}_2$ catalysts, noble (Pt and Pd) and non-noble metals (Fe, Co, Ni, and Cu) were used as promoters. However, no significant change in the yield of BL was observed. The reaction temperature is also influenced the BL yield. Increasing temperatures promoted the BL yield. However, it also promoted the FAL polymerization,

another concern at high reaction temperatures. After that, a biomass-derived sulfonated carbon catalyst was employed for this reaction.

The partial carbonization of sucrose resulted in the development of surface hydroxyl, phenolic, and carboxylic acidic groups, which have yielded 34 mol% of BL yield caused by the presence of phenolic, hydroxyl, and carboxylic acid functional groups. This carbon catalyst was further enhanced by the incorporation of strong Bronstedic –SO₃H groups by the sulfonation process, which induced a maximum surface acidity of 2.357 mmol/g to produce BL yield as high as 80 mol%. The increasing reaction temperature increased the BL yield while limiting the FAL polymers to only 20 mol%. The effect of the initial FAL concentration study revealed a further decrease (butanol:FAL ratio less than 8.5) of the initial mole ratio, resulting in decreasing the BL yield accompanied by FAL polymerization. The time profile of the study indicated that the formation of BL from 2-BMF is slower than the formation of 2-BMF from FAL, signifying the former step as a rate-determining step. Thus, this catalytic system produced high yields of BL at a butanol:FAL ratio as low as 8.5. The deactivation study described that the weakly bonded –SO₃H groups were detached from the carbon network, resulting in the reduced catalytic activity to produce 49 mol% of BL yield after 3 recycles with 100% FAL conversion. The catalyst regenerated again by performing the sulfonation process under similar conditions, resulting in a 78 mol% BL yield. Thus, this study explained the importance of catalyst acidic strength by employing two different catalysts and the reaction parameter study, such as the effect of reaction temperature, initial FAL concentration, and the reaction time.

6.1.2 Future prospects of butanolysis of FAL to BL

Butyl levulinate is an emerging gasoline additive that decreases the pollutant's formation by acting as an anti-oxidant in the fuel and also enhancing the fuel's octane/cetane number, thereby increasing its quality. The higher energy density and immiscibility with water make BL a suitable additive than other alkyl levulinates. However, the production routes of such an important fuel additive are limited, and a rigorous study has been done in the past few years. The detailed kinetic study of butanolysis of FAL to BL would provide much-needed information in developing a simulation process. The simulation results would provide more insights into the techno-

economic analysis, which could project the efficient production and market usage of BL as a fuel additive.

6.2 Hydrogenation furfural

Furfural can be easily obtained by dehydration of xylose, the main constituent in hemicellulose biomass. Furfural is an important platform chemical with a wide range capacity to produce C₄ and C₅ liquid fuels and value-added chemicals. Among the many transformative processes, the direct hydrogenation of furfural to produce the industrial green solvent such as THFA gained much attention because of the moderate reaction conditions and high selectivity with low or no undesired products. Many kinds of noble and non-noble metal catalysts were employed for this reaction, especially Pd, Ni and Cu, due to their excellent interaction strength towards furfural molecule. However, the research on simple catalyst preparation with non-noble metals and the low hydrogen pressure requires much attention to realize this process industrially. Thus, this study aimed in developing an inexpensive, efficient and versatile non-noble catalyst to achieve high yields of THFA under moderate conditions.

6.2.1 Summary of hydrogenation of furfural

In summary, furfural hydrogenation was studied using the synthesized NiCu-Al catalysts. The catalysts are prepared by the co-precipitation method, which were calcined and reduced at 500 °C to obtain the final form of the catalysts. The bimetallic NiCu on Al catalysts, especially equal molar catalyst (Ni₁Cu₁-Al₁ R), has developed stable Ni-Cu alloys on the Al surface with near equal Ni/Cu surface ratio, which was crucial in inducing high catalytic activity. This catalyst displayed excellent physicochemical properties to produce high yields of THFA compared to the monometallic catalysts. Al content has affected the metal dispersion in the bimetallic catalysts. The catalyst characterization by BET, TPR, XRD, CO & N₂O pulse, NH₃-TPD, SEM, TEM, STEM-EDS, and XPS analysis revealed detailed information about the textural, reducible species, phase properties, metal dispersion, probe molecule adsorption, topographical, and oxidation state of the metals to understand the detailed catalyst synthesis and formation process. Additionally, the formation of Ni-Cu alloys which were considered catalytically high active sites generated by the synergetic effect caused by the electronic exchange energy between Ni and Cu metals.

The hydrogenation reaction with Ni-Al and Cu-Al catalysts revealed that Cu was highly active for only the carbonyl group while Ni was active for both the carbonyl group and furan ring of furfural. The reaction parameter optimization study notified a significant effect by the reaction pressure and the time profile study indicated the formation of THFA from FAL. Additionally, the selection of solvent has influenced the yield of THFA. For example, 2-butanol has shown good solvent characteristics without forming dehydration products compared to 2-propanol and also promoted the reaction with its hydrogen donor capacity. The spent analysis study of the catalyst inferred the good reusability and regeneration ability of the Ni1Cu1-Al1 R catalyst.

The electrocatalytic hydrogenation (ECH) of furfural was carried out to widen the applicability of furfural conversion techniques. ECH of furfural was conducted using Ni foam, Cu foam, Cu foil, and Ni1Cu1-Al1 R/ Cu foam electrodes. Ni foam and Cu foam have shown contrast oxidation and reduction behaviour, respectively. Cu foam has shown a good reduction ability of furfural to 2-methyl furan (2-MF) and FAL. Additionally, incorporating the Ni1Cu1-Al1 R catalyst onto Cu foam enhanced the Cu foam activity with increasing selectivity of 2-MF while suppressing the undesired products. Thermal catalytic hydrogenation (TCH) and ECH routes have produced different products with the same catalyst material. Thus, the product selection can be selectively tuned by changing the conversion technology while using the same material as a catalyst.

The furfural hydrogenation process was simulated in Aspen Plus to evaluate the economic potential of the THFA product. The model was built using the best catalytic results of Ni1Cu1-Al1 R catalyst, and Peng-Robinson thermodynamic model was used to evaluate the property methods of furfural, FAL, THFA, and 2-butanol. The current prices of the respective compounds and utilities were added to the stream price to evaluate the economic analysis. The plant has shown positive profit data with pay over a period limited to just below two years and a minimum of 20 years to go in complete profit mode. However, this techno-economic analysis was based on the ideal scenario of the plant. For a realistic economic analysis, the kinetic data for this catalytic system could provide a comprehensive view of plant economics.

6.2.2 Future prospects of furfural utilization

The literature review shows many studies on the hydrogenation of furfural using various catalysts and process simulation models. However, not many simulation models are based on the reaction's kinetic data. Instead, they are based on the performances of the catalysts. Estimating kinetic parameters using power law, equilibrium, and Langmuir-Hinshelwood (L-H) models would provide more insights into the catalytic adsorption of hydrogen, rate of the reaction, and the time-based rate of formation of THFA. Additionally, the kinetic parameters, including the partial hydrogen pressure, would provide more realistic data that could give the simulation models an actual prediction and techno-economic analysis to realize the process at an industrial scale.

In the present situation, what appears to be clear is that the reactions involved in the up-gradation of platform chemicals to fuel additives and value-added chemicals are classical reactions of organic chemistry where the reaction mechanism and the employed catalysts are known. In these reactions, the type of catalysts used generally determines the reaction mechanism path, which is needed to understand the reactions to design a suitable production environment comprehensively. Regardless, greener processes should be developed by synthesizing versatile and high efficient catalysts as an alternative to industrial acids and bases.

APPENDIX

A.1 Methodology

The liquid phase batch reactions were carried out in high-pressure batch reactor (Parr instruments) equipped with a heating mantle and controller for pressure, temperature, and agitation speed. Fig. A1 schematic and photograph of the reactor. N₂ and H₂ gas lines were connected to the gas inlet of the reactor to pressurize the reactor. The maximum initial pressure allowed was 50 bar because of the safety concerns. A recirculating water coolant line was connected to the agitator section of the reactor. The intermediate reaction samples were collected through liquid sample valve. The gas outlet has two separate lines, one is for collecting a gas sample and another for the vent.

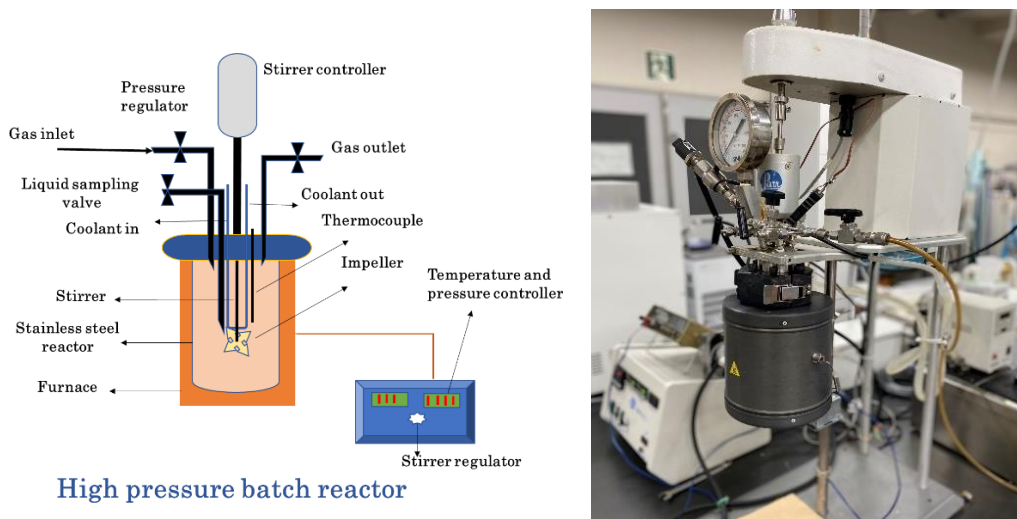


Fig.A1: Schematic (left) and photograph (right) of high-pressure batch reactor

A.2 Catalyst preparation

The schematic representation of the catalysts preparation methods that were employed in this study are shown by Fig.A2, Fig.A3, and Fig.A4. The detailed preparation methods were discussed in the chapter 2 and chapter 3.

Fig.A2 shows the synthesis of mesoporous tungstated zirconia (WO₃-ZrO₂) catalysts by evaporation induced self-assembly (EISA) method. In a typical synthesis, first, metal precursors and surfactants were dissolved in ethanol and aged with a

continuous stirring for 12 hours during which the deposition and formation of micelles would happen. After that, the solvent evaporation allows the formation of organic-inorganic hybrid structure. Thus, dried catalyst was grounded to a fine powder. Finally, the thermal treatment (calcination) removes the template to get mesoporous catalyst.

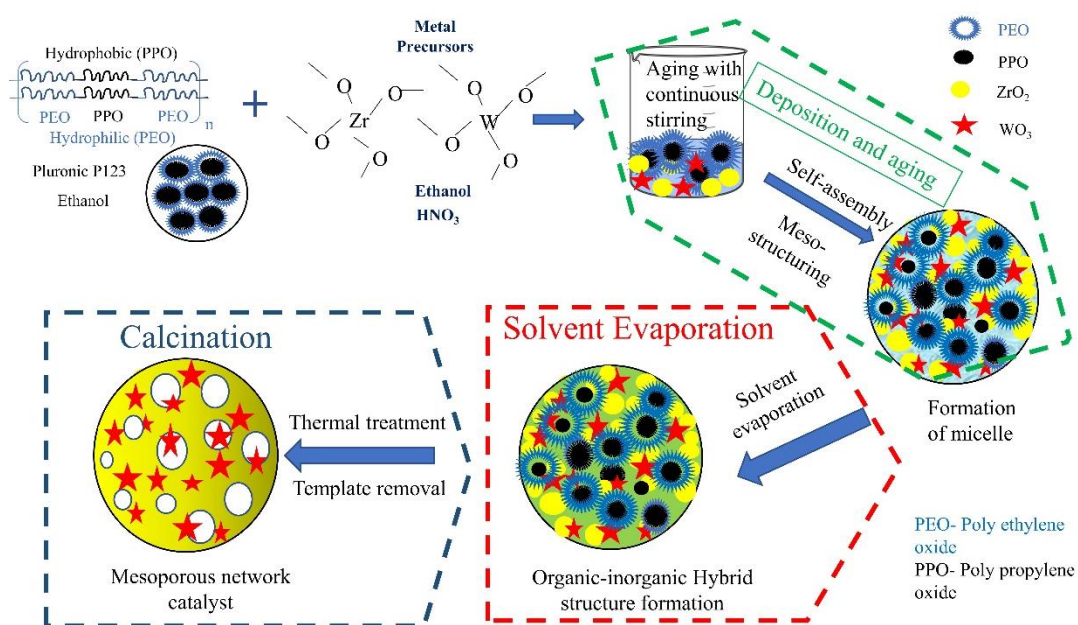


Fig.A2: Preparation of mesoporous $\text{WO}_3\text{-ZrO}_2$ catalysts by EISA method

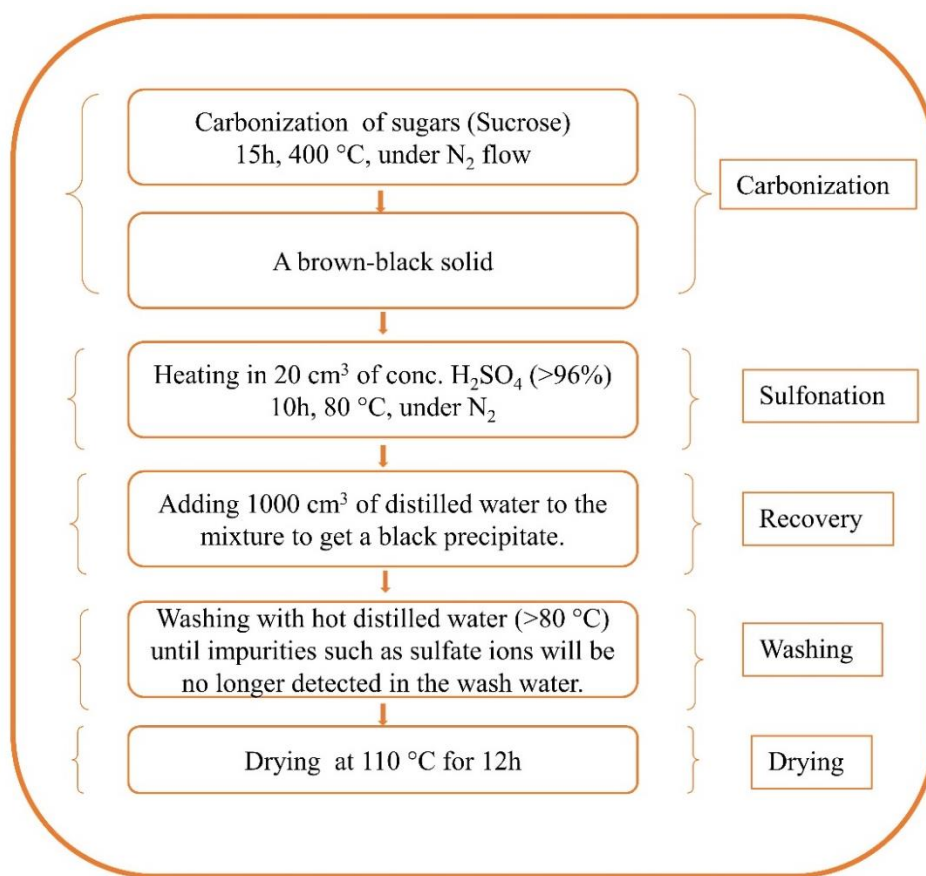


Fig.A3: Preparation sulfonated carbon (-SO₃H/C)

Fig.A3 describes the preparation of sulfonated carbon catalyst. First, the carbonation of sucrose to obtain a brownish black solid which was undergone sulfonation process under N₂ flow for 10 hours to incorporate the -SO₃H groups into the carbon network structure. After that, the solid black was collected, washed and dried to get the final form.

Fig.A4 illustrates the preparation of Ni-Al, Cu-Al, and NiCu-Al catalysts to develop a hydrotalcite like structure by a modified co-precipitation method. The precipitation of metal precursors was obtained by using Na₂CO₃ solution while NaOH was used to maintain the pH of the solution to control the particle size. After that, to promote the crystallization of metals on Al and to develop hydrotalcite like structure, the solution was kept at 65 °C for 18h in the Parr reactor. After that, the precipitate was washed and dried for 12 hours at 80 °C to obtain a solid. Finally, thus obtained solid was grounded to affine

powder to perform calcination and reduction process to obtain the final form of the catalysts.

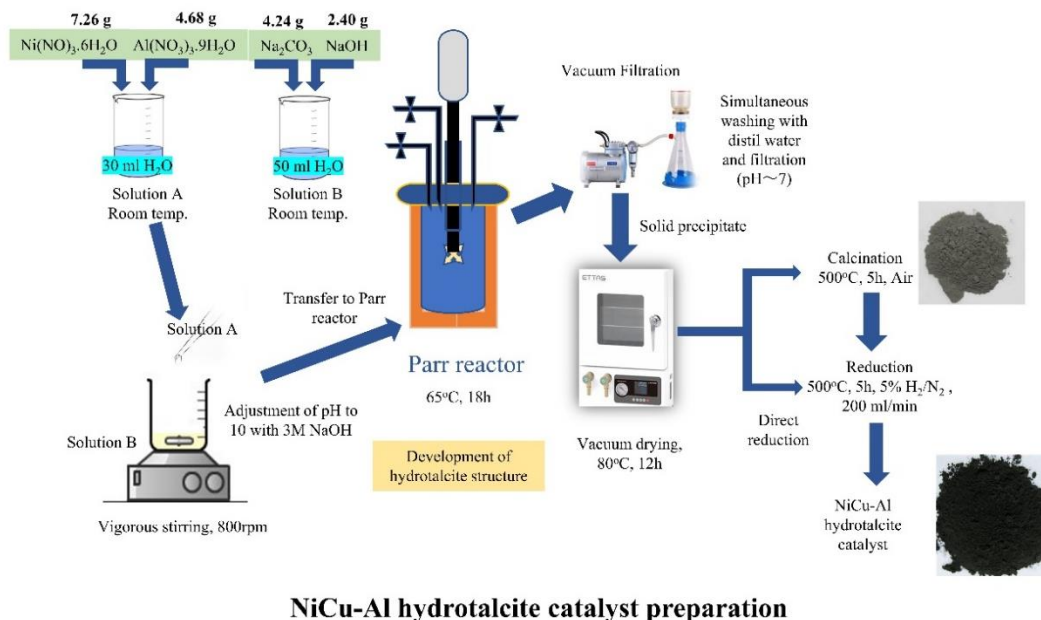


Fig.A4: Preparation of hydrotalcite NiCu-Al catalysts

A.3 Liquid product analysis

All the liquid products were quantified by GC-FID analysis against an internal solvent (CCl₄ or methanol) using the response factor (RF) of the calibrated data. The calibration data was obtained as following.

- i. First, varying amounts of reactants and products were added to a fixed amount of the internal solvent. The Wt. ratio was calculated based on the amounts of the samples taken.
- ii. Next, the samples were analysed by GC-FID to obtain the peak areas of the solvent and the chemical compounds.
- iii. After that, GC-FID peak area ratios were calculated.
- iv. Finally, the linear calibration plots were obtained by plotting Wt. ratio vs GC-FID peak area ratio data.

The following equation was used to quantify the product samples.

$$\text{Weight of the compound} = \text{RF} * \frac{\text{PA of the compound}}{\text{PA of the solvent}} * \text{weight of the solvent}$$

RF= Response factor w.r.t solvent, PA = Peak area

A.3.1 Butanolysis of FAL

Fig.A5a and b represents the chromatograms of butanolysis of FAL before and during the reactions. The product samples were quantified using the respective calibration data shown in Fig.A6.

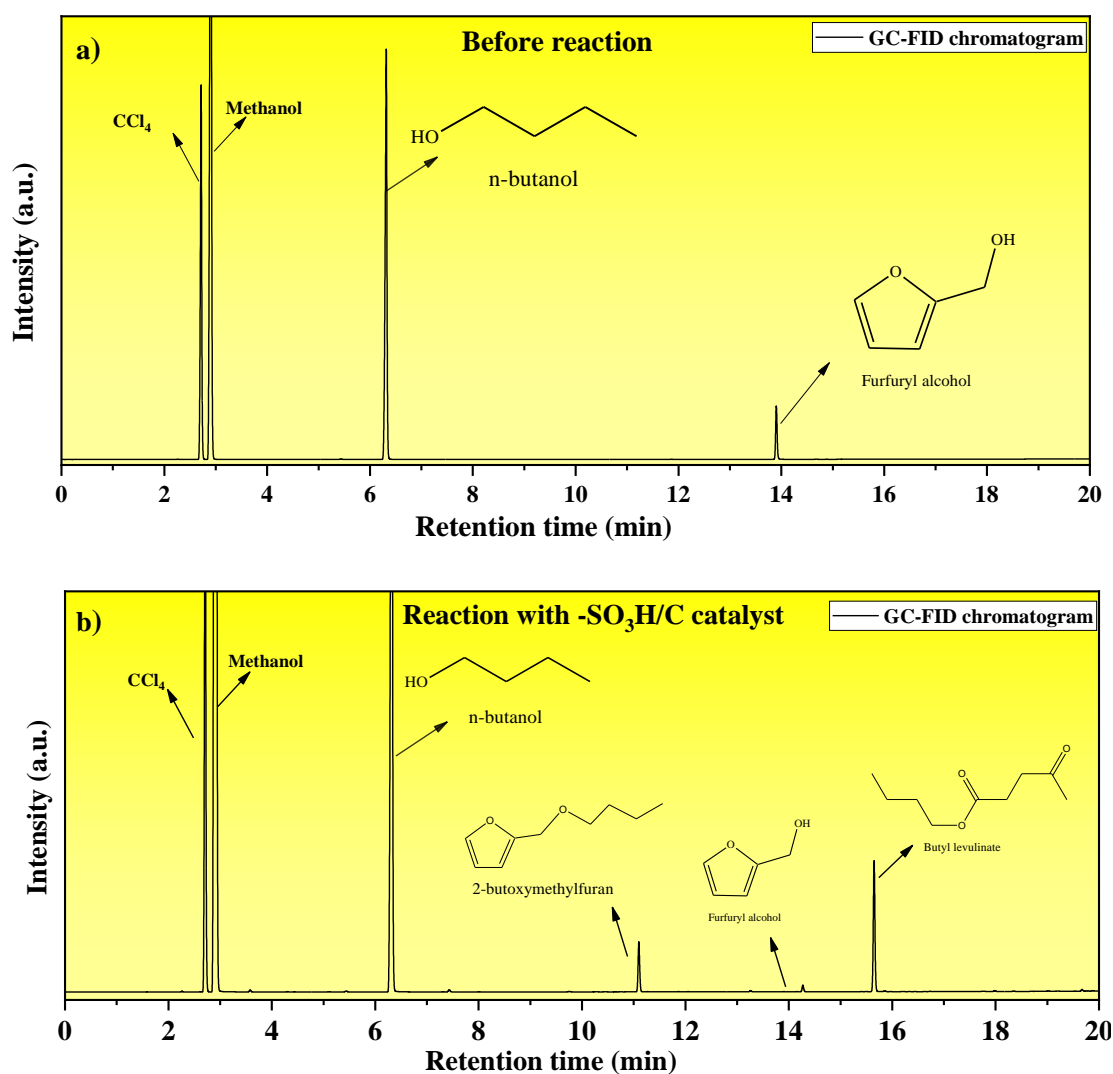


Fig.A5: GC-FID chromatograms a) before the reaction, b) reaction after 4 hours

Reaction conditions: 190 °C, 30 bar N₂, 400 rpm, 0.5 g -SO₃H/C catalyst

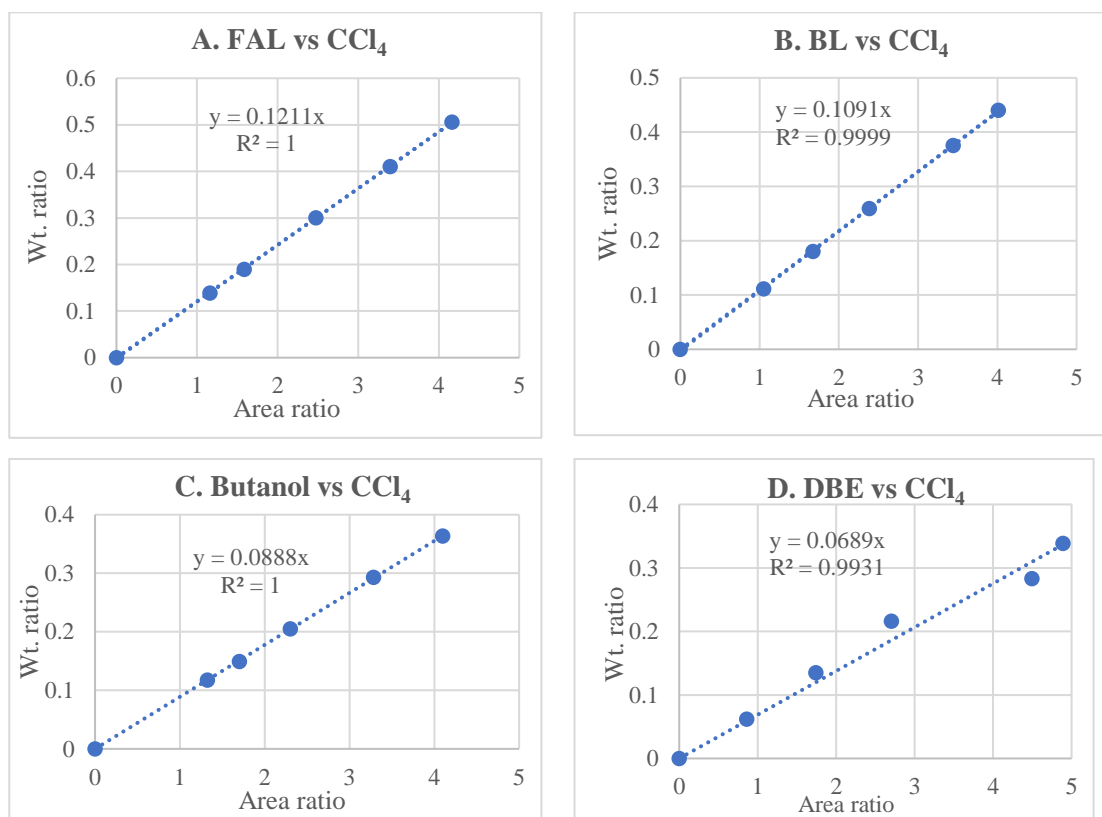
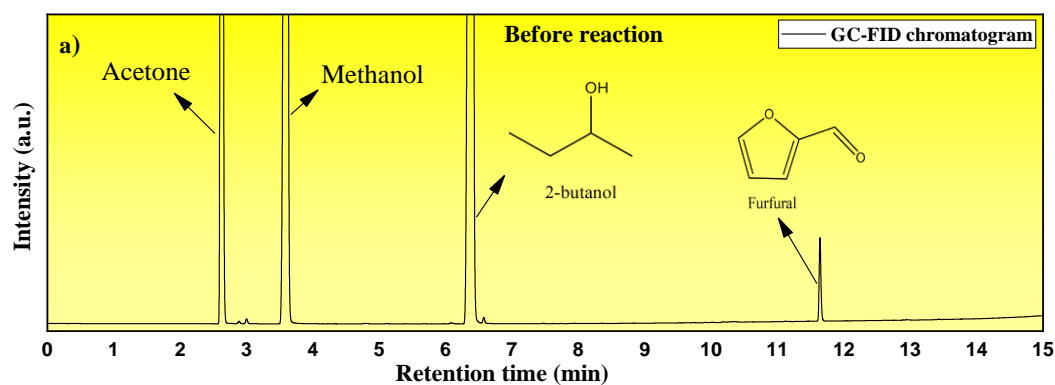


Fig.A6: Calibration data w.r.t CCl₄ solvent of A) FAL, B) BL, C) butanol, D) DBE

A.3.2 Furfural hydrogenation

Fig.A7a and b represents the chromatograms of hydrogenation of furfural to THFA before and during the reactions. The quantification of the product samples was calculated using the respective calibration data shown in Fig.A8.



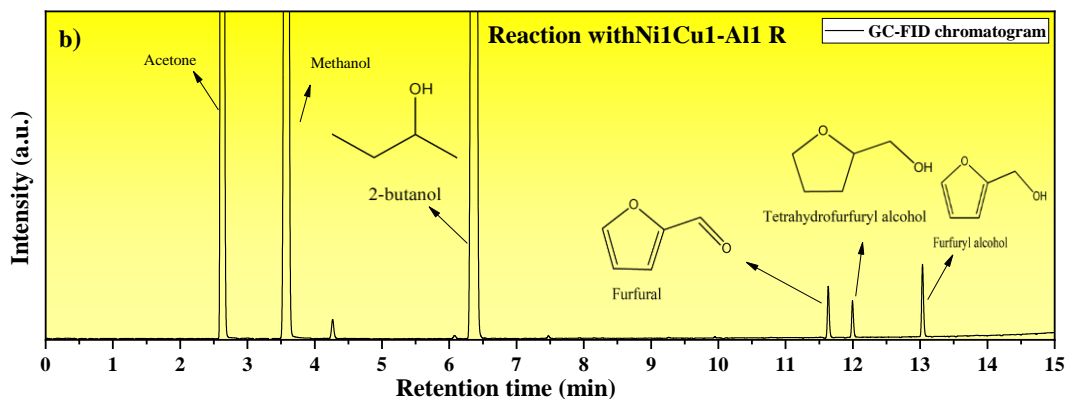
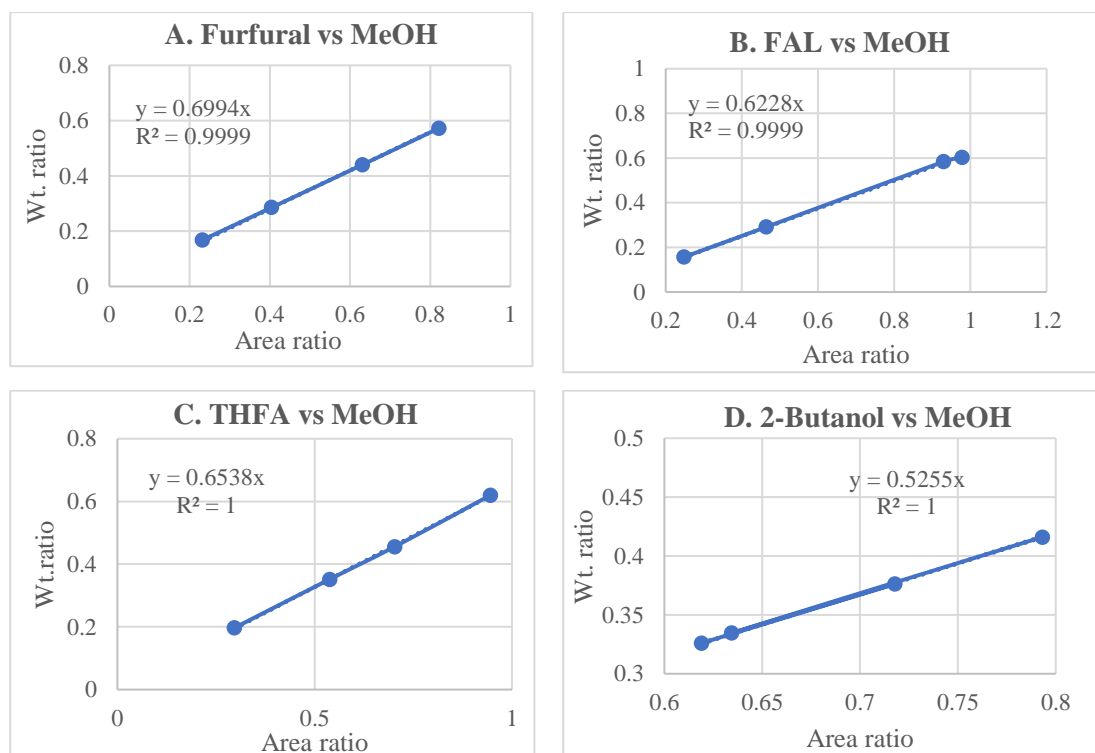


Fig.A7: GC-FID chromatograms a) before the reaction, b) reaction after 2 hours

Reaction conditions: 140 °C, 30 bar H₂, 600 rpm, 100mg Ni₁Cu₁-Al₁ R catalyst



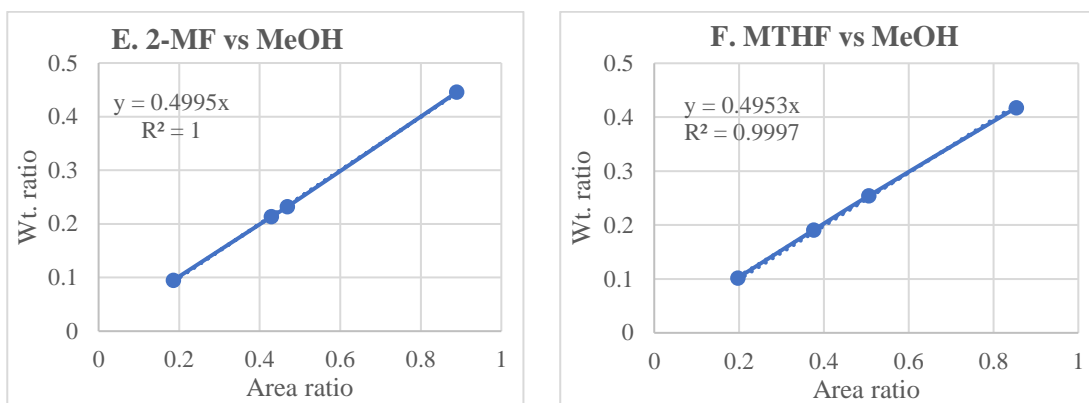


Fig.A8: Calibration data w.r.t methanol (MeOH) solvent of A) Furfural, B) FAL, C) THFA D) 2-butanol, E) 2-MF, F) MTHF